

**FABRICATION OF LEAD FREE AND  
LEAD BASED 1-3 PIEZOELECTRIC  
COMPOSITES FOR HIGH FREQUENCY  
ULTRASOUND TRANSDUCERS**

By

**TANIKAN THONGCHAI**

A thesis submitted to The University of Birmingham  
for the degree of  
DOCTOR OF PHILOSOPHY

School of Metallurgy and Materials  
College of Engineering and Physical Sciences  
University of Birmingham  
September 2017

UNIVERSITY OF  
BIRMINGHAM

**University of Birmingham Research Archive**

**e-theses repository**

This unpublished thesis/dissertation is copyright of the author and/or third parties. The intellectual property rights of the author or third parties in respect of this work are as defined by The Copyright Designs and Patents Act 1988 or as modified by any successor legislation.

Any use made of information contained in this thesis/dissertation must be in accordance with that legislation and must be properly acknowledged. Further distribution or reproduction in any format is prohibited without the permission of the copyright holder.

## Abstract

This thesis is concerned with the fabrication and characterisation of lead free piezocomposites and transducers for use in high frequency medical ultrasound imaging applications. A water based gel casting and micro moulding approach has been developed to fabricate 1-3 composites with a random pillar structure in the lead free piezoelectric material  $(\text{Ba}_{0.85}\text{Ca}_{0.15})(\text{Zr}_{0.1}\text{Ti}_{0.9})\text{O}_3$  or (50BZCT). High frequency transducers incorporating the random composites as the active components have been fabricated, characterised and demonstrated in real tissue imaging environments, For comparison, lead zirconate titanate (PZT) composites and transducers have been fabricated using the same techniques.

A water based gel casting system has been used incorporating Hydantoin Epoxy resin, amine hardener (Bis (3-aminopropyl) amine) and dispersant. The optimum quantity of hardener, resulting in the highest green strengths, was found to be 18 g hardener per 100 g of resin for both the 50BCZT and PZT systems. Viscosities of the 50BCZT and PZT systems were minimised by the addition of 2.4 and 1 wt% of dispersant respectively. The highest green strengths of around 55 and 58 MPa were achieved for the 50BCZT (40 wt% resin content and 45 vol% solids loading) and PZT (40 wt% resin content and 48 vol% solids loading), systems respectively. The influence of sintering temperature on the microstructure, physical, piezoelectric and dielectric properties of the 50BCZT samples revealed a complex behaviour. The highest values of piezoelectric and dielectric properties corresponded to 50BCZT samples fabricated with a gel casting slurry incorporating 30 wt% resin and sintered at 1425 °C, with  $d_{33}$  and  $k_p$  values of 330 pC/N and 0.43, respectively. Too high a resin

content has a deleterious effect on piezoelectric and dielectric properties of the sintered gel cast samples in both materials.

1-3 composites were successfully fabricated from the BCZT and PZT bristle block structures and only one resonance peak corresponding to the thickness mode was observed in all samples, with a complete absence of spurious modes. PZT composites offered generally higher thickness coupling coefficients than 50BCZT composites, where the highest value of 0.78 was measured for samples sintered at temperature 1425 °C. Focused PZT, focused 50BCZT, unfocussed PZT and unfocussed 50BCZT transducers were successfully fabricated using the composites with randomised structure, and have operating frequencies of 35, 40, 50 and 35 MHz respectively.



# Acknowledgements

First of all, I would like to express my deep gratitude to Prof. Tim W Button, my research supervisor, for offering me the opportunity to do this research, for his patient guidance, enthusiastic encouragement and excellent supervision throughout this work.

Special appreciation to Dr. Yun Jiang and Dr. Daniel Sanmartin, my co - supervisors and Mr. Carl Meggs for their useful suggestions, loving inspiration, timely guidance, technical assistance, practical advice on the transducer design and encourage me to work thought some of difficulties in this research.

I should also thank Prof. Stuart Blackburn and Mr. John Wedderburn for their personal training on the viscometer equipment.

I am very much thankful to Prof. Sandy Cochran, Dr. Yongqiang Qiu from the University of Glasgow, for their help in characterizing the lead based and lead free transducer, as well as Dr. Hana Hughes and Dr. Alez Matousek from Central European Institute and Technology for their contributions to the development of lead free powders.

I should also thank all my friends and the members of the Functional Materials Group for their support.

Finally, I would like to express my deepest gratitude to Mr and Mrs. Thongchai, my parents, for their encouragement, support and their love.

# Contents

<b>Contents</b>	
<b>Index of figures</b> .....	VI
<b>Index of tables</b> .....	XVI
<b>Nomenclature and acronyms</b> .....	XVII
<b>Chapter 1 Introduction</b> .....	<b>1</b>
1.1 References.....	3
<b>Chapter 2 Ultrasound imaging for medical applications</b> .....	<b>4</b>
2.1 Medical ultrasound history.....	4
2.2 Understanding Medical Ultrasound Imaging.....	6
2.2.1 Ultrasound waves.....	6
2.2.2 Principles of Ultrasound operation.....	9
2.2.3 Interaction of ultrasound wave with mediums.....	13
2.2.4 Matching ultrasound frequency to clinical applications.....	15
2.3 Basics of ultrasound transducers.....	17
2.3.1 Components and construction of a typical transducer.....	18
2.3.2 Characteristics of ultrasound transducers.....	23
2.3.2.1 Ultrasound beam shape.....	23
2.3.2.2 Ultrasound transducer imaging resolution.....	24
2.4 Summary.....	27
2.5 References.....	27
<b>Chapter 3 Piezoelectric materials, 1-3 randomised piezocomposites design and manufacture for high frequency ultrasound transducer applications</b> .....	<b>30</b>
3.1 Principle of piezoelectricity.....	30
3.1.1 Piezoelectricity.....	31
3.1.2 Poling of piezoelectric ceramics.....	33
3.1.3 Piezoelectric constitutive equations.....	34
3.2 Piezoelectric materials for high frequency ultrasound transducers.....	37
3.2.1 Lead based piezoelectric ceramics.....	38
3.2.2 Lead free piezoelectric ceramics.....	41
3.2.2.1 BaTiO <sub>3</sub> Based Materials.....	42
3.2.2.2 BNT and BKT Based Materials.....	42
3.2.2.3 KNN Based Materials.....	44
3.2.2.4 BCZT Based Materials.....	45
3.2.3 Piezoelectric Polymers.....	49

	3.2.4 Piezoelectric single crystal.....	50
	3.2.5 Piezoelectric composites.....	52
3.3	The crucial property and parameters of 1-3 composites for..... transducer applications.....	55
	3.3.1 Influence of ceramic volume fraction on acoustic impedance and eletromechanical coupling coefficient.....	56
	3.3.2 Influence of piezocomposite geometry on resonance.....	57
3.4	Piezocomposite manufacture for 1-3 piezocomposite.....	63
	3.4.1 Dice and fill.....	64
	3.4.2 Injection Moulding.....	66
	3.4.3 Lost Mould Technique.....	66
	3.4.4 Soft lithography.....	70
	3.4.5 Gel casting.....	71
	3.4.6 Gel casting for high frequency transducer.....	78
3.5	Summary.....	79
3.6	References.....	80
<b>Chapter 4</b>	<b>Aims and objectives of the project.....</b>	<b>89</b>
<b>Chapter 5</b>	<b>Research methods.....</b>	<b>92</b>
5.1	Process procedures.....	92
	5.1.1 Soft mould fabrication process.....	92
	5.1.2 Fabrication of lead based and lead free bulk ceramic by gel casting.....	94
	5.1.2.1 Powder size reduction.....	94
	5.1.2.2 Gel casting slurry preparation, de-airing, casting and drying.....	94
	5.1.2.3 Organic burnout and sintering of green samples... 98	
	5.1.3 Lead based and lead free 1-3 random piezocomposite fabrication.....	102
	5.1.3.1 Gel casting slurry preparation, de-airing, casting and drying.....	102
	5.1.3.2 Organic burnout and sintering of green samples... 103	
	5.1.3.3 Encapsulation of bristle block.....	104
	5.1.3.4 Lapping.....	104
	5.1.3.5 Contact and non-contact poling.....	105
	5.1.3.6 Electroding.....	106
5.2	Characterisation methods.....	110
	5.2.1 Characterisation of rheological behaviour.....	110
	5.2.1.1 Elastic storage and viscous loss modulus..... measurement.....	110
	5.2.1.2 Viscosity measurements.....	110
	5.2.2 Specific surface area measurement.....	111

	5.2.3 Particle size measurement.....	111
	5.2.4 Thermal analysis.....	111
	5.2.5 Density measurement.....	112
	5.2.6 Drying and sintering shrinkages.....	112
	5.2.7 Green strength measurement.....	113
	5.2.8 Dielectric and Piezoelectric property measurements.....	114
	5.2.9 X-ray diffraction analysis.....	114
	5.2.10 Microstructure characterisation.....	115
	5.2.10.1 Optical microscopy.....	115
	5.2.10.2 Scanning electron microscopy and environmental scanning electron microscope.....	115
	5.2.11 Transducer testing.....	116
	5.2.11.1 B-scan testing.....	116
	5.2.11.2 Pulse and echo testing.....	120
	5.3 References.....	120
<b>Chapter</b>	<b>6 Optimisation of the lead free gel casting process.....</b>	<b>121</b>
	6.1 Introduction.....	121
	6.2 Polymerisation of the premix solution.....	122
	6.2.1 Influence of hardener content on the premix solution.....	122
	6.2.2 Influence of reaction temperature on premix solution.....	127
	6.2.3 Influence of resin content on the premix solution.....	129
	6.3 Optimisation of lead free powder and slurries.....	133
	6.3.1 Lead free powder characterisation.....	133
	6.3.1.1 Particle size analysis.....	133
	6.3.1.2 Crystalline material structure.....	136
	6.3.2 Lead free slurries characterisation.....	137
	6.3.2.1 Influence of dispersant concentration on viscosity of lead free slurry.....	137
	6.3.2.2 Influence of solids loading on the viscosity of lead free slurries .....	141
	6.3.2.3 Influence of resin content on viscosity and gelation time of lead free slurries.....	144
	6.4 Characterization of lead free gel casting green bodies.....	148
	6.5 Characterization of lead free gel cast sintered bodies.....	154
	6.5.1 The influence of resin content on the key properties.....	154
	6.5.2 The influence of sintering temperature on the key Properties.....	159
	6.6 Summary.....	164
	6.7 References.....	166

<b>Chapter 7</b>	<b>Optimisation of the gel casting process for lead-based powders.....</b>	<b>170</b>
7.1	Introduction.....	170
7.2	Optimisation of lead based powder and slurries.....	171
7.2.1	Lead based powder characterisation.....	171
7.2.1.1	Particle size analysis.....	171
7.2.1.2	Crystalline material structure.....	173
7.2.2	Organic burnout.....	174
7.2.3	Lead based slurries characterisation.....	175
7.2.3.1	Influence of dispersant concentration on viscosity of lead based slurry.....	175
7.2.3.2	Influence of solids loading on viscosity of lead based Slurry.....	177
7.2.3.3	Influence of resin content on viscosity and gelation time of lead free slurry.....	179
7.3	Characterization of lead based gel casting green bodies.....	182
7.4	Characterization of lead based gel cast sintered bodies.....	187
7.5	Summary.....	191
7.6	References.....	192
<b>Chapter 8</b>	<b>Characterization of lead free and lead based 1-3 random piezocomposites.....</b>	<b>194</b>
8.1	Introduction.....	194
8.2	Fabrication of Green lead based and lead free randomised structures.....	194
8.2.1	Lead free randomised structures.....	194
8.2.2	Lead based randomised structures.....	199
8.3	Sintered lead based and lead free radomised structures.....	202
8.3.1	Sintering of lead free randomised structures.....	202
8.3.2	Sintering of PZT randomised structures.....	209
8.4	Impedance analysis of lead free and lead based 1-3 randomised composites.....	212
8.4.1	Impedance analysis of lead free 1-3 randomised composites.....	212
8.4.2	Impedance analysis of lead free 1-3 randomised composites.....	216
8.5	Functional performance of lead free and lead based 1-3 randomised composites.....	219
8.6	Summary.....	223
8.7	References.....	224

<b>Chapter 9</b>	<b>High frequency transducer fabrication, characterisation and imaging.....</b>	<b>226</b>
9.1	Transducer fabrication.....	226
9.2	Transducer Characterisation.....	233
9.2.1	Electrical impedance.....	233
9.2.2	Pulse-Echo response.....	235
9.2.3	Tungsten wire phantom imaging.....	240
9.3	Imaging of agar phantom and tissue.....	250
9.4	Summary.....	254
9.5	References.....	255
<b>Chapter 10</b>	<b>Conclusions and future work.....</b>	<b>256</b>
10.1	Conclusion.....	256
10.2	Future work.....	260
<b>Appendix I</b>	<b>: Vibration modes and piezoelectric coefficient of standard samples with electrode on the top and bottom.....</b>	<b>262</b>
<b>Appendix II</b>	<b>: Material Properties from electrical impedance and capacitance.....</b>	<b>263</b>
<b>Appendix III</b>	<b>: Conference Presentations.....</b>	<b>265</b>

# Index of Figures

Figure 2.1 shows examples of ultrasound images for human medical applications (a) Cysts in liver, (b) Carotid artery blood flow, (c) 3D of heart image, (d) Baby development.....	5
Figure 2.2 The Acoustic spectrum.....	7
Figure 2.3 Longitudinal and transverse waves through a solid medium.....	7
Figure 2.4 Rayleigh waves through solid.....	9
Figure 2.5 Illustration of ultrasound imaging showing (a) position of transducer, (b) Ultrasound baby scans.....	11
Figure 2.6 Schematic representation of Pulse repetition frequency per unit time...	11
Figure 2.7 Schematic diagrams showing the basic of ultrasound (a) Ultrasound pulse is generated and propagated into organs by applying voltage into piezoelectric transducer, which echo is reflected back at the interface of body tissue and converted to electrical signal by transducer. (b) A-scan mode presents the amplitude of echo are created as a function of time. (c) B-scan mode shows the grey scale of reflected echoes which determined by the amplitude of each returning ultrasound echoes signal. A different shade of grey depending on their intensity for reflection from different tissues, white and dark areas representing strong and weak echoes, respectively (d) M-mode shows the motion mode of object.....	12
Figure 2.8 Schematic illustration of an ultrasound beam encountering a boundary between two mediums of different acoustic impedance.....	14
Figure 2.9 Penetration and resolution of different ultrasound frequency.....	16
Figure 2.10 Attenuation coefficients of a various tissues in the frequency range from 10 to 100 MHz.....	17
Figure 2.11 The basic components of a single element transducer.....	19
Figure 2.12 Schematic of vibrations in active element from applying electricity...	22
Figure 2.13 Schematic of the elimination of vibration from the face of transducer by backing material (a) and (b) the relationship between spatial pulse length and bandwidth.....	22

Figure 2.14 Transducer focusing by (a) curving the active materials (b) utilizing a lens .....	23
Figure 2.15 Schematic of focus of beam from a single element transducer.....	24
Figure 2.16 Schematic of good and poor axial resolution.....	25
Figure 2.17 Schematic of good and poor lateral resolution.....	26
Figure 2.18 How the beam width separate two structures into two images.....	26
Figure 2.19 Schematic diagram of beam width and beam shape from low frequency and high frequency transducer.....	27
Figure 3.1 Crystallographic structures of lead zirconate titanate perovskite crystal (a) tetragonal, (b) cubic and (c) rhombohedral, the direction of polarization are indicated by the arrows.....	33
Figure 3.2 Designation of the coordinate axis for a piezoelectric plate pole along its thickness.....	35
Figure 3.3 Phase diagram of PZT.....	39
Figure 3.4 Phase diagram of binary system BCZT.....	46
Figure 3.5 Phase diagram of binary system BCZT with $\lambda$ phase.....	47
Figure 3.6 Polyvinylidene difluoride in $\alpha$ and $\beta$ phase.....	50
Figure 3.7 Electromechanical coupling coefficient in thickness mode versus acoustic impedance of different piezoelectric materials.....	53
Figure 3.8 Schematic of 2-2, 1-3, 0-3 and 3-3 composites.....	55
Figure 3.9 Electromechanical coupling factor ( $k_t$ ) of 1-3, 3-3 and 3-0 composites and acoustic impedance of 1-3 composite as a function of volume fraction ( $V_f$ ) .....	56
Figure 3.10 The dimensions of 1-3 composite.....	59
Figure 3.11 Randomised 1-3 piezocomposite pattern in 300 $\mu\text{m}$ square section with 40 vol% ceramic phase.....	63
Figure 3.12 Bristle block structure of 1-3 piezocomposite.....	64
Figure 3.13 Schematic procedures of dice and fill technique for making bristle block structure.....	65
Figure 3.14 Viscous polymer processing.....	69
Figure 3.15 Section of green ceramic pillars (a) arcs and (b) hexagonal fabricated by embossing viscous polymer processing paste into polymer moulds, followed by chemical dissolution of the moulds.....	69



Figure 3.16 Schematic presents the formation of egg box model by adding calcium iodate into suspension. The gel can be form after divalent metal ions ( $\text{Ca}^{2+}$ ) are cooperative bound with aligned ribbons at $60^\circ\text{C}$ .....	75
Figure 3.17 The ring open reaction mechanism of epoxy amine.....	77
Figure 3.18 Scanning electron images of green stage ceramic pillars with random geometries (a) at $60^\circ$ tiled and (b) the top view of ceramic pillars.....	78
Figure 5.1 Schematic of PDMS soft mould replication from a master mould. The PDMS is cast onto the master mould and, after curing, the soft mould is peeled off	93
Figure 5.2 Chemical structure of (a) hydantoin epoxy resin, $\text{C}_{11}\text{H}_{16}\text{N}_2\text{O}_4$ (b) Bis(3-aminopropyl)amine, $\text{C}_6\text{H}_{17}\text{N}_3$ .....	95
Figure 5.3 Schematic illustration of burnout and sintering of PZT green gel casting samples in lead rich atmosphere.....	99
Figure 5.4 the burnout and sintering profile of PZT green gel casting samples (BCZT samples were set the same sintering profile; excepted sintering temperatures were studied between $1300\text{-}1500^\circ\text{C}$ ) .....	100
Figure 5.5 Flow chart of the key materials and steps of piezoelectric ceramic gel casting.....	101
Figure 5.6 Schematic illustration of setup used for the burnout and sintering of the PZT gel cast bristle block green samples.....	103
Figure 5.7 (a) The assembly of the composite on the copper plate using a silica ring to flatten the surface of the composite (b) The custom corona poling equipment used for non-contact poling of PZT and 50BCZT 1-3 composites.....	106
Figure 5.8 Schematic illustration of electroding of 1-3 composite by using polycarbonate mask with tail.....	108
Figure 5.9 Schematic illustration of the fabrication process of a 1-3 piezocomposite.....	109
Figure 5.10 Photograph of the scanning system.....	117
Figure 5.11 Schematic diagram of the component connections of the scanning system.....	117
Figure 5.12 Photograph of experimental set up for the B-scan of Tungsten wires..	118
Figure 5.13 Photograph of the experimental set up for the B-scan of Tungsten wires in agar 8% $\text{Al}_2\text{O}_3$ .....	118

Figure 5.14 Photograph of focused transducer and pig bowel tissue placed for B-scanning.....	119
Figure 6.1 (a) Elastic modulus $G'$ and (b) viscous modulus $G''$ of 20 wt% hydantoin epoxy resin content premix solutions cross-linked with various hardener contents at 40°C.....	125
Figure 6.2 Elastic modulus $G'$ and viscous modulus $G''$ of 20 wt% hydantoin epoxy resin content premix solutions cross-linked with hardener PHR = 18 g per 100 g of resin at 40°C. ....	126
Figure 6.3 (a) Elastic modulus $G'$ and (b) viscous modulus $G''$ of 20 wt% hydantoin epoxy resin content premix solutions cross-linked with hardener PHR = 18 g per 100 g of resin measured at various temperatures.....	128
Figure 6.4 Arrhenius plots of data calculated using the gelation time obtained from figure 6.3 (a), showing that the gelation time $t_g$ is inversely proportional to the temperature T.....	129
Figure 6.5 (a) The dependence of the elastic modulus $G'$ and (b) viscous modulus $G''$ as a function of time for premix solutions with various resin contents cross-linked with a hardener concentration PHR = 18 g at 40 °C.....	130
Figure 6.6 The additional ring open polymerisation reaction in the presence of water .....	132
Figure 6.7 The two possibilities of water molecules binding with epoxy resin through hydrogen bonding (a). Type I, single hydrogen bonding between water molecules and epoxy resin. (b) Type II, multiple hydrogen bonds between water molecules and epoxy resin.....	132
Figure 6.8 The particle size distribution of 50BCZT powders (a) as-received and (b) after vibro-milling for 7 hrs.....	135
Figure 6.9 SEM micrographs of 50BCZT powders (a) as-received and (b) after vibro-milling for 7 hrs. ....	136
Figure 6.10 XRD patterns of 50BCZT powders calcined at 1100 °C and 50BCZT discs sintered at difference temperature. ....	137
Figure 6.11 Viscosity of the 50BCZT slurry with 40% vol solids loading and 20 wt% resin contents as a function of dispersant concentration measured at a shear rate 100 $s^{-1}$ .....	141

Figure 6.12 Viscosity curves as a function of shear rate of the 50BCZT slurry at various solids loadings with 20 wt% resin content using hardener concentration PHR = 18 g and the dispersant concentration was 2.4 wt%.....	143
Figure 6.13 Viscosity curves as a function of shear rate of 50BCZT 45 vol % solids loading slurries with various resin contents using hardener concentration PHR = 18 g and the dispersant concentration was 2.4 wt%.....	146
Figure 6.14 Variation of viscosity curves as a function of time of 50BCZT slurries of different resin contents. All slurries have 45 vol % solids loading using hardener concentration PHR = 18 g and the dispersant concentration was 2.4 wt%.....	148
Figure 6.15 Fracture surface of green 50BCZT samples prepared from 45 vol% solids loading, 30 wt% resin content at optimum hardener and dispersant concentrations (a) with de-airing step after casting (b) without de-airing step after casting.....	149
Figure 6.16 Green 50BCZT gel cast sample obtained from 45 vol% solids loading with 30wt% resin and 2.4 wt% Dispex AA4040 after demoulding.....	149
Figure 6.17 SEM micrographs of fracture surface of 50BCZT green bodies obtained from 45 vol% solids loading with various hydantoin epoxy resin concentrations (a) 10 wt% (b) 20 wt% (c) 30 wt% (d) 40 wt% after demoulding and drying.....	150
Figure 6.18 Green density and drying shrinkage of 50BCZT gel cast green samples versus resin content at a solid loading of 45 vol%.....	152
Figure 6.19 Effect of resin content on particles at green state (a) 10 wt% (insufficient polymer chains) (b) 40wt% (sufficient polymer chains) .....	153
Figure 6.20 Green strength of the gel cast 50BCZT obtained from 45 vol% solids loading at various resin contents.....	154
Figure 6.21 Sintered density and sintering shrinkage of 50BCZT gel samples at a solid loading of 45 vol% sintered at 1425°C versus resin content.....	156
Figure 6.22 SEM micrographs showing the fracture surfaces of sintered gel cast samples obtained from 45 vol% solids loading 50BCZT slurries with various hydantoin epoxy resin concentrations (a) 10 wt% (b) 20 wt% (c) 30 wt% (d) 40 wt%.....	157

Figure 6.23 The variation of piezoelectric charge coefficient $d_{33}$ and planar coupling coefficient $k_p$ with resin content of 50BCZT gel cast samples at a solid loading of 45 vol% sintered at 1425°C.....	158
Figure 6.24 The variation of relative permittivity and dielectric loss tangent versus resin content of 50BCZT gel cast samples at a solid loading of 45 vol% sintered at 1425°C.....	158
Figure 6.25 Sintered density of 50BCZT gel cast samples at a solids loading of 45 vol% and 30 wt% resin content sintered at different temperatures.....	160
Figure 6.26 SEM micrographs of 50BCZT gel cast samples at a solids loading of 45 vol% and 30 wt% resin content sintered at temperatures between 1300 °C and 1500 °C for 4 h.....	161
Figure 6.27 Piezoelectric coefficient and planar coupling of 50BCZT gel cast samples at a solids loading of 45 vol% and 40 wt% resin content sintered at different temperatures.....	162
Figure 6.28 Permittivity and dielectric loss tangent of 50BCZT gel cast samples at a solids loading of 45 vol% and 40 wt% resin content sintered at different temperatures.....	162
Figure 7.1 The particle size distribution of the (a) as-received PZT powder and (b) PZT powder after vibro-milling for 48 hrs .....	172
Figure 7.2 SEM micrographs of (a) as-received PZT powders and (b) after vibro-milling for 48 hrs.....	173
Figure 7.3 XRD patterns of PZT powders as-received powder and PZT discs sintered at 1200 °C.....	174
Figure 7.4 Thermal analysis of a gel cast PZT green compact with 20% resin in premixed solution at 48 Vol % solids loading measured at 5°C/minute.....	175
Figure 7.5 Viscosity of the PZT slurry with 48% vol solids loading and 20 wt% resin contents as a function of dispersant concentration measured at the shear rate 100 s <sup>-1</sup> .....	177
Figure 7.6 Viscosity curves as a function of shear rate of the PZT slurry at various solids loadings with 20 wt% resin content using optimum dispersant concentration and hardener content. ....	178

Figure 7.7 Viscosity curves as a function of shear rate of the PZT 48 vol % solids loading slurry at various resin contents loading using optimum dispersant concentration and hardener content.....	180
Figure 7.8 Viscosity curves as a function of time of the PZT 48 vol % solids loading slurry at various resin contents loading using optimum dispersant concentration and hardener content. ....	182
Figure 7.9 Green PZT gel cast sample obtained from 48 vol% solids loading with 20wt% resin and 1 wt% Dispex AA4040 after demoulding and drying.....	183
Figure 7.10 SEM micrographs of fracture surface of PZT green bodies obtained from 48 vol% solids loading with various hydantoin epoxy resin concentrations (a) 10 wt% (b) 20 wt% (c) 30 wt% (d) 40 wt% after demoulding and drying.....	184
Figure 7.11 Green density and linear drying shrinkage of PZT gel cast green samples versus resin content at a solid loading of 48 vol%.....	185
Figure 7.12 Green strength of the gel cast PZT samples obtained from 45 vol% solids loading at various resin contents.....	186
Figure 7.13 Sintered density and linear sintering shrinkage of PZT gel samples at a solid loading of 48 vol% sintered at 1200°C versus resin content.....	188
Figure 7.14 SEM micrographs showing the fracture surfaces of sintered gel cast samples obtained from 48 vol% solids loading PZT slurries with various hydantoin epoxy resin concentrations (a) 10 wt% (b) 20 wt% (c) 30 wt% (d) 40 wt%.....	189
Figure 7.15 Piezoelectric coefficient and planar coupling of PZT gel cast samples at a solid loading of 48 vol% sintered at 1200°C versus resin content. ....	190
Figure 7.16 Permittivity and dielectric loss tangent of PZT gel cast samples at a solid loading of 48 vol% sintered at 1200 °C versus resin content.....	190
Figure 8.1 SEM micrographs showing the top-view of demoulded randomised 50BCZT structures prepared from gel casting slurries with 45% solids loading with (a) 10 wt%, (b) 20 wt%, (c) 30 wt% and (d) 40 wt% resin contents.....	198
Figure 8.2 SEM micrograph of (a) the top view (b) detailed side view of the randomised 50BCZT segments fabricated by gel casting slurry with 45% solids loading and 30 wt% resin content after drying and demoulding.....	198

Figure 8.3 SEM micrographs showing the top-view of demoulded randomised PZT structures prepared from gel casting slurries 48% solids loading with (a) 10 wt%, (b) 20 wt%, (c) 30 wt% and (d) 40 wt% resin contents.....	201
Figure 8.4 SEM micrograph of (a) the top view (b) detailed side view of the randomised PZT segments fabricated by gel casting slurries with 48% solids loading and 30 wt% resin content after drying and demoulding.....	202
Figure 8.5 SEM micrograph of the top view of the randomised 50BCZT segments (a) before and (b) after sintering at 1300 °C.....	205
Figure 8.6 SEM micrographs of a(i) to j (i) top view and a(ii) to j (ii) the cross section of bristle blocks of 50BCZT randomised segments after sintering at 1300 - 1500°C.....	208
Figure 8.7 Optical image of overview of randomised 50BCZT 1-3 composites after sintering at (a) 1400 °C with ceramic volume fraction of 51.70 % (b) 1425 °C with ceramic volume fraction of 58.5 %.....	208
Figure 8.8 SEM micrographs of top view of randomised PZT segments (a) before and (b) after sintering at 1200 °C.....	210
Figure 8.9 SEM micrographs of (a) top view and (b) lateral side of randomised PZT segments.....	211
Figure 8.10 Optical images of a random composite with ceramic volume fraction of 53%.....	211
Figure 8.11 Impedance (a) and (b) phase magnitude diagrams measured from 50BCZT randomised 1-3 composites sintered at 1300 °C - 1500 °C with different thicknesses, using a bias -40 volts.....	215
Figure 8.12 Impedance (a) and (b) phase magnitude diagrams measured from PZT randomised 1-3 composites sintered at 1200 °C with different thickness.....	218
Figure 8.13 Thickness coupling coefficient ( $k_t$ ) of the 50BCZT randomised composites sintered at 1300 °C - 1500 °C and PZT randomised composites sintered at 1200 °C.....	220
Figure 8.14 Relative permittivity ( $\epsilon_r^S$ ) of the 50BCZT randomised composites sintered at 1300°C - 1500°C and PZT randomised composites sintered at 1200°C.....	221
Figure 8.15 Acoustic impedance of the 50BCZT randomised composites sintered at 1300°C - 1500°C and PZT randomised composites sintered at 1200 °C.....	222

Figure 9.1 Photograph of (a) 1-3 random composite with dimensions marked for laser cutting, and (b) laser cut 1-3 composite with diameter approximately 1.6 mm.....	227
Figure 9.2 Illustration of the fabrication procedures of transducer.....	229
Figure 9.3 Photograph of (a) The small bulb of silver epoxy fixed the wire on the random composite (b) the copper wire attached on the surface of the random composite on the PLA/PTFE mount master.....	230
Figure 9. 4 Photograph of 1-3 random composite with diameter 1.6 mm stuck onto the cast tungsten epoxy backing. ....	232
Figure 9. 5 Photograph of completed (a) focussed transducer and (b) unfocussed transducer.....	232
Figure 9. 6 The photograph of the imperfect curve within the active area of a focused PZT transducer.....	232
Figure 9.7 Electrical impedance and phase measured from transducers, using a bias - 40 volts for the 50BCZT transducers.....	234
Figure 9.8 Phase magnitude diagram measured from transducers, using a bias -40 volts for the 50BCZT transducers. ....	234
Figure 9.9 Pulse-echo measured from focussed 50BCZT transducer at focus in time and frequency domain, showing frequency, bandwidth.....	237
Figure 9.10 Pulse-echo measured from focussed PZT transducer at focus in time and frequency domain, showing frequency, bandwidth and spatial pulse length.....	237
Figure 9.11 Pulse-echo measured from unfocussed 50BCZT transducer at focus in time and frequency domain, showing frequency, bandwidth and spatial pulse length. ....	238
Figure 9.12 Pulse-echo measured from unfocussed PZT transducer at focus in time and frequency domain, showing frequency, bandwidth and spatial pulse length....	238
Figure 9.13 Schematic illustration of the tungsten wire phantom scanning experiment in which the transducer travelled along the lateral distance at different depth between transducer and tungsten wires.....	241
Figure 9.14 B-scan images of a set of 25 $\mu\text{m}$ tungsten wires at different distances using (a) focussed 50BCZT, (B) focussed PZT (c) unfocussed 50BCZT and (d) unfocussed PZT transducers .....	243

Figure 9.15 The 2D B-scan images of the amplitude at different travelling distance of (a) focussed 50BCZT, (B) focussed PZT (c) unfocussed 50BCZT and (d) unfocussed PZT transducers. ....	245
Figure 9.16 The amplitude at different travelling distance of focussed PZT, 50BCZT, unfocussed PZT and unfocussed 50BCZT transducers, cut off at -6dB.....	246
Figure 9.17 Schematic illustrate 3D B-scan image for calculating the axial and lateral resolution at -6dB of a set of tungsten wires obtained from the focussed 50BCZT transducer.....	247
Figure 9.18 Illustration of (a) the axial distance (b) close up data of the axial distance and amplitude when focussed 50BCZT scanned the second wire transducer at -6 dB (c) the lateral distance (b) close up data of lateral distance and amplitude when focussed 50BCZT scanned the second wire transducer at -6 dB for calculating the axial and lateral resolution at -6 dB. ....	248
Figure 9.19 Axial resolution of focused and unfocussed PZT and 50 BCZT transducers at different distances, measured at at -6dB .....	249
Figure 9.20 The Lateral resolutions of focused and unfocussed PZT and 50 BCZT transducers travelled at different distances, measured at -6 dB. ....	249
Figure 9.21 Photograph of B-scan of Tungsten wires in agar 8% Al <sub>2</sub> O <sub>3</sub> .....	250
Figure 9.22 The B-scan images of agar phantom with tungsten wires 100, 200, 200 μm in diameter obtained from focussed and unfocussed lead based and lead free transducers.....	251
Figure 9.23 The photograph of (a) pig bowel with a thickness 2.5 mm submerged in phosphate buffered saline (PBS) at pH 7.4 and (b) the pig bowel structure obtained using an AFM PZT transducer by Dr. Benjamin F Cox (Clinical Research Centre Tayside at University of Dundee) .....	252
Figure 9.24 B-scan images of pig bowel from (a) focussed 50BCZT , (b)focussed PZT transducer travelled by 20 mm lateral distance and (c) the side by side comparison of (c) focussed PZT and (d) focussed 50BCZT transducer.....	253



## Index of Tables

Table 2.1 Acoustic properties of various medium.....	15
Table 2.2 Percentage reflection of ultrasound wave at boundary.....	15
Table 2.3 Comparison of resolution, depth for various clinical use at different ultrasound frequency.....	17
Table 3.1 Piezoelectric, Pyroelectric and Ferroelectric crystal.....	32
Table 3.2 Characteristic of hard and soft PZT.....	40
Table 3.3 Piezoelectric properties of KNN-based Materials.....	45
Table 3.4 Curie temperature of various piezoelectric materials.....	49
Table 3.5 The dimensions and aspect ratio of a 50% volume fraction piezocomposite, assume the longitudinal velocity of 3,000 m/s and based on a square packed array of square pillars.....	61
Table 5.1 Raw materials for preparation of PZT and 50BCZT gel casting suspensions .....	95
Table 5.2 An example of a PZT gel casting composition.....	96
Table 5.3 An example of a 50BCZT gel casting composition. ....	96
Table 6.1 Gelation time by crossover criterion of 20wt% hydantoin epoxy resin premix solution cross-linked with various hardener concentration (PHR = 12-50 g per 100 g of resin) at 40 °C.....	126
Table 6.2 Gelation time calculated by the crossover criterion of $G'$ and $G''$ for 10 wt%- 40wt% hydantoin epoxy resin premix solutions cross-linked with hardener concentration PHR = 18 g per 100 g of resin) at 40 °C. ....	132
Table 8.1 The average height, grain size, finest feature size, aspect ratio and % sintering shrinkage of 50BCZT segments sintered at temperatures of 1300 °C - 1500 °C.....	209
Table 8.2 Summary of 50BCZT randomised composites sintered at 1300 °C - 1500 °C.....	216
Table 8.3 Summary of PZT randomised composites sintered at 1200 °C .....	219
Table 9.1 Characteristics and properties of focussed 50BCZT, focussed PZT, unfocussed 50BCZT, unfocussed PZT transducer .....	239

# NOMENCLATURE AND ACRONYMS

	Arrhenius pre-exponential factor
$b$	Width of rectangular bar
$C$	Capacitance (F)
$C_L$	Capacitance (F) at 1 kHz
$C_h$	Capacitance (F) at $2f_a$
$C$	Compressibility
$d_{33}$	Planar coupling coefficient
$D_M$	Diameter of soft mould (mm)
$D_d$	Diameter of dried sample (mm)
$D_s$	Diameter of the gel casting sample after sintering(mm)
$D$	Dielectric displacement ( $C/m^2$ )
$d$	Thickness of rectangular bar
$E$	Electric field (V/m)
$a$	Activation energy of polymerisation reaction (J/mol)
$f$	Frequency (Hz)
$f_r$	Resonant frequency (Hz)
$f_a$	Anti-resonant frequency (Hz)
$G'$	Elastic modulus (Pa)
$G''$	Viscous modulus (Pa)
$h$	Thickness (m)
$K_r$	Reaction rate
$k_{eff}$	Effective electromechanical coupling factor
$k_t$	Electromechanical coupling factor, thickness-extensional mode
$k_p$	Electromechanical coupling factor, planar-extensional mode
$k_{33}$	Electromechanical coupling factor, length-extensional mode
$LD$	Linear drying shrinkage
$LS$	Linear sintering shrinkage
$L$	Span length(m)

$R_L$	Lateral resolution (m)
$R_A$	Axial resolution (m)
	Gas constant 8.31 J.(k.mol) <sup>-1</sup>
$S$	Strain
$s$	Compliance of material l(m <sup>2</sup> /N)
$s_{ijkl}^E$	Elastic compliance constant at constant electric field (m <sup>2</sup> /N)
$T$	Stress
$T_K$	Absolute temperature (K)
$t_i$	Induction time
$V$	Volume fraction
$v_{pc}$	Velocity of sound in composite
$Z_a$	Acoustic impedance
$\epsilon_{ij}^T$	Dielectric constant
$s_{ijkl}^E$	Elastic constant (m <sup>2</sup> /N)
$w_d$	Dry weight of sample
$w_w$	Wet weight of sample
$\lambda$	Wavelength length (m)
$\eta$	Viscosity (Pa·s)
$\epsilon_0$	Vacuum permittivity(F/m)
$\epsilon_r$	Relative permittivity
$\epsilon^T$	Permittivity at constant stress
$\epsilon^S$	Permittivity at constant strain
$\rho$	Density (kg/m <sup>3</sup> )
$\lambda$	Wavelength length (m)
$\sigma_f$	Flexural stress
AM	Arylamide
APS	Ammonium persulfate
BaTiO <sub>3</sub>	Barium Titanate
BET	Brunauer–Emmett–Teller
BNT	Bismuth Sodium Titanate based materials
BZT	Barium Zirconate Titanate

BCT	Barium Carbonate Titanate
BKT	Bismuth potassium titanat
BCZT	Lead carbonate zirconate titanate
CT	Computed tomography
DPTA	Dipropylenetriamine
DSC	Differential scanning calorimetry
EGDG	EEthylene glycol diglycidyl ether
EEW	Equivalent Epoxide Weight
FFT	Fast Fourier Transformation
GPGE	Glycerol polyglycidyl ether
HMAM	Hydroxymethylacrylamide
IEP	Isoelectric point
KNN	Sodium Potassium Titanate based materials
MRI	Magnetic resonance imaging
MLCC	Multilayer ceramic capacitors
MPB	Morphotropic phase boundary
MBAM	Crosslinker, N,N' - methylene bisacrylamide
MAM	Methacrylamide
NVP	N-vinylpyrrolidone
NH <sub>4</sub> PAA	Solution of an ammonium salt of an acrylic polymer in water
PRF	Pulse repetition frequency
PbZrO <sub>3</sub>	Lead Zirconate
PVDF	Polyvinylidenedifluoride
PZT	Lead zirconate titanate
PbTiO <sub>3</sub>	Lead Titanate
Pb	Lead
PVA	Polyvinyl alcohol
PVB	Polyvinyl butyral
PMMA	Polymethyl methacrylate

PDMS	Poly(dimethylsiloxane)
PEGDGE	Poly ethylene glycol diglycidyl ether
RoHS	Restriction of Hazardous Substances Directive
RDGE	Rresorcinoldiglycidyl ether
SPGE	Sorbitol polyglycidyl ether
SSA	Specific surface area
PHR	Parts Per Hundred Resin
VPP	Viscous polymer processing
$T_c$	Curie temperature
TrFE	Trifluoroethylene
TEMED	Tetramethylethylenediamine
TGA	Thermogravimetric analysis

# Chapter 1 Introduction

Ultrasound scanning is one of the most popular medical imaging techniques. It offers several advantages over other imaging techniques because it is not based on ionising radiation and is therefore considered extremely safe, has good resolution, and is very economical and convenient for the user. The quality of the ultrasound imaging system depends on the characteristics of transducer used to send and receive the ultrasound pulses. Conventional medical ultrasound imaging uses frequencies between 1-15 MHz, and usually <10 MHz [1, 2]. High frequency ultrasound transducers (>30 MHz) provide micro-scale resolution useful for a wide range of diagnostic medical imaging situations, especially for surface specific structures such as ophthalmology, dermatology and intravascular applications [3]. The active component of a transducer is based on a piezoelectric material, usually ceramic, and 1-3 piezocomposites, which comprise piezoelectric ceramic pillars in a polymer matrix, offer advantages such as excellent electromechanical coupling and reduced acoustic impedance mismatch compared to monolithic piezoelectric ceramics. However, the better resolution which comes with the high operating frequency requires an ultrafine spatial scale in the structure of the piezocomposite, with high aspect ratio pillars and narrow gaps or kerfs. In addition, in order to avoid interference from unwanted or spurious resonant modes caused by the regular periodicity of the ceramic pillars, 1-3 composites are being developed in which the pillar cross-sectional shapes, sizes and positions are randomised, which are not possible to be manufactured using standard processing techniques [4, 5].

Typically, lead zirconate titanate (PZT) is the commonly used material of choice for the active component of the transducers. However, this material has a high content of lead. According to the growing concern over environmental and public health, the European Union has issued important legislation restricting the use of hazard substances in electrical and electronic equipment devices known as RoHS [6]. Hence, lead free materials are being developed as potential replacements for PZT.

This project is focused on the fabrication of lead free piezoelectric materials in the form of 1-3 composites for use as the active material for high frequency ultrasound transducers. A gel casting and micromoulding system has been developed which enables the net shape fabrication of composites with a randomised structure. The construction and characterisation of lead free composites and transducers have been studied, together with lead based comparisons. In outline, Chapter 2 and 3 describe the theory and basic knowledge of medical ultrasound imaging and the requirement for the ultrasound transducer. Also discussed are the factors affecting performance of the transducers, basic ultrasound transducer construction and how transducers operate in each component. Additionally the principles of piezoelectricity, piezoelectric materials for high frequency ultrasound transducers and methods for the manufacture of 1-3 piezocomposite are described. The aims of the project are explained in Chapter 4. Chapter 5 is describes the experimental procedures. The optimisations and characterisations of lead free and lead based materials are presented in Chapters 6 and 7, followed by the fabrication and characterisation of lead based and lead free 1-3 composites in Chapter 8. The transducer fabrication and characterisation are described explained in Chapter 9 and the final chapter, Chapter 10 contains the conclusions of this project and suggestions for future work.

## 1.1 References

1. *Ultrasound Scans: How Do They Work?* [Last accessed date 14/03/2016]; Available from: <http://www.medicalnewstoday.com/articles/245491.php>.
2. *Definition ultrasound*. [Last accessed date 14/03/2016]; Available from: <http://searchsecurity.techtarget.com/definition/ultrasound>.
3. Perlas, V.C.a.A., *Basics of Ultrasound Imaging*, in *Atlas of Ultrasound Guided Procedures in Interventional Pain Management*, S.N. Narouze, Editor. 2011, Springer: USA. p. 13-19.
4. Clipsham, T.J. and T.W. Button, *1-3 Piezocomposites realised from small feature size, high aspect ratio, hot embossed moulds. Part II: piezocomposite fabrication*. *Microsystem Technologies-Micro-and Nanosystems-Information Storage and Processing Systems*, 2010. **16**(11): p. 1983-1988.
5. Safari, A., V.F. Janas, and A. Bandyopadhyay, *Development of fine-scale piezoelectric composites for transducers*. *AIChE Journal*, 1997. **43**(S11): p. 2849-2856.
6. *Eu-Directive 2002/95/EC : the restriction of the use of certain hazardous substances in electrical and electronic equipment*. Official Journal of the European Union, 2003: p. 19-23.



# **Chapter 2    Ultrasound    imaging    for    medical applications**

## **2.1 Medical imaging history**

Medical imaging is a technique to identify any structural abnormalities or functions of some organs or tissues in the body by using visual images to represent internal body parts. This enables clinical quantification and assessment for medical treatment of organs or structures which are hidden by bones or skin. There are several methods for medical imaging. For example X-ray is the most common for medical imaging. However, X-rays can cause damage to the body and can be a cancer risk factor as it is an ionising radiation. Computed tomography (CT) and mammography provides better definition and more precise medical images of internal parts such as muscles, blood vessels and soft tissue compared to X-ray and also the image processing is faster than X-ray. However, CT also uses very high amount of radiation [1-3]. Magnetic resonance imaging (MRI) produces very good contrast between soft tissues and organs without using ionising radiation. It is adopted because it is safer. However, some patients suffer claustrophobia from entering the large magnet, patients with pacemakers cannot undergo this method for diagnosis and MRI images are not produced in real time [4, 5]. Ultrasound provides a noninvasive visualisation method albeit with reduced image quality. This method is a lot safer as it can be used without using ionising radiation and it is also very economical and particularly convenient for the user compared with other techniques [6, 7].

The use of ultrasound for medical diagnosis was first developed by using a beam transmitted into a skull for visualizing brain structure and checking for brain tumors. It was invented by Karl Theo (Theodore) Dussik, an Austrian neurologist and psychiatrist [8-11]. Ultrasound imaging has been used for medical applications for over fifty years and accounts for over 20% of medical imaging scans in hospitals worldwide [6], [12-14].

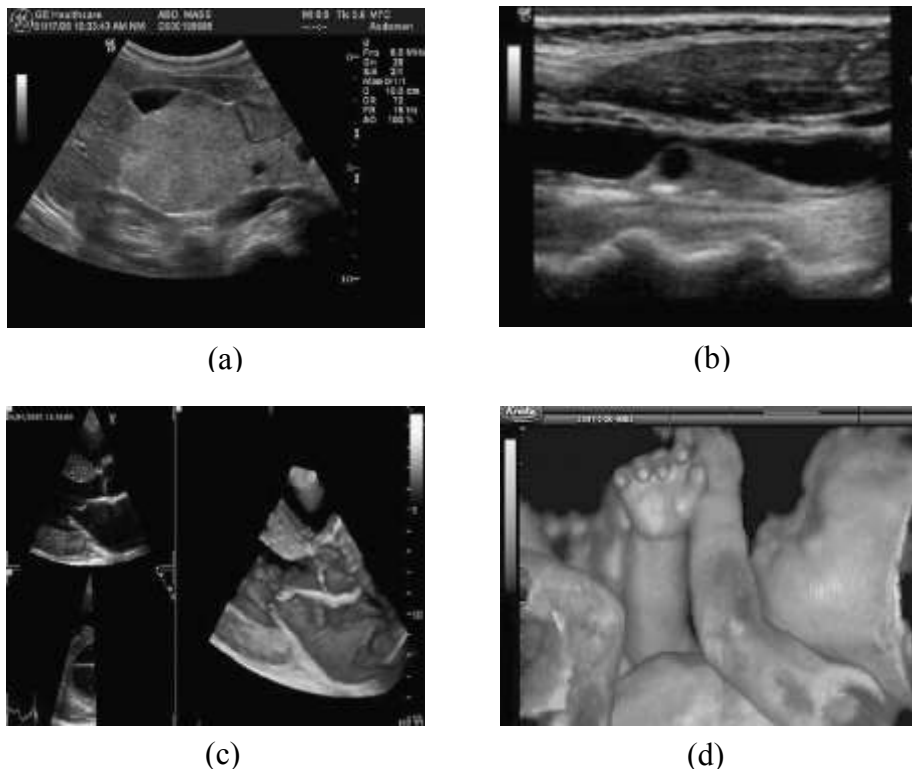


**Figure 2.1 Shows examples of ultrasound images for human medical applications [15] (a) Cysts in liver, (b) Carotid artery blood flow, (c) 3D of heart image, (d) Baby development.**

## 2.2 Understanding Medical Ultrasound Imaging

### 2.2.1 Ultrasound waves

Sound is one of the most common waves that results from the transmission of vibration through a medium such as air or water. Oscillation of atoms or molecules around their median position is then transmitted to adjacent molecules resulting in propagation of a mechanical wave. The mechanical wave and vibration can occur over a wide frequency range representing the acoustic spectrum. Figure 2.2 presents a graphical interpretation of the acoustic spectrum [16]. Sound occupies the frequency range between 10 Hz to 20 kHz. Ultrasound is a longitudinal mechanical sound wave with a frequency above that of human hearing (above 20 kHz). It can be used in many applications such as non-destructive testing, sonar systems for underwater range finding and locating objects. For medical imaging applications, ultrasound normally operates at frequencies between 1-30 MHz [17-19]. Ultrasound waves can be described as a sinusoidal wave of wavelength ( $\lambda$ ), frequency ( $f$ ) and velocity of propagation ( $v$ ), which is constant in a specific medium at the constant temperature, and also depends on the stiffness and density of the propagation medium [20]. The relationship between these parameters is shown in Equation 2.1. Thus increasing the frequency results in a decreasing wavelength at the constant velocity in specific medium. Normally, the speed of sound in solids is higher than in liquids, which in turn are higher than in gases [21-23].

$$\lambda = \frac{v}{f}$$

**Equation 2.1**

The motion of sound waves in solids can be classified into two types; compression waves (also called longitudinal waves) and shear waves (also known as transverse waves) as illustrated in Fig 2.3.

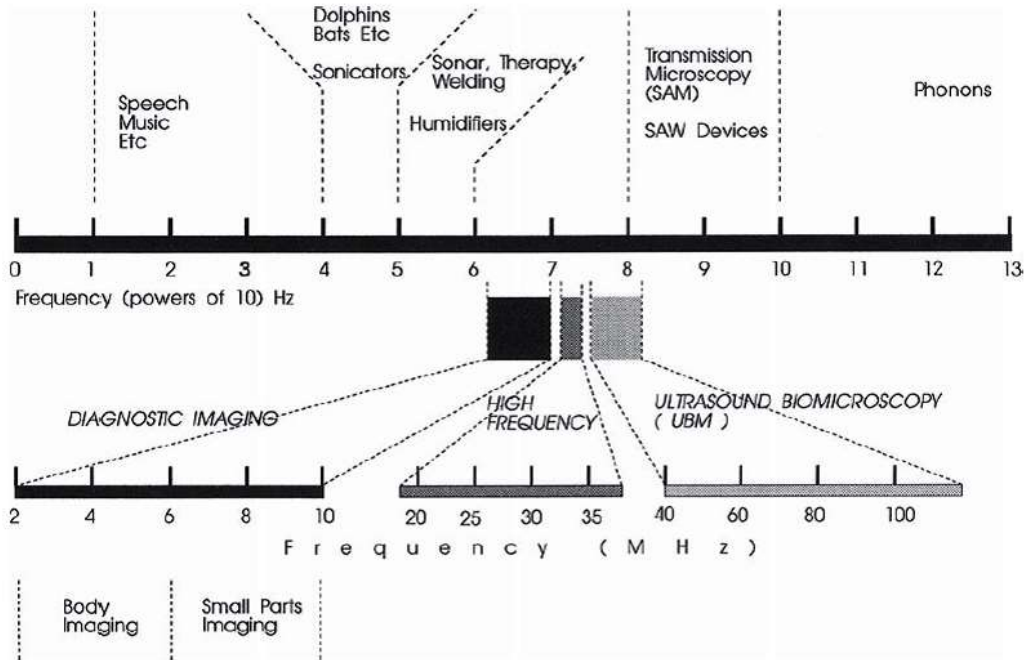


Figure 2.2 The acoustic spectrum [16].

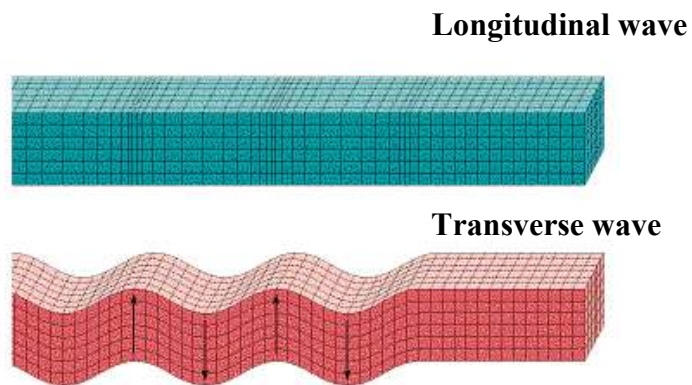


Figure 2.3 Longitudinal and transverse waves through a solid medium [24].

Longitudinal waves are the propagation of waves in which the displacement of particles is along the direction of travel of the wave. Mechanical longitudinal waves are known as compression waves, and during the wave propagate through the medium compression and rarefaction waves are produced. For transverse waves, the displacement of particles is perpendicular to the direction of the wave propagation. The speed of sound in a particular material is related to the compressibility ( $C$ ) and density ( $\rho$ ) of the medium and is expressed by Equation 2.2.

$$v = \sqrt{C/\rho} \quad \text{Equation 2.2}$$

Longitudinal wave propagation occurs in liquids, solids and gases while shear waves do not travel in liquids, only in solids. Solids provide the fastest velocity of sound wave due to their elastic compression. Shear waves only exist in solids because they require a rigid medium in which to propagate. In soft tissues, ultrasound travels in longitudinal waves while the shear waves are highly attenuated and also can only propagate at low speed as the properties are similar to liquid [25].

Longitudinal and transverse waves are the most common used in ultrasound analysis. However, at the surface and interfaces, there are other types of waves that can occur due to the elaborate vibration of the particles, e.g. surface and plate waves that also useful in ultrasound analysis. Surface or Rayleigh waves penetrate materials to a depth of only one wavelength and create an ellipsoidal movement on the surface. Rayleigh waves are sensitive to surface defects and features so are valuable for ultrasound inspection [26]. Lamb waves are similar to surface waves but can penetrate to a depth of a few wavelengths. In medical visualisation, Lamb waves generate the spurious modes that degrade image quality.

## Rayleigh wave

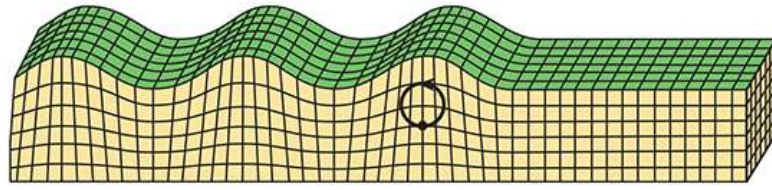


Figure 2.4 Rayleigh waves through solid [27].

### 2.2.2 Principles of Ultrasound operation

Medical ultrasound imaging is operated based on the pulse and echo principle as shown in Figure 2.5. Ultrasound devices can form medical images by transmitting beams of focused sound waves into the body and then the reflected beams are detected and processed to create the image. The device that is used to generate the focused beams of sound waves is called a piezoelectric transducer which converts between mechanical and electrical energy based on piezoelectric theory. A voltage is transmitted to the piezoelectric transducer and then the sound waves are generated in a pulse which is emitted from a face of the transducer directed into the body. Normally, each pulse has a two or three sound cycles of the same frequency (Figure. 2.6). Pulse repetition frequency (PRF) is the number of pulses per unit of time. The ultrasound pulses (length and PRF) must be timed to allow sound waves reach the target of interest or the interface of body tissue where there is an acoustic discontinuity, which then causes the reflection of the beam (which is called echo) to return to the transducer before the next pulse is generated. By timing the period elapsed between the transmitted pulse and the receiving of the echo, the geometry of the internal organ can be determined. There are several modes that can be used for the ultrasound probe to produce images. The easiest scanning mode is called A mode or amplitude modulation.

**A mode:** is a one dimensional measurement in which pulses are transmitted into targets and then amplitudes of echoes are created on the Y axis as a function of time plotted on X axis. Thus the X-axis represents depth, and Y axis represents the amplitude of the reflection which depends on the difference in acoustic impedance of the tissues. A mode is most commonly used in non-destructive testing, but for medical imaging this mode is used only for ophthalmological studies such as eye ball diameter.

**M mode:** or motion mode scan is a useful mode to detect the motion of objects such as vessel walls, and for cardiac and fetal cardiac imaging. M mode takes a single ultrasound beam to produce a one directional image of tissue motion over the time.

**B mode:** the brightness mode is the most commonly used mode in diagnostic ultrasound. This mode is based on a two dimensional measurement in which the amplitude of each returning echo is not presented on a graph as an individual point as in an A mode scan, but the amplitudes are generated by the brightness which has a different shade of grey depending on their intensity for reflection from different tissues, white and dark areas representing strong and weak echoes, respectively. This means B mode display composed of bright dots and the brightness of dots is determined by the amplitude of each returning ultrasound echoes signal [28], [29], [30]. These principles are illustrated in Fig 2.7.

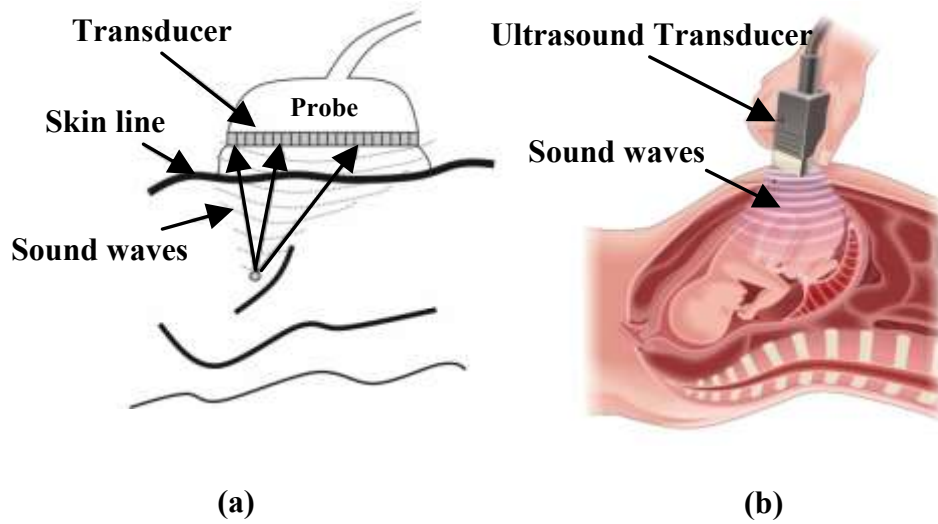


Figure 2.5 Illustration of ultrasound imaging showing (a) position of transducer [15], (b) Ultrasound baby scans [31].

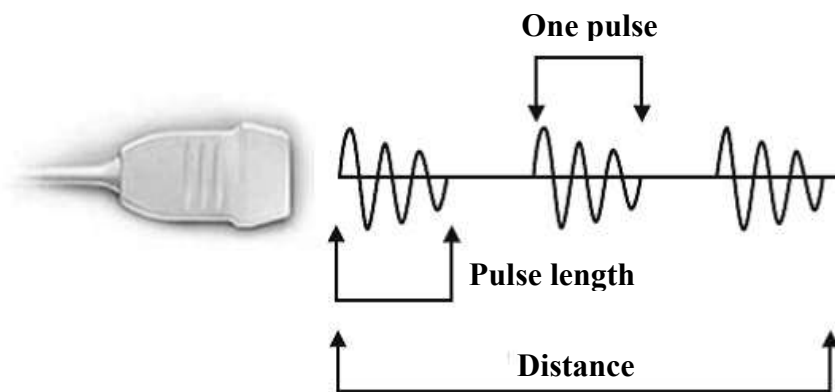


Figure 2.6 Schematic representation of Pulse repetition frequency per unit time [29].



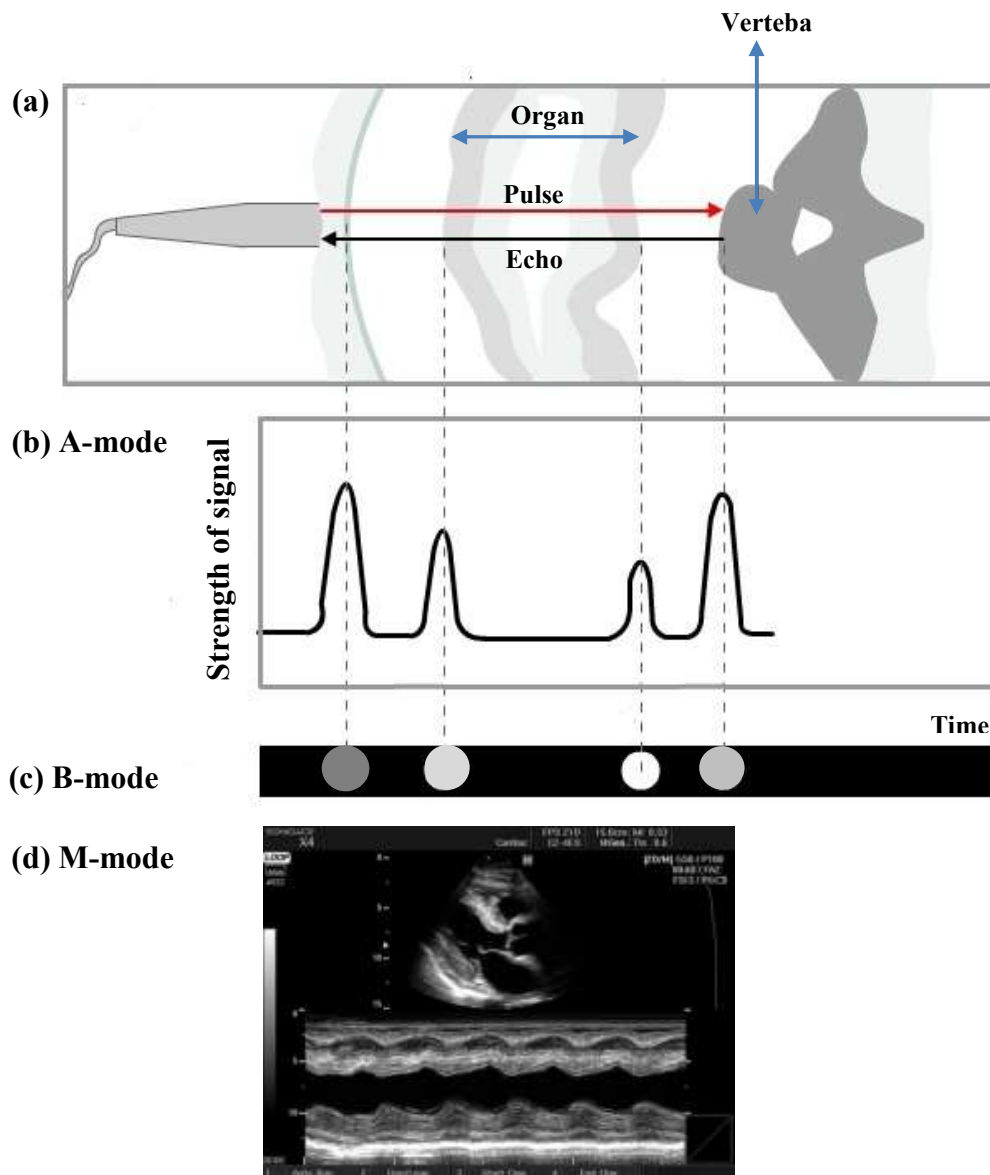


Figure 2.7 Schematic diagrams showing the basic of ultrasound (a) Ultrasound pulse is generated and propagated into organs by applying voltage into piezoelectric transducer, which echo is reflected back at the interface of body tissue and converted to electrical signal by transducer. (b) A-scan mode presents the amplitude of echo are created as a function of time. (c) B-scan mode shows the grey scale of reflected echoes which determined by the amplitude of each returning ultrasound echoes signal. A different shade of grey depending on their intensity for reflection from different tissues, white and dark areas representing strong and weak echoes, respectively (d) M-mode shows the motion mode of object [32, 33].

### 2.2.3 Interaction of ultrasound wave with mediums

When an ultrasound beam travels through human tissue and encounters some form of discontinuity, there are several interactions that happen between the wave and tissue. Part of the wave could continue being transmitted deeper into the structure and become attenuated as the depth of travelling increases. Another part of the wave will be reflected back to the transducer (which is known as the echo signal), and involves refraction, scattering and attenuation, and this is used to generate the ultrasound image. The size of the echo signal is determined by the acoustic impedance ( $Z_a$ ) of the mediums encountered, and represents the resistance of the medium to the ultrasound beam, defined as the density (  $\rho$  ) of medium times the velocity of ultrasound beam ( $v$ ) travelling in the medium as presented in Equation 2.3.

$$Z_a = \rho \cdot v \quad \text{Equation 2.3}$$

The unit of acoustic impedance is the Rayls ( $1 \text{ Rayl} = 1 \text{ kg/m}^2\text{s}$ ). The intensity of the echo is proportional to the acoustic mismatch between two mediums as illustrated in Figure 2.8. For example, if two structures have identical acoustic impedance, most of ultrasound wave will be transmitted to the next interface. If two mediums have a small acoustic mismatch, weak reflected echoes will be generated but most of waves will pass through the next medium. If the difference in acoustic impedance between two structures is large, most of the signal will be reflected and a large echo will be produced [28], [34].

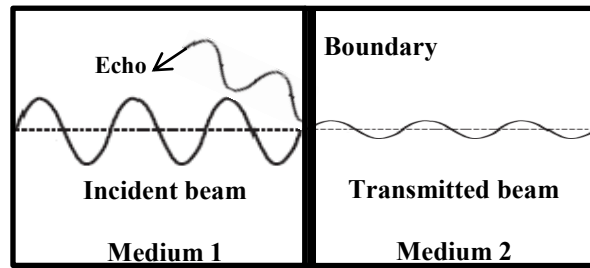


**Figure 2.8 Schematic illustration of an ultrasound beam encountering a boundary between two mediums of different acoustic impedance.**

Table 2.1 presents acoustic properties of tissues and other materials. The higher the density of medium, the greater the acoustic impedance. Air has an extremely low acoustic impedance so a high intensity echo will be reflected. Ultrasound medical imaging, therefore, some conducting gel is usually applied between the ultrasound transducer and medium as an acoustic coupling medium to reduce the air pocket. Some organs such as lung is an air-containing organs which have the lowest acoustic impedance while dense organs such as bones have a higher acoustic impedance value [29], [35]. Most tissues have similar acoustic impedance values. For this reason, the interface between soft tissues and bone creates strong echoes because of the greater difference in their acoustic impedance, and a good diagnostic image can be created. Conversely at the interface between two tissues that have the same acoustic impedance, the ultrasound wave will have no echo. Table 2.2 shows the percentage reflection of ultrasound waves at the boundaries of various materials. At the boundary of soft tissue, the amplitude of an echo is small compared to the incident beam, while if the ultrasound wave strikes some areas such as in bone or air, large echoes are produced and only a small wave being transmitted, resulting in poor visualisation of any further interfaces. The operator can avoid this problem by adjusting the angle of incident to prevent this problem.

**Table 2.1 Acoustic properties of various medium [28].**

<b>Materials</b>	<b>Speed of sound (m/s)</b>	<b>Acoustic impedance (MRayl)</b>
Air	331	0.0004
Soft tissue (mean)	1540	1.63
Blood	1575	1.62
Bone	3183	4.8
Brain	1565	1.54
Fat	1450	1.38
Liver	1604	1.63
Lung	650	0.26
Water	1498	1.50
PZT	4000	30

**Table 2.2 Percentage reflection of ultrasound wave at boundary [28].**

<b>Boundary</b>	<b>% Reflection</b>
Fat/Muscle	1.08
Fat/Kidney	0.6
Soft Tissue/Water	0.2
Bone/Fat	49
Soft tissue/Air	99

## **2.2.4 Matching ultrasound frequency to clinical applications**

Medical ultrasound imaging is operated over a wide range frequency, so choosing the right frequency is very important for each particular medical application due to the properties of different tissues, penetration depth of the ultrasound and resolution required. The standard value of the speed of sound in biological tissues can be assumed to be 1540 m/s [19], and so, using Equation 2.1, it can be shown that the wavelength range for frequencies 5-7.5 MHz are 0.380 to 0.205 mm, while the wavelength for a frequency of 30 MHz is 0.05 mm. Therefore, high ultrasound frequency has a short wavelength. Figure 2.9 and 2.10 shows the variation of penetration depth and resolution for ultrasound of different frequencies and the attenuation coefficient of a various tissues as a function of frequency, respectively. It

can be seen that the penetration, which relates to the inverse of attenuation, and resolution depend on frequency and wavelength. The attenuation increases while the penetration depth in tissue decreases with increasing operation frequency and shorter wavelengths [6] [36, 37]. Improved resolution can be provided by using shorter wavelengths and high frequencies. Thus, compared to low frequency, high frequency and the shorter wavelength ultrasound provides better resolution albeit with high attenuation [38]. Table 2.3 shows the resolution and penetration depth for various clinical uses, at low frequency range 2-5 MHz are used for characterize heart function (cardiology) and fetus development while 5-7.5 MHz are used to assesses the arteries or veins and also blood vascular system. A better resolution of image can be obtained by using high frequency. However, it comes with high attenuated. Thus, high frequency is more useful for near surface structures (e.g. ophthalmology, dermatology, intravascular).

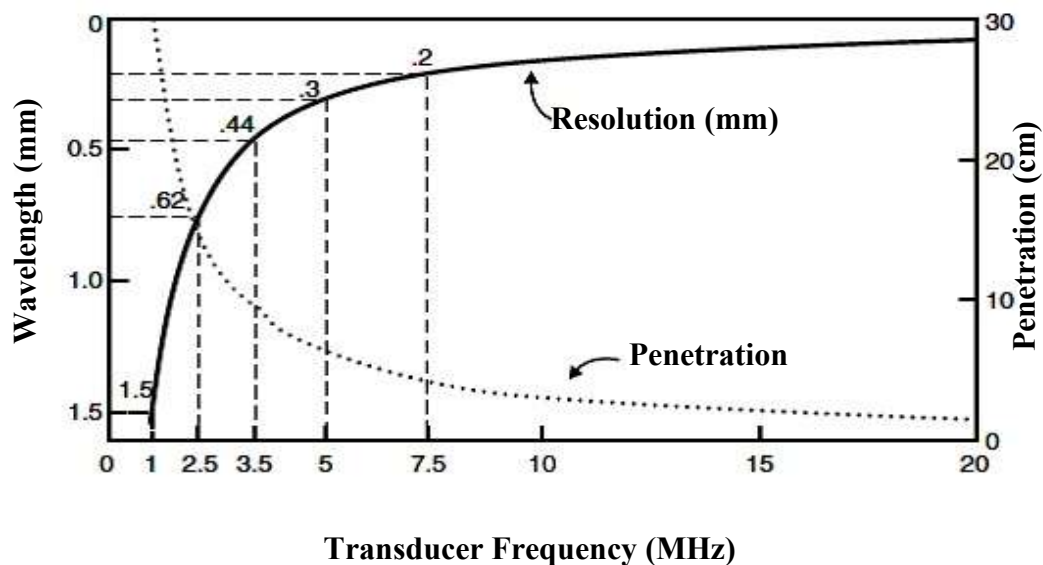


Figure 2.9 Penetration and resolution of different ultrasound frequency [29].

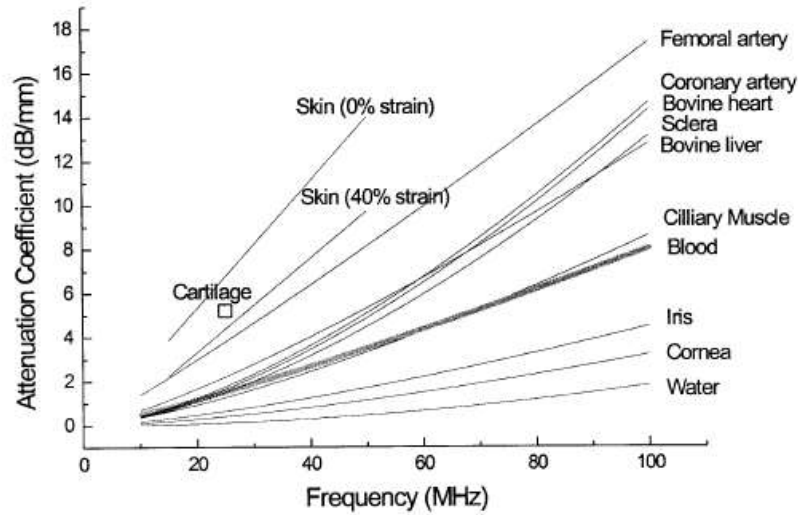


Figure 2.10 Attenuation coefficients of a various tissues in the frequency range from 10 to 100 MHz [6].

Table 2.3 Comparison of resolution, depth for various clinical use at different ultrasound frequency [15], [10], [39-42].

Clinical Use		Ultrasound Frequency (MHz)	Resolution (mm)	Depth (cm)
Characterize heart function	Cardiology	2 - 5	2 - 3	2 - 16
Imaging fetus	Obstetrics/Gynaecology	3.5 - 5	2 - 3	2 - 20
Characterize heart function	Intracardiac	5 - 7.5	0.3	< 1
Assess breast tumors, thyroid	Vascular	5 - 7.5	0.5	1 - 5
Assess severity of plaques	Intravascular	10 - 30	0.3	1 - 5

## 2.3 Basics of ultrasound transducers

The transducer is the key component of the imaging system for diagnostic ultrasound applications. Ultrasonic transducers utilise the piezoelectric effect to enable electrical signals to be converted into acoustic waves, and vice versa. The mechanical

vibrations are produced across the electrode surfaces of the ultrasound transducer by applying an electrical pulse and returned echo causes generation of an electrical signal which is then used to produce the diagnostic image. Depending on the application, there are many different types of ultrasound transducers but they normally divided into two types. The simplest ultrasound transducer is called a single element transducer whereas the current generation of transducers is based on more complex phased array systems. The single element involves only one single piezoelectric material, and utilizes mechanical steering in order to form a B scan image. This type of transducer has a single focus and can be classified as a flat or focused transducer. Focus transducers were developed to improve the lateral resolution and provide a better performance and higher resolution compared with flat transducers of the same frequency. Phased array transducers are created from multiple elements, generally arranged in a line which is called a linear array. Each element can be addressed with an individual electrical signal, thus enabling electrical steering and focusing of the beam [43-45].

### **2.3.1 Components and construction of a typical transducer**

The main components of single element and array ultrasound transducers are the same. A typical single element transducer is shown in Figure 2.11 and consists of

- Transducer housing
- Electrical connections
- Active element
- Backing material
- Matching material

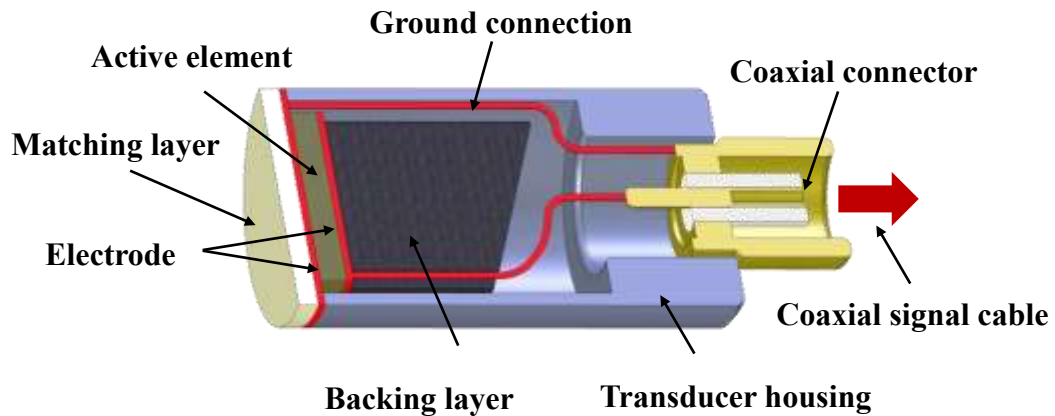


**Figure 2.11** The basic components of a single element transducer (adapted from [46]).

**Transducer housing:** As shown in Figure 2.11, the whole components of the ultrasound transducer including active material, electrodes, matching layer, backing layer components are contained in the transducer housing which supplies the structure support, provides acoustic insulation and may form part of the Ground connection [38].

**Electrical connections:** Thin films of electrically conducting materials such as gold or silver are deposited on the upper and lower main surfaces of the active element, and wires connect to a coaxial lead or connector [38].

**Active element:** The most important part of transducer is the active element which made from piezoelectric materials. The thickness of the active element is related to the operating frequency of transducer. The active element works most effectively when it is operated at its resonant frequency which occurs when the thickness of active element is equal to one half of the wavelength. Therefore, a thinner active element results in higher frequency as shown in Equation 2.4 ( $t$  is thickness,  $v$  is the velocity of ultrasound beam travelling in the medium and  $f$  is frequency) [47], [38].



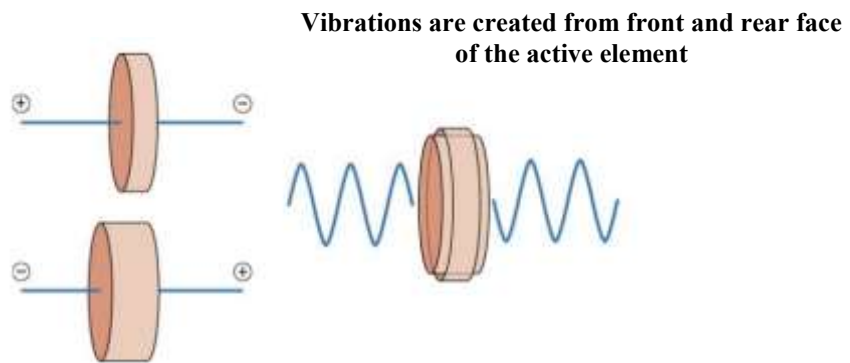
$$t = \frac{v}{2f} \quad \text{Equation 2.4}$$

**Backing material:** Material behind the rear face of the active element is made of an ultrasound absorbing material such as tungsten powder in epoxy resin. When the active element is subjected to a short electrical pulse, the main vibrations are created from both sides of active element, as presented in Figure 2.12. The large acoustic mismatch between the active element and tissue causes the oscillation back and forth between both active element sides. Therefore, the purpose of using the backing material or damping material is to prevent the reverberation in the active element, reduce the ringing from the active element, and shortening the length of pulse (spatial pulse length), producing a wide bandwidth, as presented in Figure 2.13. This results in a better axial resolution for diagnostic imaging; it is used as a support for the active material. Acoustic impedance between the active element and backing material is one of the most important factors for choosing the backing material. The most effective damping of ultrasound energy would be produced by choosing the identical acoustic impedance between active element and backing material, resulting in short pulse length and improved axial resolution. If using an active element with higher acoustic impedance than the backing materials, less ultrasound energy can be absorbed which causes internal reverberation, the ringing in the transducer increases because longer transmitted and received pulses are generated; however, the transducer has better sensitivity. For the selection of backing materials, a good trade-off between transducer sensitivity and attenuation has to be taken into account that is determined by the application requirement [19], [38], [46].

**Matching material:** The large difference in acoustic impedance between the active element and the medium causes a large reflection in the beam. Therefore, only around 20% of the acoustic energy would be transmitted into the tissues and most of it would be reflected. To decrease the acoustic mismatch a layer of matching material is placed on the front of transducer to improve the transducer performance significantly. The matching materials should have an acoustic impedance value in between that of the active material and tissues can be calculated from Equation 2.5 [44]. The energy transmitted from the active element to the medium could be maximised by using a matching layer with thickness around a quarter wavelength ( $\lambda/4$ ) at the operating frequency. This thickness provides the best performance at a single frequency, however, pulses do contain a range of frequencies. Therefore, a tapered matching layer may be used to further improve the frequency distribution, resulting in border bandwidth and better axial resolution [19], [43].

$$Z_{\text{matching materials}} = (Z_{\text{active element}} Z_{\text{medium}})^{1/2} \quad \text{Equation 2.5}$$

Focused transducers provide a better performance than unfocused transducers. Focusing of ultrasound beam can be achieved by using a lens or a curved active element as show in Figure 2.14. In this thesis, the focusing was achieved by geometrically curving the actual active element in a former with a specific radius of curvature.



An alternating voltage applied across the active element causes it to vibrate

Figure 2.12 Schematic of vibrations in active element from applying electricity [38].

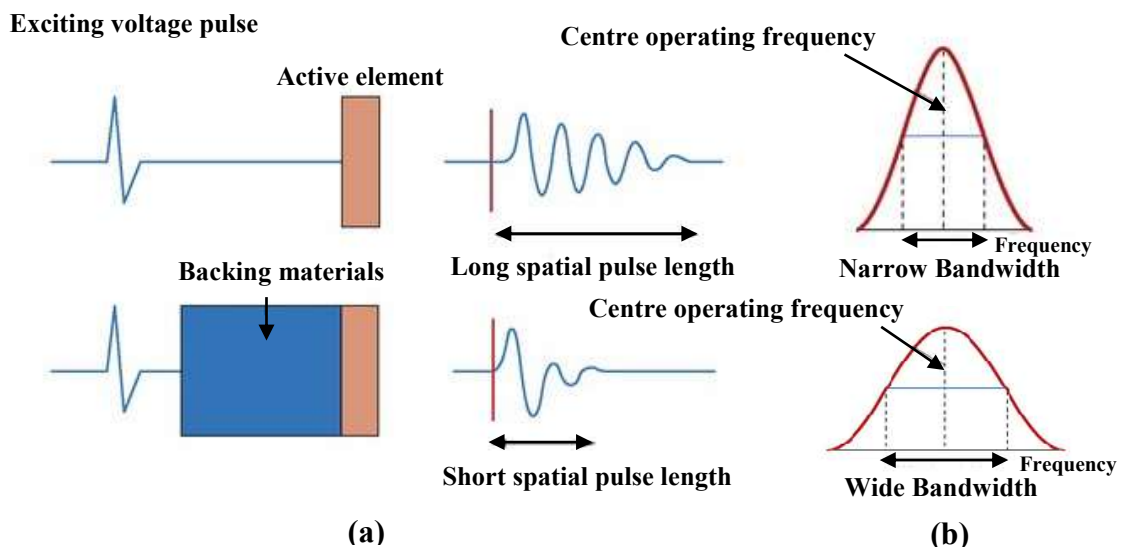


Figure 2.13 Schematic of the elimination of vibration from the face of transducer by backing material (a) and (b) the relationship between spatial pulse length and bandwidth [38].

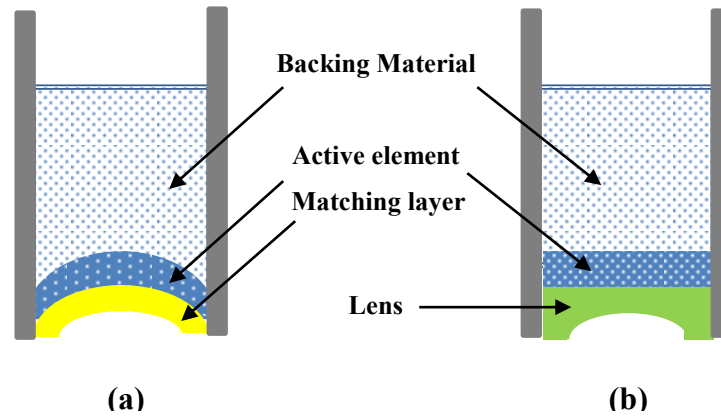


Figure 2.14 Transducer focusing by (a) curving the active materials (b) utilising a lens.

## 2.3.2 Characteristics of ultrasound transducers

### 2.3.2.1 Ultrasound beam shape

The ultrasound energy travels outwards from the transducer surface in the form of a beam. The beam has a symmetric shape in three-dimensions and its axial intensity decreases slowly as the distance from the surface of the transducer increases, while lateral intensity is diminished rapidly with distance along the central axis. Figure 2.15 presents the beam shape from a focused transducer. The beam can be separated into 3 zones: near field or fresnel zone, focal zone, and far field or fraunhofer zone. In the near far zone, the waves travel from the front of transducer and converge towards the focal zone where the greatest degree of focus is achieved. However, the ultrasound waves diverge in the fraunhofer zone and the beam spreads out as the distance from the transducer increases [47]. For an unfocused transducer, the beam zone can be divided into near field and far field or divergence zones.

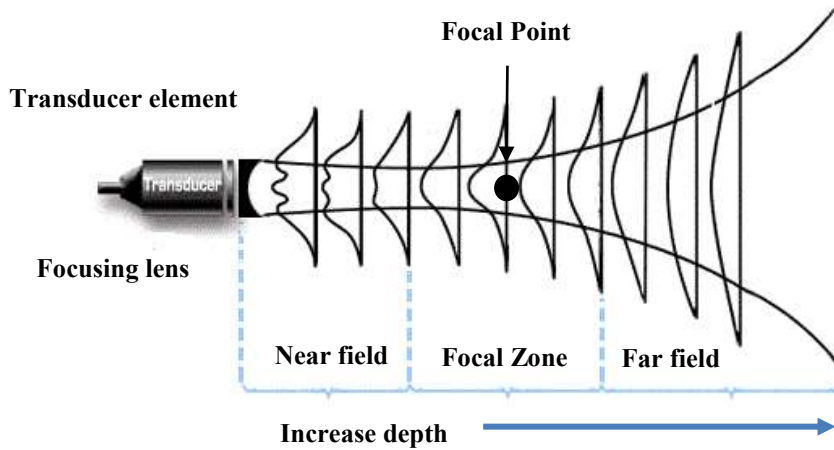


Figure 2.15 Schematic of focus of beam from a single element transducer [48].

### 2.3.2.2 Ultrasound transducer imaging resolution

The quality of diagnostic images primarily depends on the resolution of the system and the transducer. Resolution refers to the ability of the ultrasound system to differentiate between objects or structures.

**Spatial resolution:** spatial resolution is the ability to distinguish structures located close together. The ultimate factor affecting the ultrasound imaging spatial resolution is wavelength as discussed previously, with resolution improving with decreasing wavelength. Spatial resolution is categorised into axial resolution and lateral resolution [38] and can be calculated using the following Equation:

$$\text{Spatial pulse length} = \frac{\text{number of wavelength} \times \text{speed of sound}}{f} \quad \text{Equation 2.6}$$

**Axial resolution:** Axial resolution, also known as longitudinal resolution or depth resolution, refers to the minimum distance that could be distinguished between two structures situated along the ultrasound beam (Figure 2.16) and its performance depends on the spatial pulse length, which is the length of each pulse transmitted

from transducer, 2-3 wavelengths long [38]. Spatial pulse length limits the axial resolution, the best axial resolution can be obtained when the axial pulse is one half of the spatial pulse length [47]. Short spatial pulse length could be achieved by using a properly designed backing layer or increasing operating frequency. The operating frequency determines the wavelength of the ultrasound pulse; high frequency transducers have a thin active element which produces the pulse of short wavelength; therefore, using high frequency transducers provide shorter spatial and better axial resolution. The axial resolution can be calculated using the Equation 2.7 [49].

$$\text{Axial resolution} = \frac{\text{Spatial pulse length}}{2} \quad \text{Equation 2.7}$$

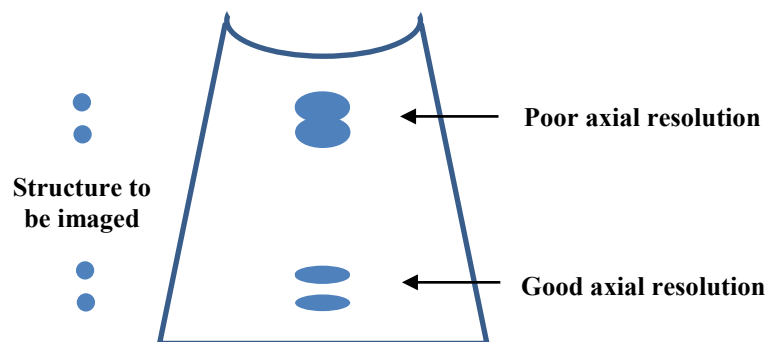


Figure 2.16 Schematic of good and poor axial resolution.

**Lateral resolution:** Lateral resolution is the ability to resolve between two reflectors located in a direction perpendicular to the ultrasound beam axis, as shown in figure 2.17 [49]. Lateral resolution in ultrasound imaging is not as good as axial resolution since there are more factors that affect resolution such as beam width and frequency. Spatial pulse length limits the axial resolution, whereas lateral resolution is restricted by beam width, which is roughly equal to the transducer diameter. The best lateral

resolution could be achieved in the focal zone of the beam where the beam width is a minimum, as determined by Equation 2.8 [46], [49].

$$\text{width of focal length} = \frac{\text{focal length} \times \text{wavelength}}{\text{aperture}} \quad \text{Equation 2.8}$$

Figure 2.18 shows how the width of the ultrasound beam resolves two structures into different images. The two reflectors would not be resolved into two images if the distance between them is less than the width of the ultrasound beam [44], [49]. The major influence is frequency because it has an effect on the beam shape, Comparison between high frequency and low frequency transducers with the same diameter, shows that the high frequency ultrasound transducer provides a shorter wavelength and broader bandwidth, resulting in better lateral resolution [50].

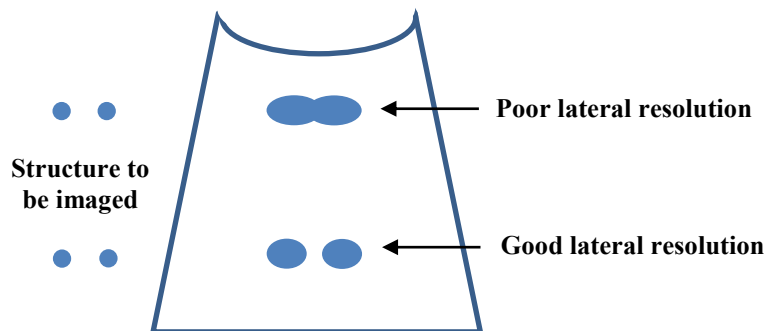


Figure 2.17 Schematic of good and poor lateral resolution

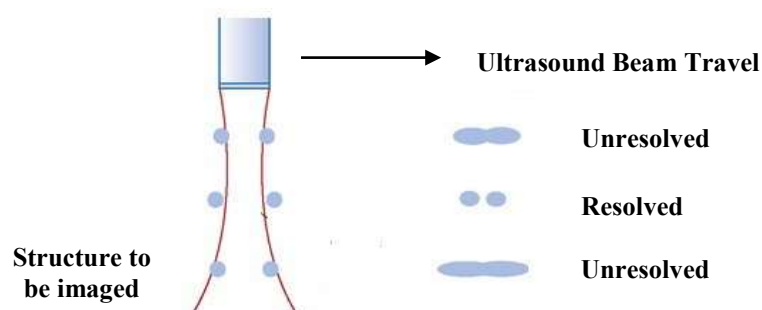
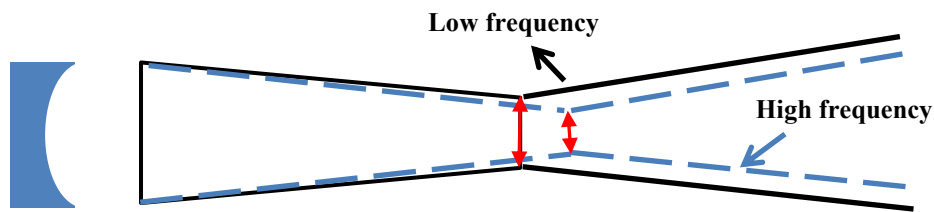


Figure 2.18 How the beam width separate two structures into two images [38].



**Figure 2.19** Schematic diagram of beam width and beam shape from low frequency and high frequency transducer.

## 2.4 Summary

This chapter includes the theory and basic knowledge of medical ultrasound imaging and explains the differences between each technique and mentions the benefits of using ultrasound imaging. The history and basics physics of ultrasound are provided. The interaction of ultrasound wave with mediums and the matching ultrasound frequency to clinical applications are discussed. The requirement for ultrasound transducer for medical imaging application is discussed. The ultrasound transducers with high frequency, short pulse length, and broad bandwidth provide a better performance and high resolution of transducer. The other factors affecting performance of transducers are also described. This chapter also presents basic ultrasound transducer construction and how transducers operate in each component.

## 2.5 References

1. Hoheisel, M., *Review of medical imaging with emphasis on X-ray detectors*. Nuclear Instruments & Methods in Physics Research Section a-Accelerators Spectrometers Detectors and Associated Equipment, 2006. **563**(1): p. 215-224.
2. Spahn, M., *X-ray detectors in medical imaging*. Nuclear Instruments & Methods in Physics Research Section a-Accelerators Spectrometers Detectors and Associated Equipment, 2013. **731**: p. 57-63.
3. *Understanding medical radiation : Radiography (Plain X-rays)*. [Last accessed 06/03/2016]; Available from: <http://www.medicalradiation.com/types-of-medical-imaging/imaging-using-x-rays/radiography-plain-x-rays/>.



4. Bauer, S., et al., *A survey of MRI-based medical image analysis for brain tumor studies*. *Physics in Medicine and Biology*, 2013. **58**(13): p. R97-R129.
5. *MEDICAL IMAGING MODALITIES*. [Last accessed date 8/03/2016 ]; Available from: <http://www.medicalimaging.org/about-mita/medical-imaging-primer/>.
6. Foster, F.S., et al., *Advances in ultrasound biomicroscopy*. *Ultrasound in Medicine & Biology*, 2000. **26**(1): p. 1-27.
7. Ganguly, D., et al., *Medical Imaging: A Review*, in *Security-Enriched Urban Computing and Smart Grid*, T.H. Kim, A. Stoica, and R.S. Chang, Editors. 2010. p. 504-516.
8. Mikla, V.I. and V.V. Mikla, *Medical Imaging Technology*. 2013: Elsevier Science.
9. *The History of Ultrasound*. [Last accessed date 08/03/2016]; Available from: <http://ultrasoundschoolsguide.com/history-of-ultrasound/>.
10. Dr. Joseph Woo. *History of Ultrasound in Obstetrics and Gynecology*. [Last accessed date 08/03/2016]; Available from: <http://www.ob-ultrasound.net/dussikbio.html>.
11. Strutt, J.W., *The Theory of Sound*. 2011: Cambridge University Press.
12. *Front Matter*, in *Physical Principles of Medical Ultrasonics*, J.R.B. C. R. Hill, G.R. ter Haar, Editor. 2005, John Wiley & Sons, Ltd. p. i-xv.
13. *Ultrasound*. [Last accessed date 11/03/2016]; Available from: <http://www.nps.org.au/medical-tests/medical-imaging/for-individuals/types-of-imaging/ultrasound-new>.
14. *Understanding medical radiation : Ultrasound imaging*. [Last accessed date 11/03/2016]; Available from: <https://www.medicalradiation.com/types-of-medical-imaging/other-types-of-medical-imaging/ultrasound-imaging/>.
15. Iniewski, K., *Medical Imaging Principles, Detectors, and Electronics*. 2009, Canada: John Wiley & Sons, Inc., Hoboken, New Jersey.
16. Pavlin, C.J. and F. Foster, *Basic Physics of High-Frequency Ultrasound Imaging*, in *Ultrasound Biomicroscopy of the Eye*, C.J. Pavlin and F.S. Foster, Editors. 1995, Springer New York: New York, NY. p. 3-16.
17. *Ultrasound Scans: How Do They Work?* [Last accessed date 14/03/2016]; Available from: <http://www.medicalnewstoday.com/articles/245491.php>.
18. *Definition ultrasound*. [Last accessed date 14/03/2016]; Available from: <http://searchsecurity.techtarget.com/definition/ultrasound>.
19. Webster, R.A., *Passive materials for high frequency piezocomposite ultrasonic transducers*, in *School of Metallurgy and Materials*. 2010, University of Birmingham.
20. Raymond A. Serway, J.W.J., *Physics for Scientists and Engineers, Volume 1, Technology Update, 9th Edition*. 2016: Cengage Learning, 2015. 784.
21. Jie, Z., *Optimization of matching layer design for medical ultrasonic transducer*. 2008, The Pennsylvania State University: ProQuest Dissertations And Theses. p. 172.
22. Senani, R., et al., *Sinusoidal Oscillators and Waveform Generators using Modern Electronic Circuit Building Blocks*. 2016: Springer International Publishing. 622.
23. Lempriere, B.M., *Ultrasound and Elastic Waves: Frequently Asked Questions*. 2002: Academic Press. 264.
24. *Earthquake Waves*. [Last accessed date 16/03/2016]; Available from: <http://www.darylscience.com/Demos/PSWaves.html>.
25. Mathias Fink , W.A.K., Jean-Paul Montagner, Arnaud Tourin, *Imaging of Complex Media with Acoustic and Seismic Waves*. Vol. 84. 2002: Springer Berlin Heidelberg.
26. Worden, K., *Rayleigh and Lamb Waves - Basic Principles*. Strain, 2001. **37**(4): p. 167-172.

27. *Types of Seismic Waves*. [Last accessed date 17/03/2016]; Available from: <http://www.kgs.ku.edu/Publications/PIC/pic37.html>.
28. Aldrich, J.E., *Basic physics of ultrasound imaging*. Critical Care Medicine, 2007. **35**(5): p. S131-S137.
29. Perlas, V.C.a.A., *Basics of Ultrasound Imaging*, in *Atlas of Ultrasound Guided Procedures in Interventional Pain Management*, S.N. Narouze, Editor. 2011, Springer: USA. p. 13-19.
30. Dhawan, A.P., *Medical Image Analysis*. 2011: Wiley.
31. *Medical images from ultrasound*. [Last accessed date 22/03/2016]; Available from: [http://www.bbc.co.uk/schools/gcsebitesize/science/add\\_gateway\\_pre\\_2011/radiation/ultrasoundrev2.shtml](http://www.bbc.co.uk/schools/gcsebitesize/science/add_gateway_pre_2011/radiation/ultrasoundrev2.shtml).
32. *Ultrasound: Physics and Basic Equipment Settings*. [Last accessed date 24/03/2016]; Available from: <http://www.rcemlearning.co.uk/modules/ultrasound-physics-and-basic-equipment-settings/types-of-ultrasound/amode/>.
33. *Heart, amyloidosis, M-mode*. [Last accessed date 10/05/2017]; Available from: <http://www.medison.ru/uzi/eho404.htm>.
34. Wilhjelm, J.E., et al., *Medical diagnostic ultrasound-physical principles and imaging*.
35. Cobbold, R.S.C., *Foundations of Biomedical Ultrasound*. 2006: Oxford University Press.
36. Arbona, F.L., Babak Khabiri, and J.A. Norton., *Ultrasound-Guided Regional Anesthesia*. 2011: Cambridge University Press.
37. Grant, S.A. and D.B. Auyoung, *Ultrasound Guided Regional Anesthesia*. 2012: OUP USA.
38. Gibbs, V., D. Cole, and A. Sassano, *Ultrasound Physics and Technology: How, Why and When*. 2011: Elsevier Health Sciences UK.
39. *Use of Ultrasound to Guide Vascular Access Procedures*. [Last accessed date 30/03/2016]; Available from: <http://www.aium.org/resources/guidelines/usgva.pdf>.
40. Cooper, J.M. and L.M. Epstein, *Use of intracardiac echocardiography to guide ablation of atrial fibrillation* Circulation, 2002. **105**(10): p. 1256-1256.
41. *Ultrasound frequencies*. [Last accessed date 02/04/2016]; Available from: <http://radiopaedia.org/articles/ultrasound-frequencies>.
42. Harald Lutz, E.B., *Manual of Diagnostic Ultrasound*, ed. 2. Vol. 1. World Health Organization. 420.
43. Zhou, Q., et al., *Piezoelectric single crystal ultrasonic transducers for biomedical applications*. Progress in Materials Science, 2014. **66**: p. 87-111.
44. O'BRIEN, W., *Single-Element Transducer*. RadioGraphics, 1993. **13**: p. 947-957.
45. *Transducer Basics*. [Last accessed date 06/04/2016]; Available from: <http://www.echocardiographer.org/Echo%20Physics/BasicTransducers.html>.
46. Jiang, Y., *Fabrication and characterisation of novel ultrasound transducers*, in *School of Metallurgy and Materials*. 2013, University of Birmingham.
47. Tole, N.M. and H. Ostensen, *Basic Physics of Ultrasonographic Imaging*. 2005: World Health Organization.
48. *Basic Principle of Ultrasound*. [Last accessed date 16/04/2016]; Available from: <http://www.sonotech.com.pk/book/271>.
49. Alexander Ng, J.S., *Resolution in ultrasound imaging*. Continuing Education in Anaesthesia, Critical Care & Pain. **11**(5): p. 186-192.
50. *Frequency and Image Resolution*. [Last accessed date 26/04/2016]; Available from: <http://www.usra.ca/transducer.php#top>.

## **Chapter 3 Piezoelectric materials, 1-3 randomised piezocomposites design and manufacture for high frequency ultrasound transducer applications**

Ultrasound transducers are employed for diagnostic application by using the piezoelectric effect. Piezoelectric materials are utilized as the active material that can determine the characteristics of the transducer. Lead zirconate titanate (PZT) based materials have dominated the piezoelectric material market, including piezocomposites for medical ultrasound applications. However, one of the critical drawbacks of PZT is the high percentage of hazardous lead which it contains, and which could be released during processing. Therefore, lead free materials are being developed as replacements for PZT. This chapter introduces and reviews basic knowledge of the piezoelectric phenomenon, piezoelectric materials, including lead based and lead free materials and 1-3 piezocomposite fabrication with emphasis on gel casing for high frequency transducer application.

### **3.1 Principle of piezoelectricity**

The piezoelectric phenomenon was first discovered in 1880 by Pierre and Jacques Curie who found out effects of pressure on the electrical charge of the surface of asymmetric crystals such Quartz, Tourmaline, Topaz and Rockshell. This phenomenon was subsequently named as piezoelectricity by W.G. Hankel in 1881 [1], [2]. Although the Curie brothers were credited to discover the direct piezoelectric effect, it was Lippmann who discovered the converse effect by using mathematical predictions from thermodynamic principles. The first piezoelectric

application, which was an ultrasonic transducer for sonar application, was developed by Paul Langevin and his colleagues during World War I [3]. The success of this first application brought up the opportunities for piezoelectric materials during and after World War II. Countries such as the United States, Japan and the Soviet Union were interested in the research and development of piezoelectric materials, leading to the discovery of piezoelectricity in polycrystalline ceramics, initially in Barium Titanate ( $\text{BaTiO}_3$ ) and subsequently in PZT. This was considered a breakthrough, as all previous piezoelectric materials had been single crystals. Therefore, the use of piezoelectric materials became widespread for many industrial applications such as microphones and accelerometers [4-6].

### **3.1.1 Piezoelectricity**

Piezoelectricity is a phenomenon that can be described by the interaction between the electrical and mechanical properties of some materials. The direct piezoelectric effect is defined as the polarization generated by the application of a mechanical stress, and is exploited in generator or sensor applications. Vice versa, when a piezoelectric material is subjected to an applied electrical field strain is induced. This phenomenon is known as the converse or indirect effect which is used in motor applications [7-9].

As shown in Table 3.1, the crystallographic symmetry of materials can be classified into 32 crystal classes or point groups of which 21 are non centrosymmetric and provide the potential for a net dipole moment since the positive and negative charge centres do not coincide. Only 20 of these crystal classes exhibit the piezoelectric effect [10], and 10 of these possess a permanent net dipole moment in the absence of an electrical field and in which the spontaneous polarization can be induced by

changing temperature. For example, the polarization in the crystal will be increased with increasing the temperature, and the critical temperature at which the polarization reduces to zero is called the Curie temperature ( $T_C$ ). All pyroelectric materials display the piezoelectric effect, but not all piezoelectric materials are pyroelectric. A special sub group of pyroelectric materials in which the direction of the polarization can be changed by the application of an external electric field, are called “Ferroelectric” [11], [12]. For ultrasound transducer applications, ferroelectric materials, which are both piezoelectric and pyroelectric, are the most commonly used.

**Table 3.1 Piezoelectric, Pyroelectric and Ferroelectric crystal classes.**

	<b>32 crystal classes</b>	
	↓	
<b>of which</b>	21 Lack of Centre of symmetry	11 are Centrosymmetric
	↓	
<b>of which</b>	20 Exhibit piezoelectricity	1 Class Non-piezoelectric
	↓	
<b>of which</b>	10 Exhibit pyroelectricity	10 do not (Non-polar classes)
	↓	
<b>of which</b>	some are ferroelectric	some are non ferroelectric

Barium Titanate ( $BaTiO_3$ ), Lead Zirconate Titanate ( $PbT_xZ_{1-x}O_3$ ), Lead Titanate ( $PbTiO_3$ ) and Lead Zirconate ( $PbZrO_3$ ) are the most commonly used commercial piezoelectric materials. The structures of these piezoceramics are based on the perovskite structure with the chemical formula  $ABO_3$ . The simplest atomic arrangement consists of oxygen anions ( $O^{2-}$ ), located at the centre of the 6 faces, large divalent metal cations ( $A^{2+}$ ) such as barium or lead, occupying the cube corners, and small tetravalent metal ions ( $B^{4+}$ ) such as zirconium or titanium, occupying the body centre position [3], [13], [14]. Above the Curie temperature, each perovskite crystal in, for example, PZT has a cubic symmetry which cannot

exhibit piezoelectricity due to the centres of the negative and positive charges in the unit cell being balanced, resulting in a zero net dipole in the crystal [15], as presented in Figure 3.1. However, when the temperature is decreased below the Curie temperature, due to the distortion of the oxygen and metal ions in the crystal, the cubic system is destroyed to non-cubic symmetry such as tetragonal or rhombohedral symmetry. The off-centre ions generate an imbalance of centre of positive and negative charges in the unit cell, resulting in a net dipole moment (Fig 3.1).

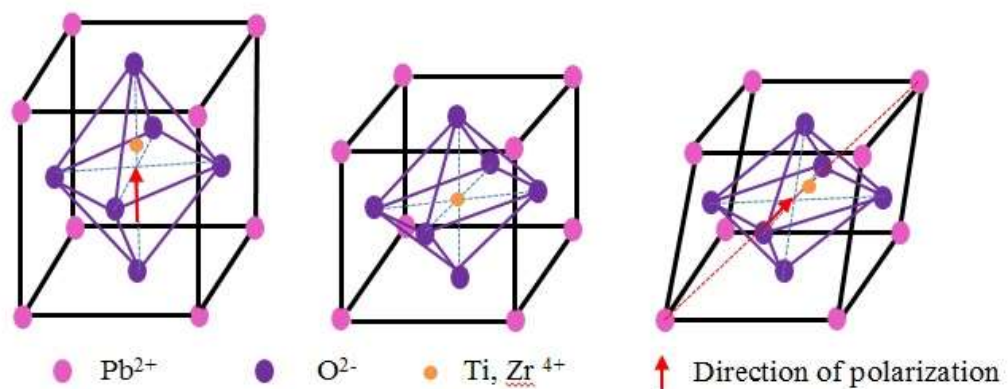


Figure 3.1 Crystallographic structures of lead zirconate titanate perovskite crystal (a) tetragonal, (b) cubic and (c) rhombohedral, the direction of polarization are indicated by the arrows.

### 3.1.2 Poling of piezoelectric ceramics

Piezoelectric ceramics are normally created by solid-state reaction methods involving calcination and sintering of precursor oxide and carbonate powders. After cooling to below the Curie temperature, each grain in a polycrystalline material will become spontaneously polarized, but as the orientation of the grains, and hence the polarisations, will be random, no net polarization will be observed. In order to observe the piezoelectric properties, an external electric field needs to be applied to

the material at a temperature below the Curie temperature ( $T_C$ ) in a process known as poling. Each domain can be switched and aligned parallel to the external electric field. Some domains change back after the external electric field is removed or are difficult to reorient. However, the ferroelectric now exhibits piezoelectricity as most of dipoles remain aligned [16], [17], [6]. Permanent polarization will be partially or totally lost by applying an external electric field with opposite polarity to the piezoelectric ceramic, by applying a strong mechanical stress to disturb the domain orientation, or heating above the Curie temperature [18].

### **3.1.3 Piezoelectric constitutive equations**

When poled piezoelectric ceramics are subjected to low mechanical stresses or electrical fields, the atomic alignments in the unit cell are changed. This is known as the intrinsic effect and is often linear. In this research, it is assumed that piezoelectric transducers are being utilised at low electrical fields and low external stresses, therefore, this thesis is mainly concerned with linear behaviour [4], [13], [19], [20].

The convention for the definition of directions relative to the poling direction in a piezoceramic is depicted in Figure 3.2. The 3 axis ( $z$ ) is defined as the direction of initial polarization (i.e. the poling direction), 1 axis ( $x$ ) and 2 axis ( $y$ ) are all orthogonal to the 3 axis, subscripts 4, 5 and 6 indicate the shear direction along 1, 2 and 3 axis, respectively. The defined directions with two subscript numbers are given with a specific piezoelectric parameter to explain their behaviour. The first and second numbers represent the input and response directions, respectively. For example,  $d_{31}$  relates to charge displacement developed in the 1 direction relative to

the stress applied along the 3 direction, while the electric field applied along the 3 direction inducing a strain along the 1 direction for the transverse effect.

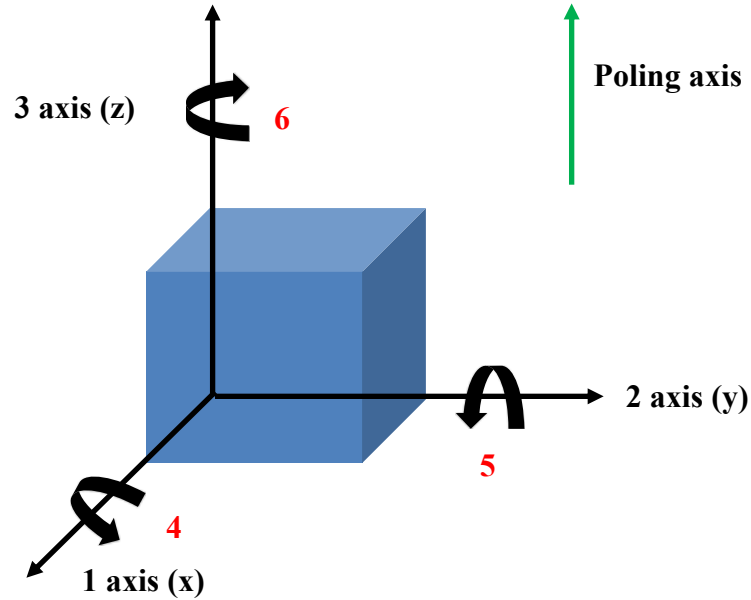


**Figure 3.2** Designation of the coordinate axis for a piezoelectric plate pole along its thickness.

The constitutive equations explaining the piezoelectricity are based on the relationship between the elastic and electrical properties. The coupled relationship can be assumed that the total mechanical strains in piezoelectric material are induced by mechanical stress caused by the applied electric field [21]. When an unstressed medium has been influenced by an electric field, the electrical behaviour can be described by dielectric displacement ( $D$ ) and electric field ( $E$ ) as:

$$D = \epsilon E \quad \text{Equation 3.1}$$

where  $\epsilon$  is the permittivity of material. The mechanical behaviour of the same medium placed at zero electric field, can be described by the applied stress ( $T$ ) and a strain ( $S$ ). The strain in piezoelectric materials can be induced by applied stress as in equation 3.2.



$$S = sT \quad \text{Equation 3.2}$$

where  $s$  is the compliance of material

The electromechanical equations of piezoelectric material, which is a strain-charge form, can be expressed as a by linear relationship form as

$$D = d_{ij}T + \varepsilon_{ij}^T E \quad \text{Equation 3.3}$$

$$S = s_{ij}^E T + \mathbf{d}_{ij} E \quad \text{Equation 3.4}$$

where:

$D$  is the vector of electric displacement ( $C/m^2$ )

$d$  and  $\mathbf{d}$  are the matrix of piezoelectric charge constants ( $m/V$ )

$T$  is the stress vector ( $N/m^2$ )

$\varepsilon$  is the matrix of dielectric constant ( $F/m$ )

$E$  is the vector of electric field ( $V/m$ )

$S$  is the strain vector ( $m/m$ )

$s$  is the matrix of compliance coefficients ( $m^2/N$ )

Dielectric constant ( $\varepsilon_{ij}^T$ ) and elastic constant ( $s_{ijkl}^E$ ) are measured under conditions of constant stress and electric field, respectively.

## **3.2 Piezoelectric materials for high frequency ultrasound transducers**

The performance of single element high frequency ultrasound transducers is significantly influenced by the properties of the piezoelectric materials from which they are made. There are many crucial determinants for piezoelectric materials to be used as active materials for the transducer; explained as follows; [22-29]. For medical ultrasound applications, the electromechanical coupling coefficient ( $k$ ) and acoustic impedance ( $Z_a$ ) are two of the most crucial factors.

### ***Electromechanical coupling coefficient***

This coefficient explains the efficiency of converting acoustic energy to electrical energy and vice versa; therefore, this coefficient should be as close to 1 as possible. Typically, for medical applications, the ultrasound wave propagates in longitudinal vibration mode in which the displacements coincide with the direction of polarization; therefore, the thickness mode  $k_t$  is normally used.

### ***Acoustic impedance***

The piezoelectric disc or plate should provide good acoustic matching to biological tissues (approximately 1.5 MRayl). A small acoustic mismatch leads to lower losses at the interfaces and results in a strong transmitted intensity of the ultrasound beam. Consequently, the signal has a good clarity.

There are a few other factors which also play a vital role in choosing the active piezoelectric materials.

### ***Electrical impedance and system electronics***

The single element transducer typically needs a large active area in order to moderate the high dielectric constant of the piezoelectric material in order to achieve compatibility between electrical impedance match to the electronics.

### ***Electrical and mechanical loss***

Minimal dissipation factor of both the electrical and mechanical signals are required in order to reduce the heat generated during operation and improving sensitivity.

### ***Machinable and mechanically flexible***

The active material should have enough strength in case for shaping to achieve the focused transducer without lenses and can be machinable.

## **3.2.1 Lead based piezoelectric ceramics**

The natural occurring piezoelectric crystals are not normally used as for industrial applications because their properties are inferior to the polycrystalline piezoelectric ceramics. Barium Titanate ( $\text{BaTiO}_3$ ) is one of most well-known and widely used polycrystalline ferroelectric materials for many of industrial utilisations, especially for multilayer ceramic capacitors (MLCC) because its large dielectric constant. However,  $\text{BaTiO}_3$  has not reached the requirements of some applications such as transducers, sensors or actuators which demand tailored performance [30], [31]. After lead zirconate titanate (PZT), which has superior piezoelectric properties such as high electrocoupling coefficient and high dielectric constant, was discovered during the 1960's,  $\text{BaTiO}_3$  was not extensively used [32]. PZT is the most popular as

piezoelectric material used today for ultrasound transducers in medical applications.

Figure 3.3 presents the phase diagram for the  $\text{PbZr}_{(1-x)}\text{Ti}_x\text{O}_3$  system.

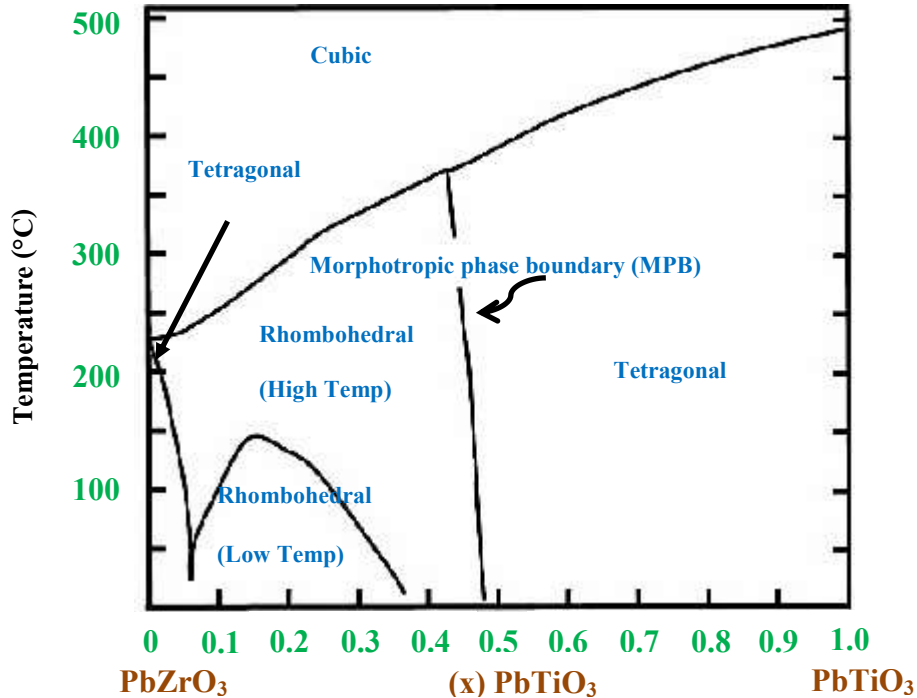


Figure 3.3 Phase diagram of PZT [33], [34].

The properties of PZT are dependent on the Zr and Ti content, temperature, and also concentration of dopant. With increasing Ti content, at  $x > 0.48$ , the structure is changed from rhombohedral to tetragonal. The Morphotropic phase boundary (MPB) refers to the boundary in a composition diagram that provides a maximum number of polarization states. In PZT phase diagram, MPB is the line that separates these tetragonal and rhombohedral phases. On the boundary, both tetragonal and rhombohedral phases co-exist; therefore the compositions close to the MPB allow PZT to achieve excellent properties. The two coexisting phases provide more equivalent directions of polarization for the material ( $\langle 001 \rangle$  in tetragonal and  $\langle 111 \rangle$  in rhombohedral). The properties also vary with temperature, with increasing temperature, the polarization decreases, and piezoelectricity of the material

disappears at the Curie point since the polarization is reduced to zero when the cubic phase is formed. The properties of PZT can also be tailored by donor or acceptor doping. For example, soft PZT, which is normally used as the transducer material for medical imaging application, can be created by donor dopants such as  $\text{Nb}^{5+}$ ,  $\text{Sb}^{5+}$ ,  $\text{Ta}^{5+}$  ions of the B-site which allow the domain movements as cation vacancies are formed. Hard PZT can be created from oxygen vacancies formed by acceptor doping with low charge ions such as  $\text{Co}^{3+}$ ,  $\text{Fe}^{3+}$ ,  $\text{Cr}^{3+}$  on the B-site, and  $\text{K}^+$  or  $\text{Rb}^+$  on the A site [4], [7], [35-39]. These are the reasons why PZT based material can be adapted for many application. Table 3.2 shows the characteristic of hard and soft PZT. Soft PZT presents high heat losses; however, it is acceptable for small devices. PZT5A and PZT 5H are two standard types of soft PZT which normally use in industrial applications. For transducer materials, PZT 5H is the common as it provides higher electromechanical coupling coefficient and dielectric constant [29], [40-42].

**Table 3.2 Characteristic of hard and soft PZT [43].**

<b>Characteristic</b>	<b>Soft PZT</b>	<b>Hard PZT</b>
Piezoelectric Constants	larger	smaller
Permittivity	higher	lower
Dielectric Constants	larger	smaller
Dielectric Losses	higher	lower
Electromechanical Coupling Factors	larger	smaller
Polarization / Depolarization	easier	more difficult

However, there are some critical drawbacks of PZT. Firstly, it has high acoustic impedance (>30 MRayl) which causes acoustic mismatch between human tissue and

the active material. Second, the nature of the ceramic is that it is hard and brittle, which can lead to fracture. These factors limit the ability to do machining of the shape required for focused transducers.

### **3.2.2 Lead free piezoelectric ceramics**

As discussed above, lead based ferroelectric materials represented by PZT are the most extensively used in piezoelectric applications and have dominated the ferroelectric device market due to their excellent properties close to the MPB [44]. Nevertheless, the most critical disadvantage of this material is that it contains lead (Pb) which is a very toxic substance which causes human health and environmental problems [45]. With the growing concern over environmental and public health risks, the Restriction of Hazardous Substances Directive (RoHS) which is a very important legislation restricting the use of hazard substances in electrical and electronic equipment (EEE) devices and was issued from the European Union in 2006. In this legislation, the maximum allowable amount of lead is 0.1%; however, typically, lead based piezoelectric materials has high percent lead content (~60%) [46]. As a result, research has turned towards the search for alternative lead free materials to replace the lead based materials. A number of well-known lead free perovskite materials such as Barium Titanate ( $\text{BaTiO}_3$ ), Bismuth Sodium Titanate based materials (BNT), Sodium Potassium Titanate based materials (KNN) have received considerable attention [47]. However, compared with PZT materials, these lead free materials still present low piezoelectric properties ( $d_{33}$  values of 100-200 pC/N) [44], [48]. The new lead free material Barium Zirconate Titanate (BZT) and Barium Carbonate Titanate (BCT) or BCZT were discovered by Liu and Ren in 2009, [49] and have

attracted more attention due to its high piezoelectric coefficient ( $d_{33} \sim 350\text{-}650$  pC/N) at the composition of 0.5BZT-0.5 BCT or 50 BCZT [49-51].

### 3.2.2.1 BaTiO<sub>3</sub> Based Materials

One of the first piezoelectric materials with perovskite structure was BaTiO<sub>3</sub>, discovered and published in open literature during mid of 1940s [52]. In 1945, Gray discovered and proved that BaTiO<sub>3</sub> can be an invaluable ferroelectric material. BaTiO<sub>3</sub> also was the first piezoceramic material for transducer applications. However, it has low electromechanical coupling factor ( $\sim 0.35$ ) and low Curie temperature ( $T_C \sim 120^\circ\text{C}$ ), which restricts the operational output and its use as a high power transducer [53]. However, BaTiO<sub>3</sub> is a superior piezoelectric material for using in discrete and multilayer capacitors due to its high dielectric constant [54]. A large amount of research has been devoted to improve its basic properties and also increase Curie temperature by using special additives. The binary system of  $(1-x)\text{BaTiO}_3\text{-}x(\text{Bi}_{0.5}\text{K}_{0.5})\text{TiO}_3$  elevates the Curie temperature but results in reduced piezoelectric properties [55]. Small amounts of Sr and Zr were used as dopants for substitution on A site and B site, respectively, resulting in a phase change from tetragonal to orthorhombic [56]. The  $(\text{Ba}_{0.95}\text{Sr}_{0.05})(\text{Zr}_{0.05}\text{Ti}_{0.95})\text{O}_3$  composition presented high  $d_{33}$  ( $\sim 300\text{pC/N}$ ) with high relative permittivity ( $\sim 1346$ ) [57]. The discovery of the binary system of BCZT led to the development of the compositions to achieve the high electromechanical coupling factor and high  $d_{33}$ .

### 3.2.2.2 BNT and BKT Based Materials

Bismuth sodium titanate ( $\text{Bi}_{0.5}\text{Na}_{0.5}\text{TiO}_3$  : BNT) and bismuth potassium titanate ( $\text{Bi}_{0.5}\text{K}_{0.5}\text{TiO}_3$  : BKT) were first reported by Smolenskii in the 1960s [58]. They both

adopt the perovskite structure with the mixture of  $\text{Bi}^{3+}$  and  $\text{Na}^+/\text{K}^+$  on the A site, but BNT exhibits tetragonal symmetry at room temperature whereas BKT is rhombohedral [59]. These two materials are promising alternative lead free piezoelectric materials due to their advantages such as high remnant polarization ( $\sim 38 \mu\text{C}\cdot\text{cm}^{-2}$ ), and high Curie temperatures (BNT  $\sim 325^\circ\text{C}$ , BKT  $\sim 380^\circ\text{C}$ ) with depolarization temperature ( $T_d$ ) at  $187^\circ\text{C}$  and  $270^\circ\text{C}$  for BNT and BKT, respectively [60], [61]. However, there are several drawbacks of these materials, such as, difficult poling process due to high coercive field and conductivity, low piezoelectric and dielectric constant, and poor sinterability. BNT and BKT require temperatures above  $1200^\circ\text{C}$  to achieve sintered ceramics, but such high sintering temperatures result in the loss of bismuth which causes high conductivity and low density in the sintered ceramics, leading to difficulties in poling [62]. The sinterability can be improved by using hot pressing methods at  $1100^\circ\text{C}$  [63]. The use of sintering aids was studied by Hiruma *et al.* by using 0.3%wt bismuth excess which can improve piezoelectric properties in the BKT system [64]. As the properties of pure BNT and BKT themselves are not good enough, a number of the binary and ternary systems have been studied to overcome the drawbacks. Barium modified bismuth sodium titanate  $(1-x)\text{Bi}_{0.5}\text{Na}_{0.5}\text{TiO}_3-x\text{BaTiO}_3$  (BNT-BT) can reduce the sintering temperature to  $1100\text{-}1200^\circ\text{C}$  [62], The dielectric and piezoelectric properties can be enhanced at the value  $x = 0.6$  where the MPB exists between tetragonal and rhombohedral phase ( $d_{33} \sim 125\text{pC/N}$ ,  $\frac{\epsilon_{33}}{\epsilon_0} = 580$ ,  $k_{33} = 0.5$ ); however,  $T_d$  dropped to  $228^\circ\text{C}$  [65]. In contrast to BNT-BT, the piezoelectric properties of BKT-BT are not as good as BNT-BT [66]. Binary  $\text{Bi}_{0.5}\text{Na}_{0.5}\text{TiO}_3$  and  $\text{Bi}_{0.5}\text{K}_{0.5}\text{TiO}_3$  (BNT-BKT) mixtures were first studied by Elkechai *et al* [67], later research revealed that, compared with other binary systems,



BNT-BKT possesses higher  $d_{33}$ , relative permittivity, and also high Curie temperature and depolarization temperature, as expected from BKT. Although piezoelectric properties can be achieved at the MPB, the lowest  $T_d$  are also observed [62], [68]. The most well known ternary systems are BNT- BT-BKT and BNT-BT-KNN where compositions near the MPBs were mostly researched. The properties of BNT- BT-BKT are comparable to those binary systems due to its high  $T_c$  and piezoelectric properties, also the lowest  $T_d$  can be observed near the MPB, similar to binary systems. It also was suggested by Choy *et al.* to be an alternative piezoelectric materials for replacement of PZT in accelerometer [69] and transducer applications [70]. The BNT-BT-KNN system can improve domain wall movement and poling ability due to its MPB exhibiting 3 phases of rhombohedral, tetragonal and orthorhombic from BNT, BT and BKK, respectively, resulting in a high strain induced material [62] [71].

### 3.2.2.3 KNN Based Materials

Another lead free piezoelectric material alternative to PZT is  $K_{1-x}Na_xNbO_3$  (KNN). KNN has a perovskite structure and is a solid solution of ferroelectric ( $KNbO_3$ ) and antiferroelectric ( $NaNbO_3$ ) [72], which have orthorhombic structures at room temperature. The highest piezoelectric properties occur at the 50/50 composition near the MPB where the two orthorhombic phases are separated [47]. The main advantage of this system is that it has a high Curie temperature (about  $\sim 400^\circ C$ ). However, there are several drawbacks; for example, KNN is difficult to achieve in fully dense form due to the instability of  $KNbO_3$  above  $1040^\circ C$  and  $NaNbO_3$  above  $1140^\circ C$ , resulting in stoichiometry changes due to the volatility of the components at high temperature. It is difficult to produce dense KNN using ordinary sintering methods: however, fully

dense of KNN can be achieved by using hot pressing which provides double the  $d_{33}$  value ( $\sim 160$  pC/N) compared with materials produced using a conventional sintering method. KNN also has a low dielectric constant and planar electromechanical coupling ( $k_p \sim 0.2-0.4$ ) [47], [73-75]. The difficulty of processing KNN makes it a less attractive lead free alternative to PZT. Nevertheless, by adding dopants such as LiTaO<sub>3</sub> (LT) or LiSbO<sub>3</sub> (LS) the density and piezoelectric properties can be enhanced due to the decrease of the phase transition temperature from tetragonal to orthorhombic ( $T_{t-o}$ ). A planar coupling coefficient of 0.5,  $d_{33}$  of 230 pC/N with high dielectric constant of 1255 has been reported for  $(K_{0.5}Na_{0.5})_{0.07}Li_{0.03}(Nb_{0.8}Ta_{0.2})O_3$  by Saito *et al* [76]. KNN with LS dopant exhibits  $d_{33}$  values of 265 pC/N while the highest  $d_{33}$  can be obtained from KNN- LT-LS ceramics as presented in Table 3.3.

**Table 3.3 Piezoelectric properties of KNN-based Materials [77].**

KNN-based materials	$\epsilon_{33}^T/\epsilon_0$	$T_c$ (°C)	$T_d$ (°C)	$d_{33}$ (pC/N)	$k_{33}$
KNN-BKT	1260	376	75	251	
KNN-LT	540-1256	323	70	200-230	0.3-0.5
KNN-LS	1380	368	35	265	50
KNN-LT-LS	665-1865	265-290	60	315	48.4

### 3.2.2.4 BCZT Based Material

As discussed above, a significant amount of research is now focused on alternative lead free piezoelectric materials with perovskite structure. Although BT, BNT and BKT, and KNN related materials have received extensive attention due to their good piezoelectric properties and high Curie temperature, the  $d_{33}$  values are much lower than PZT. In 2009, Liu and Ren discovered a new binary system by doping Ca and Zr into BaTiO<sub>3</sub> based materials, resulting in a solid solution of BCZT lead free piezoelectric materials with the extremely high piezoelectric constant value about

~620 pC/N (comparable to lead based materials) at the composition  $x = 0.5$  (where  $x$  is the molar percent of BCT) [49]. The pseudo binary system of BCZT was originally developed by attempting to improve the piezoelectric properties of barium titanate by using  $\text{Ca}^{2+}$  and  $\text{Zr}^{4+}$  ion as dopants to substitute onto the A site ( $\text{Ba}^{2+}$ ) and B site ( $\text{Ti}^{4+}$ ), respectively [78]. The BCZT samples were prepared by solid state reaction methods from high purity of  $\text{BaZrO}_3$ ,  $\text{BaCO}_3$ ,  $\text{CaCO}_3$ ,  $\text{TiO}_2$  [49], or  $\text{BaCO}_3$ ,  $\text{CaCO}_3$ ,  $\text{TiO}_2$  and  $\text{ZrO}_2$  raw materials [79]. Figure 3.4 shows the phase diagram of BCZT. An MPB separates the rhombohedral and tetragonal phases. The dominant feature of BCZT that makes it different from other lead free systems is that it has a strongly curved MPB and there is a cubic-rhombohedral-tetragonal triple point or tricritical point (TCP) at  $\sim 52^\circ\text{C}$  and  $x \sim 32\%$  [49].

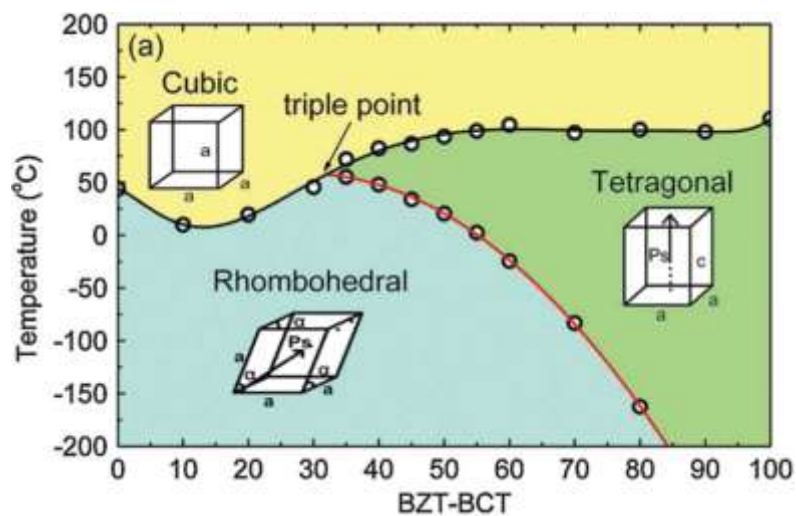


Figure 3.4 Phase diagram of binary system BCZT [49].

The BCZT binary system could be a good alternative piezoelectric material to lead based materials - it is an environmentally friendly material, and has a similar phase diagram to PZT with a triple point of cubic-rhombohedral-tetragonal phases – so having the potential to exhibit enhanced piezoelectric properties compared to the end members. However, the MPB in BCZT is tilted and varies with temperature and

composition indicating poor temperature stability. Revised phase diagrams have been presented by Keeble *et al.* in 2013 [80], and Bai *et al.* in 2015 [79], both showing that there is an additional orthorhombic phase,  $\lambda$ , region between the tetragonal and rhombohedral phases, similar to BaTiO<sub>3</sub>, as shown in figure 3.5 (orthorhombic phase indicated as  $\lambda$  phase).

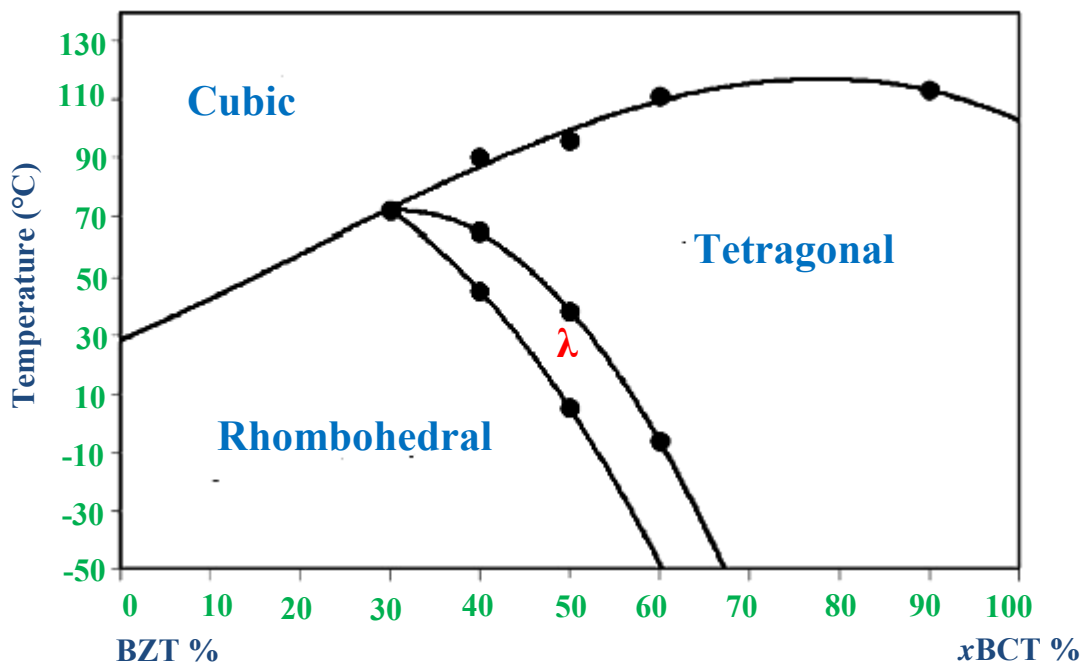


Figure 3.5 Phase diagram of binary system BCZT with  $\lambda$  phase [79].

Recently, many more investigations of BCZT have been reported including effects of composition and phase diagram, fabrication methods (thick film, sol gel, gel casting), calcination and sintering temperature, dopants, poling conditions and microstructure on properties. For example, thick films for micro actuator applications of 0.5BZT-0.5BCT have been produced by screen printing with  $d_{33} = 427$  pm/V and remnant polarization  $P_r = 15.8$   $\mu\text{C}/\text{cm}^2$  [81]. Thin films of 50BCZT on Pt/TiO<sub>2</sub>/SiO<sub>2</sub>/Si substrates have been fabricated by pulsed laser deposition, with  $d_{33} = 80$  pm/V and relative permittivity 1010 being observed [82]. The effects of sintering temperature

on piezoelectric and dielectric properties have been studied by Mishra *et al.*, reporting that the density, grain size and  $d_{33}$  increased with increasing sintering temperature. A  $d_{33}$  (~281 pC/N) has been reported for samples sintered at 1400°C [83]. Moreover, it has been reported that with increased calcination temperature, the piezoelectric constant, planar and thickness coupling coefficients and dielectric constant can be enhanced. Using a calcination temperature of 1300°C for 0.5BZT-0.5BCT and sintering at 1540°C properties of  $d_{33} = 650$  pC/N,  $k_p = 0.53$ ,  $k_t = 0.38$  and relative permittivity = 4500 were reported [44]. It has also been reported that  $d_{33}$  values can be improved with increasing poling temperature, by poling the samples at temperatures above the Curie temperature (120°C) and then cooling to room temperature under the applied electric field, the highest  $d_{33}$  value of 510 pC/N was observed [84].

The effect of additions have also been studied.  $Y_2O_3$  added to BCZT shows enhanced sinterability, resulting in a decreased sintering temperature from 1530 to 1350°C, and increased Curie temperature from 85 to 95°C, the highest  $d_{33}$  560 pC/N and  $k_p$  0.53 were found for  $x=0.06$  [48]. Bai *et al.* reported an investigation of the effect of composition (ratio of  $Ba(Zr,Ti)O_3$  to  $(Ba,Ca)TiO_3$ ), sintering temperature, cooling rate and particle size on density and piezoelectric properties. The density of samples prepared from 1 and 3  $\mu m$  powders decreased with increasing sintering temperature due to the incomplete densification of samples leading to trapped porosity, while the density of samples prepared from 5  $\mu m$  powder increased with increasing sintering temperature. However, the grain size of samples produced from 1, 3 and 5  $\mu m$  powders followed the same trend of sintering temperature. The density also can be controlled by cooling rate, with slower cooling rates (1°C / min), the

relative density tends to increase by 2-3%. The grain sizes can also vary according to the compositions. Powder particle size was shown to influence  $d_{33}$ , samples produced from 1  $\mu\text{m}$  powder revealed a highest  $d_{33}$  of 300 pC/N while 3 and 5  $\mu\text{m}$  powders produced samples with  $d_{33} = 300\text{-}500$  pC/N, and the highest  $d_{33}$  was obtained from 5  $\mu\text{m}$  powders of the 0.5BZT-0.5BCT composition, sintered at 1475°C with slow cooling rate [79].

The main drawback of the BCZT system is that it has a low Curie temperature as presented in Table 3.4, which limits its wide use in piezoelectric applications. However, a needle ultrasound transducer for intravascular imaging using the 0.5BZT- 0.50BCT composition with a thickness of active material  $\sim 75$   $\mu\text{m}$  has been fabricated by Yan *et al.*, presenting a transducer with  $k_{eff} = 0.51$ , centre frequency was 30 MHz and bandwidth of 53% at -6 dB [85], showing the potential of the material for medical ultrasound applications.

**Table 3.4 Curie temperature of various piezoelectric materials [49, 55, 62, 63, 86, 87]**

Piezoelectric materials	$T_c$ (°C)
0.5BZT-0.5BCT	$\sim 90$
BT based	$\sim 120$
KNN based	$\sim 400$
BNT based	$\sim 325$
BKT based	$\sim 380$
PZT based	$\sim 385$

### 3.2.3 Piezoelectric Polymers

In addition to lead based materials, piezoelectric polymers have also been found to be useful for making ultrasound transducers. A 5 MHz single element transducer for medical diagnosis using Polyvinylidene difluoride (PVDF) as the transducer material

was reported in 1979 [88], then PVDF became a commonly used material [89], [90]. During melting, the non-polar  $\alpha$  phase is formed, and this phase can be changed to the polar  $\beta$  phase by a drawing process which causes the reorientation of the dipole moments. After processing, the thin piezoelectric polymer sheet with thickness 5-25  $\mu\text{m}$  can be used as a piezoelectric polymer for transducer fabrication [36]. There are several advantages of PVDF such as low cost, high flexibility, and low acoustic impedance (4 MRayl), leading to simplification of acoustic matching with biological tissues. Though transducers produced by PVDF are wideband, PVDF is not a good transmitting material since it has a piezoelectric activity, low electromechanical coupling coefficient, low dielectric constant, and high dielectric loss. Copolymers such as trifluoroethylene (TrFE) have been used for enhancing properties but the properties are still not enough to achieve good sensitivity and widespread transducer applications [27], [29], [88], [91].

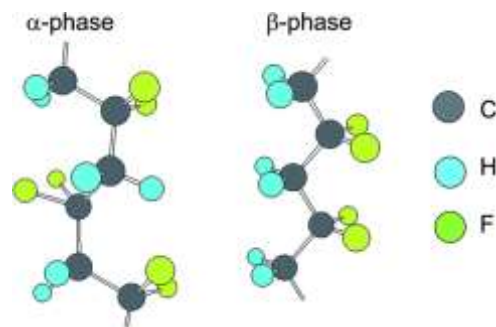


Figure 3.6 Polyvinylidene difluoride in  $\alpha$  and  $\beta$  phase [92].

### 3.2.4 Piezoelectric single crystal

The piezoelectricity was investigated in single crystals as quartz and lithium niobate; however they were not the material of choice for industrial applications due to the low piezoelectric properties compared to PZT [93]. Transducer materials for medical

imaging have been dominated by solid solutions of the PZT compositions near the MPB. More recently, the development of relaxor-based piezoelectric single crystals has demonstrated exceptional piezoelectric properties compared to their polycrystalline counterparts. Typically, the formula of the relaxor-based piezoelectric single crystals is  $\text{Pb}(\text{B}_1\text{B}_2)\text{O}_3$  ( $\text{B}_1$ :  $\text{Zn}^{2+}$ ,  $\text{Mg}^{2+}$ ,  $\text{Sc}^{3+}$ ,  $\text{Ni}^{2+}$ ...,  $\text{B}_2$ :  $\text{Nb}^{5+}$ ,  $\text{Ta}^{5+}$ ). Two relaxor-based piezoelectric compositions,  $\text{Pb}(\text{Mg}_{1/3}\text{Nb}_{2/3})\text{O}_3 - \text{PbTiO}_3$  (PMN-PT) and  $\text{Pb}(\text{Zn}_{1/3}\text{Nb}_{2/3})\text{O}_3 - \text{PbTiO}_3$  (PZN-PT), are the most commonly used as single crystal transducer materials. Compared with PZT, there are some similarities between these two single crystals compositions and PZT as they have a perovskite structure and the best piezoelectric properties can be achieved near the MPB where the rhombohedral-tetragonal phases coexist [94]. However, relaxor-based piezoelectric single crystals provide better piezoelectric properties, including electromechanical coupling,  $k_{33} \sim 0.85-0.95$ , lower acoustic impedance (22-28 MRayl), ultrahigh piezoelectric coefficient ( $d_{33} \sim 1500-2800$  pC/N), dielectric constant 1000-5000 with low dielectric loss (<1%). Therefore, these single crystals are preferable for designing high transducer performance with broad bandwidth and high sensitivity [95-97]. The first commercial single crystal transducer with low frequency (5 MHz) for cardiac harmonic medical imaging from Philips Ultrasound was launched to the market in 2004 [98]. Although single crystals can be a material for commercial transducers, their commercialisation has been limited by low yield and high cost [97], caused by difficulties in crystal growth [99]. One of the critical limitations for using these materials is the low Curie temperature ( $T_C < 160^\circ\text{C}$ ) which is important in determining thermal stability, which restricts the temperature during fabrication and operation [27], [29].



### 3.2.5 Piezoelectric composites

As discussed above, PZT based materials, piezoelectric polymers and single crystals have several limitations to be the material of choice for medical transducers as PZT based materials and single crystal have high  $k_t$  and acoustic impedance; therefore, acoustic mismatch will be a problem, which restricts extensive use for medical diagnostic applications. Piezoelectric polymers can be a choice for acoustic matching but they are not good transmitting materials. This means one single piezoelectric material can only partially meet all these requirements and no readily available materials combine two of the most important parameters for ultrasound transducer medical applications (high electromechanical coupling and low acoustic impedance), as shown in Figure 3.7. Therefore, the performance of the transducer is restricted [100]. One solution to this problem is to use piezoelectric composites (or piezocomposites) which offer the ability to tailor piezoelectric properties. Piezoelectric composites have many advantages over one single piezoelectric material phase which lead to the improvement of the transducer performance. In general, piezocomposites consist of a piezoelectric active material and non-piezoelectric passive polymer, to create piezoelectric composite materials. The properties of piezocomposites correspond to the connectivity between the piezoceramic and polymer phases. Connectivity can be described the arrangement and the number of dimensions in which the individual phases are continuously distributed [101]. There are various connectivities for each phase in a piezoelectric composite including: 0-3, 1-3, 2-2, 2-3, 3-0, 3-1, 3-2, 3-3, where the connectivity of the active phase (piezoceramic) and the passive phase (polymer) are represented by the first and second number in the notation, respectively. For example, a 0-3

composite consists of random piezoceramic particles such as PZT or  $\text{PbTiO}_3$  dispersed in a 3 dimensional passive polymer phases. One of the most obvious advantages of this pattern is high flexibility which provide more possibility to fabricate complicated shapes [102].

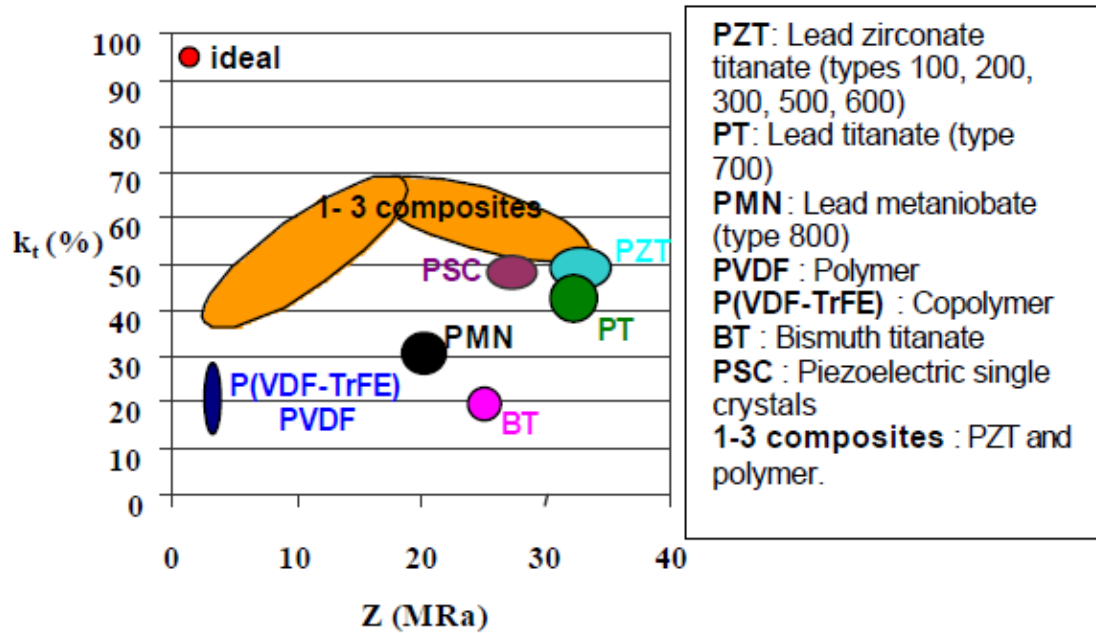


Figure 3.7 Electromechanical coupling coefficient in thickness mode versus acoustic impedance of different piezoelectric materials [28].

In order to achieve high performance of transducer, the electromechanical coupling coefficient must be sufficiently high by adjusting the piezoceramic volume fraction ( $V$ ) ( $> 50\%$ ) therefore some randomly dispersed particles could be connected to other particles, in this case the 0-3 composite can be considered as a 3-3 composite [103]. A notation of 2-2 refers to layers of the piezoceramic and polymer phases sandwiched together so that each phase is connected to itself in two directions. A notation of 1-3 connectivity is defined as parallel rods or pillars of piezoceramic active phase connected in one direction embedded in the polymer passive phase which is connected in three directions as illustrated in Figure 3.8 [27], [104].

The 1-3 composite configuration is the most widely used for many applications; including active materials in high performance transducers for medical imaging. The piezoelectric phase in the piezocomposite exhibits an excellent electromechanical thickness coupling coefficient [105] whereas the non-piezoelectric passive polymer can reduce the acoustic impedance mismatch to biological tissues, and prevent unwanted resonance modes. Piezocomposites can also possess a wide range of relative permittivity and low losses [106]. The benefits from combining of two phases results in enhancement of the transducer performance in terms of increased sensitivity, broader bandwidth and improved image resolution. Compared with single phase piezoceramics or piezopolymers, piezocomposites also offer more mechanical flexibility and can be geometrically focused. Therefore, lenses may not be necessary resulting in reduced acoustic attenuation [107], [108]. Piezocomposite properties can be tailored by adjusting the piezoceramic and polymer phases and composition, the volume fraction of phases, size and shape of piezocomposites, and therefore a new range of their properties can be offered to meet the requirement for various applications. These are especially useful for medical diagnosis applications including ultrasound transducers for medical imaging [109], [110]. However, these composites still have several difficulties for use as high frequency transducer materials due to the high processing cost to achieve an ultra-fine structure which meets the high frequency requirement.

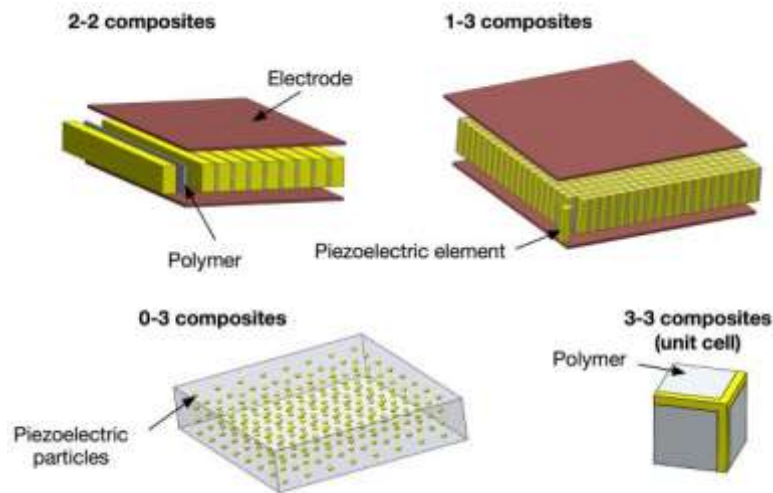


Figure 3.8 Schematic of 2-2, 1-3, 0-3 and 3-3 composites [109].

### 3.3 The crucial property and parameters of 1-3 composites for transducer applications

As explained in section 3.2, the most important property of active material for ultrasound transducer applications is high electro-mechanical coupling coefficient with low acoustic impedance which relates directly to the performance of thickness mode ultrasound transducers. A good tradeoff between these two properties can be obtained by piezoelectric composite materials. Composite with 1-3 and 2-2 connectivity are the two major composites on the market for ultrasound transducers, sensor and actuator applications. For medical diagnostic applications, 2-2 composites can only be used to fabricate transducer with frequencies below 20 MHz [111], while 1-3 composites are the materials of choice for low to high frequency transducers. There are several crucial factors which need to be taken into account in order to maximize 1-3 composite performance and to achieve an appropriate design for each particular transducer application.

### 3.3.1 Influence of ceramic volume fraction on acoustic impedance and electromechanical coupling coefficient

A model for designing 1-3 composites was first suggested by Smith, who explained that the electromechanical coupling coefficient and acoustic impedance of piezocomposite active materials can be modified by the ceramic volume fraction [106]. Figure 3.9 presents the electromechanical coupling factor for 3-3, 0-3, 1-3 composites, and the acoustic impedance of 1-3 composites as a function of ceramic volume fraction.

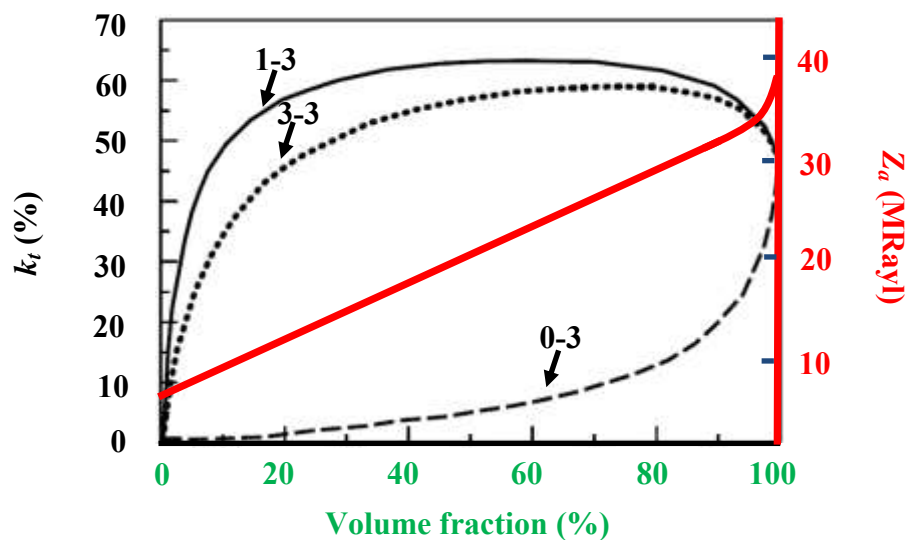


Figure 3.9 Electromechanical coupling factor ( $k_t$ ) of 1-3, 3-3 and 3-0 composites and acoustic impedance of 1-3 composite as a function of volume fraction ( $V_f$ ) [109].

The 1-3 connectivity shows clearly superior high electrocoupling factor with better stability over a wide range of ceramic volume fractions compared with the other two composites and also the end member piezoceramic and polymers phases [112]. The ceramic volume fraction can be modified in the range of 20-80% to achieve the maximum of  $k_t$  values and small variation. Conversely, at ceramic volume fractions

lower than 20 and higher than 80%, a different behaviour is observed. The effect of volume fraction can be explained by considering the two situations between the ceramic pillars surrounded by a light polymer compared to a stiff ceramic. At small piezoceramic volume fractions, the acoustic impedance can be reduced; leading to the more acoustic matching with tissues. However, the large amount of polymer stiffens the pillars, resulting in the reducing of  $k_t$  by this elastic loading. For over 80% ceramic volume fraction, the deformation of polymer become more difficult due to insufficient polymer limiting the lateral movement of the pillars, leading it behave like a solid block [113, 114]. Acoustic impedance follows the same trend as the ceramic volume fraction. Even though, a high ceramic volume fraction leads to an increasing of electromechanical coupling, the acoustic impedance is increased [115]. The optimum performance of 1-3 composite can be obtained by modifying the volume fraction; therefore, a good trade-off must be made between these properties.

### **3.3.2 Influence of piezocomposite geometry on resonance**

Geometry and spatial scale of piezocomposites are important factors affecting the performance of ultrasound transducers as they are both related with the resonance of the piezoelectric elements. When an AC electric field is applied to a piezocomposite, a cyclical change in its dimensions and a series of resonances can be observed at specific frequencies. The frequency at which the piezocomposite vibrates most easily with the most efficient conversion between both electrical and mechanical energy occurs when the driving frequency is equivalent to the natural frequency of motion of the piezoelectric element [116]. Typically, the radial resonance is the resonance at the lowest frequency and corresponds to the vibration in the largest dimension of

piezocomposite. This thesis is concerned with high frequency ultrasound transducers; therefore, the resonance of 1-3 composite is of interest in thickness mode.

The thickness resonance occurs when the ultrasound wave being reflected back into the piezocomposite is exactly in phase or in step with the next wave and the amplitude of each peak coincides, which is referred to the constructive interference phenomena, resulting in the increasing of amplitude [117]. Consequently, the first thickness resonance can be observed when the thickness of the piezocomposite ( $t$ ) is equal to the half wavelength ( $\lambda/2$ ), in this case the piezocomposite has a minimum loss of the energy. The relationship between the operating frequency ( $f$ ) and thickness of piezocomposite can be determined by substituting  $t = \lambda/2$  into the equation 2.1 and rearranging to give  $f = \frac{v}{2t}$  [114], where  $v$  is the speed of sound in the piezoelectric material. In a piezocomposite, the velocity of sound depends on the volume fraction of ceramic and polymer phases, and can be calculated by the rule of mixtures as presented in Equation 3.5.  $V$  is the volume fraction, subscripts  $pc$ ,  $c$  and  $p$  refer to piezocomposite, ceramic and polymer, respectively.

$$v_{pc} = v_c V_c + v_p V_p \quad \text{Equation 3.5}$$

For example, if  $V_c$  is 50 %, the speed of sound in ceramic is 4000 m/s and in polymer is 2000 m/s, the velocity of sound in the piezocomposite can be calculated to be 3000 m/s [114]. Typically, the most effective conversion energy occurs at the fundamental thickness frequency. Therefore, this resonance frequency can be defined by the thickness of piezocomposite. As discussed in chapter 2, a better resolution can be achieved by using the high operating frequency. Therefore, the short wavelength and the small thickness of piezocomposite are required. For example, super

resolution for facial imaging, the operating frequency is required approximately 30 MHz, the velocity of sound in PZT composite is 3000 m/s; therefore, the thickness of piezocomposite should be 50  $\mu\text{m}$  [107]. This means that the thickness resonant frequency mainly depends on the thickness of device. Hence for high frequency a very small thickness is required which brings difficulties for fabrication.

However, not only the thickness or pillar height is important, but also the geometry and spacing of the pillars. The distribution, size and shape of pillars can be modified to achieve the best performance of the transducer. The geometry of a 1-3 composite can be described as shown in Figure 3.10. The pillar shape depends on the fabrication method used and also can be arranged in a pattern or randomly distributed. Kerf is the gap between each pillar which related to the required volume fraction of piezocomposite. Typically, the kerf is smaller than the thickness and width of pillar.

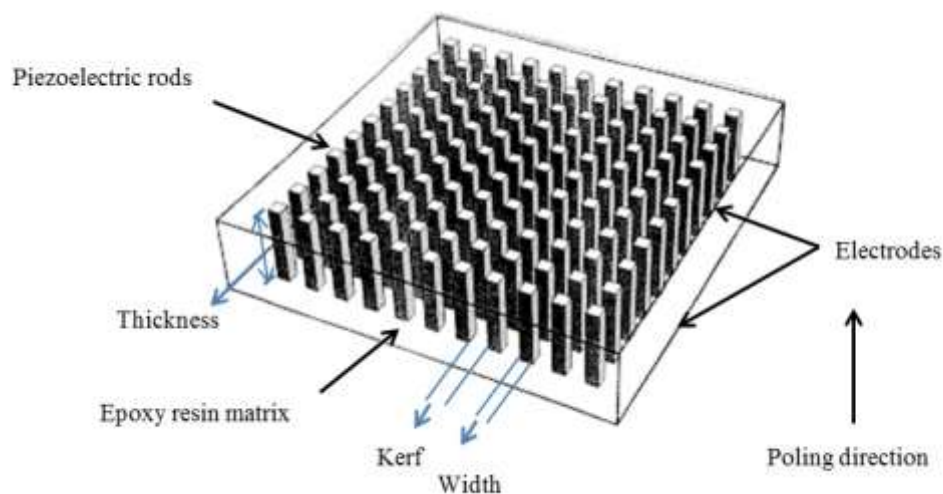


**Figure 3.10** The dimensions of 1-3 composite [118].



The required width of the pillars can be determined by the height or thickness of the 1-3 composite based on the aspect ratio of the pillars, the ratio of the height (length) of a pillar compared to its lateral dimension. This in turn is related to the performance of the transducer. A number of investigations have reported the relationship between the ceramic volume fraction, geometry and aspect ratio on the electromechanical coupling coefficient. The results show that for composites based on square section pillars with high aspect ratio and high piezoceramic volume fraction, the pillars are more closely spaced. The lateral mode resonance is, therefore, shifted from the thickness resonance which can be exploited in practical applications [119]. However, high aspect ratio pillars in piezocomposites with low ceramic volume fraction causes degradation of the thickness mode due to the wide spacing between pillars [120]. The resonance mode of composites fabricated with cylindrical piezoceramic pillars showed similar behaviour to the square pillars from which can be concluded that there is no benefit to be gained by using circular pillars. However, the electromechanical conversion may be improved by triangular pillars, because their orientations have no facing parallel surfaces, leading to the lateral resonances being reduced, even in composites with high aspect ratio and low ceramic volume fraction. The effect of tapered pillars was also investigated, but the lateral resonance was not significantly reduced [119]. In practical terms, to maximize the coupling coefficient, the 1-3 composite should have high volume fraction of ceramic with high aspect ratio pillars (greater than 2) [121] with no adjacent sides being parallel.

When the piezocomposite is excited by an electrical field or mechanical pressure, acoustic Lamb waves normally propagate in the surface and also reflect at the ceramic/polymer interfaces. If the wavelength of the Lamb waves match with the

lateral periodicity of the pillar spacing, a spurious resonance mode is built up. To avoid this, the kerf between pillars, or inter-planar spacing, should be sufficiently fine scale, and consequently the resonant wavelength so short, that the lateral mode is pushed away from the spectrum of the required thickness resonance [106, 112, 115, 122]. Therefore, to avoid lateral resonances the kerf should be as small as possible and the width of the pillars in the 1-3 composite should be less than half of the pillars height [123].

The dimensions and aspect ratio of 1-3 composite with 50% volume fraction of PZT is presented in table 3.5. It can be seen that for higher frequency operation, smaller dimensions are required. For example, with the pillar aspect ratio of 3.5, a 1-3 composite operating at over 40 MHz requires the thickness and kerf less than 38 and 4  $\mu\text{m}$ , respectively. Note that as the kerf is much smaller than the pillar width, the aspect ratio of the kerf is correspondingly larger.

**Table 3.5 The dimensions and aspect ratio of a 50% volume fraction piezocomposite, assume the longitudinal velocity of 3,000 m/s and based on a square packed array of square pillars [107].**

Frequency	Thickness ( $\mu\text{m}$ )	Pillar width ( $\mu\text{m}$ )	Kerf ( $\mu\text{m}$ )	Pillar aspect ratio	Kerf aspect ratio
20 MHz	75	21	6	3.5	12.25
30 MHz	50	14	4	3.5	12.25
40 MHz	37.5	10	3	3.5	12.25
50 MHz	30	9	2	3.5	12.25

These dimensional restrictions have limited the development of 1-3 composites for high frequency applications, in particular the extremely fine scale of pillars and kerfs required to avoid the interference [124] due to the lateral resonance in pillar and spurious modes caused by the regular periodicity of ceramic pillar arrays [122]. Many attempts to suppress these resonances have been studied. Triangular pillars have been studied; the results suggest that the lateral resonance and spurious mode

which can be clearly seen in rectangular pillar arrays can be suppressed by using triangular geometries [124], [125]. An ultrasound transducer made from a 1-3 piezocomposite with pseudo random geometry has been investigated by Brown *et al.* [125]. The results at 15 MHz show that the pseudo random geometry provides a higher  $k_t$  value compared with square and triangular geometries and is able to suppress that lateral resonance modes, and it can also be implied that the more complex geometry, the more lateral resonance and spurious mode would be reduced or eliminated [126].

A 1-3 piezocomposite with a fully random distribution of geometries and dimensions of the ceramic phase has been studied in order to achieve the optimum performance of transducers by suppressing the interference of lateral modes [127]. The randomised piezocomposite pattern was designed as irregular shapes of ceramic pillars in order to provide better stability and fewer tendencies for the pillars to lean or fall over during fabrication [128]. The pattern is presented in Figure 3.11, and examples realized in PZT have demonstrated  $k_t$  of 0.68, corresponding to a coupling coefficient of 40 vol% of ceramic phase.

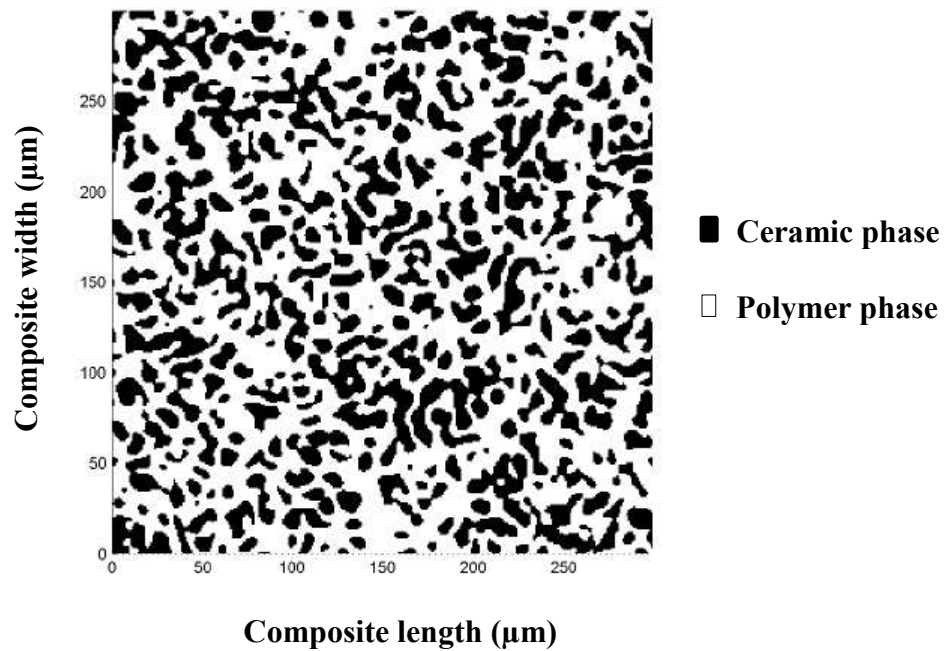


**Figure 3.11** Randomised 1-3 piezocomposite pattern in 300  $\mu\text{m}$  square section with 40 vol% ceramic phase [127].

There is only one attempt to fabricate a very complex 1-3 composite structure from PZT based materials. However, there have been no reports to fabricate ultrasound transducers by using lead free piezocomposite materials with randomised structure.

### **3.4 Piezocomposite manufacture for 1-3 piezocomposite**

Typically, the manufacturing of 1-3 piezocomposite is based on the basic structure called a “bristle block” as presented in Figure 3.12.

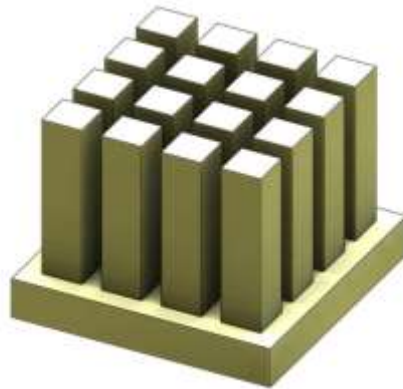


**Figure 3.12 Bristle block structure of 1-3 piezocomposite.**

All fabrication methods have the purpose to form this structure which consists of thin and tall active piezoceramic pillars on a ceramic base or stock. The polymer or epoxy matrix is infiltrated into the bristle block, followed by lapping processes. The pillars have to be fabricated taller than the final required thickness of the composite to allow for removal of material from the top and bottom side of the piezocomposite during lapping in order to expose the pillars and achieve a parallel sided piezocomposite. A number of fabrication methods have been developed for 1-3 piezocomposite including dice and fill, injection moulding, and lost mould techniques. The characteristics, capabilities, advantages and limitations of each process are discussed below.

### **3.4.1 Dice and fill**

Among various methods for 1-3 piezocomposite fabrication, dice and fill is the standard method for commercial products because of its simplicity. A bristle block of pillars can be created by using dicing saw to cut a set of parallel grooves into a dense sintered piezoceramic block and then a second set of parallel grooves are cut after the

piezoceramic block is rotated by 90 degrees [129]. After the infiltration, lapping and electroding stages the active 1-3 composite can be achieved by applying the electric field across the two parallel electroded faces. The schematic procedure of the dice and fill technique is shown in Figure 3.13.

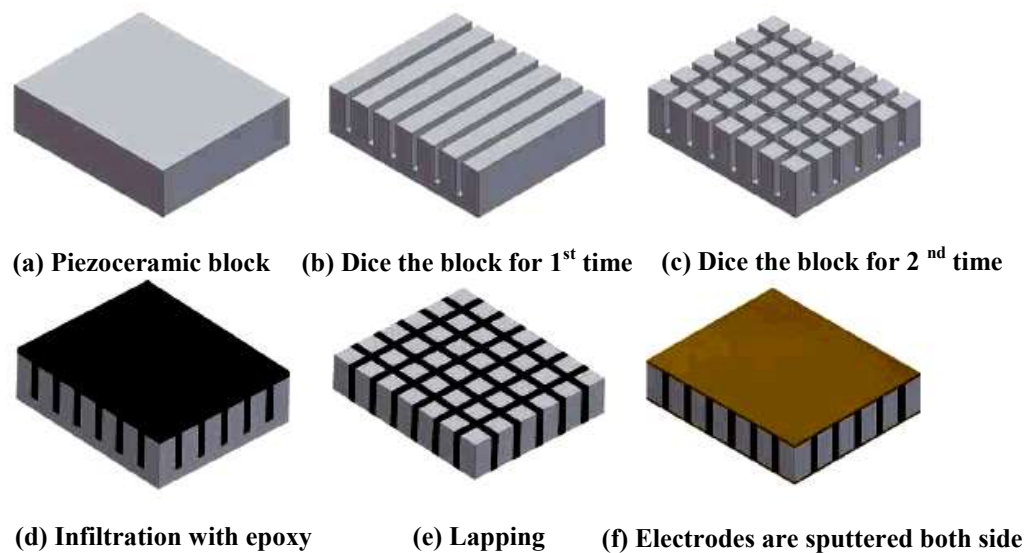


**Figure 3.13 Schematic procedures of dice and fill technique for making bristle block structure [130].**

Although this technique can create not only square pillars but also hexagonal and triangle geometries [131], [132], unfortunately, this technique is only suitable for high frequency transducer fabrication operating at frequencies up to 20 MHz. For higher operating frequencies the ultrafine scale lateral dimensions are required for efficient operation, as discussed previously. In the dice and fill technique it is difficult to create a piezocomposite with the pillars less than 100  $\mu\text{m}$  [100], [133], and due to the size of dicing blades kerfs are limited to approximately 15-20  $\mu\text{m}$ . In addition, the pillars may have defects which causes pillars to break off during machining, thus reducing device yields [121], [134]. The other disadvantages of this process is that it has high tooling cost, long process time and the structure of the

piezocomposites are limited to simple geometric designs. Thus alternative fabrication techniques have been investigated for high frequency transducers.

### **3.4.2 Injection moulding**

Injection moulding is widely use in plastics production to produce mass products of complex shape. It has also been used for ceramics fabrication by mixing the ceramic powders with suitable polymer binders, and has been demonstrated for the fabrication of bristle blocks from piezoceramics [135]. The mixtures are injected into a cold mould under heat and pressure to create the required shape. The bristle block is removed from the mould after cooling, followed by heating in order to remove the organic binder before sintering [136]. The advantage of this method over the dice and fill technique is that variations of geometry and spacing can be possible depending on the mould. However, this process has several disadvantages, although the mould is reusable, this process has high tooling and manufacturing costs and has long process cycle. Moreover, the pillars can easily be destroyed during demoulding for pillar pitches less than 50  $\mu\text{m}$ . Ceramic volume fraction of bristle block tend to have low volume fractions and creating the ultrafine scale of 1-3 piezocomposite with high respect ratio is still difficult [121, 135, 137].

### **3.4.3 Lost Mould Technique**

The lost mould technique is based on using a sacrificial or dissolvable mould to create fine pillars with aspect ratios of 3-9 and spacing approximately 20-25  $\mu\text{m}$ . The basic of this technique is that the mixture of piezoceramic and polymer binder in the form of a dough, slurry or paste are poured into a negative mould with the bristle block structure, which can be crated from various mould materials such as polymer.

After drying process, the mould is removed by dissolving in solvent or thermal processes such as plasma etching, depending on the mould material [138, 139]. The piezocomposite can be created into a various sizes and geometries depending on the desired mould. However, this technique requires a new mould for each composite, as the moulds cannot be reused [133, 140]. By using acrylic or plastic moulds to produce fine scale pillars (~20  $\mu\text{m}$ ), the mould removal step has to be done by plasma etching instead of burnt out processes because the structure can be damaged by the flow during heating of the binder [140]. However, for creating very fine structures with this type of mould, the deformation of pillar structure seems almost inevitable. Another alternative method to avoid pillar deformation and distortion and offer the high green strength of bristle block structure is viscous polymer processing (VPP) [141], [142].

For a range of designs of 1-3 piezocomposite with the ultrafine lateral scale, kerf sizes of approximately 4  $\mu\text{m}$  with the ultrafine lateral scale pillars below 10  $\mu\text{m}$  and aspect ratios up to nearly 10 [127], and ceramic volume fractions of approximately 60% [143] have been achieved. VPP offers the suitable ability for the fabrication because the high green strength of the ceramic pillar maintains the shapes without damage from the mould-dissolving step. The uniform shrinkage can be achieved due to the good homogeneity of ceramic paste. Therefore, this technique can be used for net shape processing, the choice of binder system is flexible, resulting in the selection of a range of mould materials and the possibility to selectively dissolve the mould without destruction of the pillars [121, 143].

VPP ceramic paste or dough comprises ceramic powder with some binder such as polyvinyl alcohol (PVA) or polyvinyl butyral (PVB) and some processing additives



for improving the mixture texture and rheological behaviour [100], [142], which are combined using twin roll mill machine, as shown in Figure 3.14. The high green strength of the bristle block structure can be achieved due to the high shear mixing and the high molecular weight of the polymer, which also result in a reduced size of strength limiting defects in the sintered material. The 1-3 piezocomposite can be produced by embossing the viscous polymer paste into a polymethyl methacrylate (PMMA) mould under a pressure of approximately 50 MPa [144] and then the mould can be either burnt out or dissolved in a suitable solvent such as tetrahydrofuran. After sintering, the bristle block is back-filled with polymer/epoxy resin to fabricate 1-3 composite in the normal way.

A range of sizes and geometries of ceramic pillars have been produced using different lost mould techniques. For example, PZT slurry was cast into polymer moulds and the moulds were removed by burnout and pillars with hexagonal shape with the width and kerf  $\sim 50 \mu\text{m}$  with the aspect ratio 8 were reported. However, the pillars were distorted due to the polymer flow during burnout [138, 145]. Other workers have reported the fabrication of square and circular ceramic segments by injecting ceramic slurry into polymer moulds which were then removed by plasma etching mould before sintering. Pillar widths of approximately  $25 \mu\text{m}$  with the aspect ratio 2.5-7 were achieved [138, 140, 145]. Pillars with hexagonal, ellipse and arc shapes have been fabricated by embossing PZT dough into polymer moulds, followed by chemical dissolution. Pillars with the fine scale (width  $\geq 8 \mu\text{m}$  with height  $100 \mu\text{m}$  and aspect ratio approximately 10) have been achieved as shown in Figure 3.15 [127].

However, the lost mould technique has several limitations due to the costs of the mould fabrication, plasma etching processing, are relatively high and mould is easily damaged during processing [139, 140].

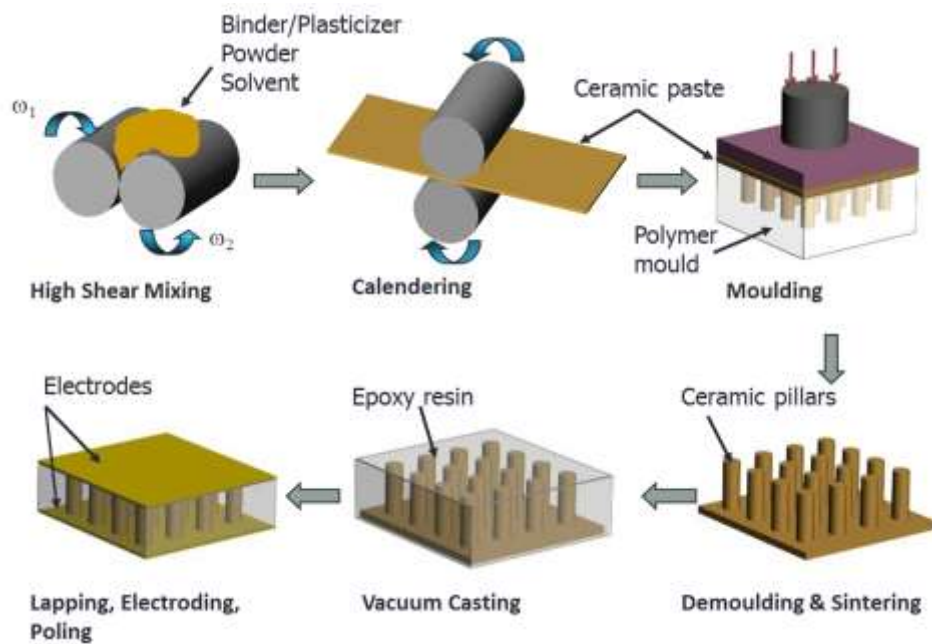


Figure 3.14 Viscous polymer processing [143]

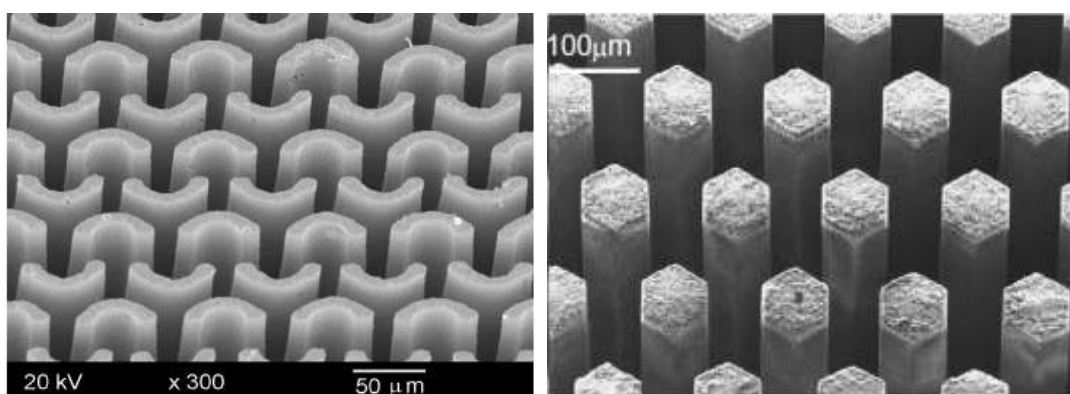


Figure 3.15 Section of green ceramic pillars (a) arcs and (b) hexagonal fabricated by embossing viscous polymer processing paste into polymer moulds, followed by chemical dissolution of the moulds [127, 143].

### 3.4.4 Soft lithography

Soft lithography is a cost effective technique because it can replicate and transform the pattern of a master mould down to nanometers in flexible elastomers. In this way a reusable polymer mould is created and both the elastomer mould and the master mould can be reused many times. Poly(dimethylsiloxane) or (PDMS) is the most popular elastomer mould material that is used due to the several advantages. For example, it offers biocompatibility, low toxicity and its viscoelastic properties allow PDMS to spread over the surface of the master mould [146] with low surface energy and great chemical stability [147]. As a result, the adherence and reaction between master mould and the PDMS can be minimised.

The master mould can be fabricated by using various techniques such as electron beam lithography, photolithography, micromachining, or etching (chemical or plasma) [107, 148]. The PDMS is poured over the master mould, followed by peeling off after the PDMS is hardened. The bristle block structure can be fabricated by casting ceramic slurry into the polymer mould. Once the structure has dried, the mould can be removed by carefully peeling off the soft mould.

The forming of 1-3 composites for ultrasound transducer application by using soft mould techniques has been reported by a number of researchers. For example, 1-3 composites with square pillars with lateral dimensions of 85 and 145  $\mu\text{m}$  and kerfs of 45  $\mu\text{m}$  have been successfully fabricated, with measured  $k_t$  values of 0.71 and 0.79, respectively and working frequencies  $\sim$ 5-10 MHz [148]. Gebhardt et al. created 1-3 composites with square and cylindrical shape pillars with diameter  $\sim$  65  $\mu\text{m}$  and inter pillar spacings varying between 36-79  $\mu\text{m}$ . Hence these composites were

suitable only for low frequency applications [149, 150]. However, in 2011 it was reported that 1-3 composites with arc and ellipsoidal shape of pillars for high frequency devices had been successfully fabricated by soft mould techniques [151] using sintered ceramic mater moulds fabricated by VPP.

### **3.4.5 Gel casting**

Gel casting is one of the colloidal ceramics processes which improve ceramic reliability. The advantages of this processing route over dry processing are that the interactions between the ceramic particles can be controlled and the homogeneity can be improved. Therefore, small ceramic particles can be solidified to form high green strength and uniform ceramic bodies with fewer imperfections in the microstructure. It is inherently a low cost manufacturing route. [152].

Gel casting has been widely developed in the past ten years due to its ability of near net shape fabrication of small ceramic products [153]. This technique was first developed during the 1980s by Omatete and colleagues at Oak Ridge National Laboratory (ORNL) in the USA in order to overcome some drawbacks of the complex shape forming of injection moulding.

The standard gel casting method is based on a combining traditional ceramics with polymer chemistry [154]. The generic principle of gel casting is that the ceramic powders are dispersed in a pre-mixed solution of monomer, crosslinker, catalyst and initiator in order to achieve a homogeneous slurry with low viscosity and high solid loading [155, 156]. After milling, the homogeneous slurry is cast into the required mould. The monomer solution is polymerised and crosslinked in situ to form a water-polymer irreversible gel as a three dimension network structure that holds the

dispersed ceramic particles. After drying, the ceramic product is removed from the mould, and then the homogeneous high strength green body, can be realised. The drying stage will be required under controlled conditions to allow the green product to dry properly without cracking. Polymer removal can be done by thermal pyrolysis, followed by sintering process [152, 154-158]. There are a number of advantages of the gel casting technique. Gel casting can produce high quality ceramic in complex shapes, similar to injection moulding, but the gel casting technique offers lower cost due to the cheaper equipment and mould materials. Water is used as the suspension medium and thereby good homogeneity of particles in the wet stage can be achieved. The green ceramic bodies have high homogeneity and green strength that lead to excellent ability for handling and machining the green bodies before sintering without damage. This process requires a relatively small amount of binders, which results in the critical binder removal step being avoided and gel casting can be applied to both ceramic and metal powders [159]. The irreversible gel can be created based on different mechanisms, summarised as follows.

- **Free radical initiated polymerisation of monomer**

The initial gel casting technique reported by Omatete and colleagues was based on the free radical polymerisation of two organic monomers [154]. The main monomer normally forms a linear polymer and the second is crosslinking monomer. The solvent gel is formed after polymerisation and crosslinking of both monomers. The aqueous monomer solution consists of monomer, crosslinker, initiator and catalyst. The monomer, acrylamide (AM), and crosslinker, N,N'-methylene bisacrylamide (MBAM), are mixed together in a weight ratio 24:1. Ammonium persulfate (APS) is used as initiator while tetramethylethylenediamine (TEMED) is utilised as a catalyst

for the polymerisation [160]. However, industry was unwilling to use the acrylamide system due to its neurotoxicity. [161]. To mitigate the problem, a number of low toxicity monomers such as methacrylamide (MAM) N-vinylpyrrolidone (NVP) and hydroxymethylacrylamide (HMAM) have been developed to be an alternative to AM. The most common crosslinker, initiator and catalyst used are MBAM, APS and TEMED, respectively. The reaction of monomer and crosslinker lead to the formation of a high molecular weight polymer; therefore, the molecule of solvent can be trapped.

The free radical initiated polymerisation has several limitations. In general, the strength of the gelcast product improves with increasing the concentration of monomer and crosslinker in solution. However, the solubility limit of the crosslinker in water is relatively low (~2 wt%) at room temperature and this leads to inappropriate solutions resulting in the low green strength of ceramic bodies [160]. Moreover, this mechanism results in the surface exfoliation of green bodies because the reaction is inhibited by oxygen when it is carried out in air. Although the use of an N<sub>2</sub> chamber overcome this problem, the system is complicated and increases the manufacturer cost [162].

#### • **Cooperative binding of metal ion**

The acrylamide system is neurotoxic and sensitive when carried out in air. Therefore, the development of a harmless gel casting system has been actively researched. Agarose and gelatin have been reported as alternatives to the AM system but both systems are expensive. Alginate is a type of gelling polysaccharide that is normally extracted from kelp [163]. Compared with AM, alginate is a nontoxic, cost effective

natural polymer. At room temperature, it can be dissolved in water and then when the temperature is increased, the three-dimension network is formed with the divalent metal ions.

In this process, the mechanism of crosslinking involves the cooperative bonding of calcium ions with alginate. Calcium iodate is added into the process as a solidifying agent to cooperative bonding with the carboxyl and hydroxyl groups [164]. Therefore, a strong three-dimension network can be formed in an “egg box” structure, as shown in Figure 3.16. The solubility of this solidifying agent can be increased by increasing the temperature to 60 °C; therefore, the process is temperature controllable [165].

The gel casting of alumina bars has been reported by utilising this mechanism. The nontoxic polymer solution can be prepared by mixing sodium alginate solution with distilled water to coagulate the alumina suspension, and then the solidifying agents were added into the suspension. After increasing the temperature, the network structure was formed because the chains of alginate were bonded with the released calcium, and the gel cast green body was created. However, the green ceramic products fabricated by this mechanism possess low green strength and the gelation rate is difficult to control because the gel is formed relatively quickly due to a fast reaction rate between the calcium ions and alginate molecule. Although a time delay in the release of calcium ions can be achieved by adding hexanedioic acid, a satisfactory process still cannot be achieved [166].

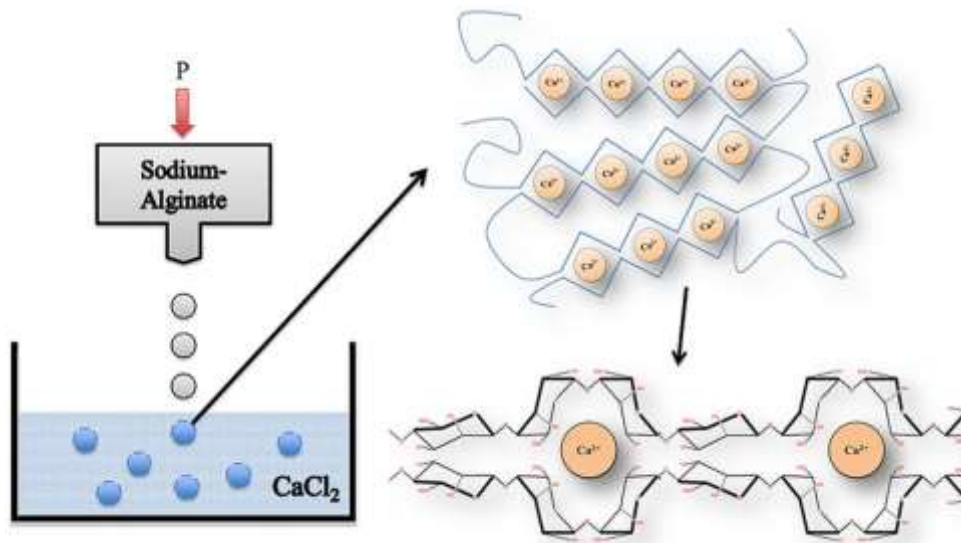


Figure 3.16 Schematic presents the formation of egg box model by adding calcium iodate into suspension. The gel can be form after divalent metal ions ( $\text{Ca}^{2+}$ ) are cooperative bound with aligned ribbons at  $60^\circ\text{C}$  [167].

#### • Protein forming

It has been reported that the globular protein generally obtained from blood plasma or egg white was used as gelling agent due to its ability to change under some conditions such as pH and temperature. At room temperature, the protein molecules are folded into the circular shape. However, when the protein is heated up to a certain temperature or the pH is adjusted, a metastable form occurs due to the breaking of the hydrogen bonds and formation of a new bond. Hence the formation of thermo irreversible gel with three dimension network is achieved [168].

#### • Ring-opening reaction

A new system has been developed to overcome the problems reported above. In 1997, Takeshita and Kurita studied an alternative system which is called the KN-process, which offers a self-hardening slip casting method by using epoxy resin and



Y-PSZ [169]. Alumina gel cast ceramic samples have been developed by using sorbitol polyglycidyl ether (SPGE) as the gelling agent and 3,3'-iminodipropylamine as an amine hardener [162]. The results showed that the process can be carried out in air without any surface problem. However, this epoxy resin is difficult to dissolve in water and the suspension has a relatively high viscosity approximately 5 Pa.s [170].

To overcome the drawback from the SPGE based system, the development of a new system was necessary. This involved using ethylene glycol diglycidyl ether (EGDGE), poly ethylene glycol diglycidyl ether (PEGDGE), glycerol polyglycidyl ether (GPGE) and resorcinol diglycidyl ether (RDGE) as a gelling agent and dipropylentriamine (DPTA) as a hardener for alumina gel casting. The results showed that all gelling agents resulted in slurries with low viscosity ( $<1$  Pa.s at  $100\text{ s}^{-1}$ ) and excellent flexural strength of alumina green bodies was obtained by EGDGE (17 MPa) and GPGE (19 MPa) [170].

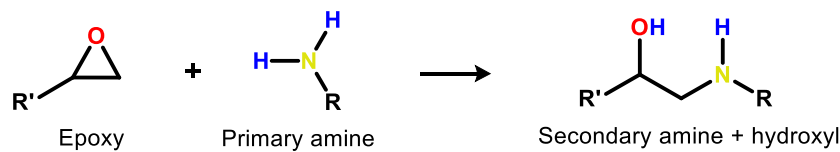
The gel casting of PZT 1-3 composites with randomised structure with EGDGE epoxy resin has been studied [107, 134, 151]. EGDGE and bis(3-aminopropyl)amine were utilised as gelling agent and hardener, respectively. The slurry viscosity was less than 2 Pa.s and the highest green strength (35 MPa) was observed at a resin content of 40%wt [107].

Although EGDGE results in low viscosity slurries and high green strength bodies, it causes irritation to the skin and eyes [171]. Hydantoin Epoxy resin has recently been studied and reported as a new candidate in gel casting systems because it has high water solubility, is non-toxic, low cost and crystallises at ambient temperatures, and thus is easy to store and transport. The gel casting of aluminum nitride and alumina

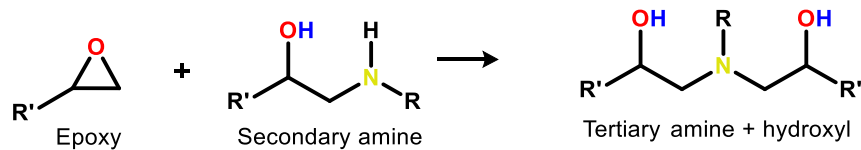
powder has been demonstrated by using hydantoin epoxy resin. The strength of the green bodies were significantly higher than those fabricated using EGDGE [171, 172].

The polymerisation between the epoxide groups of the epoxy resins and the active hydrogen atoms of the amine hardener is via a ring-opening reaction. The greatest advantage of this reaction is that the system is not affected by oxygen [173]. The concept of amino epoxy curing is shown in Figure 3.17. There are three main reactions. First, the primary amine links to the epoxide group, and then a secondary amine is formed. Second, the secondary amine continues to react with the epoxide group and, finally, hydroxyl formed from the second step reacts with the epoxide group and ends up forming a three-dimensional network.

#### Primary reaction



#### Secondary reaction



#### Esterification

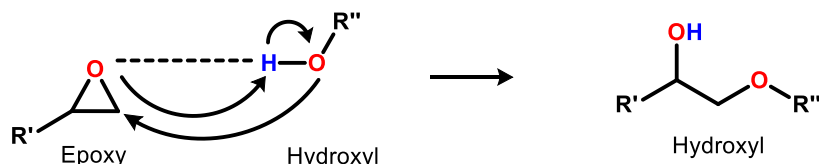


Figure 3.17 The ring opening reaction mechanism of epoxy amine (adopted from [174]).

### 3.4.6 Gel casting for high frequency transducer

The combination of gel casting and soft moulding methods offer new route for the fabrication of various sizes, geometries and complex shapes for 1-3 PZT piezocomposites for high frequency transducer for medical applications. Pillars with lateral dimensions less than 10  $\mu\text{m}$ , 100  $\mu\text{m}$  in height and with excellent green strength (38 MPa) have been achieved. The slurry of PZT powders were mixed with the solution of epoxy resin and cast into PDMS moulds that had been created by the soft lithography of Si moulds with randomised 1-3 pillar structures. The irregular PZT pillars with overall area of 2 mm x 2 mm square had sizes less than 2  $\mu\text{m}$  with 150  $\mu\text{m}$  height (aspect ratio approximately about 70) without distortion as shown in Figure 3.18. The 1-3 piezocomposites possessed ceramic volume fractions  $\sim 40\%$ , and exhibited  $k_t$  of approximately 0.68 and no spurious modes were observed [128].

The random composites were used to successfully fabricate single element transducers at frequencies between 30 and 60 MHz, with only a single thickness mode being observed.

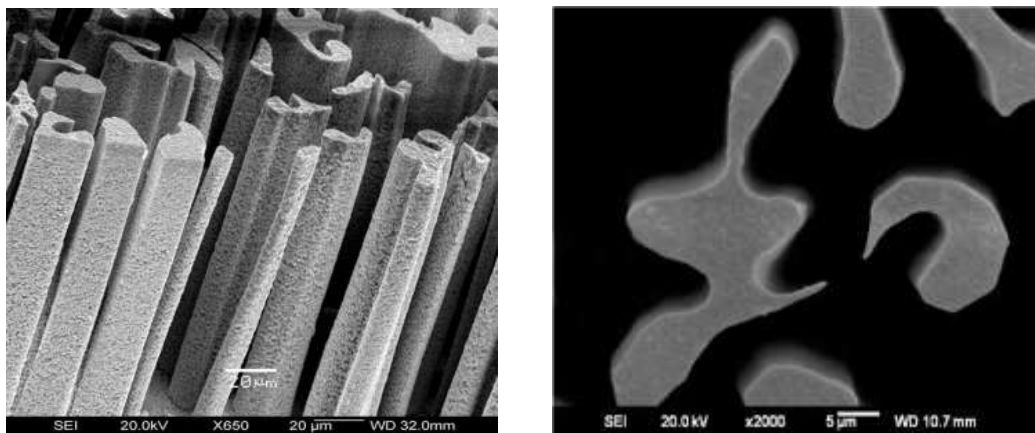


Figure 3.18 Scanning electron images of green stage ceramic pillars with random geometries (a) at 60° tiled and (b) the top view of ceramic pillars [107, 128].

### **3.5 Summary**

This chapter has introduced and discussed the background theory required for study of 1-3 piezocomposites for high frequency transducer applications. The fundamentals and principles of piezoelectricity including the piezoelectric effect, polarization, piezoelectric coefficients and crucial determinants were discussed as the background for understanding the conceptualisation of piezoceramics. Lead based, lead free, piezoelectric polymer, and piezoelectric single crystal and piezocomposite materials were introduced to provide their characteristics and properties in order to choose suitable materials for transducer applications. Due to a good tradeoff between high coupling coefficient and low acoustic impedance, the 1-3 composite was introduced as a candidate active material used for high frequency transducers. In order to achieve the high performance of this piezocomposite, the crucial properties and important parameters of 1-3 piezocomposites were discussed. An appropriate design in term of volume fraction, size and geometry of 1-3 composites was introduced. In order to suppress the interference of lateral and spurious modes, a fully random pattern with ultrafine structure of the 1-3 were addressed. However, considering the formation of ultrafine size and complex structures, the fabrication routes need to be taken into account. Therefore, the fundamental advantages and drawbacks of dice and fill, injection moulding, soft mould and lost mould techniques were reviewed to draw a clear picture of ultrafine 1-3 composite fabrication. Compared with other techniques, the advantages of the gel casting process in terms of forming complex shape, improvements to the ceramic reliability, lower cost, high green strength and avoiding the critical binder removal were introduced. The mechanism of gel casting, compatibility between ceramic powder and polymer/binder system, advantages and

disadvantages of various polymer monomers were discussed. The ceramic powder with epoxy resin system was introduced as a new alternative to the acrylamide and monomer and biopolymer. The system was used for various studies including PZT 1-3 piezocomposite with a random structure. The process can be carried out in air without green body exfoliation and high green strength of the ceramic body was reported.

### 3.6 References

1. Mould, R.F., *Pierre Curie, 1859–1906*. Current Oncology, 2007. **14**(2): p. 74-82.
2. Curie, M., C. Kellogg, and V.L. Kellogg, *Pierre Curie*. 1923, New York: Macmillan Co.
3. Moheimani, S.O.R. and A.J. Fleming, *Piezoelectric Transducers for Vibration Control and Damping*. 2006: Springer London.
4. Jaffe, B., *Piezoelectric Ceramics*. 2012: Elsevier Science.
5. T.L. Jordan, Z.O., *Piezoelectric Ceramics Characterization*. 2001.
6. Groves, P., *A review of: "Piezoelectricity"*. Phase Transitions, 1986. **6**(4): p. 329-330.
7. Moulson, A.J. and J.M. Herbert, *Piezoelectric Ceramics*, in *Electroceramics*. 2003, John Wiley & Sons, Ltd. p. 339-410.
8. PATRANABI, D., *SENSORS AND TRANSDUCERS*. 2003: PHI Learning.
9. Sinclair, I.R., *Chapter 1 - Strain and pressure*, in *Sensors and Transducers (Third Edition)*. 2001, Newnes: Oxford. p. 1-20.
10. Kholkin, A.L., N.A. Pertsev, and A.V. Goltsev, *Piezoelectricity and Crystal Symmetry*, in *Piezoelectric and Acoustic Materials for Transducer Applications*, A. Safari and E.K. Akdoğan, Editors. 2008, Springer US: Boston, MA. p. 17-38.
11. Defaÿ, E., *Dielectricity, Piezoelectricity, Pyroelectricity and Ferroelectricity*, in *Integration of Ferroelectric and Piezoelectric Thin Films*. 2013, John Wiley & Sons, Inc. p. 1-24.
12. Whatmore, R.W., *Piezoelectric and Pyroelectric Materials and Their Applications*, in *Electronic Materials: From Silicon to Organics*, L.S. Miller and J.B. Mullin, Editors. 1991, Springer US: Boston, MA. p. 283-290.
13. Gallego-Juarez, J.A., *Piezoelectric ceramics and ultrasonic transducers*. Journal of Physics E: Scientific Instruments, 1989. **22**(10): p. 804.
14. M. Lach, M.P., A. Ries. *Piezoelectric materials for ultrasonic probes*. September 1996 [Last accessed date 01/05/2016]; Available from: <http://www.ndt.net/article/platte2/platte2.htm>.
15. Sanmartín, D.R., *Fabrication and characterisation of high frequency ultrasound transducers*, in *Department of Metallurgy and Materials*. 2007, University of Birmingham. p. 68.
16. Zhong, W.L., et al., *Domain reorientation by poling of PZT ceramics in the morphotropic phase boundary region*. Solid State Communications, 1994. **90**(6): p. 383-385.

17. Berlincourt, D. and H.H.A. Krueger, *Domain Processes in Lead Titanate Zirconate and Barium Titanate Ceramics*. Journal of Applied Physics, 1959. **30**(11): p. 1804-1810.
18. *Piezoelectric Ceramics Properties and Applications*. [Last accessed date 10/05/2016]; Available from: <http://www.morgantechnicalceramics.com/products/product-groups/piezo-ceramic-components/piezoelectric-ceramics-prop-apps>.
19. Tiersten, H.F., *Linear piezoelectric plate vibrations: elements of the linear theory of piezoelectricity and the vibrations of piezoelectric plates*. 1969: Plenum Press.
20. *Linear Theory of Piezoelectric Materials*, in *Piezoelectric Multilayer Beam Bending Actuators: Static and Dynamic Behavior and Aspects of Sensor Integration*. 2007, Springer Berlin Heidelberg: Berlin, Heidelberg. p. 31-45.
21. *IEEE Standard on Piezoelectricity*. ANSI/IEEE Std 176-1987, 1988: p. 0\_1.
22. Smith, W.A., A.A. Shaulov, and B.A. Auld, *Design of piezocomposites for ultrasonic transducers*. Ferroelectrics, 1989. **91**(1): p. 155-162.
23. Smith, W.A., *Piezocomposite Materials for Acoustical Imaging Transducers*, in *Acoustical Imaging*, J.P. Jones, Editor. 1995, Springer US: Boston, MA. p. 121-138.
24. Jaffe, H. and D.A. Berlincourt, *Piezoelectric transducer materials*. Proceedings of the IEEE, 1965. **53**(10): p. 1372-1386.
25. Waller, D., C. Jie, and T.R. Gururaja. *Requirements of piezoelectric materials for medical ultrasound transducers*. in *Applications of Ferroelectrics, 1996. ISAF '96., Proceedings of the Tenth IEEE International Symposium on*. 1996.
26. Tandon, R.P., et al. *Fabrication, properties and design considerations of piezocomposite transducers for ultrasonic imaging*. in *Engineering in Medicine and Biology Society, 1995 and 14th Conference of the Biomedical Engineering Society of India. An International Meeting, Proceedings of the First Regional Conference., IEEE*. 1995.
27. Shung, K.K., J.M. Cannata, and Q.F. Zhou, *Piezoelectric materials for high frequency medical imaging applications: A review*. Journal of Electroceramics, 2007. **19**(1): p. 141-147.
28. Franck Levassort, D.C., Marc Lethiecq. *PIEZOELECTRIC MATERIALS FOR ULTRASONIC TRANSDUCERS : REVIEW OF RECENT DEVELOPMENTS*. Available from: <http://www.sea-acustica.es/Sevilla02/ult04010.pdf>.
29. Zhou, Q., et al., *Piezoelectric films for high frequency ultrasonic transducers in biomedical applications*. Progress in Materials Science, 2011. **56**(2): p. 139-174.
30. Marteel-Parrish, A., et al., *Toward a more environmentally benign synthesis of doped barium titanate*. Green Chemistry Letters and Reviews, 2008. **1**(4): p. 197-203.
31. Dyer, C.K., et al., *Encyclopedia of Electrochemical Power Sources*. 2013: Elsevier Science.
32. Fleming, A.J. and K.K. Leang, *Design, Modeling and Control of Nanopositioning Systems*. 2014: Springer International Publishing.
33. Pramanik, S., B. Pingguan-Murphy, and N. Osman, *Developments of immobilized surface modified piezoelectric crystal biosensors for advanced applications*. International Journal of Electrochemical Science, 2013. **8**(6): p. 8863-8892.
34. Coondoo, I., N. Panwar, and A. Kholkin, *Lead-free piezoelectrics: Current status and perspectives*. Journal of Advanced Dielectrics, 2013. **03**(02): p. 1330002.
35. Damjanovic, D., *Lead-Based Piezoelectric Materials*, in *Piezoelectric and Acoustic Materials for Transducer Applications*, A. Safari and E.K. Akdoğan, Editors. 2008, Springer US: Boston, MA. p. 59-79.

36. Uchino, K., *Piezoelectric ceramics for transducers* in *Ultrasonic Transducers*. 2012, Woodhead Publishing. p. 70-116.
37. Erturk, A. and D.J. Inman, *Piezoelectric Energy Harvesting*. 2011: Wiley.
38. Mohiddon, M.A., A. Kumar, and K.L. Yadav, *Effect of Nd doping on structural, dielectric and thermodynamic properties of PZT (65/35) ceramic*. *Physica B: Condensed Matter*, 2007. **395**(1–2): p. 1-9.
39. Laurent, M., et al., *Microstructural and electrical characterization of La-doped PZT ceramics prepared by a precursor route*. *Journal of the European Ceramic Society*, 2001. **21**(10–11): p. 1495-1498.
40. Yoon, Y.S., et al., *Fabrication and frequency response of dual-element ultrasonic transducer using PZT-5A thick film*. *Sensors and Actuators A: Physical*, 2006. **125**(2): p. 463-470.
41. Chaplya, P.M. and G.P. Carman. *Compression of PZT-5H piezoelectric ceramic at constant electric field: investigation of energy absorption mechanism*. 2002.
42. Singh, P., et al. *Additive manufacturing of PZT-5H piezoceramic for ultrasound transducers*. in *2011 IEEE International Ultrasonics Symposium*. 2011.
43. *Soft and Hard PZT*. [Last accessed 19/09/2017]; Available from: <https://www.americanpiezo.com/piezo-theory/ceramics.html>.
44. Wang, P., Y. Li, and Y. Lu, *Enhanced piezoelectric properties of (Ba<sub>0.85</sub>Ca<sub>0.15</sub>)(Ti<sub>0.9</sub>Zr<sub>0.1</sub>)O<sub>3</sub> lead-free ceramics by optimizing calcination and sintering temperature*. *Journal of the European Ceramic Society*, 2011. **31**(11): p. 2005-2012.
45. Shi, M., et al., *Effect of annealing processes on the structural and electrical properties of the lead-free thin films of (Ba<sub>0.9</sub>Ca<sub>0.1</sub>)(Ti<sub>0.9</sub>Zr<sub>0.1</sub>)O<sub>3</sub>*. *Journal of Alloys and Compounds*, 2013. **562**(0): p. 116-122.
46. *Eu-Directive 2002/95/EC : the restriction of the use of certain hazardous substances in electrical and electronic equipment*. Official Journal of the European Union, 2003: p. 19-23.
47. Maeder, M.D., D. Damjanovic, and N. Setter, *Lead Free Piezoelectric Materials*. *Journal of Electroceramics*, 2004. **13**(1): p. 385-392.
48. Cui, Y.R., et al., *Lead-free (Ba<sub>0.85</sub>Ca<sub>0.15</sub>)(Ti<sub>0.9</sub>Zr<sub>0.1</sub>)O-3-Y<sub>2</sub>O<sub>3</sub> ceramics with large piezoelectric coefficient obtained by low-temperature sintering*. *Journal of Materials Science-Materials in Electronics*, 2013. **24**(2): p. 654-657.
49. Liu, W. and X. Ren, *Large Piezoelectric Effect in Pb-Free Ceramics*. *Physical Review Letters*, 2009. **103**(25).
50. Li, W., et al., *High piezoelectric d<sub>33</sub> coefficient in (Ba<sub>1-x</sub>Cax)(Ti<sub>0.98</sub>Zr<sub>0.02</sub>)O<sub>3</sub> lead-free ceramics with relative high Curie temperature*. *Materials Letters*, 2010. **64**(21): p. 2325-2327.
51. Li, W., et al., *Piezoelectric and Dielectric Properties of (Ba<sub>1-x</sub>Cax)(Ti<sub>0.95</sub>Zr<sub>0.05</sub>)O<sub>3</sub> Lead-Free Ceramics*. *Journal of the American Ceramic Society*, 2010. **93**(10): p. 2942-2944.
52. Haertling, G.H., *Ferroelectric ceramics: history and technology*. *Journal of the American Ceramic Society*, 1999. **82**(4): p. 797-818.
53. Gray, R.B., *Transducer and method of making the same*. 1949, Google Patents.
54. Berlincourt, D. and H. Jaffe, *Elastic and piezoelectric coefficients of single-crystal barium titanate*. *Physical Review*, 1958. **111**(1): p. 143.
55. Takenaka, T. and H. Nagata, *Current status and prospects of lead-free piezoelectric ceramics*. *Journal of the European Ceramic Society*, 2005. **25**(12): p. 2693-2700.
56. Sen, S. and R.N.P. Choudhary, *Impedance studies of Sr modified BaZr<sub>0.05</sub>Ti<sub>0.95</sub>O<sub>3</sub> ceramics*. *Materials Chemistry and Physics*, 2004. **87**(2–3): p. 256-263.

57. Lee, S.T.F., et al., *High-frequency ultrasonic transducer based on lead-free BSZT piezoceramics*. Ultrasonics, 2011. **51**(7): p. 811-814.
58. Smolenskii, G.A., et al., *New Ferroelectrics of Complex Composition. IV*. Soviet Physics-Solid State, 1961. **2**: p. 2651-2654.
59. Aksel, E. and J.L. Jones, *Advances in Lead-Free Piezoelectric Materials for Sensors and Actuators*. Sensors, 2010. **10**(3): p. 1935-1954.
60. Hiruma, Y., H. Nagata, and T. Takenaka, *Phase Transition Temperatures and Piezoelectric Properties of  $(\text{Bi } 1/2 \text{ Na } 1/2) \text{TiO}_3 - (\text{Bi } 1/2 \text{ K } 1/2) \text{TiO}_3 - \text{BaTiO}_3$  Lead-Free Piezoelectric Ceramics*. Japanese Journal of Applied Physics, 2006. **45**(9S): p. 7409-7412.
61. Hiruma, Y., H. Nagata, and T. Takenaka, *Thermal depoling process and piezoelectric properties of bismuth sodium titanate ceramics*. Journal of Applied Physics, 2009. **105**(8): p. 084112-1-084112-8.
62. Rödel, J., et al., *Perspective on the Development of Lead-free Piezoceramics*. Journal of the American Ceramic Society, 2009. **92**(6): p. 1153-1177.
63. Takenaka, T., H. Nagata, and Y. Hiruma, *Current Developments and Prospective of Lead-Free Piezoelectric Ceramics*. Japanese Journal of Applied Physics, 2008. **47**(5S): p. 3787.
64. Hiruma, Y., et al., *Ferroelectric and Piezoelectric Properties of  $(\text{Bi } 1/2 \text{ K } 1/2) \text{TiO}_3$  Ceramics*. Japanese Journal of Applied Physics, 2005. **44**(7R): p. 5040-5044.
65. Tadashi, T., M. Kei-ichi, and S. Koichiro,  *$(\text{Bi } 1/2 \text{ Na } 1/2) \text{TiO}_3 - \text{BaTiO}_3$  System for Lead-Free Piezoelectric Ceramics*. Japanese Journal of Applied Physics, 1991. **30**(9S): p. 2236.
66. Hiruma, Y., et al., *Piezoelectric Properties of  $\text{BaTiO}_3?(\text{Bi}1/2\text{K}1/2) \text{TiO}_3$  Ferroelectric Ceramics*. Japanese journal of applied physics, 2004. **43**(11R): p. 7556.
67. Elkechai, O., M. Manier, and J. Mercurio,  *$\text{Na}_0.5\text{Bi}_0.5\text{TiO}_3 - \text{K}_0.5\text{Bi}_0.5\text{TiO}_3$  (NBT-KBT) system: A structural and electrical study*. physica status solidi (a), 1996. **157**(2): p. 499-506.
68. Atsushi, S., et al., *Dielectric and Piezoelectric Properties of  $(\text{Bi } 0.5 \text{ Na } 0.5) \text{TiO}_3 - (\text{Bi } 0.5 \text{ K } 0.5) \text{TiO}_3$  Systems*. Japanese Journal of Applied Physics, 1999. **38**(9S): p. 5564.
69. Choy, S.H., et al., *Study of compressive type accelerometer based on lead-free BNKBT piezoceramics*. Applied Physics A, 2006. **82**(4): p. 715-718.
70. Choy, S.H., et al.,  *$0.90(\text{Bi}1/2\text{Na}1/2)\text{TiO}_3 - 0.05(\text{Bi}1/2\text{K}1/2)\text{TiO}_3 - 0.05\text{BaTiO}_3$  transducer for ultrasonic wirebonding applications*. Applied Physics A, 2006. **84**(3): p. 313-316.
71. Zhang, S.-T., et al., *Lead-free piezoceramics with giant strain in the system  $\text{Bi}_0.5\text{Na}_0.5\text{TiO}_3 - \text{BaTiO}_3 - \text{K}_0.5\text{Na}_0.5\text{NbO}_3$ . I. Structure and room temperature properties*. Journal of Applied Physics, 2008. **103**(3): p. 034107.
72. Wood, E.A., *Polymorphism in potassium niobate, sodium niobate, and other ABO<sub>3</sub> compounds*. Acta Crystallographica, 1951. **4**(4): p. 353-362.
73. Shirane, G., R. Newnham, and R. Pepinsky, *Dielectric Properties and Phase Transitions of  $\text{NaNbO}_3$  and  $(\text{Na}, \text{K}) \text{NbO}_3$* . Physical Review, 1954. **96**(3): p. 581.
74. Egerton, L. and D.M. Dillon, *Piezoelectric and dielectric properties of ceramics in the system potassium—sodium niobate*. Journal of the American Ceramic Society, 1959. **42**(9): p. 438-442.
75. Singh, K., et al., *Dielectric properties of potassium sodium niobate mixed system*. Materials Research Bulletin, 2001. **36**(13–14): p. 2365-2374.
76. Saito, Y. and H. Takao, *High performance lead-free piezoelectric ceramics in the  $(\text{K}, \text{Na}) \text{NbO}_3 - \text{LiTaO}_3$  solid solution system*. Ferroelectrics, 2006. **338**(1): p. 17-32.



77. Taghaddos, E., M. Hejazi, and A. Safari, *Lead-free piezoelectric materials and ultrasonic transducers for medical imaging*. Journal of Advanced Dielectrics, 2015. **5**(2).
78. Reyes-Montero, A., et al., *Lead-free Ba<sub>0.9</sub>Ca<sub>0.1</sub>Ti<sub>0.9</sub>Zr<sub>0.1</sub>O<sub>3</sub> piezoelectric ceramics processed below 1300°C*. Journal of Alloys and Compounds, 2014. **584**(0): p. 28-33.
79. Bai, Y., et al., *(Ba,Ca)(Zr,Ti)O<sub>3</sub> lead-free piezoelectric ceramics—The critical role of processing on properties*. Journal of the European Ceramic Society, 2015. **35**(13): p. 3445-3456.
80. Keeble, D.S., et al., *Revised structural phase diagram of (Ba<sub>0.7</sub>Ca<sub>0.3</sub>TiO<sub>3</sub>)-(BaZr<sub>0.2</sub>Ti<sub>0.8</sub>O<sub>3</sub>)*. Applied Physics Letters, 2013. **102**(9): p. 092903.
81. Bai, W.F., et al., *Dielectric, ferroelectric, and piezoelectric properties of textured BZT-BCT lead-free thick film by screen printing*. Materials Letters, 2012. **83**: p. 20-22.
82. Piorra, A., et al., *Piezoelectric properties of 0.5(Ba<sub>0.7</sub>Ca<sub>0.3</sub>TiO<sub>3</sub>)-0.5 Ba(Zr<sub>0.2</sub>Ti<sub>0.8</sub>O<sub>3</sub>)<sub>0-3</sub> ferroelectric lead-free laser deposited thin films*. Journal of Applied Physics, 2011. **109**(10): p. 4.
83. Mishra, P., Sonia, and P. Kumar, *Effect of sintering temperature on dielectric, piezoelectric and ferroelectric properties of BZT-BCT 50/50 ceramics*. Journal of Alloys and Compounds, 2012. **545**: p. 210-215.
84. Li, B., J.E. Blendell, and K.J. Bowman, *Temperature-Dependent Poling Behavior of Lead-free BZT-BCT Piezoelectrics*. Journal of the American Ceramic Society, 2011. **94**(10): p. 3192-3194.
85. Yan, X., et al., *Lead-Free Intravascular Ultrasound Transducer Using BZT-50BCT Ceramics*. IEEE Transactions on Ultrasonics Ferroelectrics and Frequency Control, 2013. **60**(6): p. 1272-1276.
86. Bai, Y., *Vibrational energy harvesting using piezoelectric ceramics and free-standing thick-film structures*. 2015, University of Birmingham.
87. Hu, W., *Experimental search for high Curie temperature piezoelectric ceramics with combinatorial approaches*, in *Materials Science and Engineering*. 2011, Iowa State University.
88. Foster, F.S., K.A. Harasiewicz, and M.D. Sherar, *A history of medical and biological imaging with polyvinylidene fluoride (PVDF) transducers*. IEEE Transactions on Ultrasonics, Ferroelectrics, and Frequency Control, 2000. **47**(6): p. 1363-1371.
89. Fukada, E., *History and recent progress in piezoelectric polymers*. IEEE Transactions on Ultrasonics, Ferroelectrics, and Frequency Control, 2000. **47**(6): p. 1277-1290.
90. Olabisi, O. and K. Adewale, *Handbook of Thermoplastics, Second Edition*. 2016: CRC Press.
91. Robert, M., et al., *Fabrication of focused poly(vinylidene fluoride-trifluoroethylene) P(VDF-TrFE) copolymer 40–50 MHz ultrasound transducers on curved surfaces*. Journal of Applied Physics, 2004. **96**(1): p. 252-256.
92. Fontananova, E., et al., *From hydrophobic to hydrophilic polyvinylidene fluoride (PVDF) membranes by gaining new insight into material's properties*. RSC Advances, 2015. **5**(69): p. 56219-56231.
93. Zhou, Q., et al., *Piezoelectric single crystal ultrasonic transducers for biomedical applications*. Progress in Materials Science, 2014. **66**: p. 87-111.
94. Oakley, C.G. and M.J. Zipparo. *Single crystal piezoelectrics: a revolutionary development for transducers*. in *Ultrasonics Symposium, 2000 IEEE*. 2000.
95. Lu, X.M. and T.L. Proulx. *Single crystals vs. pzt ceramics for medical ultrasound applications*. in *IEEE Ultrasonics Symposium, 2005*. 2005.

96. Zhou, Q., et al., *PMN-PT single crystal, high-frequency ultrasonic needle transducers for pulsed-wave Doppler application*. IEEE Transactions on Ultrasonics, Ferroelectrics, and Frequency Control, 2007. **54**(3): p. 668-675.
97. Rehrig, P.W., et al. *Status of piezoelectric single crystal growth for medical transducer applications*. in *Ultrasonics, 2003 IEEE Symposium on*. 2003.
98. Jie, C. and R. Panda. *Review: commercialization of piezoelectric single crystals for medical imaging applications*. in *IEEE Ultrasonics Symposium, 2005*. 2005.
99. Gururaja, T.R., et al. *Single crystal transducers for medical imaging applications*. in *Ultrasonics Symposium, 1999. Proceedings. 1999 IEEE*. 1999.
100. Clipsham, T.J. and T.W. Button, *1-3 Piezocomposites realised from small feature size, high aspect ratio, hot embossed moulds. Part II: piezocomposite fabrication*. Microsystem Technologies-Micro-and Nanosystems-Information Storage and Processing Systems, 2010. **16**(11): p. 1983-1988.
101. Topolov, V.Y. and S.V. Glushanin, *Evolution of connectivity patterns and links between interfaces and piezoelectric properties of two-component composites*. Journal of Physics D: Applied Physics, 2002. **35**(16): p. 2008.
102. Ramadan, K.S., D. Sameoto, and S. Evoy, *A review of piezoelectric polymers as functional materials for electromechanical transducers*. Smart Materials and Structures, 2014. **23**(3).
103. Levassort, F., et al., *Effective electroelastic moduli of 3-3(0-3) piezocomposites*. IEEE Transactions on Ultrasonics, Ferroelectrics, and Frequency Control, 1999. **46**(4): p. 1028-1034.
104. Splitt, G. *Piezocomposite Transducers - a Milestone for Ultrasonic Testing*. [Last accessed date 20/05/2016]; Available from: [http://www.ndt.net/article/splitt/splitt\\_e.htm](http://www.ndt.net/article/splitt/splitt_e.htm).
105. Rouffaud, R., et al. *Influence of 1-3 piezocomposite fabrications on lateral modes*. in *Ultrasonics Symposium (IUS), 2012 IEEE International*. 2012.
106. Smith, W.A. and B.A. Auld, *MODELING 1-3 COMPOSITE PIEZOELECTRICS - THICKNESS-MODE OSCILLATIONS*. Ieee Transactions on Ultrasonics Ferroelectrics and Frequency Control, 1991. **38**(1): p. 40-47.
107. Jiang, Y., *Fabrication and characterisation of novel ultrasound transducers*, in *School of Metallurgy and Materials*. 2013, University of Birmingham.
108. Bernassau, A.L., et al., *Microfabrication of Electrode Patterns for High-Frequency Ultrasound Transducer Arrays*. Ieee Transactions on Ultrasonics Ferroelectrics and Frequency Control, 2012. **59**(8): p. 1820-1829.
109. Lee, H., et al., *High Temperature, High Power Piezoelectric Composite Transducers*. Sensors, 2014. **14**(8): p. 14526.
110. Kar-Gupta, R. and T.A. Venkatesh, *Electromechanical response of 1-3 piezoelectric composites: Effect of poling characteristics*. Journal of Applied Physics, 2005. **98**(5): p. 054102.
111. Jiang, X., et al. *Single crystal piezoelectric composites for advanced NDT ultrasound*. in *The 14th International Symposium on: Smart Structures and Materials & Nondestructive Evaluation and Health Monitoring*. 2007. International Society for Optics and Photonics.
112. Smith, W.A. *The application of 1-3 piezocomposites in acoustic transducers*. in *Applications of Ferroelectrics, 1990., IEEE 7th International Symposium on*. 1990.
113. Thurston, R.N., A.D. Pierce, and E.P. Papadakis, *Reference for Modern Instrumentation, Techniques, and Technology: Ultrasonic Instruments and Devices II: Ultrasonic Instruments and Devices II*. 1998: Elsevier Science.

114. Clipsham, T.J., *THE REPLICATION OF MICRON SCALE PILLAR ARRAYS FOR MEDICAL ULTRASOUND APPLICATIONS*, in *Department of Metallurgy and Materials*. 2010, University of Birmingham.
115. Smith, W.A., *THE ROLE OF PIEZOCOMPOSITES IN ULTRASONIC TRANSDUCERS*. Ieee 1989 Ultrasonics Symposium : Proceedings, Vols 1 and 2, 1989: p. 755-766.
116. Pope, J.A., *Medical Physics: Imaging*. 1999: Pearson Education.
117. Hoskins, P. and A. Thrush, *Diagnostic Ultrasound: Physics and Equipment*. 2003: Greenwich Medical Media.
118. Sigmund, O., S. Torquato, and I.A. Aksay, *On the design of 1-3 piezocomposites using topology optimization*. *Journal of Materials Research*, 1998. **13**(4): p. 1038-1048.
119. Hossack, J.A. and G. Hayward, *Finite-element analysis of 1-3 composite transducers*. *IEEE Transactions on Ultrasonics, Ferroelectrics, and Frequency Control*, 1991. **38**(6): p. 618-629.
120. Hayward, G. and J. Bennett, *Assessing the influence of pillar aspect ratio on the behavior of 1-3 connectivity composite transducers*. *IEEE Transactions on Ultrasonics, Ferroelectrics, and Frequency Control*, 1996. **43**(1): p. 98-108.
121. Abrar, A., et al., *1-3 connectivity piezoelectric ceramic-polymer composite transducers made with viscous polymer processing for high frequency ultrasound*. *Ultrasonics*, 2004. **42**(1-9): p. 479-484.
122. Gururaja, T.R., et al., *Piezoelectric Composite Materials for Ultrasonic Transducer Applications. Part I: Resonant Modes of Vibration of PZT Rod-Polymer Composites*. *IEEE Transactions on Sonics and Ultrasonics*, 1985. **32**(4): p. 481-498.
123. Brown, J.A., et al., *Fabrication and Performance of a 40-MHz Linear Array Based on a 1-3 Composite with Geometric Elevation Focusing*. *IEEE Transactions on Ultrasonics, Ferroelectrics, and Frequency Control*, 2007. **54**(9): p. 1888-1894.
124. Yin, J., et al. *Geometry effect on piezo-composite transducers with triangular pillars*. in *2008 IEEE Ultrasonics Symposium*. 2008.
125. Brown, J.A., et al., *Fabrication and performance of high-frequency composite transducers with triangular-pillar geometry*. *Ultrasonics, Ferroelectrics and Frequency Control, IEEE Transactions on*, 2009. **56**(4): p. 827-836.
126. Hao-Chung, Y., et al. *A study of 1-3 pseudo-random pillar piezocomposites for ultrasound transducers*. in *Ultrasonics Symposium (IUS), 2011 IEEE International*. 2011.
127. Demore, C., et al. *1-3 piezocomposite design optimised for high frequency kerfless transducer arrays*. in *IEEE Ultrason. Symp.* 2009.
128. Jiang, Y., et al. *Micro-moulded randomised piezocomposites for high frequency ultrasound imaging*. in *2012 IEEE International Ultrasonics Symposium*. 2012.
129. Lia, Y.Z.a.J.-F., *Preparation and electrical properties of fine-scale 1-3 lead zirconic titanate/epoxy composite thick films for high-frequency ultrasonic transducers*. *JOURNAL OF APPLIED PHYSICS* 2008. **03**, **084119**.
130. Ralf, S. *Modelling and characterixation of piezoelectric 1-3 fibre composites*. in *sensor+test conferences 2011*. Germany.
131. Yin, J., et al. *High frequency piezo-composite transducer with hexagonal pillars*. in *2009 IEEE International Ultrasonics Symposium*. 2009.
132. Jianhua, Y., et al., *Effect of triangular pillar geometry on high- frequency piezocomposite transducers*. *Ultrasonics, Ferroelectrics and Frequency Control, IEEE Transactions on*, 2010. **57**(4): p. 957-968.
133. Safari, A., V.F. Janas, and A. Bandyopadhyay, *Development of fine-scale piezoelectric composites for transducers*. *AIChE Journal*, 1997. **43**(S11): p. 2849-2856.

134. Garcia-Gancedo, L., et al., *Application of gel-casting to the fabrication of 1-3 piezoelectric ceramic-polymer composites for high-frequency ultrasound devices*. Journal of Micromechanics and Microengineering, 2012. **22**(12).
135. L.J.Bowen, R.L.G., H.T. Pham, D. F. Fiore, K W. French. *Injection molded fine-scale piezoelectric composite transducers*. in *Ultrasonics Symposium, 1993. Proceedings., IEEE 1993*. 1993.
136. Bowen, L.J. and K.W. French, *FABRICATION OF PIEZOELECTRIC CERAMIC POLYMER COMPOSITES BY INJECTION-MOLDING*. Isaf 92 : Proceedings of the Eighth IEEE International Symposium on Applications of Ferroelectrics, ed. M. Liu, et al. 1992. 160-163.
137. Pazol, B.G., et al. *Ultrafine scale piezoelectric composite materials for high frequency ultrasonic imaging arrays*. in *Ultrasonics Symposium, 1995. Proceedings., 1995 IEEE*. 1995.
138. Hirata, Y., T. Numazawa, and H. Takada, *Effects of Aspect Ratio of Lead Zirconate Titanate on 1-3 Piezoelectric Composite Properties*. Japanese Journal of Applied Physics, 1997. **36**(9S): p. 6062.
139. K. Libitz, A.W., G. Preu. *Microstructuring technology*. in *Ultrasonics Symposium, 1993. Proceedings., IEEE 1993*. 1993.
140. Hirata, Y., et al. *Piezocomposite of fine PZT rods realized with synchrotron radiation lithography*. in *Ultrasonics Symposium, 1997. Proceedings., 1997 IEEE*. 1997.
141. Su, B., et al., *Embossing of 3D ceramic microstructures*. Microsystem technologies, 2002. **8**(4-5): p. 359-362.
142. Su, B., D.H. Pearce, and T.W. Button, *Routes to net shape electroceramic devices and thick films*. Journal of the European Ceramic Society, 2001. **21**(10–11): p. 2005-2009.
143. Cochran, S., et al., *Net-shape ceramic processing as a route to ultrafine scale 1-3 connectivity piezoelectric ceramic-polymer composite transducers*, in *2004 IEEE Ultrasonics Symposium, Vols 1-3*, M.P. Yuhas, Editor. 2004. p. 1682-1685.
144. Zhang, D., et al., *Piezoelectric 1–3 Composites for High Frequency Ultrasonic Transducer Applications*. Ferroelectrics, 2004. **304**(1): p. 201-205.
145. S.Wang, J.-F.L., K.Wakabayashi, M.Esashi, *Lost Silicon Mould Process for PZT Microstructures*. Advanced materials, 1999. **11**(10): p. 873-876.
146. Ruiz, A., et al., *Large-area protein nano-arrays patterned by soft lithography*. Nanotechnology, 2007. **18**(50): p. 505306.
147. Kim, M.S., et al., *Synthesis of monodisperse PS-co-PDMS microspheres by dispersion polymerization*. Materials Science and Engineering: C, 2007. **27**(5–8): p. 1247-1251.
148. Starke, S., A. Schonecker, and W. Gebhardt. *Fine scale piezoelectric 1-3 composites: a new approach of cost effective fabrication*. in *Applications of Ferroelectrics, 1998. ISAF 98. Proceedings of the Eleventh IEEE International Symposium on*. 1998.
149. Gebhardt, S., et al., *Fine scale 1-3 composites fabricated by the soft mold process: Preparation and modeling*. Ferroelectrics, 2000. **241**(1): p. 67-73.
150. Gebhardt, S., et al., *Quasistatic and dynamic properties of 1–3 composites made by soft molding*. Journal of the European Ceramic Society, 2003. **23**(1): p. 153-159.
151. Olhero, S.M., et al., *Innovative fabrication of PZT pillar arrays by a colloidal approach*, in *Journal of the European Ceramic Society* 2012. p. 1067-1075.
152. Yang, J., J. Yu, and Y. Huang, *Recent developments in gelcasting of ceramics*. Journal of the European Ceramic Society, 2011. **31**(14): p. 2569-2591.
153. Liu, X., Y. Huang, and J. Yang, *Effect of rheological properties of the suspension on the mechanical strength of Al<sub>2</sub>O<sub>3</sub>–ZrO<sub>2</sub> composites prepared by gelcasting*. Ceramics International, 2002. **28**(2): p. 159-164.

154. Omatete, O.O., M.A. Janney, and S.D. Nunn, *Gelcasting: From laboratory development toward industrial production*. Journal of the European Ceramic Society, 1997. **17**(2): p. 407-413.
155. Olhero, S.M., Garcia-Gancedo, L. Zhang, D., Button, T.W., Alves, F.J., *Preparation of ceramic microelectromechanical systems (MEMS) using a gelcasting consolidation technique*.
156. Guo, D., et al., *Gelcasting based solid freeform fabrication of piezoelectric ceramic objects*. Scripta Materialia, 2002. **47**(6): p. 383-387.
157. Dongliang, J. and Z. Jingxian, *Properties of Carbide Ceramics from Gelcasting and Pressure-less Sintering*. IOP Conference Series: Materials Science and Engineering, 2011. **18**(20): p. 202001.
158. Omatete, O.O., M.A. Janney, and R.A. Strehlow, *Gelcasting: a new ceramic forming process*. American Ceramic Society Bulletin, 1991. **70**(10): p. 1641-1649.
159. Gilissen, R., et al., *Gelcasting, a near net shape technique*. Materials & Design, 2000. **21**(4): p. 251-257.
160. Janney, M., et al., *Gelcasting*. The handbook of ceramic engineering, 1998: p. 1-15.
161. Janney, M.A., et al., *Development of low-toxicity gelcasting systems*. Journal of the American Ceramic Society, 1998. **81**(3): p. 581-591.
162. Mao, X., et al., *Gelcasting of alumina using epoxy resin as a gelling agent*. Journal of the American Ceramic Society, 2007. **90**(3): p. 986-988.
163. Alkoy, S., H. Yanik, and B. Yapar, *Fabrication of lead zirconate titanate ceramic fibers by gelation of sodium alginate*. Ceramics International, 2007. **33**(3): p. 389-394.
164. Xie, Z.-P., et al., *A new gel casting of ceramics by reaction of sodium alginate and calcium iodate at increased temperatures*. Journal of Materials Science Letters, 2001. **20**(13): p. 1255-1257.
165. Xie, Z.-p., et al., *Ceramic forming based on gelation principle and process of sodium alginate*. Materials Letters, 2003. **57**(9-10): p. 1635-1641.
166. Jia, Y., Y. Kanno, and Z.P. Xie, *New gel-casting process for alumina ceramics based on gelation of alginate*. Journal of the European Ceramic Society, 2002. **22**(12): p. 1911-1916.
167. Paredes Juárez, G.A., et al., *Immunological and Technical Considerations in Application of Alginate-Based Microencapsulation Systems*. Frontiers in Bioengineering and Biotechnology, 2014. **2**(26).
168. Lyckfeldt, O., J. Brandt, and S. Lesca, *Protein forming — a novel shaping technique for ceramics*. Journal of the European Ceramic Society, 2000. **20**(14-15): p. 2551-2559.
169. Takeshita, M. and S. Kurita, *Development of self-hardening slip casting*. Journal of the European Ceramic Society, 1997. **17**(2): p. 415-419.
170. Mao, X., et al., *Investigation of New Epoxy Resins for the Gel Casting of Ceramics*. Journal of the American Ceramic Society, 2008. **91**(4): p. 1354-1356.
171. Xie, R., et al., *Gelcasting of alumina ceramics with improved green strength*. Ceramics International, 2012. **38**(8): p. 6923-6926.
172. Jiang, C., et al., *Gelcasting of aluminum nitride ceramics using hydantion epoxy resin as gelling agent*. Ceramics International, 2013. **39**(8): p. 9429-9433.
173. Mao, X., et al., *Rheological characterization of gel casting system based on epoxy resin*. Ceramics International, 2009. **35**: p. 415-420.
174. Mahendran, R.S., *Characterisation of cross-linking and moisture ingress detection in an epoxy/amine resin using fibre-optic sensors*, in *School of Metallurgy and Materials*. 2010, university of Birmingham.

## Chapter 4 Aims and objectives of the project

Monolithic piezoelectric materials have several limitations as the material of choice for medical ultrasound transducers. PZT based ceramic materials and single crystals have high  $k_t$  but they also come with high acoustic impedance leading to acoustic mismatch. Piezoelectric polymers offer better acoustic matching but they are not good transmitting materials due to their low piezoelectric activity. 1-3 piezocomposites represent an alternative to monolithic materials for the active component of transducers as the piezoelectric phase in the piezocomposite offers excellent electromechanical thickness coupling coefficient, and the non-piezoelectric passive polymer can reduce the acoustic impedance mismatch to tissues and offers improved mechanical and geometrical flexibility.

In order to diagnose smaller structures with better resolution ultrasound transducers have to be operated at high frequencies. Therefore, an ultrafine spatial scale composite with small kerf and high aspect ratio is required in order to avoid interference due to spurious resonant modes. A random design of 1-3 piezocomposites has been studied and reported in which the spurious and lateral resonance modes caused by regular ceramic pillar structures can be suppressed. The fabrication of ceramic segments with small lateral dimensions and random geometries required for these composites brings great difficulties. The industrial standard method of dice and fill cannot fabricate the ultrafine ( $<50 \mu\text{m}$ ) and random geometries required, and so new processes need to be developed. The randomised structures of 1-3 piezocomposites with an ultrafine dimension can be obtained by combining a gel casting and soft moulding method, providing excellent green

strength ceramic pillars. A gel casting system requires suitable ceramic powders and water soluble epoxy resin as the main components.

PZT ceramic powders are the most commonly used. However, the critical drawback of PZT is that it has high percent lead content; hence lead free materials are being developed as replacements for PZT, and recently, BCZT has been reported as a suitable candidate due to its high piezoelectric constant. Hydantoin Epoxy resin is a new candidate epoxy resin for gel casting systems because of it has high water solubility, and is non-toxic, low cost and offers high ceramic green strength.

The overall aim of this project is to develop, fabricate and characterise lead free and lead based materials and composites for use in high frequency medical ultrasound transducers. PZT, BCZT and hydantoin epoxy resin have been selected for the preparation of the PZT and BCZT gel casting slurries. In order to achieve this aim a number of specific objectives will be studied as detailed below.

1. To optimise all process parameters of soft PZT/epoxy resin and 50BCZT/epoxy resin gel casting systems from the premixed solution preparation to the sintering of bulk ceramics/ 1-3 composites.
2. To study the casting and demoulding techniques suitable for soft PZT/epoxy resin and 50BCZT/epoxy resin gel casting systems.
3. To fabricate bulk gel casting samples by using soft PZT and 50BCZT, and compare their properties related to high frequency ultrasound transducers.
4. To study the possibilities of lead free material with gel casting systems, in order to fabricate the high frequency transducer and considering the properties for the replacement of soft PZT.

5. To fabricate 1-3 piezocomposite with random mould structure using soft PZT/epoxy resin and 50BCZT/epoxy resin gel casting systems.
6. To characterise and compare the properties of 1-3 piezocomposite with random structure in lead free piezoelectric/epoxy resin and soft PZT/epoxy resin gel casting system.
7. To fabricate and characterise flat and focused high frequency transducers incorporating 1-3 composites made from the soft PZT and lead free gelcasting systems.



# Chapter 5 Research methods

## 5.1 Process procedures

### 5.1.1 Soft mould fabrication process

In this project, the elastomer soft moulds for 1-3 piezocomposite fabrication have been replicated from Si master moulds with randomised structure using a soft lithography technique. The master moulds were fabricated by deep dry etching of Si at the University of Edinburgh, as discussed in detail in reference [1]. The replication process is detailed below:

*Step 1:* the Si master mould with the randomised design facing upward was placed on a plastic weighing boat. The position was fixed by applying a small amount of glue on the bottom of the master mould.

*Step 2:* Poly(dimethylsiloxane)-Sylgard silicone (PDMS) elastomer 184 was mixed by hand with Sylgard curing agent (Dow Corning Corporation Limited, UK) with 10:1 weight ratio in a clean and dry beaker, followed by de-airing in vacuum chamber for 10-20 minutes in order to eliminate bubbles in the mixture.

*Step 3:* the mixture was heated to 50°C in an oven (Lenton Thermal Designs, UK) for 10 minutes and after that it was slowly poured on top the master mould, ensuring the PDMS mixture spreads over the whole master mould as shown in Figure 5.1, followed by de-airing in vacuum chamber for 3 minutes in order to ensure that the master mould was completely filled with PDMS.

*Step 4:* the PDMS was cured at room temperature for 24 hours before transferring to an oven at 60°C for a further 24 hours.

*Step 5:* The whole assembly was removed from the plastic weighing boat and then the bottom of the master mould was glued onto a glass slide by using adhesive tape, followed by peeling the cured PDMS from the master mould, resulting in a negative replication of the structure in the soft mould.

This process was also used to produce circular, disc-shaped PDMS moulds for the fabrication of bulk gel cast ceramics. Aluminum discs 12.53 mm diameter and 3 mm high were used as master mould templates.

#### **PDMS is poured onto the master mould**

The mixture of silicone elastomer and curing agent

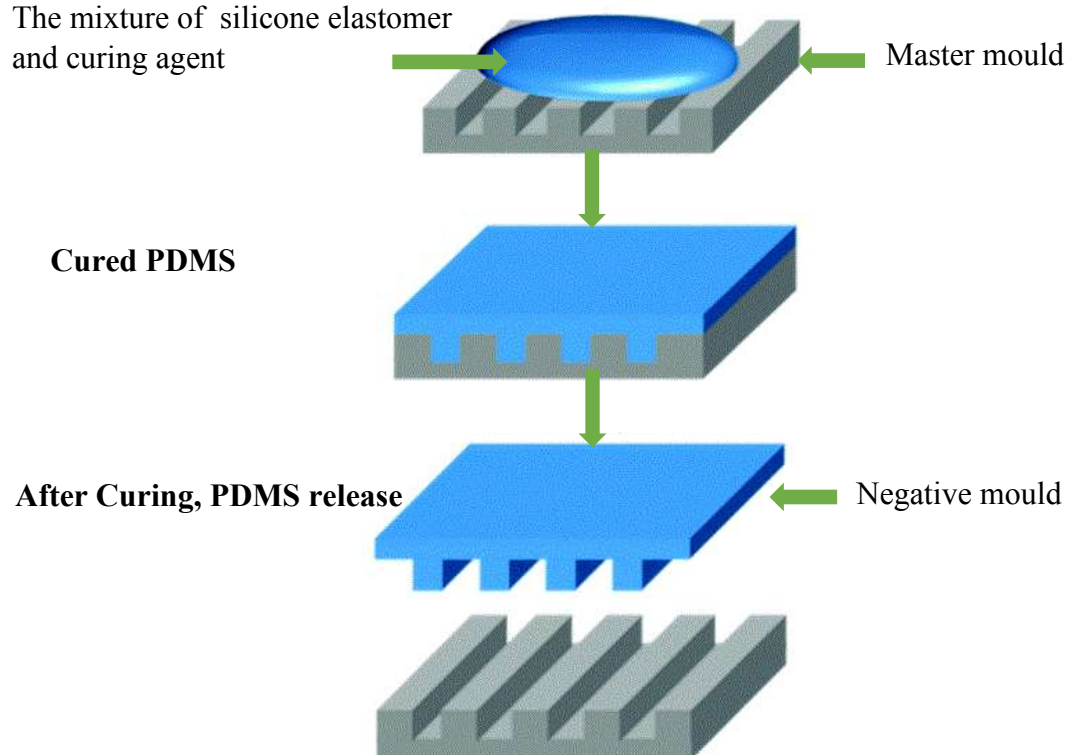


**Figure 5.1 Schematic of PDMS soft mould replication from a master mould. The PDMS is cast onto the master mould and, after curing, the soft mould is peeled off [2].**

## **5.1.2 Fabrication of lead based and lead free bulk ceramic by gel casting**

### **5.1.2.1 Powder size reduction**

In this project, lead based and lead free piezoelectric materials were the two main ceramic powders used for fabricating 1-3 composites. For lead free materials, the  $0.5\text{Ba}(\text{Zr}_{0.2}\text{Ti}_{0.8})\text{O}_3-0.5(\text{Ba}_{0.7}\text{Ca}_{0.3})\text{TiO}_3$  or 0.5BZT-0.5BCT composition (designated 50BCZT in this thesis) was chosen due to its good piezoelectric properties over other lead free piezoelectric materials as discussed in Chapter 3.2.2 and 3.2.2.4. These powders were supplied from the Central European Institute of Technology (CEITEC), Czech Republic, prepared through the solid state reaction with the density of  $5.73 \text{ g/cm}^3$  and mean particle size of  $3.31 \mu\text{m}$ . A commercial soft PZT 5H-TRS 610C [3] from TRS Technologies, USA with density of  $7.95 \text{ g/cm}^3$  was used as the lead based piezoelectric material.

Prior to being used for gel casting, all powders were subjected to a vibro-milling procedure in order to break down any hard agglomerates. Suspensions were prepared by adding 250 g powder and 200 g of the zirconia balls with 5 and 10 mm diameter into 300 ml of distilled water in a polyethylene bottle and placed in a vibro-milling machine (Model M.18, Sweco Europe S.A., Belgium) for 48 and 7 hours for the PZT and 50BCZT powders respectively. After milling the suspensions were freeze dried (Edwards Modulyo Freeze dryer, Labconco Crop., Kansas City, USA).

### **5.1.2.2 Gel casting slurry preparation, de-airing, casting and drying**

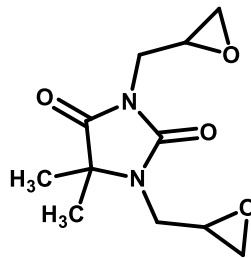
- *Gel casting slurry preparation*

The details of raw materials including their purpose and supplier for preparing the PZT and 50BCZT gel casting suspensions, are shown in table 5.1.

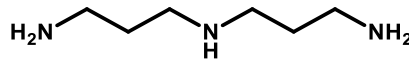
**Table 5.1 Raw materials for preparation of PZT and 50BCZT gel casting suspensions**

Materials	Purpose	Product and Supplier	Details
Vibro milled PZT	Piezoelectric powder	TRS, USA	Mean particle size : 1.20 $\mu\text{m}$
Vibro milled BCZT	Piezoelectric powder	CEITEC, Czech Republic	Mean particle size : 3 and 1.28 $\mu\text{m}$
Distilled water		-	Resistivity at 20°C : 16.5 M $\Omega$ .cm
Solution of an Ammonium salt of an acrylic polymer in water	Dispersing agent	BASF, -, Germany	Concentration : 45 wt% Density : 1.16 g/cm <sup>3</sup> at 20°C
Hydantoin Epoxy Resin	Epoxy Monomer	Hubei Xitai Chemical, China	Epoxy equivalent weight : 139 g/mol Density : 1.35 g/cm <sup>3</sup> at 20°C
Bis(3-aminopropyl)amine	Cross-linker	Sigma-Aldrich,, Germany	Molecular weight 131.22 g/mol

For the preparation of the slurry, hydantoin epoxy resin and Bis(3-aminopropyl)amine were used as epoxy monomer and cross-linker monomer, respectively. Figure 5.2 shows the chemical structure of these two monomers.



(a) hydantoin epoxy resin



(b) Bis(3-aminopropyl)amine

**Figure 5.2 Chemical structure of (a) hydantoin epoxy resin, C<sub>11</sub>H<sub>16</sub>N<sub>2</sub>O<sub>4</sub> (b) Bis(3-aminopropyl)amine, C<sub>6</sub>H<sub>17</sub>N<sub>3</sub> [4-6].**

The hydantoin epoxy resin and distilled water were weighed as a weight percent of the premix solution, followed by mixing both of them by magnetic stirrer until the epoxy resin had dissolved. The Bis(3-aminopropyl)amine is used as a hardener, and is expressed as the number of moles per equivalent weight of hydantoin epoxy resin in the premix solution. Dispex AA4040 was used as an additive to make the dispersion of the powders easier and provide better stability of the slurry. In this work, the dispersing agent is expressed as a weight percentage of the dry weight of ceramic powder (wt. /wt. basis of piezoelectric powders). The amounts of both piezoelectric powders are expressed as the volume fraction of the solid in the slurry (vol% solid loading). An example of a gel casting composition of each material for PZT and 50BCZT gel casting slurries are shown in Tables 5.2 and 5.3, respectively.

**Table 5.2 An example of a PZT gel casting composition.**

	<b>PZT</b>	<b>DispexAA4040</b>	<b>Distilled water</b>	<b>Hydantoin epoxy resin</b>	<b>Bis(3-aminopropyl) amine</b>
<b>Actual amount (g)</b>	36.2	0.362	3.5	1.5	0.375
<b>Actual wt% in the slurry</b>	86.32 wt%	0.86 wt%	8.35 wt%	3.58 wt%	0.89 wt%
<b>Definition in this project</b>	48 vol%	1 wt%	N/A	30 wt%	Parts Per Hundred Resin (PHR) = 18

**Table 5.3 An example of a 50BCZT gel casting composition.**

	<b>50BCZT</b>	<b>DispexAA4040</b>	<b>Distilled water</b>	<b>Hydantoin epoxy resin</b>	<b>Bis(3-aminopropyl) amine</b>
<b>Actual amount (g)</b>	24	0.576	3.5	1.5	0.374
<b>Actual wt% in the slurry</b>	80.13 wt%	1.92 wt%	11.68 wt%	5 wt%	1.25 wt%
<b>Definition in this project</b>	45 vol%	2.4 wt%	N/A	30 wt%	Parts Per Hundred Resin (PHR) = 18

In this work, all slurries were prepared at room temperature in batch sizes of approximately 40 g, using a 60 ml plastic bottle (Azlon, UK) as a container in which

a total of 20 g of 3 and 5 mm diameter zirconia balls were also placed. The amount of each material was calculated and weighed to 4 decimal places using a balance (R300S, Sartorius GMBH Gottingen, Germany). The procedures of preparation gel casting slurry are explained as follows. The appropriate amount of hydantoin epoxy resin was dissolved in distilled water before adding the dispersing agent, and the mixture was stirred for 20 minutes using a magnetic stirrer. One of the most important steps was adding the ceramic power into pre mix solution which could affect the slurry behavior. This work aims for a high solid loading and low viscosity, well-mixed slurry; therefore, the staged addition of PZT and BCZT powders was required [1, 7]. For the PZT slurry, the powder addition was separated into 4 stages in the pattern 1/2, 1/4, 1/8 and 1/8 of the required amount. After each addition, the slurries were ball milled for 2 hours with the milling speed approximately 70 rpm in order to achieve good mixing and limit the air bubbles in the slurry. However, 50BCZT slurries were ball milled only 20 minutes after each powder addition to maintain the flowability of slurries.

- *De-airing*

After adding all the constituents, each slurry was poured into a clean container, followed by the addition of the appropriate amount of hardener. In this stage, the slurry had to be slowly mixed by hand and then degassed in a vacuum chamber for 2 minutes in order to minimize the formation of air bubbles during casting.

- *Casting*

The slurry was gradually poured (cast) on the top of the negative PDMS soft mould. After the casting, the filled mould was placed into a vacuum chamber for degassing

for 2 minutes in order to eliminate all air bubbles and assist the slurry to completely fill the soft mould cavities. However, the total of processing time needed to be considered to ensure that the time was not longer than the induction time of the cross-linking reaction. Therefore, the time for mixing hardener, slurry casting and vacuuming had to be controlled.

- *Drying*

Drying was one of the critical steps in gel casting fabrication because at this stage the green body was weak and cracks could be formed. Therefore, slow drying were required to prevent drying defects such as cracking or warping. Drying was carried out for 24 hours at room temperature and another 24 hours in an oven at 40°C, following which the green pieces were carefully demoulded by hand before further drying in which the temperature of the oven was increased from 40°C to 100°C at 1°C /minute and then held for 1 hour to ensure that the green gel cast samples were fully dried.

### **5.1.2.3 Organic burnout and sintering of green samples**

- *PZT gel cast samples*

For PZT samples, the sintering atmosphere is a crucial factor in the success of sintering due to the volatility of the lead oxide component in PZT at temperatures above 800 °C [8] which can affect the stoichiometry and functional properties of the PZT samples [9]. In order to maintain the chemical composition of PZT and prevent the lead loss during sintering, lead II oxide (Sigma-Aldrich, Germany) and Doped ZrO<sub>2</sub> sand (Ferro corporation, USA ) were used to provide a lead rich atmosphere.

The PZT gel cast samples were buried in the sand, using an alumina crucible as a container. A flat layer of coarse and fine sand were put into the alumina crucible as

shown in Figure 5.3, the PZT green samples were put on top of the flat surface of the fine sand, and then covered by another layer the fine sand. An alumina lid was put on the top of the crucible to help maintain a lead rich atmosphere.

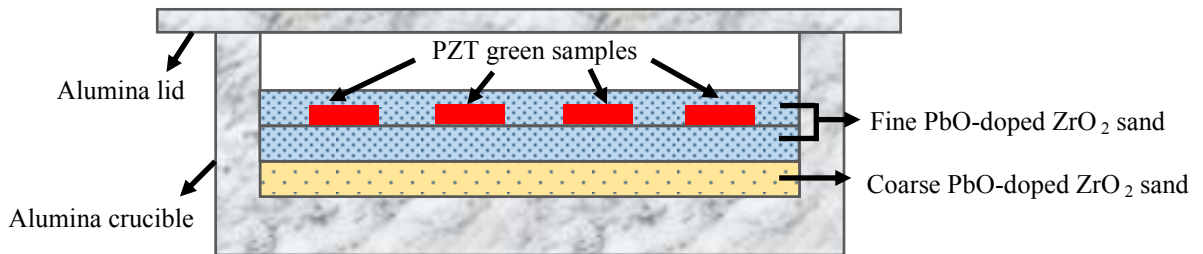


**Figure 5.3 Schematic illustration of burnout and sintering of PZT green gel casting samples in lead rich atmosphere (adopted from [1]).**

Figure 5.4 presents the burnout and sintering profile of PZT green samples which was carried out in a muffle furnace (Serial No. 3967, Lenton Furnaces, UK). To ensure that the polymer was completely removed from the green samples, the process of the organic burnout was separated into 2 steps. Firstly, the samples were heated from 40 to 250°C at 1°C/minute and dwelled at 250°C for 60 minutes, Secondly, the temperature was increased from 250°C to 400°C at the same heating rate, followed dwelling for 1 hour. After that, the ramp rate was changed to 5°C/minute to the sintering temperature of 1200°C, followed by dwelling for 1 hour and then cooling to 40°C at 5°C/minute.

- *BCZT gel cast samples*

The BCZT green gel cast samples were sintered in another muffle furnace (Serial No. 5079, Lenton Furnaces, UK) in order to avoid cross-contamination. The burn out and sintering profile was the same as the sintering profile of the PZT samples.



However, the BCZT samples were studied at sintering temperatures between 1300-1500 °C and samples were not embedded in sand like PZT.

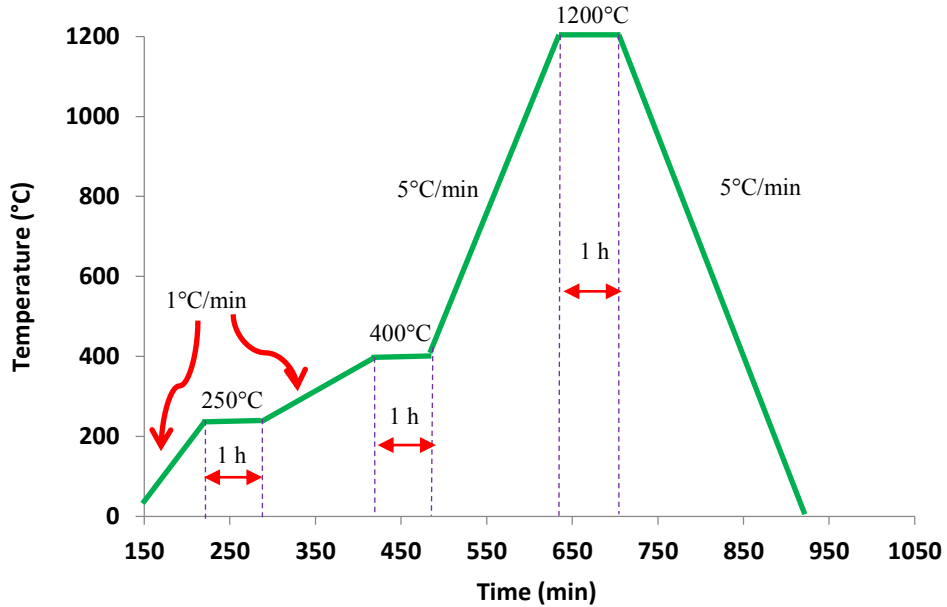


**Figure 5.4** the burnout and sintering profile of PZT green gel casting samples (BCZT samples were set the same sintering profile; excepted sintering temperatures were studied between 1300-1500°C)

The key materials and steps of piezoelectric ceramic gel casting can be summarised as shown in the flow chart in Figure 5.5.

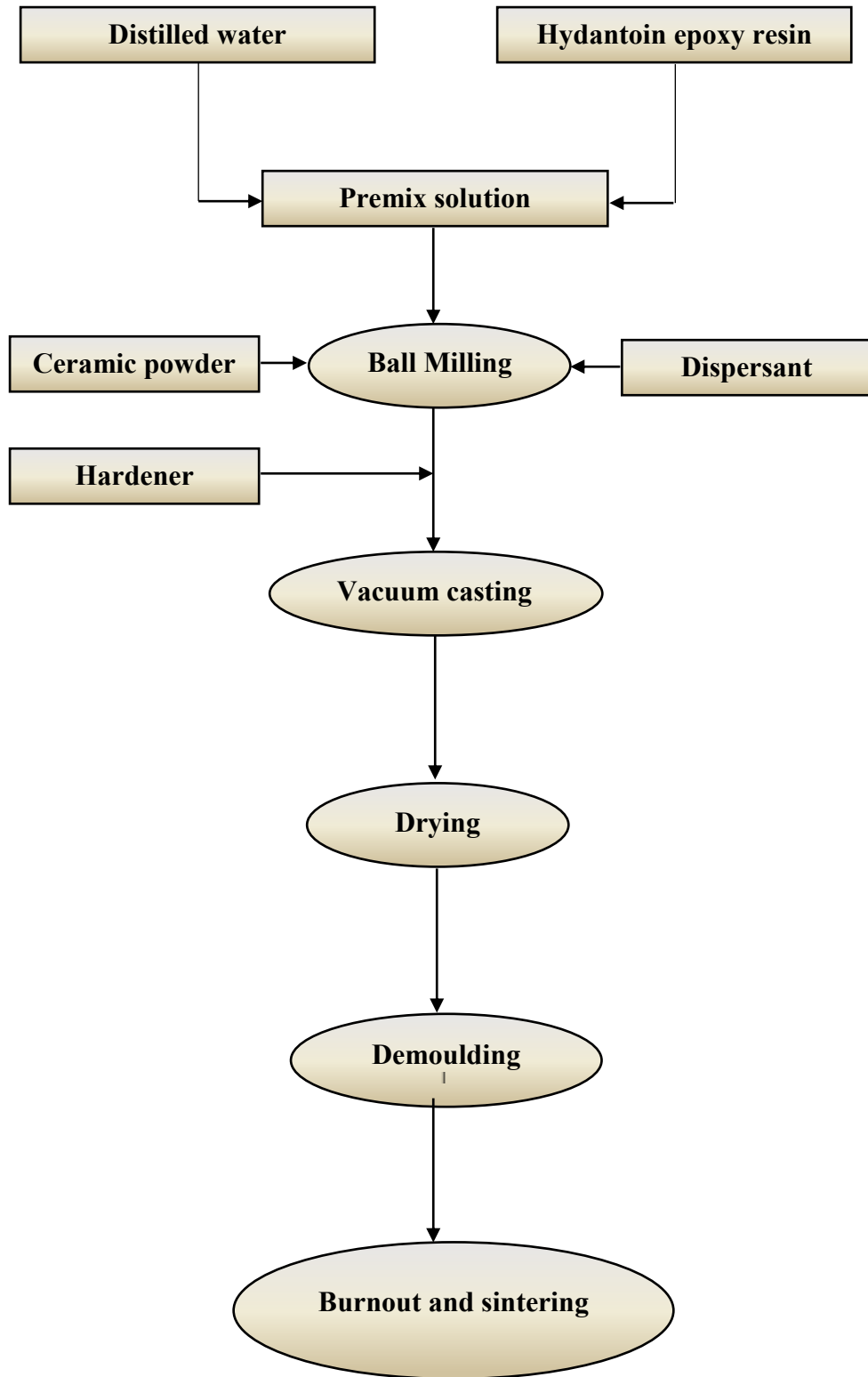


Figure 5.5 Flow chart of the key materials and steps of piezoelectric ceramic gel casting.

### **5.1.3 Lead based and lead free 1-3 random piezocomposite fabrication**

#### **5.1.3.1 Gel casting slurry preparation, de-airing, casting and drying**

For the fabrication of 1-3 piezocomposites, the PZT and 50 BCZT powders with mean particle size approximately 1.2-1.3  $\mu\text{m}$  were used as the ceramic materials. The preparation of the slurries was the same as used for the preparation of the bulk PZT and 50BCZT samples described in the previous section. Two steps of de-airing were applied; after adding hardener into the slurry and after casting the slurry into the soft mould. The soft mould for 1-3 composites, which presented a negative structure, were replicated from the randomised design of Si master mould as explained in section 5.1.1. After casting, a flat and clean glass slide was placed on top of the slurry, followed by gentle pressing by hand. The purpose of this was not only to guarantee the slurry had fully filled the mould cavities but also to ensure that the stock layer side and the top surface of ceramic pillars were parallel, for ease of subsequent processing. The bristle block was left upside down until dried properly.

The drying steps were the same as were carried out for bulk PZT and 50BCZT green samples except the initial drying at room temperature was done for 48 hours in order to prevent the pillars from cracking followed by drying at 40°C in the oven for another 24 hours. At this stage the 1-3 composite was carefully demoulded and then dried further by heating from 40°C to 100°C at 1°C/minute and dwelled for 1 hour.

One of the critical process steps for gel casting is demoulding. It is very dependent on the skill and experience of the operator, and proved particularly difficult with the randomised ultrafine scale structures of ceramic segments produced in this work. After the glass slide was removed from the bottom of the 1-3 composite, the stock

side of the casting was positioned on a new glass slide (right side up), and then the soft mould was slowly peeled away from the bristle block green body.

### 5.1.3.2 Organic burnout and sintering of green samples

The burnout and sintering processes for both PZT and 50BCZT bristle block samples followed the same programmes as were used for the bulk ceramics. However, care had to be taken for the sintering of the PZT bristle blocks, in order to prevent the contamination of doped sand in the fragile structure, especially between ceramic segments. Each PZT bristle block was put on a small alumina substrate with the pillars facing upwards, surrounded by an alumina ring and covered with a small alumina lid before the whole assembly was buried in the doped sand, as shown in Figure 5.6. For 50BCZT bristle block samples, samples were put in the furnace on a substrate with the pillars facing upwards and using the same sintering programme as for the bulk materials.

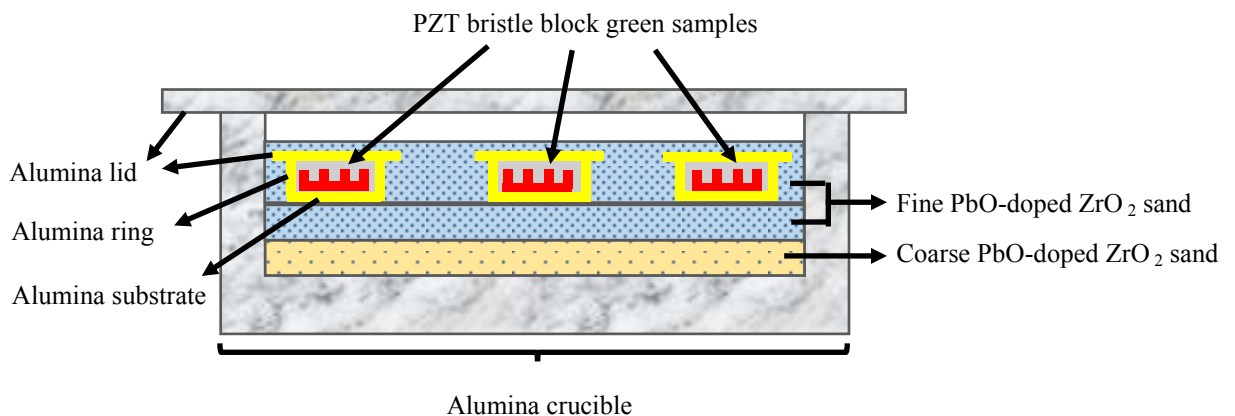


**Figure 5.6 Schematic illustration of setup used for the burnout and sintering of the PZT gel cast bristle block green samples.**

### **5.1.3.3 Encapsulation of bristle block**

After the bristle block was sintered, the vacant spaces between ceramic segments of the bristle block were filled with the Epofix epoxy (Struers, UK) by an encapsulation technique. A PDMS soft mould with cylindrical cavity approximately 20 mm diameter and 35 mm high was fabricated for use as a container for the encapsulation process. The sintered bristle block sample was placed in the mould cavity, and then the epofix resin which was mixed with the hardener with the weight ratio of 25:3, was slowly poured on top the sintered bristle block. To prevent the entrapment of air bubbles in the samples, assembly was degassed for 20 minutes and then left for 30 minutes at room temperature. Finally, the 1-3 composite was placed in an oven and heated from 40 to 60 °C at 1°C/minute, followed by holding at 60°C for 2 hour. In order to aid the curing of the polymer. The mould was removed from the oven and cooled down to room temperature. Eventually, the fully cured 1-3 composite was ready for lapping.

### **5.1.3.4 Lapping**

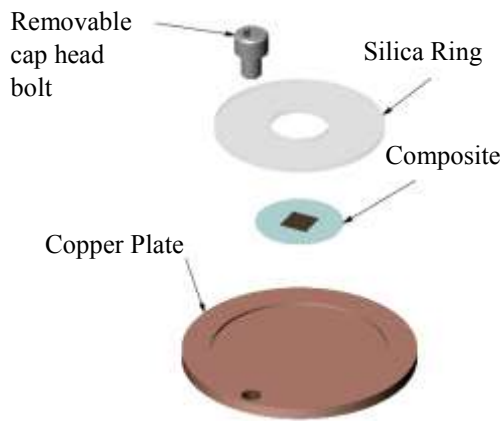
The thickness of the 1-3 composite needs to be matched to the operating frequency of the transducer, and the composite should be flat with the two major faces parallel to each other. This was achieved by a lapping process using a MP5 lapping machine (Logitech, Glasgow, UK). The process enables precise lapping to a precise thickness by using suspensions that were mixed from a range of alumina lapping media, distilled water and ethanediol. Initially a suspension of 9 µm alumina was used to remove the meniscus and excess Epofix resin on the stock side of the 1-3 composite. After the meniscus and excess Epofix were removed, the sample was turned over and

lapped from the stock side to expose the pillars by using a suspension of 3  $\mu\text{m}$  alumina, then turning the sample over and lapping from the other side until the thickness reached 200  $\mu\text{m}$ , then the sample were lapped to the required thickness by using a suspension of 1  $\mu\text{m}$ .

#### **5.1.3.5 Contact and non-contact poling**

Typically, a contact poling method using an oil bath is used for almost all piezoelectric ceramics. However, high frequency 1-3 composites are very thin (approximately 50  $\mu\text{m}$ ) and the surface might be scratched by the top of the contact pin. In order to avoid such defects, a non-contact poling method was adopted using a custom made corona poling machine, which can be carried out before electrodes are applied. The corona poling machine and assembly for holding the composite in place is shown in Figure 5.7.

A high voltage (30 kV) was applied to the copper pin to create the corona discharges in an insulated chamber. The copper plate was utilised as a ground electrode and provided the required temperature via a heater plate in the base of the equipment. The composite was placed on the plate and covered by a silica ring in order to keep the surface of composite flat and then the copper plate was put in the chamber with its centre below the copper pin to ensure that the corona discharge covered the whole sample. For the PZT composites, samples were pre-heated to 110°C whereas the 50BCZT composites were pre-heated to 80 °C, followed by poling at 30 kV for 10 minutes. After leaving for 10 minutes, the temperature of PZT and 50BCZT composites were slowly reduced to 50°C and 25°C ,respectively, using a fan, with the 30 kV still applied.



(a)



(b)

**Figure 5.7 (a) The assembly of the composite on the copper plate using a silica ring to flatten the surface of the composite (b) The custom corona poling equipment used for non-contact poling of PZT and 50BCZT 1-3 composites.**

Contact poling in silicone oil was used to re-pole some of the 50BCZT 1-3 composites. An applied electric field of 3kV/mm at 80°C was applied for 10 minutes, following which the temperature was slowly decreased to 25°C and then the voltage was gradually decreased to zero. The sample was gently removed from the contact pin and removed the excess oil on the sample surface by submerging in 2-propanol for 20 seconds and then in distilled water for 20 seconds.

### **5.1.3.6 Electroding**

The composites were placed on a glass slide and a 2x2 mm square kapton film mask with a small tail created by laser cutting was placed on top, as shown in Figure 5.8, in order to allow only the active area of 1-3 composite to be electroded and also prevent shorting through holes between two surfaces caused by any air bubbles trapped in the epoxy during encapsulation. The small tail was created as a holding

area for carrying the composite and to avoid scratches from the impedance analyser contact pin during impedance measurement.

The glass slide with the composite and mask on top was electroded in a Peltier cooled sputter coater (Emitech K575, Emitech Ltd., UK) by depositing 1 cycle of target A (Cr with 10 nm at 100 mA), followed by 2 cycle of target B ( Au with 80 nm layer at 80 mA), each cycle was set at 2 minutes. After complete electroding one side of composite, the composite was turned over to electrode the side using the same procedure.



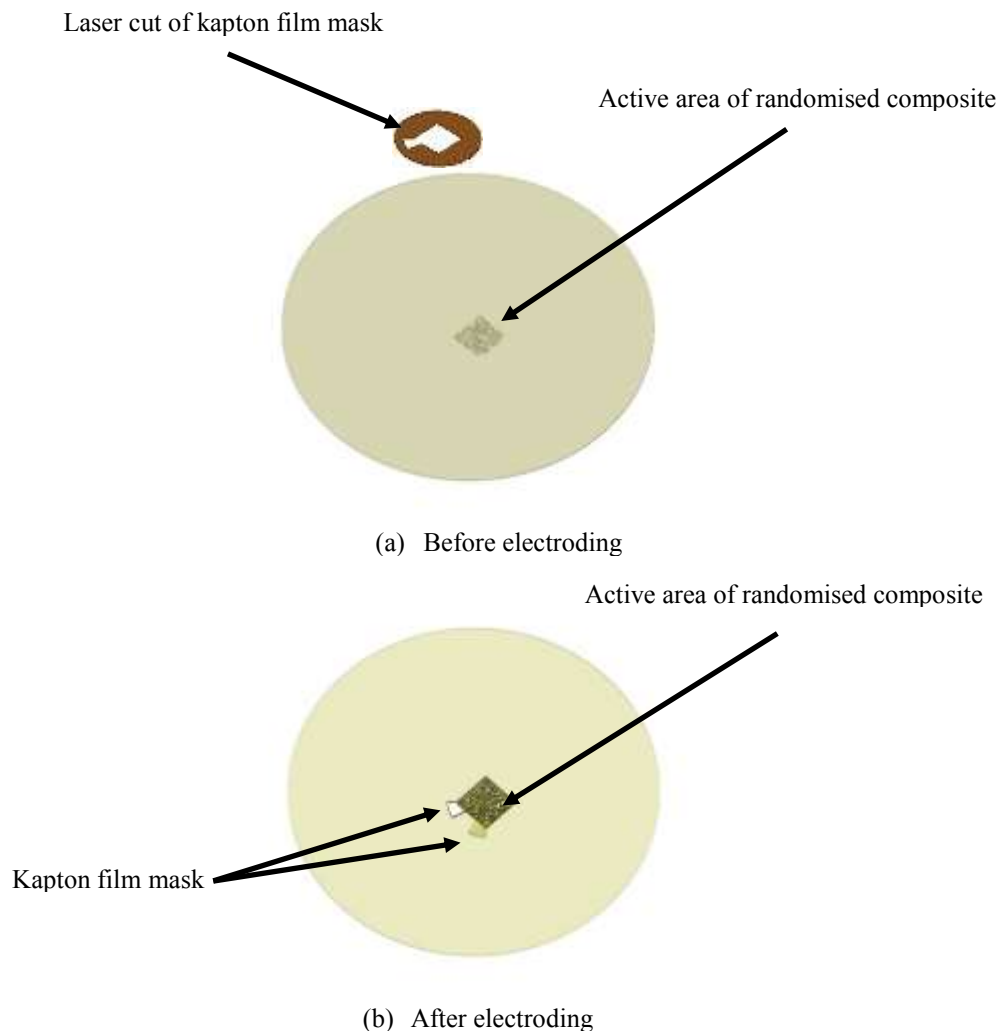


**Figure 5.8 Schematic illustration of electroding of 1-3 composite by using polycarbonate mask with tail.**

The complete fabrication procedures for a 1-3 composite, including the PDMS soft mould replication, slurry casting, PDMS peeling, composite encapsulation and electroding are presented in Figure 5.9. As a final step, after characterisation, composites to use for transducer fabrication were cut into 1.6 mm diameter circular discs. This was carried out in the Machining Center Mechanical Engineering, University of Birmingham.

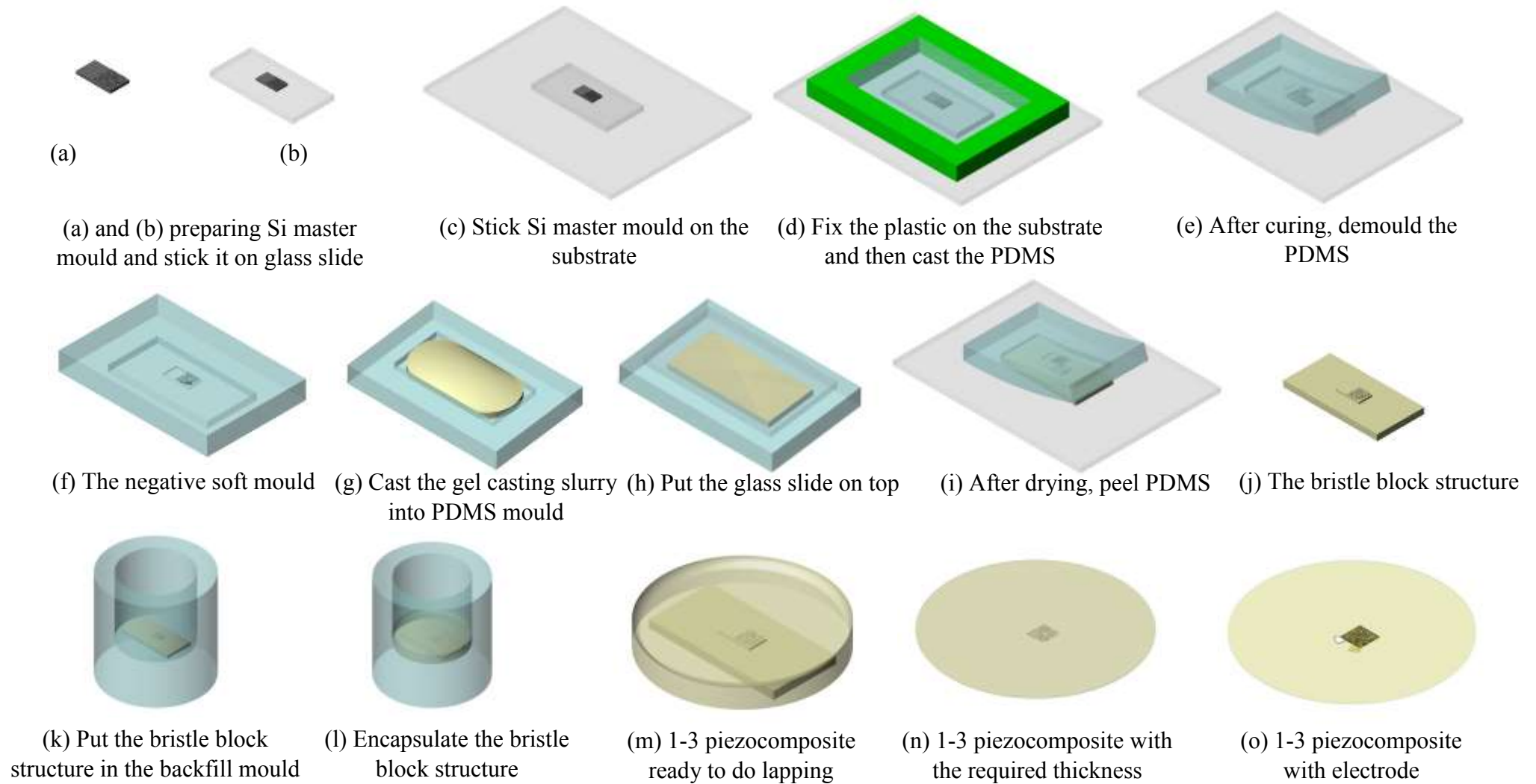


**Figure 5.9 Schematic illustration of the fabrication process of a 1-3 piezocomposite**

## **5.2 Characterisation methods**

### **5.2.1 Characterisation of rheological behaviour**

The rheological behaviour of the premixed solutions and the lead based and lead free slurries were measured using an AR 500 rotational rheometer (TA instruments, USA). The experiments were carried out using a cone and plate geometry with a 40 mm diameter, cone angle 2° and gap 55 µm, rotating against the flat measuring plate. 8-10 drops of the solutions or slurries were dropped on the centre of the measuring plate and then the excess liquid that spread out after the cone reached the required gap was cleaned. The reason for using a cone and plate was for comparison with other people's work in Functional Material Group, University of Birmingham.

#### **5.2.1.1 Elastic storage and viscous loss modulus measurement**

The dynamic oscillation shear tests of premixed solutions and ceramic slurries were measured at the strain of 0.2% and fixed frequency of 1 Hz at different temperatures relative to the elastic storage modulus and viscous loss modulus ( $G'$  and  $G''$ , respectively).

#### **5.2.1.2 Viscosity measurements**

The effect of dispersant concentrations and amount of resin on the flowability of the ceramic slurries were investigated by viscosity measurements. The slurries were pre-sheared for 10 seconds before measuring the shear mode with the speed of deformation (shear rate) in the range 0.1-600 s<sup>-1</sup> at 20°C. The effect of resin content on the gelation time of the ceramic slurries were investigated by measuring the change in viscosity at a shear rate of 0.1 s<sup>-1</sup> at 20°C.

### **5.2.2 Specific surface area measurement**

The specific surface area (SSA) of PZT and 50BCZT powders in the as received state and after vibro-milling were measured using a Brunauer–Emmett–Teller (BET) single point nitrogen adsorption (Micromeritics Area ASAP2010c, Norcross, USA).

### **5.2.3 Particle size measurement**

Particle size measurements of the PZT and 50BCZT powders were carried out using a laser diffraction particle size analyser (Sympatec, Bury, UK) with integral ultrasonic bath. Suspensions consisting of 0.5 g of the PZT or 50BCZT powders were prepared using 3 g of distilled water and 2 drops of  $\text{Na}_4\text{P}_2\text{O}_7$  as a dispersing agent. Soft agglomerates can be broken down by ultrasonic vibrations which normally takes about 15 seconds and then the laser beam detected the particles in suspension and scattered the incident light to the lens. Finally, the data of diffraction from the lens created the particle size distribution.

### **5.2.4 Thermal analysis**

TGA and DSC were measured to study the effect of polymer burnout on weight loss of gel cast samples using a NETZSCH simultaneous thermal analysis (STA 449C Jupiter). The samples (approximately 15 mg) were measured in an alumina crucible in an air atmosphere at a heating rate of  $5^\circ\text{C}/\text{minute}$  to  $600^\circ\text{C}$ .

### 5.2.5 Density measurement

The density of the green and sintered bulk samples of PZT and 50 BCZT were measured based on Archimedes principle. The following formula was used for the density calculation.

$$\rho = \frac{w_d}{w_d - w_w} \quad \text{Equation 5.1}$$

where  $\rho$  is a density

$w_d$  is the dry weight of the sample

$w_w$  is the weight of the sample in water.

### 5.2.6 Drying and sintering shrinkages

The drying shrinkage of gel cast bulk samples was calculated from measurements of the diameter of the soft mould and the dried samples after demoulding using the following equation;

$$LD = \frac{D_M - D_d}{D_M} \times 100 \quad \text{Equation 5.2}$$

where  $LD$  is the drying shrinkage

$D_M$  is the diameter of soft mould

$D_d$  is the diameter of the gel cast sample after complete drying

The sintering shrinkage of the gel cast bulk samples carried using the same basis but the diameter of sample before burnout and sintering and after sintering were measured instead, followed by calculation using the equation as follows;

$$LS = \frac{D_d - D_s}{D_s} \times 100 \quad \text{Equation 5.3}$$

where  $LS$  is the sintering shrinkage

$D_d$  is the diameter of dried sample

$D_s$  is the diameter of the gel casting sample after sintering

All measurements were carried out to 0.01 mm using precision digital calipers. 3 measurements of each sample was made and an average taken.

### 5.2.7 Green strength measurement

The flexural strength of green PZT and 50BCZT were measured in order to study the influences of the resin concentration on the green strength. Test bars (45 mm length, 4 mm width and 3 mm thickness) were fabricated by casting the slurries into appropriate PDMS soft moulds and, after complete drying (see section 5.1.2.2), bars were tested in three point bending an Instron testing machine (Instron, Buckinghamshire, UK) with the span length of 50 mm and crosshead speed of 1 mm/minute. The flexural stress  $\sigma_f$  of rectangular cross section can be calculated as a following equation;

$$\sigma_f = \frac{3PL}{2bd^2} \quad \text{Equation 5.4}$$

where  $P$  is fracture load

$L$  is the span length (distance between support pins)

$b$  is the width of rectangular bar

$d$  is the thickness of rectangular bar

For each test condition 20 bars were tested and averages and standard deviations calculated.

### 5.2.8 Dielectric and Piezoelectric property measurements

The impedance magnitude, phase and capacitance of the PZT and 50BCZT composites and high frequency transducers were measured using an Agilent 4294A impedance analyser (Agilent Ltd, UK) with a frequency range of 40 Hz-110 MHz. The capacitance was measured at 1 kHz and  $2f_a$  for low and high frequency samples respectively. The electromechanical coupling factor, planar-extensional mode ( $k_p$ ), thickness-extensional mode ( $k_t$ ) and relative permittivity at constant stress ( $\epsilon^T$ ), at constant strain ( $\epsilon^S$ ) were calculated by using the value of parameters from each sample along the active area and thickness using the equation as follows;

$$k_p = \sqrt{\left(2.51 \cdot \frac{f_a - f_r}{f_r} - \left(\frac{f_a - f_r}{f_r}\right)^2\right)} \quad \text{Equation 5.5}$$

$$k_t = \sqrt{\frac{\pi}{2} \cdot \frac{f_r}{f_a} \cdot \tan\left(\frac{\pi}{2} \cdot \frac{f_a - f_r}{f_a}\right)} \quad \text{Equation 5.6}$$

$$\epsilon^T = \frac{C_L h}{A \epsilon_0} \quad \text{Equation 5.7}$$

$$\epsilon^S = \frac{C_h h}{A \epsilon_0} \quad \text{Equation 5.8}$$

The  $d_{33}$  was measured using  $d_{33}$  meter model YE2730A with the range of 10 to 2000 pC/N (Sinocera, China). 5 samples for each composition were measured and 3 measurements were made on each sample.

### 5.2.9 X-ray diffraction analysis

As-received PZT and 50BCZT powders and sintered discs were measured on X-ray diffractometer (Equinox 3000, Intel Inc, Artenay France) using Cu-K $\alpha$ 1 radiation with wavelength 1.54056 Å and  $2\theta$  between 15-90. The intensity spectra were

analysed by using the Match software with PDF-2 data base (ICDD : International Centre for Diffraction Data - JCPDS : Joint Committee on Powder Diffraction Standards, copyright 2004, Newton Square, USA).

### **5.2.10 Microstructure characterisation**

#### **5.2.10.1 Optical microscopy**

During the lapping process the ceramic pillars of the 1-3 composites were observed using a confocal scanning laser microscope (OLS3100/3000, Olympus, UK) to ensure that the pillars were exposed. Image J software was used for analysis the volume percentage of ceramics in each 1-3 composite. To aid fabrication of the high frequency transducers, an optical microscope (RZ, Meiji Techno microscopy, UK) were used, combined with digicam control software.

#### **5.2.10.2 Scanning electron microscopy and environmental scanning electron microscope**

The morphology of material powders, ceramic bulks, 1-3 composites were studied using a scanning electron microscope (JSM6060, Jeol, Tokyo, Japan) and an environmental scanning electron microscope (XL30, Philips, Amsterdam). For grain size observation, the sintered samples were polished then thermal etched at 150 °C below sintering temperature for 10 minutes using heating and cooling rate of 600°C/hour. The samples for testing were attached to an aluminium stub using a carbon adhesive disc A Peltier cooled sputter coater (Emitech K575, Emitech Ltd., UK) was used for gold coating the sample surface at 80mA for 2 minutes.



## 5.2.11 Transducer testing

### 5.2.11.1 B-scan testing

- *Tungsten wire scanning*

The resolution of focused and unfocused transducers fabricated in this work were carried out in the Systems Power and Energy Group at the University of Glasgow. A high frequency scanning system consisting of a computer controller, a pulser/receiver (DPR/500, JSR Ultrasonics, UK), remote pulse box (JRS RP-H2, Ultrasonics, UK), NI PXIe controller (National Instruments, USA), frame and scanning stage were set up for this measurement as shown in Figure 5.10.

The transducer was placed on the JRS RP-H2 pulse box which was placed on the frame (Thorlabs, UK) in order to minimise vibration during testing. A LabView interface software controlled the system, including the scanning directions, the pulse/receiver and the NI PXIe controller. The motion controller (Motion Link Ltd, UK) controlled the scanning stage with a resolution of 2  $\mu\text{m}$ . The transducer received a pulse from the pulser/receiver and was moved at the same time via the scanning stage. The NI PXIe controller collected and sent all the data to the LabView software and then the data were processed by MATLAB. The basic components and their connections for this measurement are presented in Figures 5.10 and 5.11, respectively. The resolution of the PZT and 50BCZT focused and unfocused transducers were evaluated using the B-scan of 5 x 25  $\mu\text{m}$  diameter tungsten wires. The tungsten wires were submerged in water and each wire was separated by 1 mm and placed on a holder as shown in Figure 5.12. The surface of transducer was submerged in water, keeping the distance between the wires less than the focal length

of the transducer. Scanning of tungsten wires in agar with 8% of 3  $\mu\text{m}$   $\text{Al}_2\text{O}_3$  particles was done with the same basic set up, except using 100, 200 and 200  $\mu\text{m}$  diameter wires, respectively, as shown in Figure 5.13.

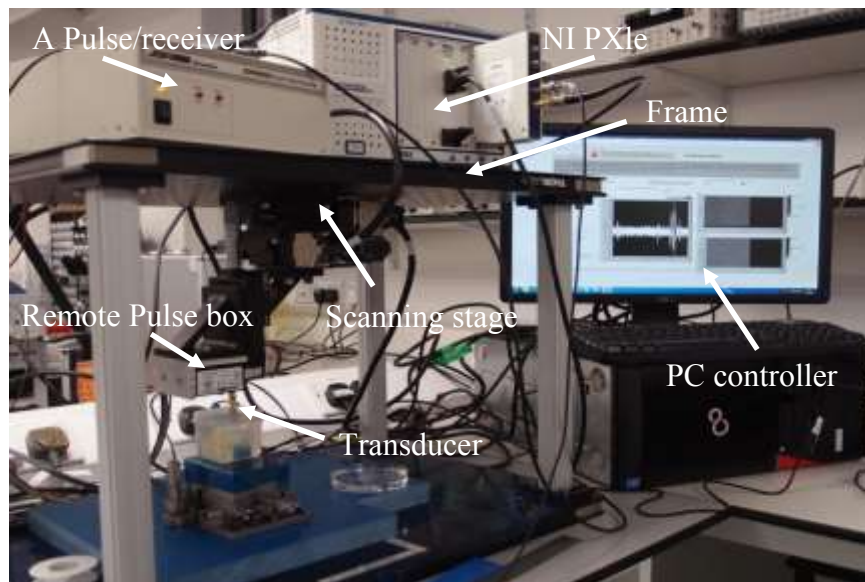


Figure 5.10 Photograph of the scanning system.

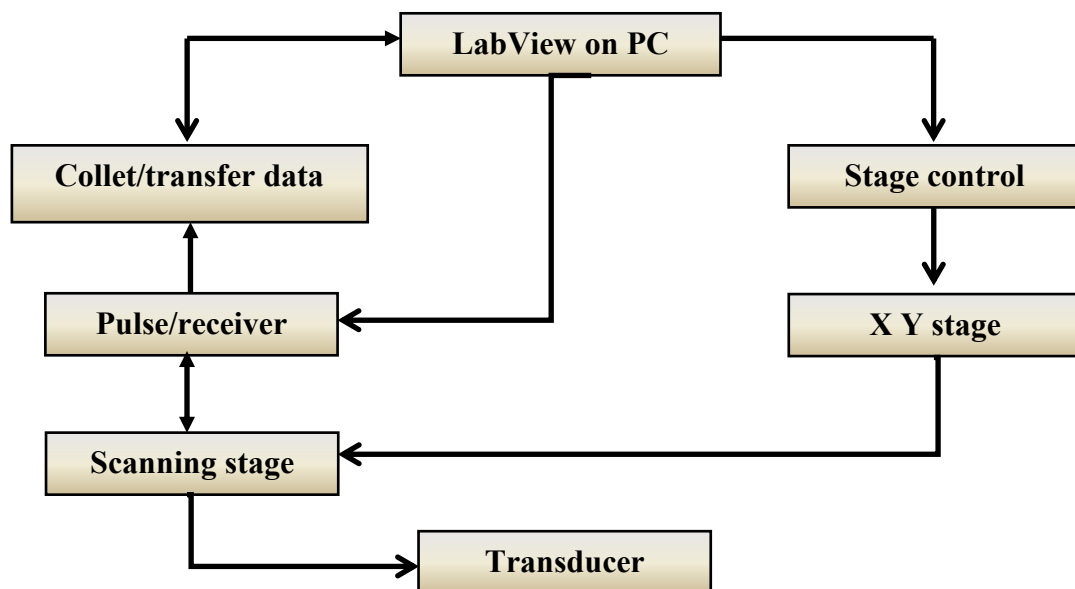
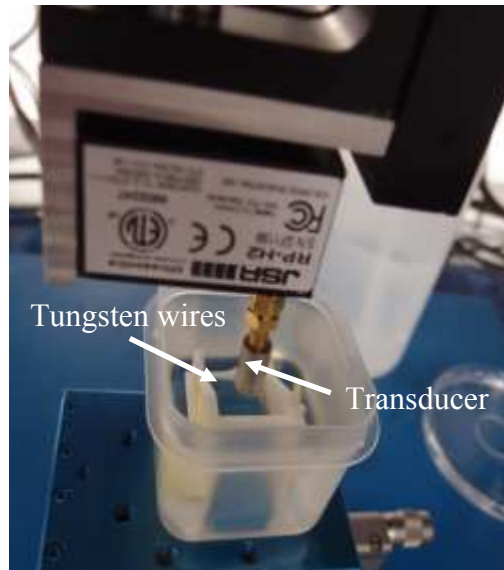
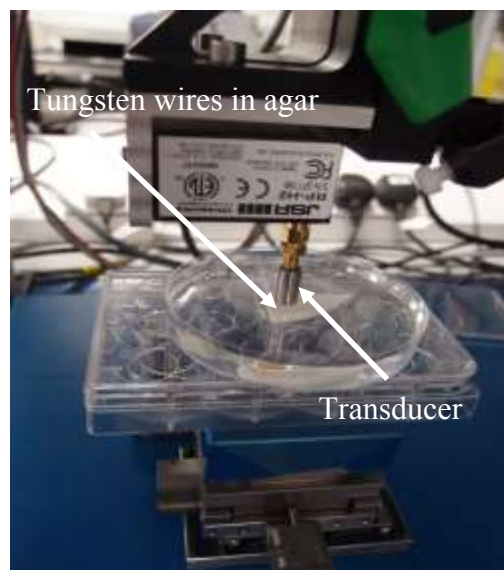


Figure 5.11 Schematic diagram of the component connections of the scanning system.



**Figure 5.12** Photograph of experimental set up for the B-scan of Tungsten wires.



**Figure 5.13** Photograph of the experimental set up for the B-scan of Tungsten wires in agar 8%  $\text{Al}_2\text{O}_3$ .

- *Tissue scanning*

The real time capabilities of the lead based and lead free focused transducers for medical imaging applications were tested by tissue scanning in the Clinical Research Centre Tayside at the University of Dundee. A 2.5 mm thick cross section of pig bowel in the area of serosa was adopted as the target. The pig bowel was pinned onto a flat agar surface which was then placed on top of an absorber and submerged into a phosphate buffered saline solution (PBS) at pH 7.4. The surface of the transducer was lower down into the PBS solution and placed perpendicular to the tissue surface, as shown in Figure 5.14. All experiments were done based on the same system for tungsten wire scanning, carried out at 37°C, with the scanning distance 20 mm from the tissue.

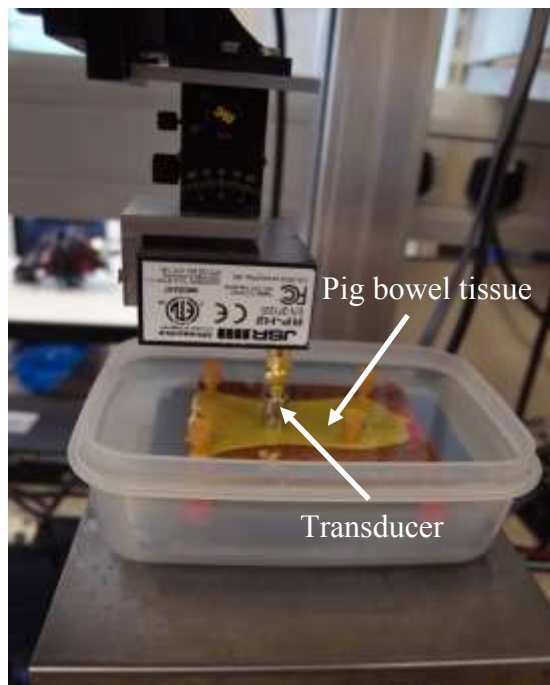


**Figure 5.14** Photograph of focused transducer and pig bowel tissue placed for B-scanning.

### 5.2.11.2 Pulse and echo testing

For pulse-echo measurements of the focussed and unfocussed transducers, a flat quartz block with 5 mm thickness was used as the echo target. The surface of the transducer was submerged vertically into the water. The echoes from the target were input into a Fast Fourier Transformation (FFT) to create frequency spectra from which the bandwidths of each transducer were calculated.

## 5.3 References

1. Jiang, Y., *Fabrication and characterisation of novel ultrasound transducers*, in *School of Metallurgy and Materials*. 2013, University of Birmingham.
2. Wisser, F.M., et al., *Precursor strategies for metallic nano- and micropatterns using soft lithography*. *Journal of Materials Chemistry C*, 2015. **3**(12): p. 2717-2731.
3. *High Performance soft PZT*. [Last accessed 23/09/2017]; Available from: <http://www.trstechnologies.com/Materials/High-Performance-PMN-PT-Piezoelectric-Single-Crystal>.
4. Xie, R., et al., *Gelcasting of alumina ceramics with improved green strength*. *Ceramics International*, 2012. **38**(8): p. 6923-6926.
5. Jiang, C., et al., *Gelcasting of aluminum nitride ceramics using hydantion epoxy resin as gelling agent*. *Ceramics International*, 2013. **39**(8): p. 9429-9433.
6. Mao, X., et al., *Rheological characterization of gel casting system based on epoxy resin*. *Ceramics International*, 2009. **35**: p. 415-420.
7. Janney, M., et al., *Gelcasting*. *The handbook of ceramic engineering*, 1998: p. 1-15.
8. Su, B., T. Button, and C. Ponton, *Control of the particle size and morphology of hydrothermally synthesised lead zirconate titanate powders*. *Journal of materials science*, 2004. **39**(21): p. 6439-6447.
9. Cochran, S., et al., *Net-shape ceramic processing as a route to ultrafine scale 1-3 connectivity piezoelectric ceramic-polymer composite transducers*, in *2004 IEEE Ultrasonics Symposium, Vols 1-3*, M.P. Yuhas, Editor. 2004. p. 1682-1685.

# **Chapter 6 Optimisation of the lead free gel casting process**

## **6.1 Introduction**

One of the main aims of this thesis is to fabricate lead free high frequency transducers for ultrasound medical imaging. 1-3 composites were chosen as the active material for the transducers, and utilising the gel casting process to fabricate the bristle-block structure. 50BCZT powders and hydantoin epoxy resin were selected as the main materials for gel casting system as 50BCZT powders have been reported to possess good piezoelectric properties, while hydantoin epoxy resin was reported to have high water solubility, low toxicity, low cost and crystallise at ambient temperatures to provide high green strength green bodies as mentioned in Chapter 3.

The optimisation of the key parameters and compositions for the gel casting method have been studied, starting with the premix solution, including hardener content, gelation time and temperature. The influence of the key compositional variables for producing slurries including dispersant and resin concentration and % volume solids loading on working time and viscosity were studied in order to optimise the slurry compositions that provided the best flowability. Before fabricating the micro bristle block structure, a range of lead – free gel casting slurries were cast into PDMS soft moulds with bulk and bar shapes in order to study the microstructure and the series properties of samples in green and sintered stage including shrinkage, green density,

green strength, dielectric, piezoelectric and functional properties as the initial datum for further steps. The results are presented and discussed in this chapter.

## **6.2 Polymerisation of the premix solution**

### **6.2.1 Influence of hardener content on the premix solution**

In this gel casting system, a ring-opening reaction is the main polymerisation mechanism that takes place between the epoxide groups of the epoxy resin and active hydrogen atoms of the amine hardener in order to achieve the bonding between epoxy resin and amine. In the hydantoin epoxy system used in this work, the epoxy-amine curing occurred by HN, NH<sub>2</sub> and NH<sub>2</sub> groups at the end of Bis(3-aminopropyl) amine hardener opening the epoxide ring of the hydantoin epoxy resin [1] as mentioned in section 3.4.5. The stoichiometric ratio between amine hardener and epoxy resin of the amine hardener need to be calculated in order to ensure the stability of the curing mechanism [2, 3]. Hydantoin epoxy resin has an Equivalent Epoxide Weight (EEW) of around 139 g/eq this means 139 g of epoxy contains one mole of reactive epoxy group while Bis (3-aminopropyl) amine hardener has 5 functional hydrogen atoms per molecule and acts with molecular weight 131 g/mol; therefore, the Amine Hydrogen Equivalent Weight (AHEW) of this amine hardener is 26.2 g/eq. This means that in theory that hydantoin epoxy resin with 139 g/eq needs to be mixed with an amine hardener with an equivalent weight of 26.2 g/eq in order to completely react with no unreacted amine hardener or epoxy resin remaining. Hence, the amount of hardener needed per hundred grams of epoxy resin (Parts Per Hundred Resin or PHR) is 18 g. This implies that the complete reaction can be done by using 1 g of epoxy resin per 0.18 g of amine hardener, the amount of

hardener larger or smaller than this will cause excess amine and excess epoxy resin, respectively. Figure 6.1 presents the elastic modulus  $G'$  and viscous modulus  $G''$  of 20 wt% hydantoin epoxy resin premix solutions with hardener PHR 12 g - 50 g during polymerisation as a function of time at 40°C. The elastic modulus increased with increasing hardener and most of premix solutions exhibited a plateau region which corresponds to the strength of gel. The highest elastic modulus value of 175,900 Pa can be achieved by increasing the hardener to PHR 18 which corresponds to the stoichiometric ratio of amine hardener and epoxide group as mentioned above. This means by using this stoichiometric ratio, a network of interconnected rings occurred between all amine epoxide groups and all amine active hydrogen atoms were linked with a high degree of crosslinking. At a hardener PHR = 12 g, the maximum  $G'$  value of only 10,780 Pa is obtained after 1 hr, and the gel was being formed after 31 minutes. However, within 1 hr a  $G'$  plateau region was not detected, which implied that the gel was not completely formed in this time as there was insufficient amine hardener to react with epoxide groups. At the hardener addition of PHR = 25 g and 37 g, the plateau regions were slightly lower than for PHR = 18 g and reached peak values of 156,100 Pa and 72,330 Pa, respectively. Further increase of the hardener concentration to PHR = 50 g, resulted in the  $G'$  value decreasing to a plateau region of around 10,360 Pa. As shown in Figure 3.17, there are three main crosslinking reactions that involve the ring open reactions between amine hardeners and epoxide groups. Generally, the primary reaction dominates the initial curing and offers only the linear structure. Therefore, in these three amine-rich systems, there is a strong possibility that the linear structure increases and the network of interconnected rings do not start until the epoxide groups were reacted with



secondary amine. However, there were insufficient epoxide groups resulting in increase of unreacted secondary amine and decrease in the amount of cross-linking. This led to the decrease of  $G'$  [4]. It can be observed in Figure 6.1 (b) that the viscous response also increases with increasing hardener and the highest  $G''$  can be obtained at the stoichiometric ratio. Thus the largest concentration of interconnected rings between the amine hardener and epoxide groups, leads to an increase in the viscous modulus of this premix system. Figure 6.2 presents the elastic and viscous moduli of premix solution prepared from 20 wt% resin content with hardener PHR = 18 g measured at 40°C. From this figure, an example of the available time for mixing and casting, the gelation time, can be determined by using the crossover point between the two moduli [5]. At the early stage of the curing process, elastic and viscous modulus were observed a low value as the reaction between amine hardener and epoxide group just started. However, it can be observed that at the start  $G''$  dominates while  $G'$  represents the entanglement of polymer chains. As the reaction progresses cross-linking between amine hardener and epoxide groups of premix solution can be observed as both moduli increase sharply when the molecular weight of the polymer chain increased. However, the elastic behaviour became dominant in this stage due to the increasing of cross-linking from the ring opening reaction. Finally, the plateau regions of the elastic and viscous moduli can be observed when the ring open reaction has completed. From an example of crossover point between the elastic and viscous moduli, the gelation time at 40 °C for 20wt% epoxy resin premix solution with hardener concentration PHR = 18 g was 14 minutes, while the gelation time for other premix solutions studied at various hardener concentrations are presented in Table 6.1.

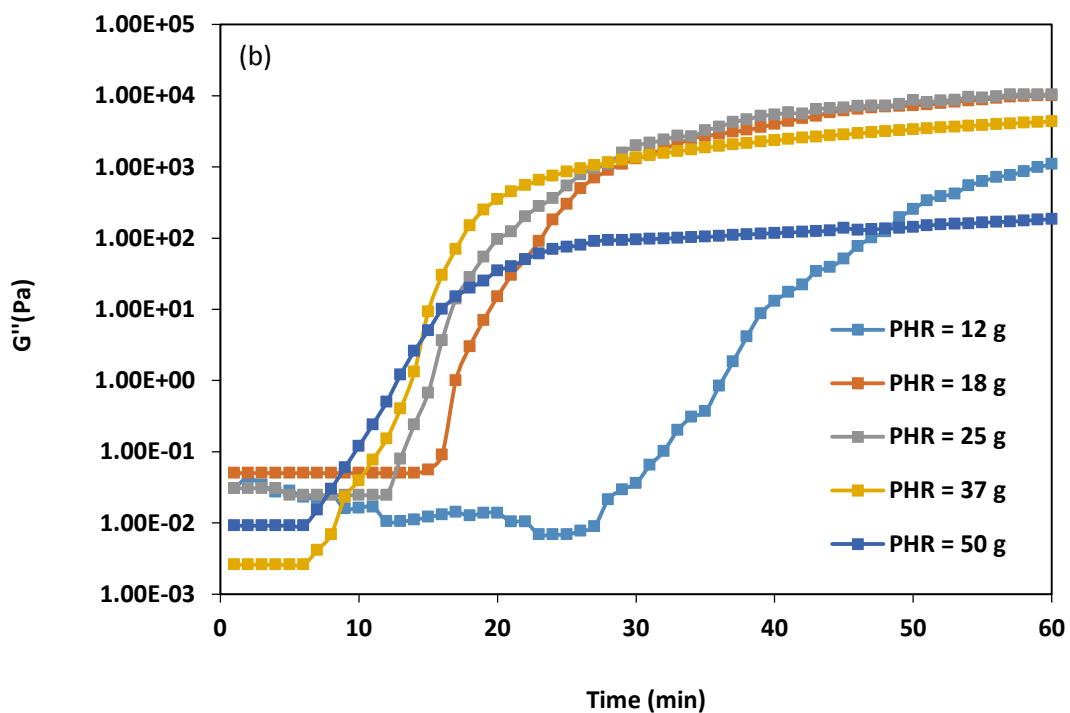
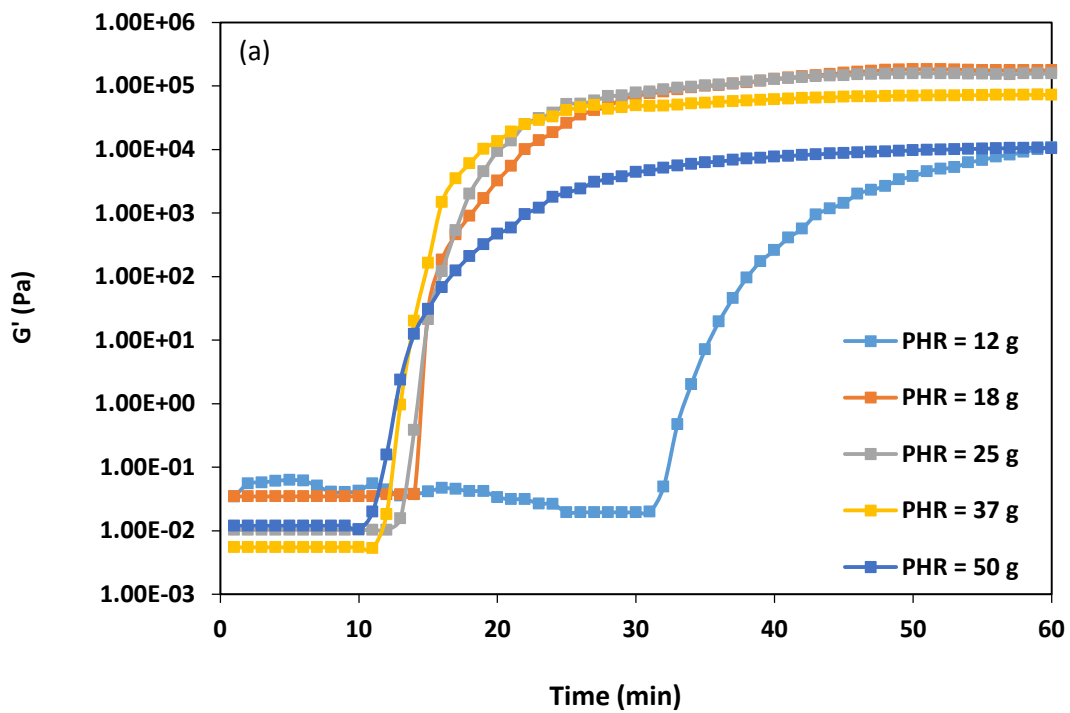


Figure 6.1 (a) Elastic modulus  $G'$  and (b) viscous modulus  $G''$  of 20 wt% hydantoin epoxy resin content premix solutions cross-linked with various hardener contents at 40°C.

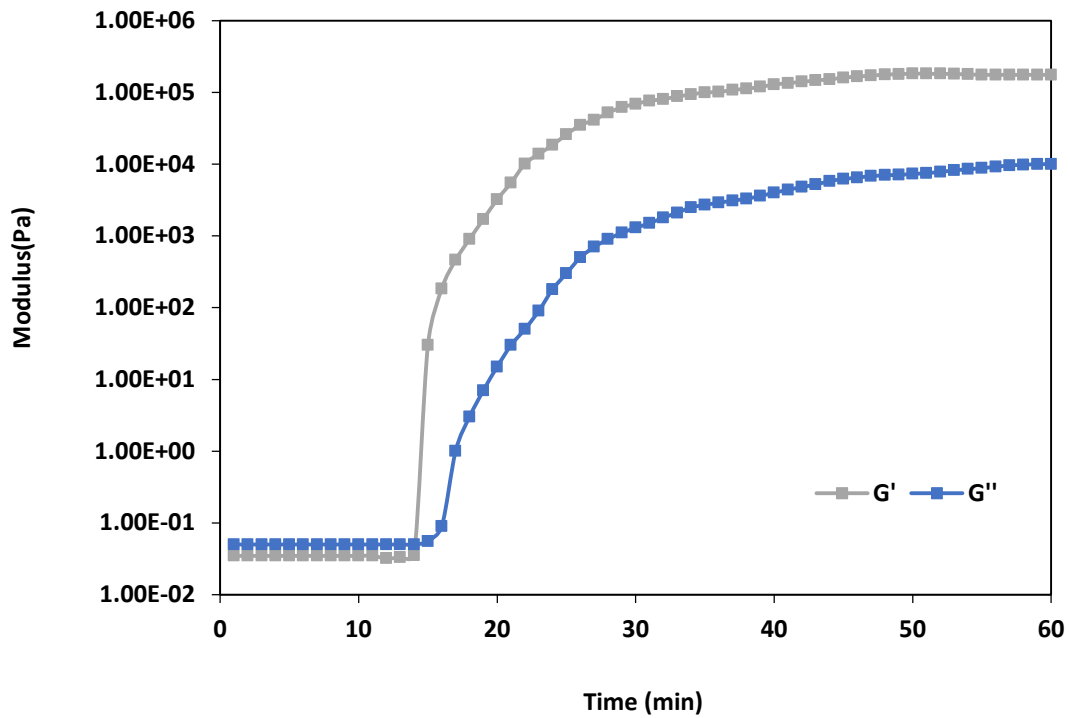


Figure 6.2 Elastic modulus  $G'$  and viscous modulus  $G''$  of 20 wt% hydantoin epoxy resin content premix solutions cross-linked with hardener PHR = 18 g per 100 g of resin at 40°C.

The results show that the available time for mixing and casting is shortened with increasing amine hardener concentration due to the increase in the concentration of amine active hydrogen atoms to create the ring open reaction. An alternative criterion to the crossover point is monitoring the time corresponding to the abrupt change of  $G'$  for the slurries [6, 7]. Using this criterion the gelation time for hardener concentration with PHR = 12, 18, 25, 37 and 50 g would be obviously shortened from 31 to 14, 12, 11 and 10 minutes, respectively.

Table 6.1 Gelation time by crossover criterion of 20wt% hydantoin epoxy resin premix solution cross-linked with various hardener concentration (PHR = 12-50 g per 100 g of resin) at 40 °C.

Hardener concentration (Parts Per Hundred Resin)	12	18	25	37	50
Gelation time at 40 °C (min)	28	14	13	8	6

## 6.2.2 Influence of reaction temperature on premix solution

The gelation behaviour of the premix solution can be controlled by temperature. Figure 6.3 shows the elastic and viscous moduli of premix solutions prepared from 20 wt% hydantoin epoxy resin with hardener concentration PHR = 18 g at various temperatures. It can be seen that the gelation time of both moduli show great dependence on temperature as the gelation time displays a tendency to decrease from nearly 50 minutes to around 5 minutes when the temperature is increased from 20 °C to 50 °C, in agreement with several other reports [1, 7-11]. This means the gelation kinetics or reaction rate for curing can be accelerated by increasing temperature [9, 10]. This relationship can be expressed by an Arrhenius-type equation as shown in Equation 6.1 [1, 12].

$$t_1 \propto \frac{1}{K_r} = A e^{E_a/RT} \quad \text{Equation 6.1}$$

When ( ) is the induction time,  $K_r$  is the reaction rate,  $A$  is the Arrhenius pre-exponential factor,  $R$  is the gas constant  $8.31 \text{ J} \cdot (\text{k} \cdot \text{mol})^{-1}$ ,  $E_a$  is the activation energy of the polymerisation reaction and  $T$  is the absolute temperature (K). Figure 6.4 shows the Arrhenius plot calculated from the data obtained from Figure 6.3 (a). It can be seen that the logarithm of the gelation time is inversely proportional to the temperature and the slope of line is equal to the  $E_a/R$ , therefore the activation energy of polymerisation reaction of 20 wt% hydantoin epoxy resin with hardener concentration with PHR = 18 premix solution was calculated value as 82 kJ/mol in good agreement with other reports (47.6, 59.1 and 27.5 kJ/mol) [1, 8-11].

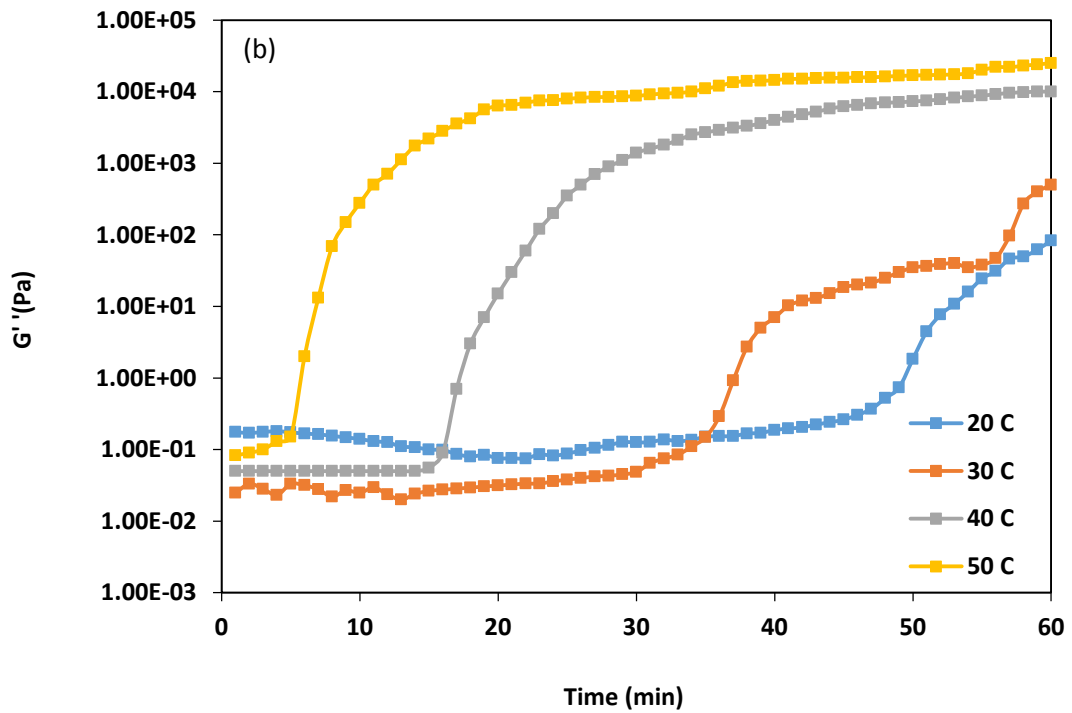
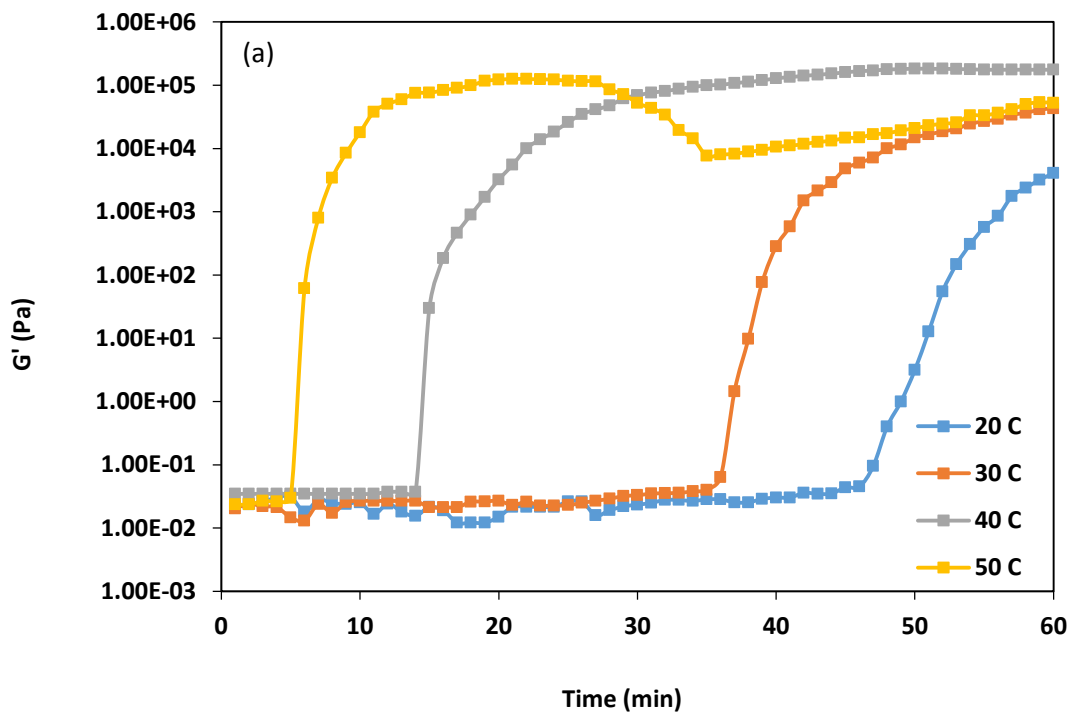


Figure 6.3 (a) Elastic modulus  $G'$  and (b) viscous modulus  $G''$  of 20 wt% hydantoin epoxy resin content premix solutions cross-linked with hardener PHR = 18 g per 100 g of resin measured at various temperatures.

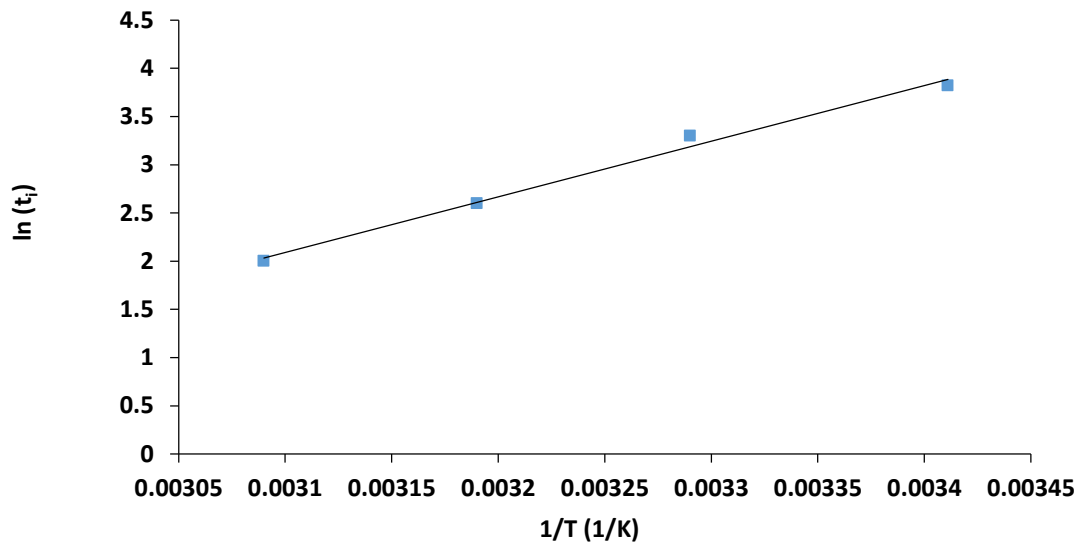


Figure 6.4 Arrhenius plots of data calculated using the gelation time obtained from Figure 6.3 (a), showing that the gelation time is inversely proportional to the temperature.

### 6.2.3 Influence of resin content on the premix solution

Apart from hardener concentration and temperature, resin content also plays a vital role in the elastic and viscous behaviour of the premix solutions. Figure 6.5 shows the elastic and viscous moduli of premix solutions with various resin contents (10-40 wt%) with hardener concentration PHR = 18 g measured at 40 °C as a function of time. It can be observed that both  $G'$  and  $G''$  show great dependence on resin content as the  $G'$  and  $G''$  values increased with increasing resin content. The highest values of  $G'$  and  $G''$  in the plateau region were around 1.57 MPa and 0.025 MPa, respectively for the premix solution with 40 wt% epoxy resin, while the solution with 10 wt% epoxy resin offered maximum values of  $G'$  and  $G''$  of around 16000 Pa and 1250 Pa, respectively. This means the strength of gel after the ring opening reaction can be improved by increasing the resin content. This can be explained by considering the curing reaction of epoxy in the presence of water, which cause

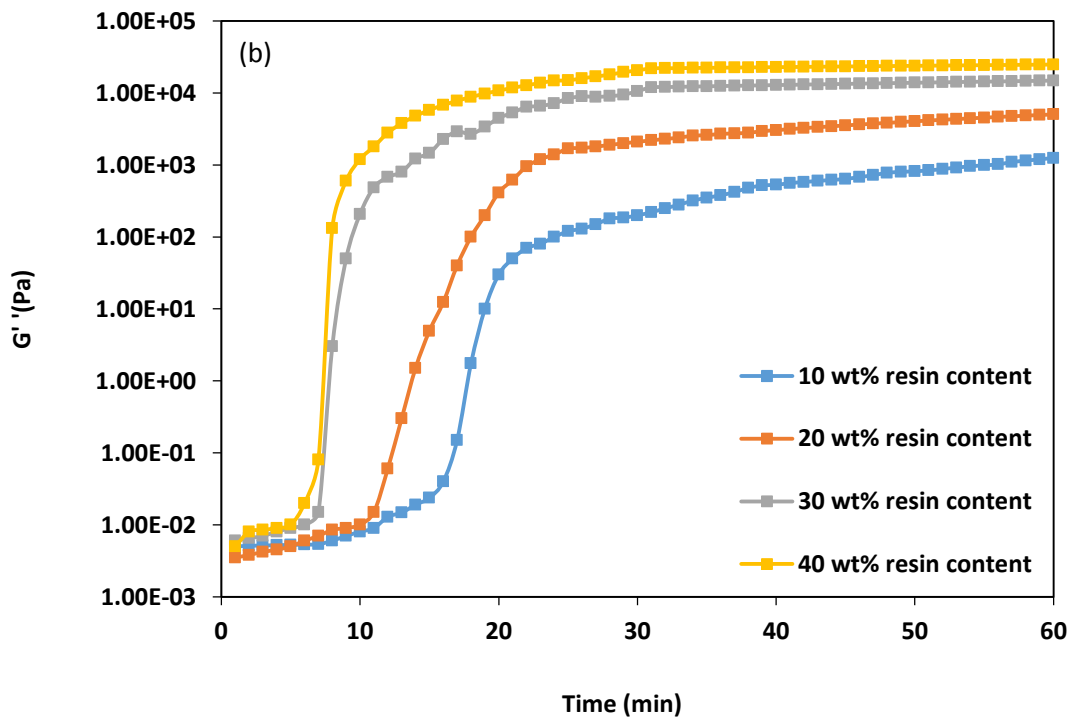
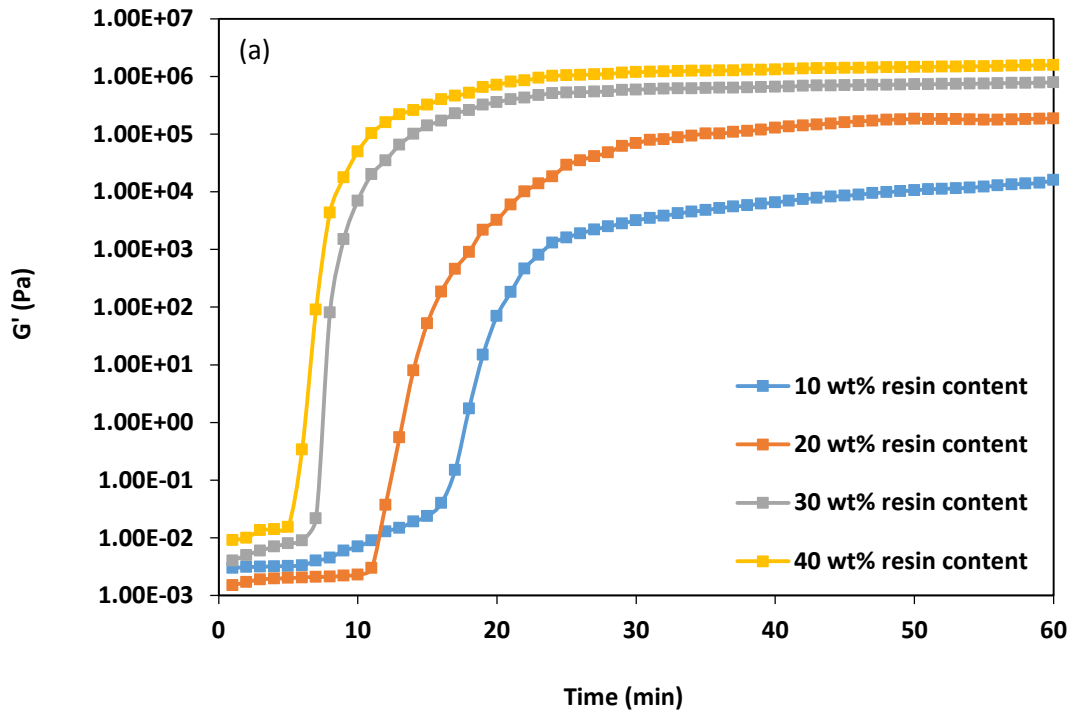


Figure 6.5 (a) The dependence of the elastic modulus  $G'$  and (b) viscous modulus  $G''$  as a function of time for premix solutions with various resin contents cross-linked with a hardener concentration PHR = 18 g at 40 °C.

additional ring open polymerisation reactions through hydrogen bonding, as presented in Figure 6.6. However, it has been reported that bonding and diffusion of molecules of water into the epoxy resin network can occur by two mechanisms. First, some molecules of water diffuse and bond with the epoxy resin by forming hydrogen bonds with hydrophilic functional groups in the epoxy resin. An alternative mechanism is that some molecules of water are retained in the epoxy resin network as free water. Based on the hydrogen bonding between water molecules and epoxy resin, two types of bonding were found and classified into types I and II [13], depending on the activation energy and hydrogen bond complex as shown in Figure 6.7. Generally, type I bonding is the dominant form, possesses lower activation energy and acts only as plasticizer [13, 14] while the amount of type II bonding depends on temperature and time and offers higher activation energy as the presence of water forms multiple hydrogen bonds with the epoxy resin network and creates bridging resulting in additional cross-linking [13]. It has been reported by Wu *et al.* [15] that the presence of a small amount water of in the epoxy and hardener system can increase the ability of polymer chains to move and acts as a catalyst accelerator. However, an increasing amount of water diffuses into the polymer network and acts as plasticizer [14], leading to a lower degree of the curing reaction and decreasing of the cross-linked density [16] and elastic modulus [15]. Therefore, increasing the resin content in the premix solution leads to a reduction in the presence and retention of water that acts as plasticizer in the epoxy/hardener system, resulting in a stronger gel and higher modulus, This is also in agreement with a study of premix solutions with EGDGE epoxy resin at 10 wt% - 40 wt% resin contents reported by Jiang [11]. By using the crossover point between  $G'$  and  $G''$  to determine the gelation time, it can be



observed that the gelation times were obviously shortened with increasing amounts of resin as presented in Table 6.2. These values are in close agreement with those determined by monitoring the time that corresponds to the abrupt increase in  $G'$  of the slurries, where the gelation time decreases from 16, 11, 7 and 5 minutes for increasing resin contents of 10, 20, 30 and 40 wt%, respectively.

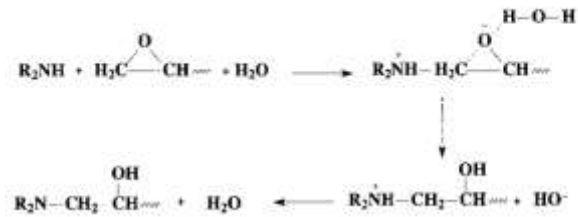


Figure 6.6 The additional ring open polymerisation reaction in the presence of water [15].

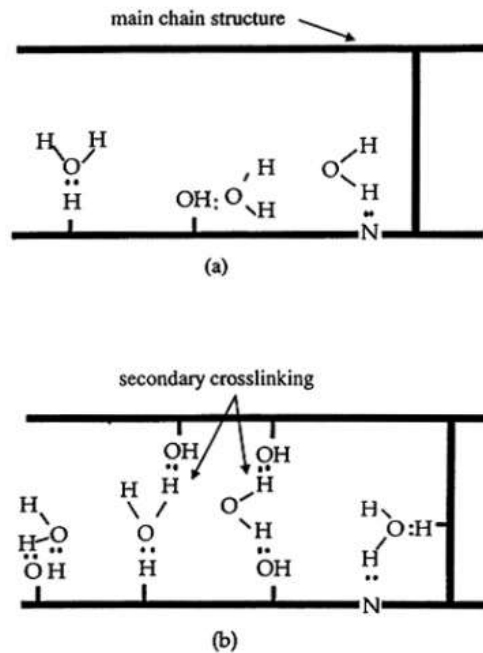


Figure 6.7 The two possibilities of water molecules binding with epoxy resin through hydrogen bonding (a). Type I, single hydrogen bonding between water molecules and epoxy resin. (b) Type II, multiple hydrogen bonds between water molecules and epoxy resin [13].

Table 6.2 Gelation time calculated by the crossover criterion of  $G'$  and  $G''$  for 10 wt%- 40wt% hydantoin epoxy resin premix solutions cross-linked with hardener concentration PHR = 18 g per 100 g of resin) at 40 °C.

Resin content	10	20	30	40
Gelation time at 40 °C (min)	15	13	7	5

## 6.3 Optimisation of lead free powder and slurries

### 6.3.1 Lead free powder characterisation

#### 6.3.1.1 Particle size analysis

As one of the aims of this project is to fabricate fine scale 1-3 composites for high frequency transducers using gel coating and micromould techniques, the choice of the BCZT powder needs to be taken into account in order to achieve an appropriate particle size. The randomised segments for this application require an ultrafine structure. Consequently, the particle size of the 50BCZT powder should be smaller than 2  $\mu\text{m}$  to fully fill the mould cavities [11]. Smaller particles can also increase the sintering efficiency and reduce the sintering temperature due to the higher solid-solid interfacial area and surface energy [17, 18]. However, using small particle size 50BCZT powders can cause the excessive grain sizes and diminish the piezoelectric charge coefficient ( $d_{33}$ ) [19]. From the point of view of mixing the slurry, fine particles not only possess high surface area but also high surface tension. Therefore, small particles have a higher tendency to agglomerate in the slurry, leading to high viscosity and difficulties in achieving a homogeneous slurry [20, 21]. Consequently, the selection of particle size had to be a compromise between these factors and requirements.

50BCZT powders with the average particle size of 3.3  $\mu\text{m}$  were supplied from Central European Institute of Technology (CEITEC). Particle size characterization of the as-received powders revealed a bimodal distribution with the centres of large and small peaks at 0.6  $\mu\text{m}$  and 27.9  $\mu\text{m}$ , respectively as shown in Figure 6.8 (a). After the 50BCZT powders were vibro milled for 7 hrs, the average particle size was reduced

to 0.95  $\mu\text{m}$ . The average particle size can also be calculated by using the specific surface area (SSA) and the density of 50BCZT powders (5.73  $\text{g}/\text{cm}^3$ ) [22] as presented in Equation 6.2 [23, 24] assuming the powders are spherical and nonporous. The SSA of as-received and vibro-milled 50BCZT powders measured by BET single point nitrogen adsorption were 1.5022  $\text{m}^2/\text{g}$  and 2.2022  $\text{m}^2/\text{g}$ , respectively, resulting in the average particle size calculated from Equation 6.2 as 0.70  $\mu\text{m}$  and 0.48  $\mu\text{m}$ , respectively. However, these values did not correspond precisely to the results from the laser diffraction method. This might be due to the non-spherical shape of the powders, inaccuracies between the true and theoretical densities, or some agglomeration.

$$\textit{Average particle size} = \frac{6}{\textit{SSA} \times \textit{density}} \quad \textbf{Equation 6.2}$$

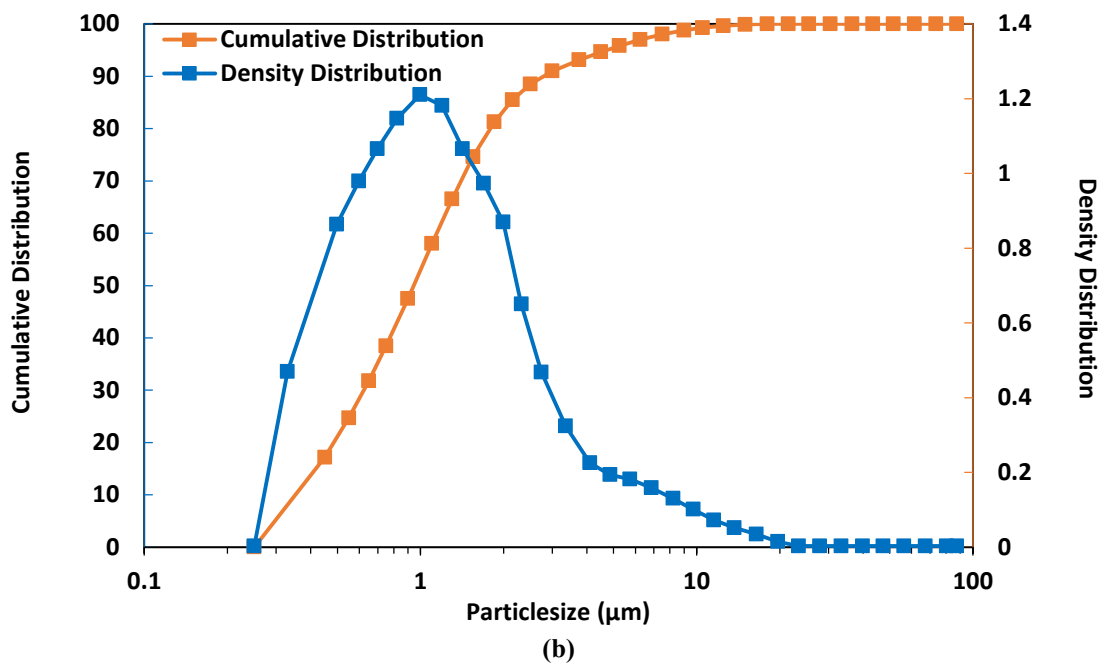
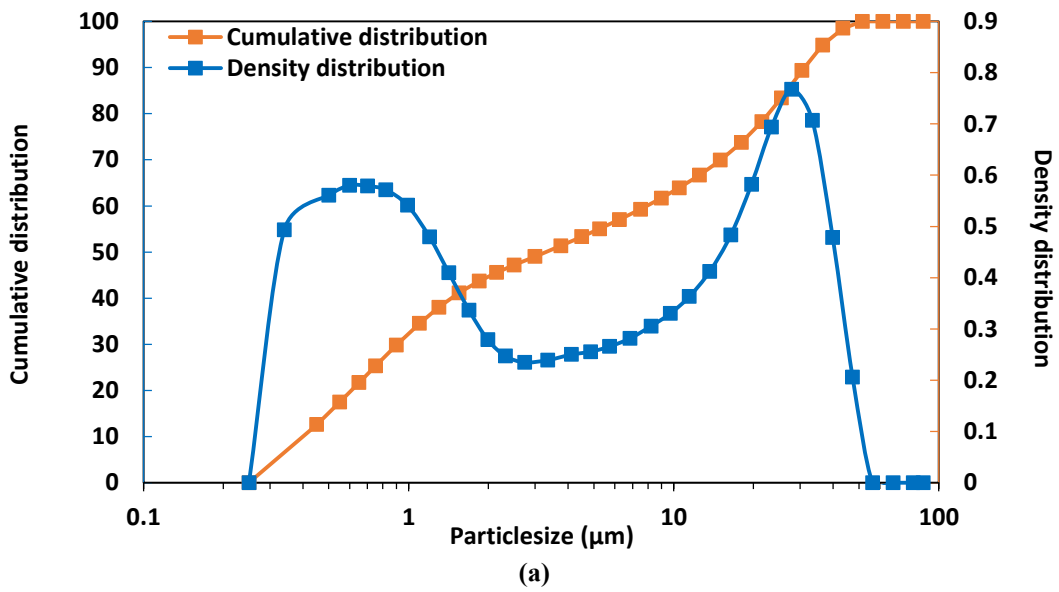
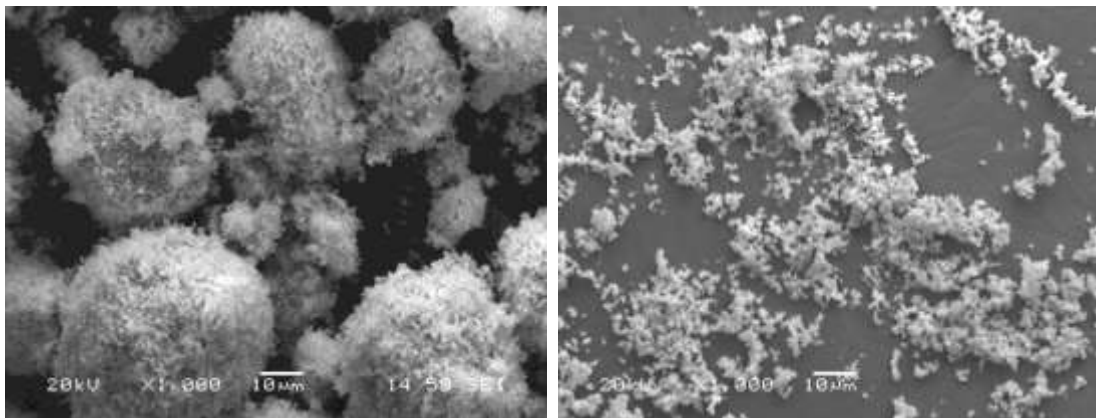


Figure 6.8 The particle size distribution of 50BCZT powders (a) as-received and (b) after vibro-milling for 7 hrs.

Figure 6.9 (a) shows the SEM micrograph of as-received powders, although the primary particle size is  $< 1 \mu\text{m}$ , agglomeration can be seen with a broad range of sizes from less than  $10 \mu\text{m}$  to over  $50 \mu\text{m}$ . The powders after vibro-milling 7 hrs are shown in in Figure 6.9 (b) where it can see that the large agglomerates were broken down and obviously smaller particles are observed.



(a)

(b)

**Figure 6.9 SEM micrographs of 50BCZT powders (a) as-received and (b) after vibro-milling for 7 hrs.**

### 6.3.1.2 Crystalline material structure

XRD patterns of the as-received 50BCZT powders (calcined at  $1100 \text{ }^{\circ}\text{C}$ ) and 50BCZT discs from gelcasting sintered at various temperatures are shown in Figure 6.10. All XRD patterns were indexed on the perovskite phase structure (ICSD code : 187675 [25]) and it can be seen that the XRD patterns of the samples sintered at  $1300 \text{ }^{\circ}\text{C}$  -  $1500^{\circ}\text{C}$  have similar patterns which are in agreement with XRD patterns of 50BCZT sintered at  $1325 \text{ }^{\circ}\text{C}$  and  $1500^{\circ}\text{C}$  using  $1 \mu\text{m}$  powder size reported by Bai [26]. However, the XRD pattern of the calcined powder shows a small additional peak at  $2\theta = 30^{\circ}$  and other peaks are shifted slightly to the right. It has been reported

[26] that for 50BCZT powders calcined at 1350°C, there are no additional peaks in the XRD pattern. However, in this project, the as-received 50BCZT powders were calcined at 1100°C, which obviously is not a high enough temperature for complete reaction and homogenisation of the oxide and carbonate precursors.

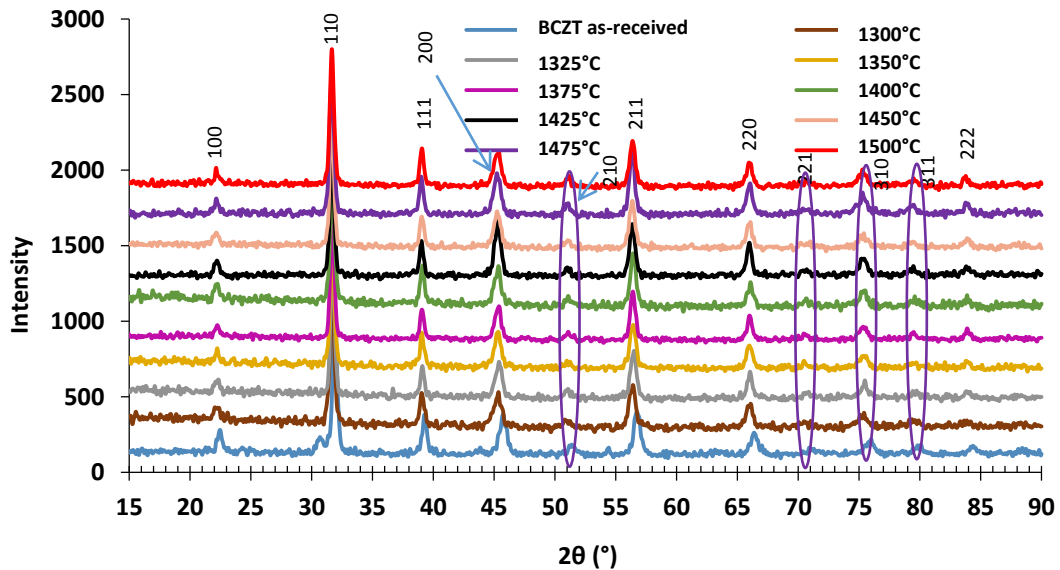


Figure 6.10 XRD patterns of 50BCZT powders calcined at 1100 °C and 50BCZT discs sintered at difference temperature.

## 6.3.2 Lead free slurries characterisation

### 6.3.2.1 Influence of dispersant concentration on viscosity of lead free slurry

The key parameters for the successful slurry preparation with well-dispersed ceramic powders in a suspension suitable for gel casting system are homogenisation, flowability, low viscosity and stability with high ceramic solids content. However, the viscosity of slurry increases with increasing solid loading while low solid loading can cause defects and damage of the surface in the finished ceramic [27-29]. An effective dispersant is one of the most important constituents in the slurry that will

help achieve high solids loading and low viscosity. In this thesis, a solution of an ammonium salt of an acrylic polymer in water ( $\text{NH}_4\text{PAA}$ ) or Dispex AA4040, was utilised as a dispersing agent because it has been reported as a good dispersant for aqueous ceramic systems [11, 30-32].

Typically, the interparticle forces in most ceramic suspensions are dominated by two key forces. The first one is an attractive force which arises from van der Waals forces, and the second one is repulsive force comprising electrostatic and steric repulsive forces of the polymer or dispersing agent on the surface of the ceramic particles [33, 34]. Most ceramic powders exhibit van der Waals attraction between like particles and also depends on the nature of solvent and surface of particle. In order to achieve the desired degree of colloidal suspension stability, the electrostatic and steric repulsive stabilisation need to be introduced to overcome and mitigate the van der Waals attraction between the particles [35, 36].

The electrostatic effect arises from the net surface charge between particle and liquid interface which depends on the zeta potential of colloidal suspensions, and can be adjusted by modifying the pH of the aqueous ceramic suspensions. Previous works has reported the effect of pH value and  $\text{NH}_4\text{PAA}$  at various pH values on the zeta potential and isoelectric point (IEP) of PZT suspensions [32]. The electrostatic force between particles tends to dominate when the suspension has a high zeta potential while a lower zeta potential (close to IEP) results in flocculation. The zeta potential of ceramic suspensions without dispersant agent has been shown to have the IEP at around pH 8 which means an alkaline environment might not be suitable to disperse the suspension, and it was also found that from pH 7 to around 12 the zeta potential was only slightly changed. Conversely, with a dispersant, the IEP was shifted to pH

around 2 and offered a more negative zeta potential value which means the dispersant was effective. The different pH values of ceramic suspensions with and without dispersant were studied in order to determine the influence of pH and dispersant on the viscosity of the suspension. It has been reported that changing the pH values only slightly affected viscosity while the presence of a dispersant significantly decreased the viscosity of the suspensions [27, 32, 34].

The steric effect comes from the absorption of polymer molecules on the particle surface which the polymer particles should cover completely with enough thickness to avoid particles from approaching each other too closely where the net attraction force and bridging flocculation can occur due to van der Waals force. The polymer molecules should be firmly anchored on the ceramic particles in order to prevent desorption during particle collision and, with the appropriate condition, the interpenetration of the polymer surface layer can create the steric repulsion. [33, 35]. Therefore, the stabilisation of electrostatic and steric repulsive forces in the suspension can be created by the dispersing agent, overcoming or reducing the van der Waals force attraction [27, 32, 34].

The well-dispersed slurry can be developed by adjusting the dispersant concentration in the slurries. Figure 6.11 shows the influence of dispersant concentration on the viscosity behaviour of 50BCZT slurries with 40% vol solids loading and 20% resin content at the shear rate of  $100 \text{ s}^{-1}$ . It can be clearly seen that the dispersant essentially reduced the viscosity of slurries. The optimum dispersant concentration was found at 2.4 wt% which provided the lowest viscosity of the slurry with a value of 0.11 Pa.s. This indicates that the dispersant effectively dispersed the ceramic particles in the slurry by providing enough negative charge of PAA to absorb on the



surface of 50BCZT particles, increasing the repulsion force and, at the lowest viscosity, the dispersant concentration was enough to overcome van der Waals force and provided a well-dispersed system. At concentration below 2.4 wt%, a higher viscosity of the slurry was found due to insufficient dispersant to cover the surface of the particles, resulting in some flocculation due to attraction from the van der Waals force [9, 11, 27, 37-39]. However, increasing the dispersant concentration over 2.4 wt% also led to an increase in viscosity which may relate to the interlocking of the unabsorbed dispersant in the slurry causing bridging between ceramic particles [9] and could also function as an electrolyte, thereby resulting in the reduction of the range of the electrical double layer repulsion and distance between particles [9, 40, 41]. The optimum dispersant concentration for this 50BCZT slurry with 40%vol solids loading and 20 wt% epoxy resin was 2.4 wt% that offered the lowest viscosity for the slurry.

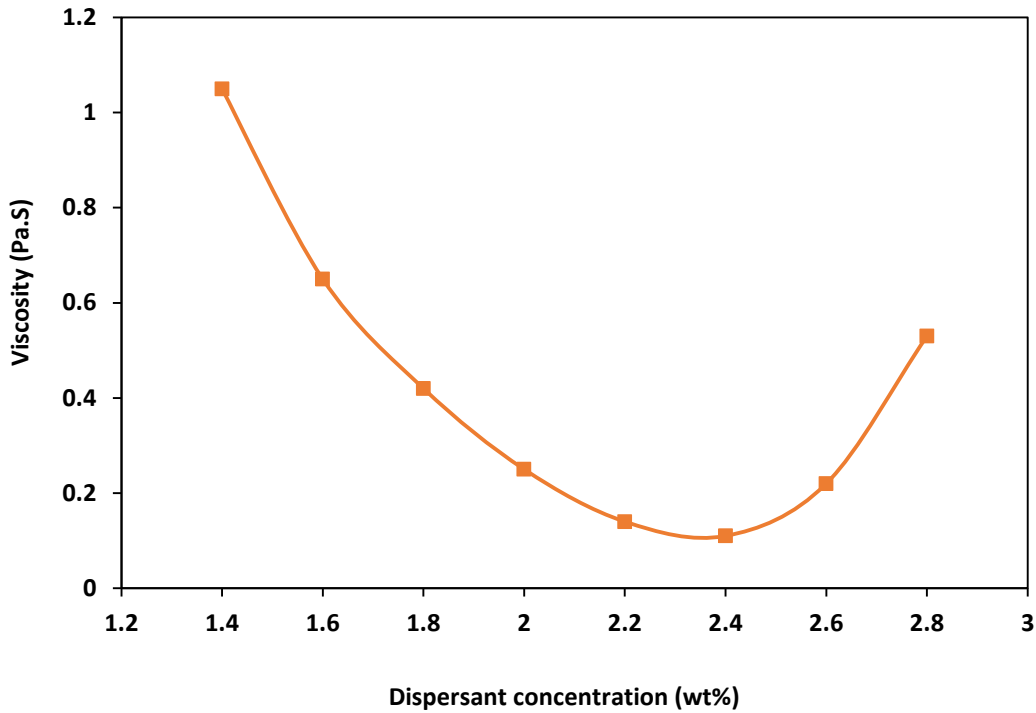


Figure 6.11 Viscosity of the 50BCZT slurry with 40% vol solids loading and 20 wt% resin contents as a function of dispersant concentration measured at a shear rate  $100 \text{ s}^{-1}$ .

### 6.3.2.2 Influence of solids loading on the viscosity of lead free slurries

As mentioned above, a ceramic slurry for a gel casting system requires well-dispersed ceramic powders in a suspension with low viscosity and high ceramic solids loading. This can be beneficial to the green density of ceramic part as the green density has a correlation with the solids loading of the slurry. A higher solids loading results in higher green density and minimises the drying shrinkage [42], hence resulting in better control of geometry and structure, improving green strength and reducing the possibility of distortion of the ceramic part during drying and sintering [38, 43]. In this thesis, the Si master mould with the random geometry and complex shape were used for fabricating the bristle block structure, therefore, a low viscosity slurry is required during mixing and casting in order to achieve a

homogeneous slurry that can be completely fill the complex mould shape. According to these two conditions, this means that it is necessary to tailor the slurry with low viscosity and optimum solids content. The solids loading of the slurry can be calculated according to the following Equation 6.3 [37, 44].

$$\phi = \frac{m/\rho}{\frac{m}{\rho} + V} \quad \text{Equation 6.3}$$

where  $\phi$  is the solids loading,  $m$  (g) and  $\rho$  (g/cm<sup>3</sup>) are the mass and density of the 50BCZT powder, respectively,  $V$  is the volume (ml) of the premix solution in the slurry.

Figure 6.12 presents the rheological curves of 50BCZT slurries at various solids loadings with 20 wt% resin content and optimum dispersant agent (based on dry solid). It can be seen that all slurries exhibited higher viscosity at higher solids loadings with Non-Newtonian flow behaviour [45]. As the solids loading ranged from 40 to 47 vol%, the viscosity of slurries changed with changing of shear rate and volume fraction of 50BCZT powder. All slurries exhibited shear thinning behaviour which may be a result of the perturbation of the slurry structure by the shear [8]. At low shear rate, high viscosities were observed because the slurries were close to their equilibrium state and the ceramic particles were close to each other because the thermal motion of ceramic particles was dominant over the viscous force. On the other hand, at high shear rate, the viscous force dominated the structure of slurry; thereby, resulting in the shear thinning behaviour and most slurries having a constant viscosity [8, 9, 46] which is in agreement with other research [8, 9, 38,

42, 44, 46-49]. This means that, for the various volume fractions, the differences in viscosity are more significant at low shear rate [42].

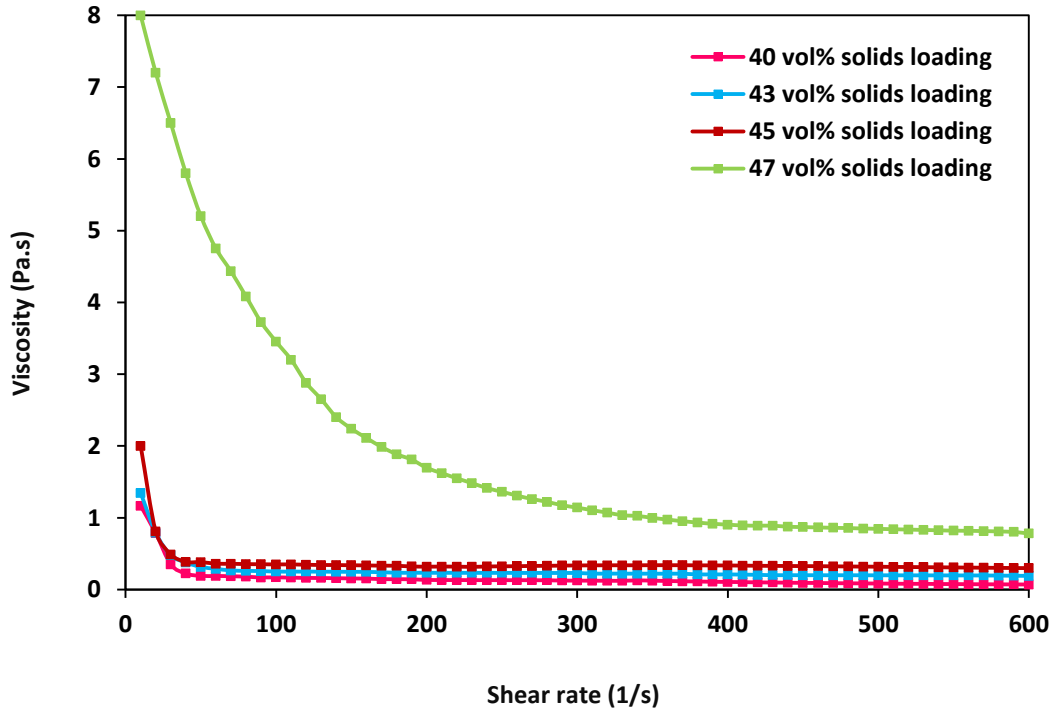


Figure 6.12 Viscosity curves as a function of shear rate of the 50BCZT slurry at various solids loadings with 20 wt% resin content using hardener concentration PHR = 18 g and the dispersant concentration was 2.4 wt%.

For the slurries with 40, 43 and 45 vol% solid loading, the viscosities at a shear rate of  $100 \text{ s}^{-1}$  were about 0.17, 0.25 and 0.35 Pa.s, respectively, which were relatively low viscosity and also suitable for gelcasting because the viscosity was less than 1.0 Pa.s, which ensures the slurries have flowability for casting into the mould cavity [37, 48, 50]. The viscosity of the slurry with a solid loading 47 vol% at a shear rate of  $100 \text{ s}^{-1}$  was about 3.45 Pa.s, which was too high for the gelcasting process. Therefore, the optimum solid loading was determined as 45 vol%.

### **6.3.2.3 Influence of resin content on viscosity and gelation time of lead free slurries**

Apart from the amount of dispersant and the solids loading, the epoxy resin is also one of the key constituents affecting the rheological behaviour of the slurries. Therefore, the influence of resin content on the viscosity of the 50BCZT gel casting system has been studied by considering the viscosity at a critical shear rate ( $100 \text{ s}^{-1}$ ) as it is close to the condition during the casting stage. Figure 6.13 shows the viscosity as a function of shear rate of 45 vol% solids loading 50BCZT slurries with 2.4 wt% Dispex AA4040 after being mixed with optimum hardener amount for resin contents ranging from 10 wt% to 40 wt %. All the slurries exhibited shear thinning behaviour indicating suitability for gel casting. As expected, the amount of resin affected the viscosity of the slurry. The viscosity gradually increased with increasing resin content which were in agreement with other research [9, 10, 37, 41, 50]. There are several reasons that can explain this behaviour. For example, compared to the viscosity of the resin, the distilled water which was utilised as the dispersed medium, possessed a lower viscosity. Therefore, with increasing addition of resin into the water the overall viscosity of the solution increases. The second possible reason is that the increase of resin content of the slurry may cause an increase in intermolecular entanglement, resulting in an increase in the viscosity of the slurry due to difficulties of individual chain movement [11]. Moreover, another possible reason is the depletion flocculation effect which can be caused by the non-absorbed polymer leading to the flocculation of particles. Generally, the polymer is lyophilic, in that the flexible polymer chains like to dissolve in the dispersed medium rather than precipitate out. The polymer chains can move freely in the colloid and do not

interact with the ceramic particles. At low amounts of resin, the resin is more likely to cover the surface of the particles. However, with increasing resin content, excess resin can float around in the dispersed medium and does not absorb on the surface of the particles. When the concentration of free polymer exceeds a critical value and the gaps between adjacent particles are less than the effective radius of the polymer, the polymer tends to not fit into the gaps and then the non-absorbed polymers are pushed into the bulk dispersed medium. This means there is no polymer between the ceramic particles. In the region between particles, there is a reduced concentration of polymer, whereas everywhere else there is a higher concentration of polymer. This creates an osmotic pressure on the dispersed medium between particles where it wants to reach equilibrium by moving the solvent to the region where the polymer is concentrated. If the polymer could get into the gap, the system would achieve equilibrium but the polymer cannot get into the gap so the dispersed medium moves instead. The movement of the dispersed medium from the gap between particles by osmosis to the concentrated polymer region creates a lower pressure region in the gap which leads to an attraction between the particles. With increasing resin content, more non-absorbed polymers were introduced into the slurry. Therefore, the viscosity of slurry increased [41, 51]. It can be found that with increasing the resin concentrations from 10 wt% to 40 wt%, the viscosity increased from 0.19 to 0.97 Pa.s at the shear rate of  $100 \text{ s}^{-1}$ . This means even at the highest resin concentration with 40 wt%, the viscosity was still relatively low and acceptable for gel casting.

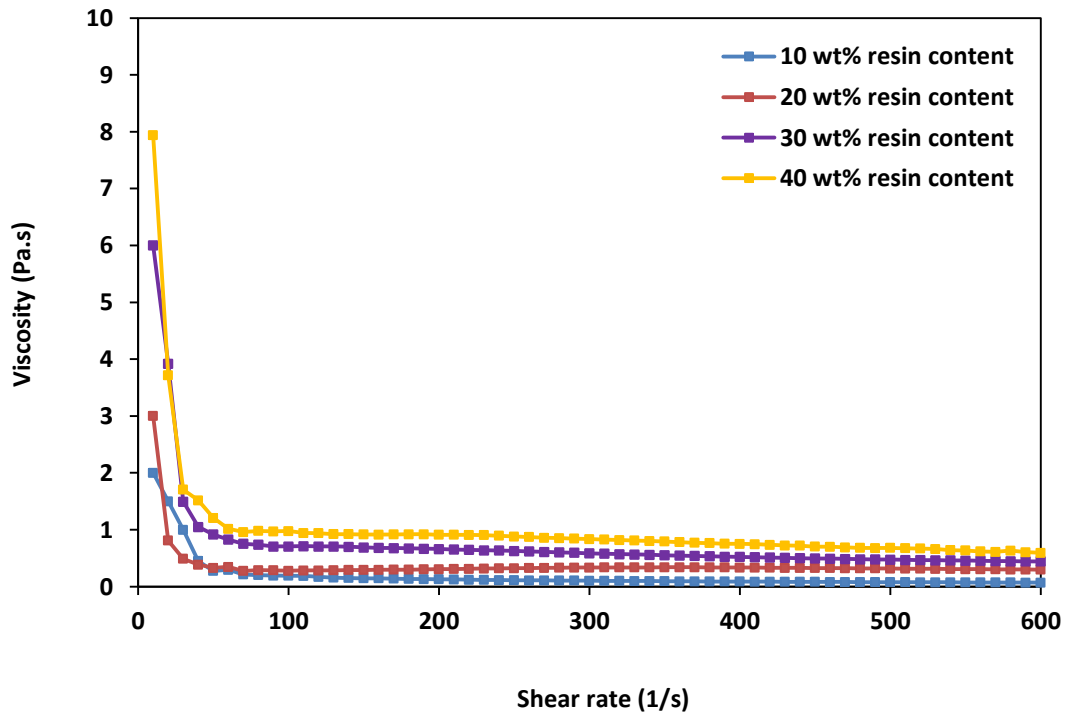


Figure 6.13 Viscosity curves as a function of shear rate of 50BCZT 45 vol % solids loading slurries with various resin contents using hardener concentration PHR = 18 g and the dispersant concentration was 2.4 wt%.

Another important parameter for a gel casting slurry is the time available for the whole gel casting process including mixing, casting and degassing. This is represented by the gelation time which can determine the efficiency of production. After the slurry was mixed and cast into the soft mould, the gelation time should be long enough to let the gel casting slurry completely fill the mould cavity allow the slurry to be degassed effectively before curing begins to minimise trapped bubbles in the slurry and finished sample. Thus the effect of resin content on the gelation time has been studied. As described previously, there are a number of criteria for the indication of the gelation time. The traditional criteria has been reported by using the

crossover point of elastic modulus ( $G'$ ) and loss modulus ( $G''$ ) [5]. However, this traditional way was not applicable for several gel casting systems based on ceramic and epoxy resin because the crossover point between the elastic modulus and loss modulus cannot be observed [1, 6, 7, 11, 52]. An alternative criteria is monitoring the time corresponding to an abrupt increase of  $G'$  for the slurry [6, 7]. However, this criteria also was not suitable for the gel casting system with ceramic powders and high resin contents (over 30 wt%) as the sudden change of  $G'$  was difficult to determine [11]. Another criterion for determination of gelation time has been reported based on the detection of the time when an abrupt change of viscosity of slurry occurs [9-11, 50, 53].

The gelation times of 50BCZT slurries with 45 vol% solids loading, 2.4 wt% of Dispex AA4040 at various resin contents were monitored by measuring the viscosity as a function of time at constant shear rate of  $0.1 \text{ s}^{-1}$  and temperature of  $25^\circ\text{C}$ . The start time was taken as the point of hardener addition. Figure 6.14 shows the effect of hydantoin epoxy resin concentration on gelation behaviour. It can be clearly seen that all of the slurries presented a period of time with constant viscosity and then the viscosity suddenly increased, which is in agreement with the results reported by Jiang [11], Xie [9, 50] and Liu [53]. In this gel casting system, the increase of resin concentration from 10, 20, 30 to 40 wt% resulted in a decrease in gelation time from 25, 15, 11 to 7 minutes, respectively. It has been reported that the gelation may happen during mixing the hardener if the gelation time is  $\leq 10$  minutes, which will cause problems during processing, and gelation times  $\geq 70$  minutes will cause production inefficiencies [53]. Therefore, in term of gelation time, 10, 20 and 30 wt% resin contents are suitable for a gel casting process.



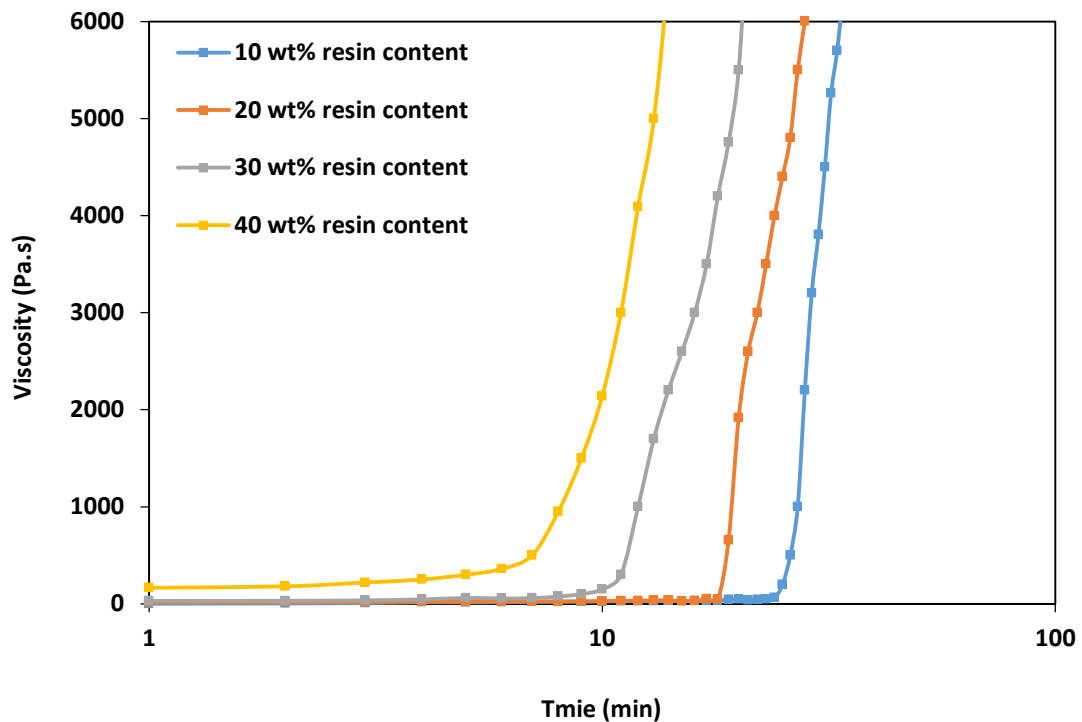
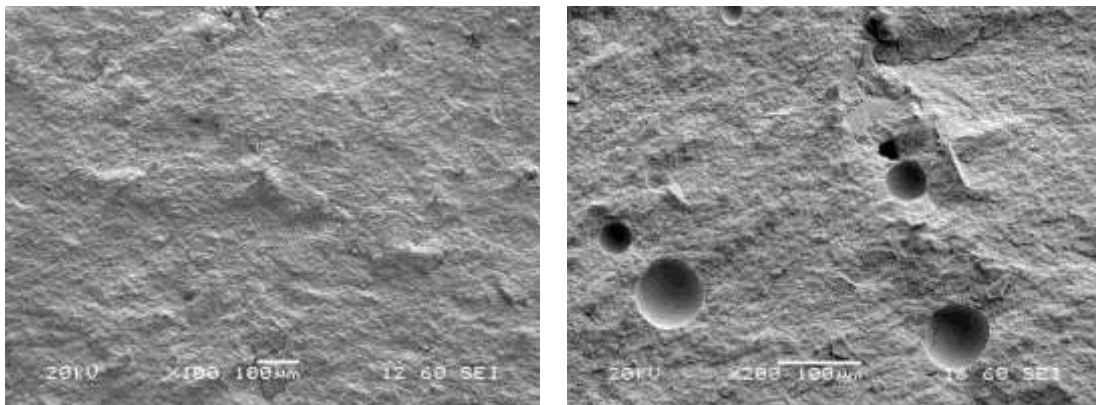


Figure 6.14 Variation of viscosity curves as a function of time of 50BCZT slurries of different resin contents. All slurries have 45 vol % solids loading using hardener concentration PHR = 18 g and the dispersant concentration was 2.4 wt%.

## 6.4 Characterization of lead free gel casting green bodies

In this thesis, for the purpose of studying lead free gel casting green bodies, the optimum hardener and dispersant were utilised for preparing gel casting slurry with 45 vol% solids loading at different resin contents. All slurries were prepared at room temperature, degassed and then gradually cast into the PDMS soft moulds, followed by another de-airing step in vacuum for 2 minutes. Figure 6.15 shows the comparison of the microstructure of the fracture surfaces of green 50BCZT gelcasting samples with and without the de-airing step after casting. It can be clearly seen that the sample without de-airing had some pores which were caused by the presence of air entrapped in the gel casting slurry during casting. These pores could jeopardise the

mechanical properties and inhibit the polymerisation reaction [43], leading to low strength and density of green and sintered samples. Figure 6.16 shows a typical gel casting sample of around 12 mm in diameter and around 1.5 mm in height after demoulding and drying prepared from 50BCZT powders. Samples shows well-shaped with no visible cracks and also have sufficient strength for handling.



(a)

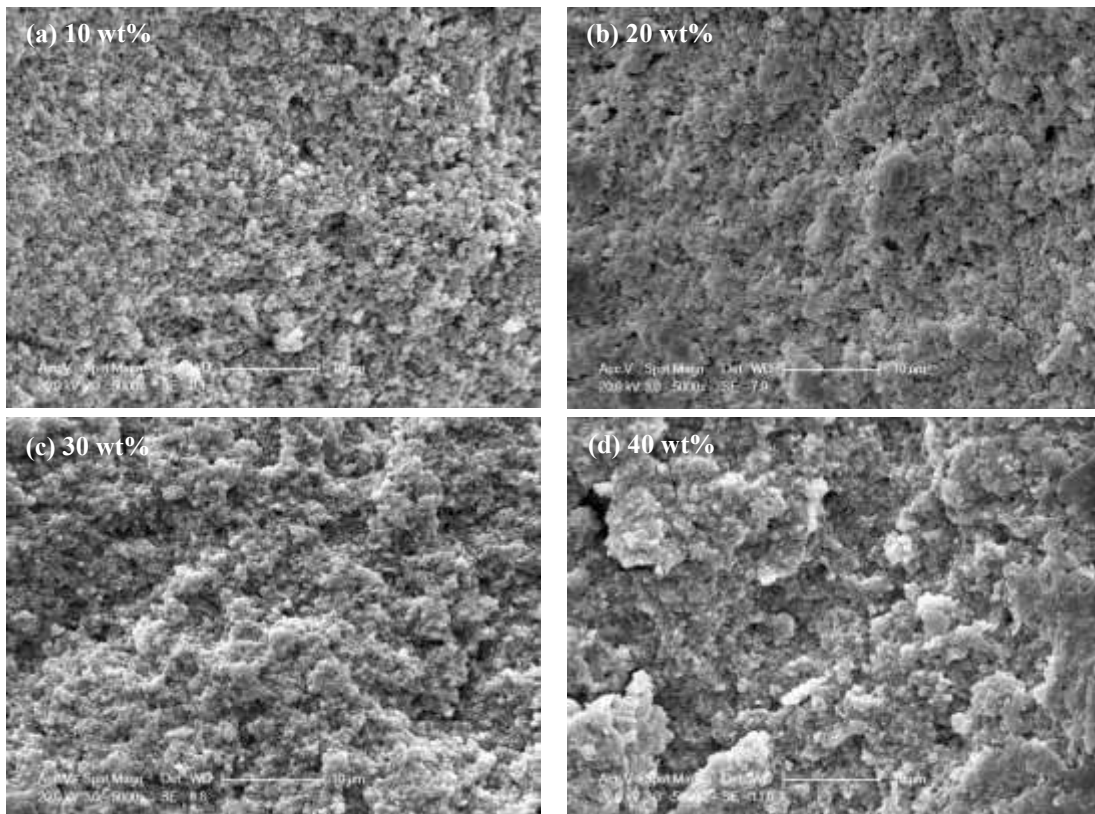
(b)

**Figure 6.15** Fracture surface of green 50BCZT samples prepared from 45 vol% solids loading, 30 wt% resin content at optimum hardener and dispersant concentrations (a) with de-airing step after casting (b) without de-airing step after casting.



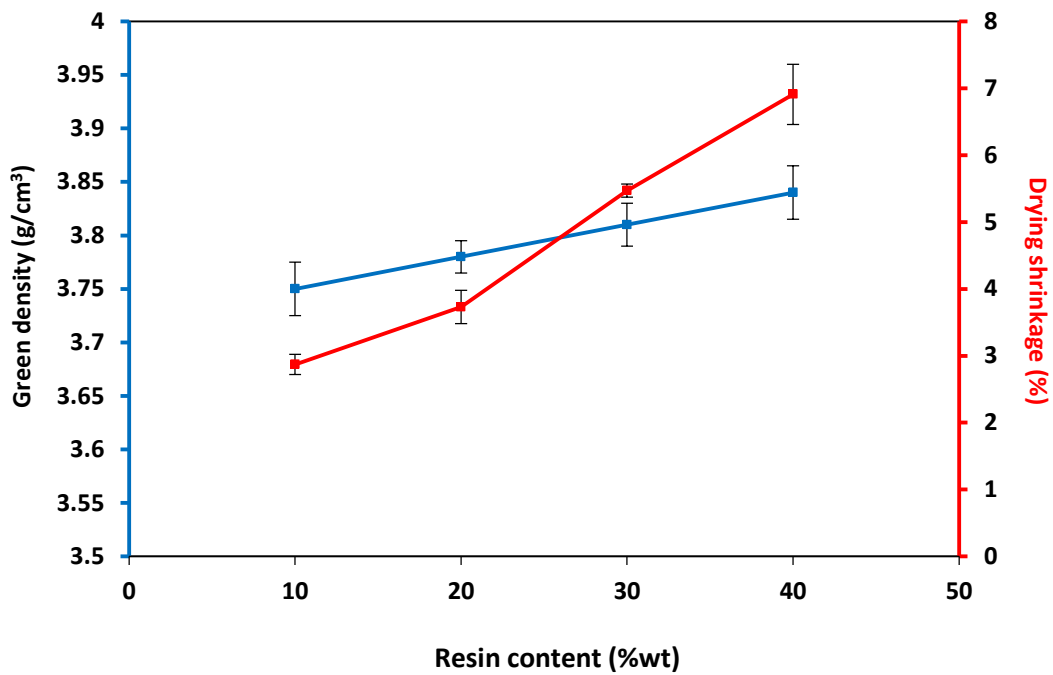
**Figure 6.16** Green 50BCZT gel cast sample obtained from 45 vol% solids loading with 30wt% resin and 2.4 wt% Dispex AA4040 after demoulding.

Figure 6.17 shows SEM micrographs of the fracture surfaces of the gel cast green bodies obtained from 45 vol% solids loading with resin contents ranging from 10 wt% - 40 wt%. It can be observed that the green bodies presented a tendency to gradually reduce pore size with increasing resin content while the outline of 50BCZT particles in green bodies can be more defined and distinct at lower resin concentrations while at higher resin content, the outline of particles was difficult to define, which is indicative of the green bodies having more cross-linked polymer between the spaces between the 50BCZT particles. All green bodies were packed uniformly without obvious defects, indicating relative homogeneous microstructures [9, 11].



**Figure 6.17 SEM micrographs of fracture surface of 50BCZT green bodies obtained from 45 vol% solids loading with various hydantoin epoxy resin concentrations (a) 10 wt% (b) 20 wt% (c) 30 wt% (d) 40 wt% after demoulding and drying.**

The strong influence of resin content on green density and drying shrinkage of green 50BCZT gel cast samples obtained from 45 vol% solids loading at various resin contents are presented in Figure 6.18. With increasing resin content, green density and drying shrinkages were enhanced indicating improved particle packing of the green compacts, which should lead to enhanced sintering because of the increase in the number of material transport paths for densification. These results are in agreement with the study of the effect of EGDEG epoxy resin concentrations on shrinkage and density of green bodies prepared from PZT 45 vol % solids loading reported by Jiang [11] [32]. As can be seen from the SEM micrographs in Figure 6.17, samples from all resin contents had relatively homogeneous microstructures and the influence of resin content on particle packing were not clearly observable. However, the drying shrinkage data can help explain about the particle packing of green samples. Generally, there are two main sources that influence the drying shrinkage. Firstly, the cross-linking of the epoxy-amine will cause a contraction and the second relates to the evaporation of water. Typically, the gel casting slurries with lower resin concentrations possess higher amounts of water; therefore, compared to gel casting slurries with higher resin concentrations, the drying shrinkage contribution from the removal of water from lower resin concentrations should be higher. As can be seen from Figure 6.18, the drying shrinkage of green bodies with lower resin concentrations presented smaller values of net shrinkage.



**Figure 6.18** Green density and drying shrinkage of 50BCZT gel cast green samples versus resin content at a solid loading of 45 vol%.

According to Jiang [11] and Olhero *et al.* [32], the possible reasons for this phenomenon can be explained as follows. The lower resin contents caused the inhomogeneous distribution of polymer chains as the polymer molecules were attracted and interconnected mainly only at the surface of particles. Therefore, the drying shrinkage occurred from a small amount of contraction between the close particles to create 3 dimensional networks. On the other hand, at higher resin concentrations which contained smaller amounts of water but exhibited higher drying shrinkages, a more uniform distribution of polymer chains was considered important. At higher resin contents, the molecules of resin were sufficient to anchor and fill the spaces between individual particles as presents in Figure 6.19. Therefore, during curing, the higher resin contents provide higher fractions of 3 dimensional networks between the gaps which means that neighboring particles in the suspension can be

dragged closer together. Moreover, Olhero *et al.* [32] suggested that at higher resin contents, finer pore networks can be developed, leading to a high capillary suction pressure, resulting in the possibility of a higher drying shrinkage.

As can be seen in Figure 6.18, the green density was significantly improved by increasing the resin contents from 10 wt% to 40 wt% due to the improved packing of particles and the increasing of fractions of polymer chains completely filling the gap between ceramic particles. It is well known that green density is one of the most important parameters that has a strong influence on the green strength of samples [46]. Therefore, the higher green density should enhance the green strength of samples. It can be seen in Figure 6.20 that increasing hydantoin epoxy resin content of samples from 10 wt% to 40 wt% increases the measured green strength from 18 MPa to 55 MPa respectively. This can be attributed to the enhanced green density of the samples with higher resin contents, resulting in the better green strength. The results also are in agreement with Jiang *et al.* [37], and Xie *et al.* [50], for AlN and Al<sub>2</sub>O<sub>3</sub>, respectively. Compared to the green strength obtained from the green bodies using EGDGE resin at the same resin content the sample prepared from hydantoin epoxy resin system provided higher green strength than those based on the EGDGE system [54].

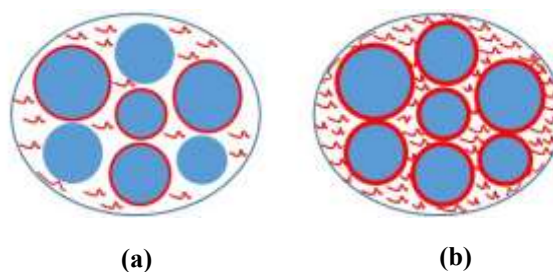


**Figure 6.19 Effect of resin content on particles at green state (a) 10 wt% (insufficient polymer chains) (b) 40wt% (sufficient polymer chains).**

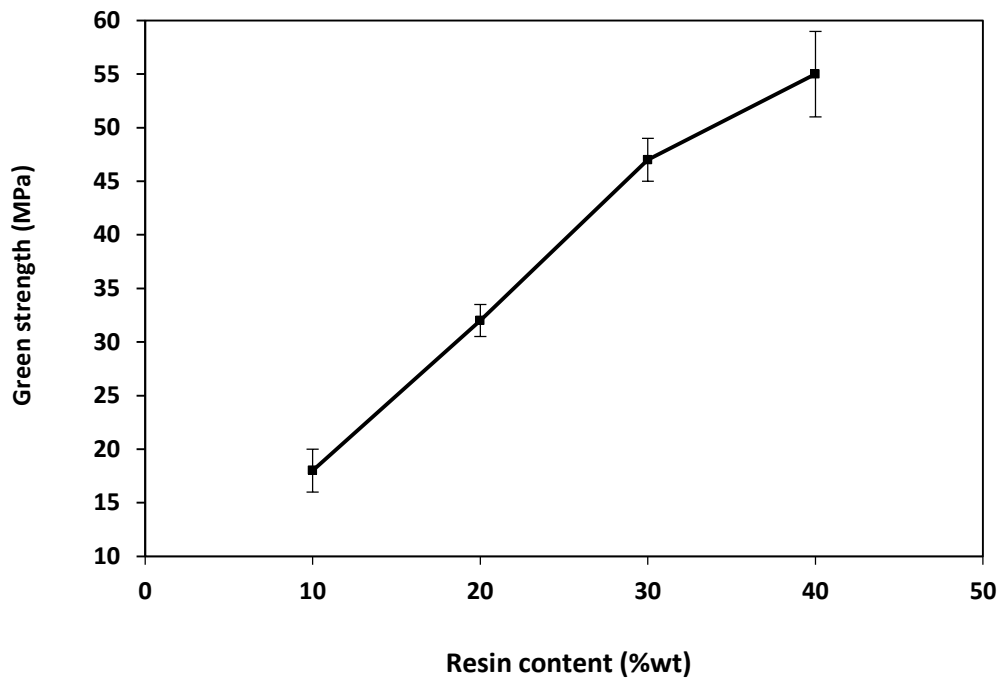


**Figure 6.20** Green strength of the gel cast 50BCZT obtained from 45 vol% solids loading at various resin contents.

The green strength of samples is an important factor for successful demoulding and handling the green structures. Generally, the strength of green bodies for bulk samples was recommended to be higher than 10 MPa [54]. This means the green strength values obtained from bulk green samples at all resin contents were sufficient for demoulding and handling for the initial study of these gel casting systems. However, in this work, the aim is to produce ultrafine randomised bristle block structures for high frequency ultrasound transducers. Therefore, in practical work, higher green strength values would be beneficial for successful demoulding of the delicate pillar structures.

## **6.5 Characterization of lead free gel cast sintered bodies**

### **6.5.1 The influence of resin content on the key properties**

It has been shown above that the optimum solids loading for the 50BCZT gel casting system was 45 vol% as it presented the maximum ceramic content of the slurry with viscosity and flowability suitable for gelcasting (viscosity < 1.0 Pa.s at a shear rate of  $100 \text{ s}^{-1}$ ). In the search for the optimum resin content of the gel casting system, the green bulk samples obtained from 45 vol% solid loading at various resin concentrations were produced in order to initially study the effect of resin content on sintered density and shrinkage and other the key parameters including the piezoelectric coefficient ( $d_{33}$ ), the planar coupling coefficient ( $k_p$ ), the relative permittivity at constant stress  $\epsilon^T$  and the dielectric lost tangent. For an initial study the green bulk samples were sintered at  $1425 \text{ }^\circ\text{C}$  as a maximum  $d_{33}$  value of approximately  $410.8 \pm 13.2 \text{ pC/N}$  had been reported at this sintering temperature on similar powders by Castkova *et al.* [55]. Figures 6.21 - 6.24, show the key parameters of the gel cast 50BCZT sintered samples versus resin content at solid loading of 45 vol% sintered at  $1425 \text{ }^\circ\text{C}$ . It can be seen that there is a strong influence of resin content on all the measured parameters.

Figure 6.21 shows the sintered density and shrinkage of the gel cast 50BCZT sintered samples versus resin content. In the green stage, higher green densities were found with higher resin contents. However, it can be seen that high green density does not result in high sintered density. With increasing resin content from 10 wt% to 40 wt%, the sintered density decreased from  $5.5 \text{ g/cm}^3$  to  $5.21 \text{ g/cm}^3$ , which is in agreement with the results according to Jiang [11] and Olhero *et al.* [32] in other material systems.



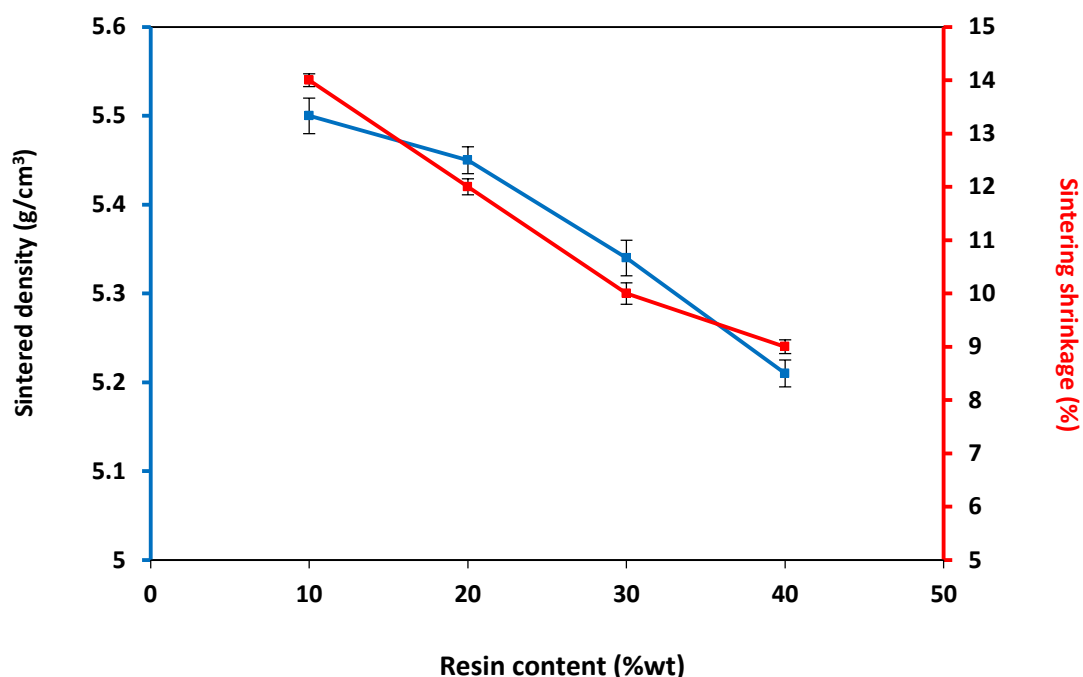


**Figure 6.21** Sintered density and sintering shrinkage of 50BCZT gel samples at a solid loading of 45 vol% sintered at 1425°C versus resin content.

Figure 6.22 shows SEM micrographs of fracture surfaces of the sintered gel cast samples obtained from 45 vol% solids loading 50BCZT slurries with various hydantoin epoxy resin concentrations. All samples presented a relatively dense and homogeneous microstructure. However, the sintered samples with 10 wt% and 20 wt% seemed to present the smaller amount of porosity compared to those obtained from 30 wt% and 40 wt% resin content. This indicates that the porosity tended to increase with increasing resin content. These results are in agreement with the reduced value of sintered density when the resin content was increased. The higher resin contents might cause an obstacle to the structure during burnout of the polymer during the binder burnout stage, the organic binders are either melted (thermoplastic) or decomposed to gas (thermoset). Epoxy resin systems are thermosetting polymers. Generally, gases can be released by flowing through porous structure between the

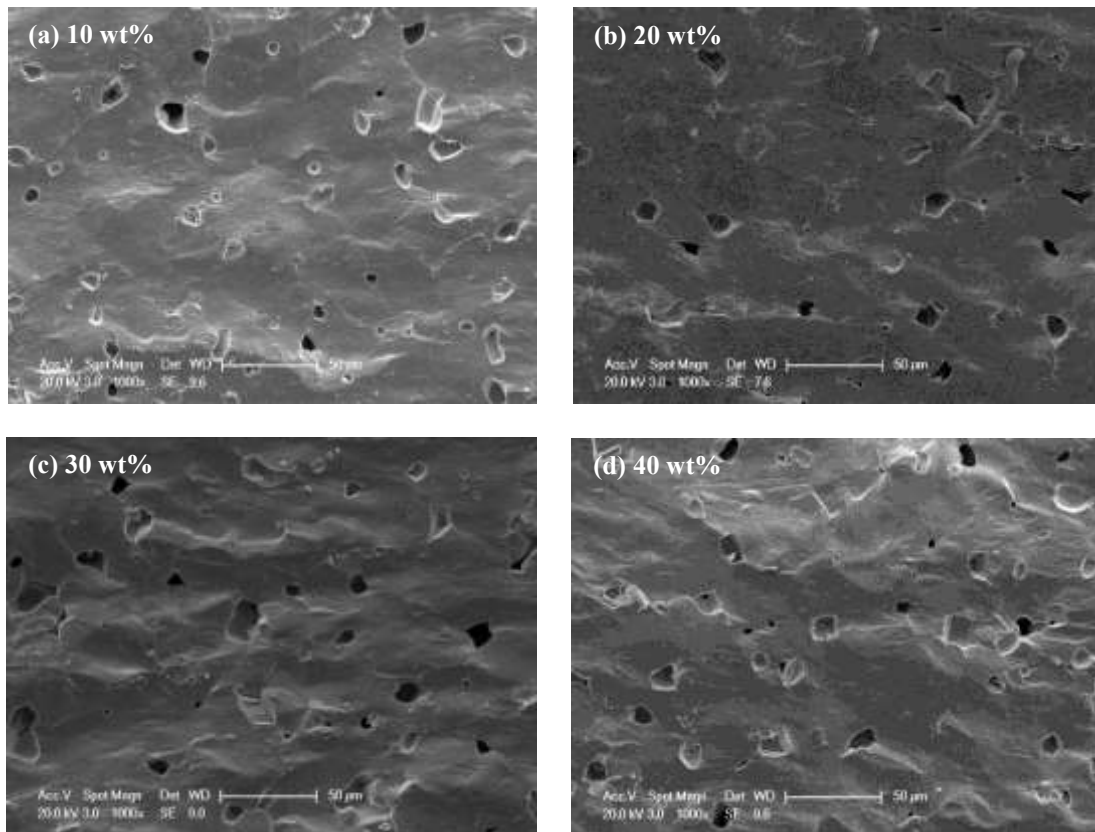


**Figure 6.22 SEM micrographs showing the fracture surfaces of sintered gel cast samples obtained from 45 vol% solids loading 50BCZT slurries with various hydantoin epoxy resin concentrations (a) 10 wt% (b) 20 wt% (c) 30 wt% (d) 40 wt%.**

ceramic particles. However, the accumulation of gas during decomposition can cause an internal pressure leading to internal stresses in the ceramic body. The gel casting sample prepared from the higher resin contents may have higher gas accumulation. Considering the high particle packing, the gas permeation will be restricted which might cause a greater pressure difference in the microstructure and bring problems to the sintered body such as blisters, cracks and also trapped organics. The increase of trapped gases and porosity with increasing resin content leads to the decreased ability of the sample to sinter, resulting in a decrease of the sintering shrinkage and sintered density [11, 56].

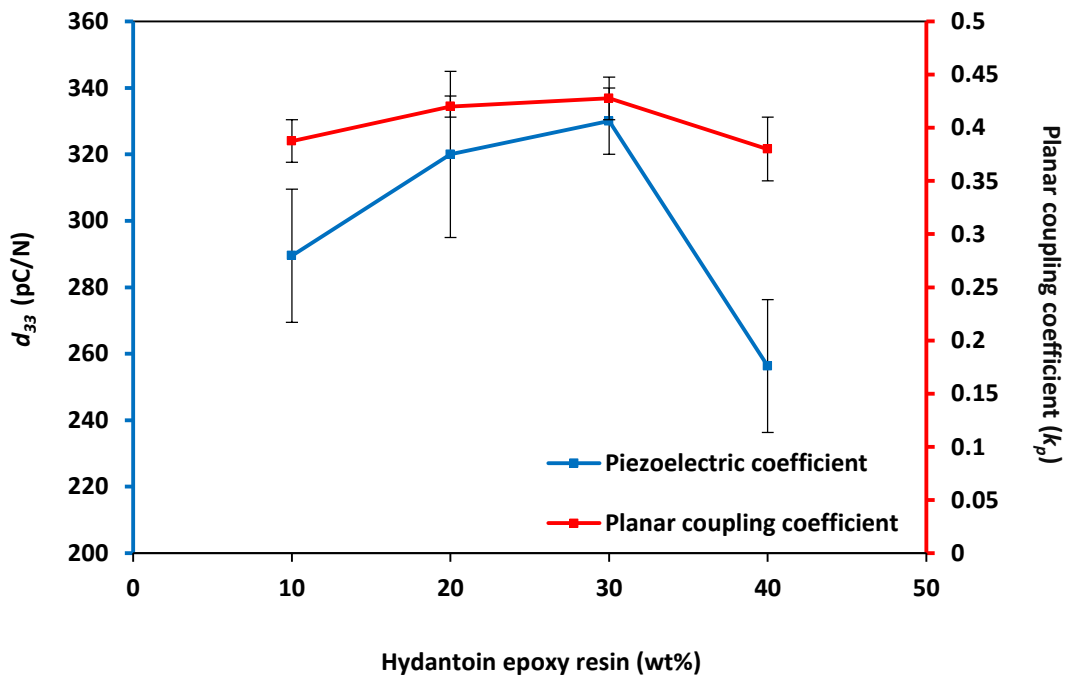


Figure 6.23 The variation of piezoelectric charge coefficient  $d_{33}$  and planar coupling coefficient  $k_p$  with resin content of 50BCZT gel cast samples at a solid loading of 45 vol% sintered at 1425°C.

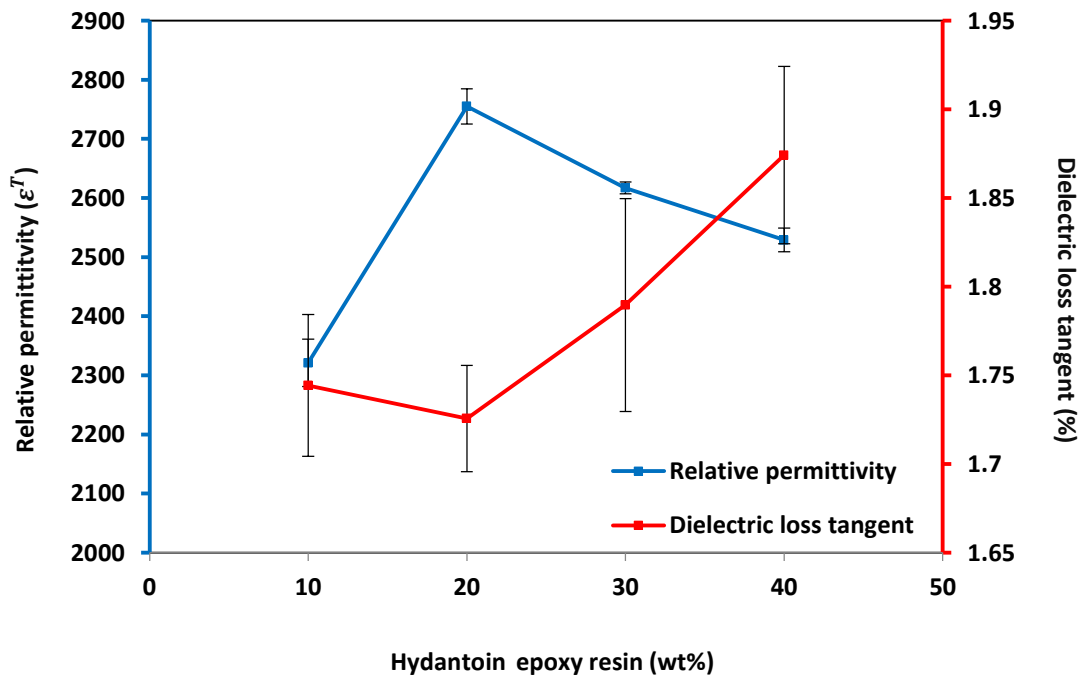
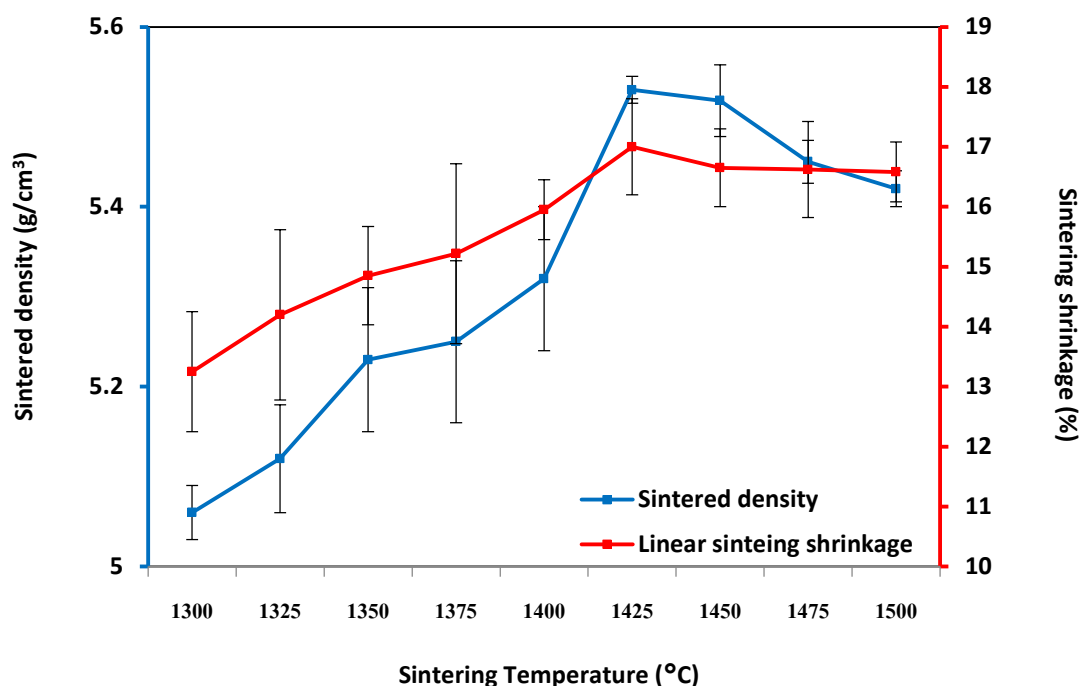


Figure 6.24 The variation of relative permittivity and dielectric loss tangent versus resin content of 50BCZT gel cast samples at a solid loading of 45 vol% sintered at 1425°C.

Figures 6.23 and 6.24 show the influence of resin content on the piezoelectric coefficient ( $d_{33}$ ), the planar coupling coefficient ( $k_p$ ), the relative permittivity at constant stress ( $\epsilon^T$ ) and the dielectric loss tangent of 50BCZT gel cast green samples sintered at 1425°C at solids loading 45 vol%. The highest  $d_{33}$  and  $k_p$  of around 330 pC/N and 0.43, respectively was obtained by using 30 wt% resin content while the highest  $\epsilon^T$  and the smallest dielectric loss tangent were measured in samples with 20 wt% resin content. However, for samples with 40 wt% resin these properties showed decreasing trends indicating that too high a resin content. The sintered density decreased with increasing resin content this might lead to a deleterious effect on piezoelectric and dielectric properties of sintered gel cast samples.

### **6.5.2 The influence of sintering temperature on the key properties**

As mentioned above, 30 wt% resin content provided the highest value of  $d_{33}$  and  $k_p$ ; therefore, this resin content was selected for preparing the gel casting slurries with 45 vol% solids loading for sintering at various temperatures.



**Figure 6.25 Sintered density of 50BCZT gel cast samples at a solids loading of 45 vol% and 30 wt% resin content sintered at different temperatures.**

Figure 6.25 shows the sintered density and sintering shrinkage of 50BCZT gel cast samples at a solid loading of 45 vol% and 30 wt% resin content sintered at temperatures from 1300 °C - 1500 °C, and the microstructures of polished and thermally etched samples are shown in Figure 6.26. It can be seen that the sintering shrinkage tends to increase with an increase of sintering temperature which supports the increasing trend of sintered density and the decreasing of porosity (see Figure 6.26) which is in agreement with the result of 50BCZT powder pressed samples reported by Bai [26]. The highest value of sintered density  $5.53 \text{ g/cm}^3$  (~ 96.60 % of theoretical density) was observed for a sintering temperature of 1425 °C, indicating the improvement of densification at elevated temperature which corresponds to the reduction in porosity presented in Figure 6.26. When the sintering temperature increased from 1300 °C to 1425 °C, it can be considered not only as an increase of

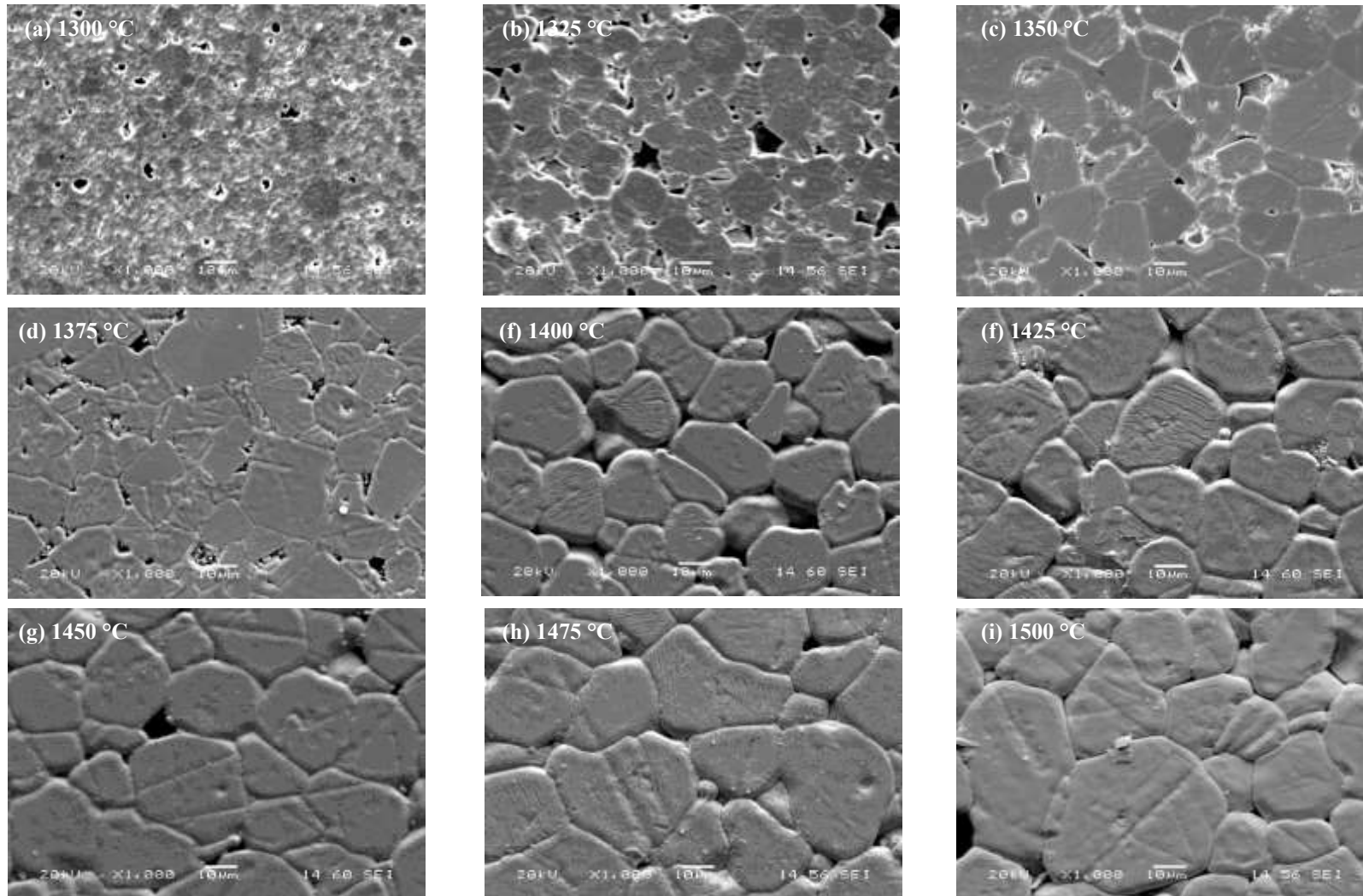


Figure 6.26 SEM micrographs of 50BCZT gel cast samples at a solids loading of 45 vol% and 30 wt% resin content sintered at temperatures between 1300 °C and 1500 °C for 4 h.

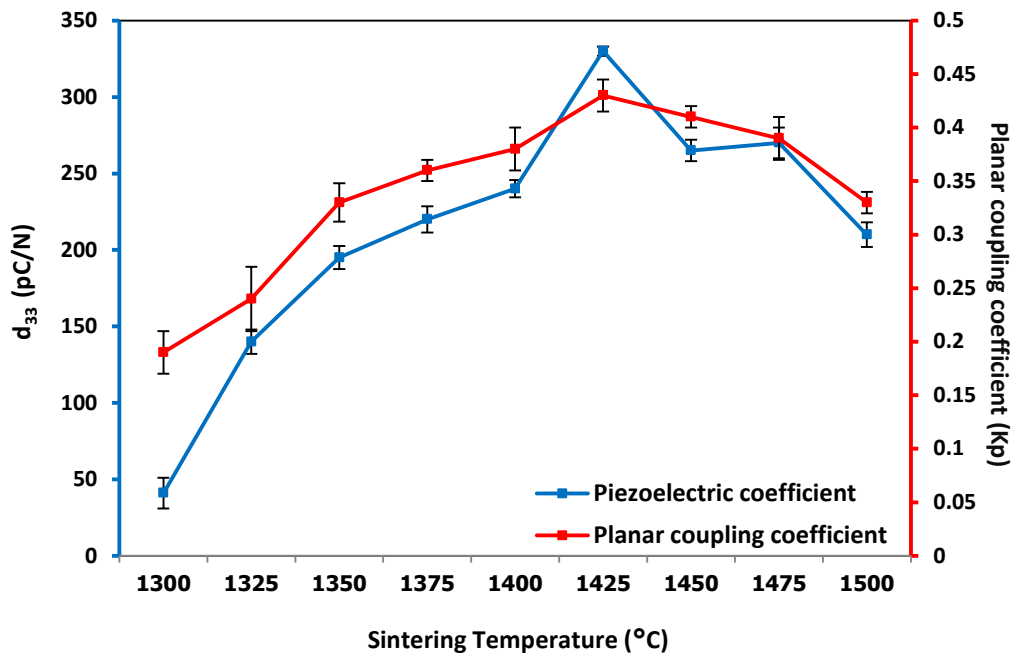


Figure 6.27 Piezoelectric coefficient and planar coupling of 50BCZT gel cast samples at a solids loading of 45 vol% and 40 wt% resin content sintered at different temperatures.

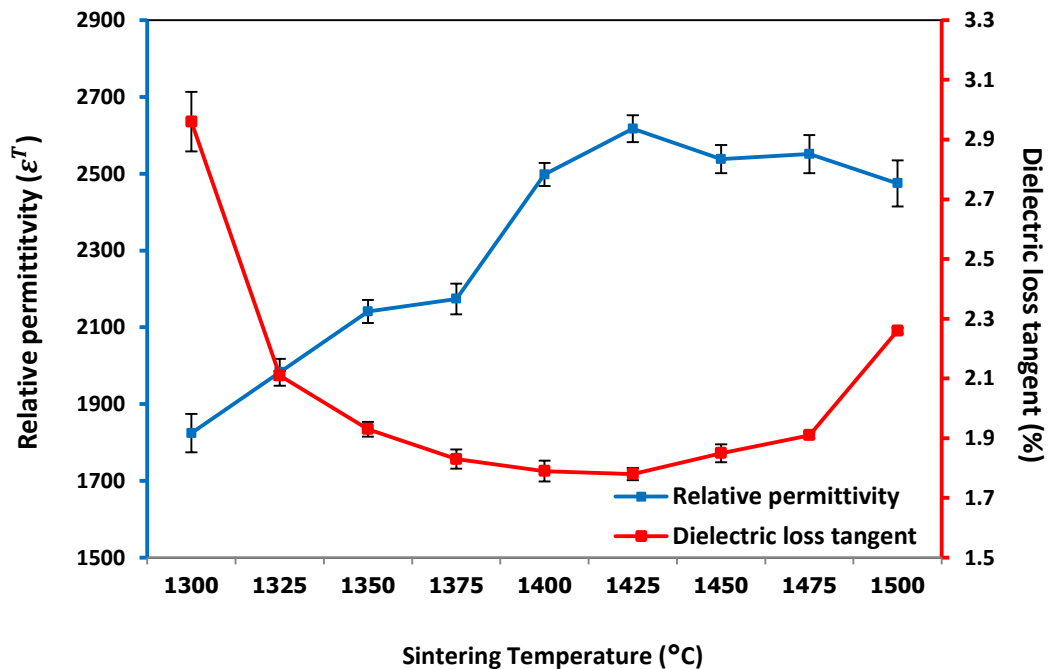


Figure 6.28 Permittivity and dielectric loss tangent of 50BCZT gel cast samples at a solids loading of 45 vol% and 40 wt% resin content sintered at different temperatures.

densification but also an increase of grain size. During the sintering process both densification and grain growth will occur, but can dominant at different temperatures. For the sample sintered at 1300 °C, the average of grain size was around  $1.03 \pm 0.25 \mu\text{m}$  with a small pore size. When the sintering temperature was increased to 1325, 1350, 1375 1400 and 1425 °C, the grain size increased to approximately  $13.67 \pm 0.32$ ,  $16.69 \pm 0.67$ ,  $20.05 \pm 0.70$ ,  $21.20 \pm 1.46$ , and  $25.69 \pm 1.73 \mu\text{m}$ , respectively and a corresponding reduction in porosity can be seen. In this range of sintering temperatures, densification dominated the sintering behaviour leading to the reduced porosity and increase in sintered density, while the average grain size increased but between 1375 °C - 1425 °C the grain size was maintained in the range of 20-25  $\mu\text{m}$ . The increase of sintering temperature above 1425 °C results in samples with average grain sizes of  $29.60 \pm 1.80$ ,  $30.23 \pm 1.57$  and  $31.81 \pm 0.92 \mu\text{m}$  for samples sintered at 1450, 1475 and 1500 °C , respectively while the sintering shrinkage and density decreased. The average grain size increased because the grain growth dominated over the densification which might cause trapped pores between grains according to Bai [19, 26], resulting in lower sintered densities and shrinkage. BCZT has been reported to have rapid grain growth [57] which could be bring some issues for fabricating of ultrafine structure bristle brock structures.

The influence of sintering temperature on the piezoelectric coefficient, planar coupling coefficient, dielectric constant and dielectric loss are presented in Figures 6.27 - 6.28. It can be seen that the  $d_{33}$ ,  $k_p$  and  $\epsilon^T$  increased while dielectric loss tangent decreased with increasing sintering temperature, corresponding to the increased sintered density. As expected, the sample sintered at 1300 °C showed the lowest values of  $d_{33}$ ,  $k_p$  and  $\epsilon^T$  with highest dielectric loss tangent compared to



samples sintered at 1325 °C - 1500 °C. It has been reported that the sintered density and grain size influence the piezoelectric and dielectric properties of sintered samples [58, 59], the increasing values the  $d_{33}$ ,  $k_p$  and  $\varepsilon^T$  with increased sintering temperature due to increased sintered density and grain size. When the sintering temperature increased from 1300 °C to 1425 °C, the sintered density and the average grain size increased thus improving  $d_{33}$ ,  $k_p$  and  $\varepsilon_r^T$  [58], and leading to a reduction in the dielectric loss tangent. The highest values of  $d_{33}$ ,  $k_p$  and  $\varepsilon^T$  were 330 pC/N, 0.43 and around 2617, respectively for samples sintered at 1425 °C. However, for sintering temperatures above 1425 °C, although the average grain size tended to increase with increasing sintering temperature, the dielectric loss tangent increased while  $d_{33}$ ,  $k_p$  and  $\varepsilon^T$  tended to decrease which is in agreement with reports from Bai [19] who explained that the large grain size will diminish the piezoelectric charge coefficient. Thus optimisation of properties requires a careful control of densification and grain growth during the sintering process.

## 6.6 Summary

This chapter has reported on the development of gel casting of lead free 50BCZT bulk samples based on a hydantoin epoxy resin and amine hardener system. The results can be summarised as follows;

(1) The amount of hardener, resin and curing temperature have a great influence on the polymerisation reaction of the premix solution. The optimum value for amine hardener (Bis (3-aminopropyl) amine) was PHR = 18 g per 100 g of resin as it provided the highest strength (highest  $G'$ ) with a gelation time of approximately 14 minutes which is reasonable for the casting and degassing process. The gelation time

is also dependent on curing temperature as the gelation time displays a tendency to decrease when the curing temperature is increased. The activation energy of the polymerisation reaction of this gel casting system was calculated as 82 kJ/mol while the elastic modulus slightly increased with increasing curing temperature. The strength of the gel formed by the ring open reaction can be improved by increasing resin content; with increasing the resin content to 40 wt% the elastic modulus showed 's highest value 1,570,000 Pa while the gelation time decreased to 5 minutes.

(2) The dispersant has an effect on the dispersion of the suspension, and it was found that 2.4 wt% of dispersant based on the dried 50BCZT powder weight offered the lowest viscosity.

(3) The viscosity increased with an increase in resin content and solids loading, the optimum solid loading was determined as 45 vol% as it was tailored between high solids loading with low viscosity suitable for this gel casting system.

(4) In this gel casting slurry, the increase of resin concentration from 10, 20, 30 to 40 wt% resulted in a decrease in gelation time from 25, 15, 11 to 7 minutes, respectively.

(5) Without de-airing processes, air entrapment in the gel casting slurry can give rise to pores in the green bodies leading to low strength and density of green and sintered samples.

(6) For green samples, with increasing resin content, the green density, drying shrinkage and green strength were enhanced, with the highest green strength of around 55 MPa being achieved for samples with 40 wt% resin. This is a much higher

value than that reported for EGDGE epoxy resins which have been has been promoted as a resin offering high green strength.

(7) For sintered samples, with increasing resin content, the sintered density and sintering shrinkage decreased possibly due to the increase of trapped gases and porosity, resulting in a decrease of sinterability. The highest  $d_{33}$  and  $k_p$  of around 330 pC/N and 0.43, respectively were obtained by using 30 wt% resin content while the highest  $\epsilon^T$  and the smallest dielectric lost tangent were found for samples with 20 wt% resin content. However, too high a resin content has a deleterious effect on piezoelectric and dielectric properties of sintered gel cast samples, as the properties were reduced for samples with a resin content of 40 wt%.

(8) The sintered temperature has a strong and complicated influence on key properties including sintered density, sintering shrinkage, piezoelectric and dielectric properties. When the sintered temperature increased from 1300 °C - 1425 °C, the densification slightly dominated the sintering behaviour as the reducing of porosity, increasing of sintered density and shrinkage can be observed while the grain size tended to be increase. On the other hand, above 1425 °C sintering shrinkage and density tented to decrease while the average grain size increased because the grain growth dominated over the densification which might cause trapped pores between grains. The highest values of piezoelectric and dielectric properties corresponded to samples sintered at 1425 °C.

## 6.7 References

1. Mao, X., et al., *Rheological characterization of gel casting system based on epoxy resin*. *Ceramics International*, 2009. **35**: p. 415-420.

2. Li, Y.F., et al., *Effects of epoxy/hardener stoichiometry on structures and properties of a diethanolamine-cured epoxy encapsulant*. IOP Conference Series: Materials Science and Engineering, 2016. **137**(1): p. 012012.
3. *How do you know how much hardener to mix with how much resin?* [Last accessed date 11/12/2016]; Available from: <http://www.mereco.com/resources/ask-the-doctor/hardener-to-resin-ratio>.
4. VANLANDINGHAM, M.R., R.F. EDULJEE, and J. J. W. GILLESPIE, *Relationships between stoichiometry, microstructure, and properties for amine-cured epoxies*. Journal of Applied Polymer Science, 1999. **71**: p. 699-712.
5. Tung, C.Y.M. and P.J. Dynes, *Relationship between viscoelastic properties and gelation in thermosetting systems*. Journal of Applied Polymer Science, 1982. **27**(2): p. 569-574.
6. Mao, X., et al., *Gelcasting of alumina using epoxy resin as a gelling agent*. Journal of the American Ceramic Society, 2007. **90**(3): p. 986-988.
7. Manjiang Dong, X.M., Zhaoquan Zhang, Qian Liu, *Gelcasting of SiC using epoxy resin as gel former*. Ceramics International, 2009. **35**: p. 1363-1366.
8. Xiaogang Xu, Z.W., Xiangwei Wu, Jiu Lin, Xiuyan Wang, *Rheology and chemorheology of aqueous LiAlO<sub>2</sub> slurries for gel-casting*. Ceramics International, 2009. **35**: p. 2191-2195.
9. Rui Xie, K.Z., Xueping Gan, Dou Zhang, *Effects of Epoxy Resin on Gelcasting Process and Mechanical Properties of Alumina Ceramics*. Journal of the American Ceramic Society, 2013. **96**(4): p. 1107-1112.
10. Xie, R., et al., *Fabrication of Fine-Scale 1–3 Piezoelectric Arrays by Aqueous Gelcasting*. Journal of the American Ceramic Society, 2014: p. n/a-n/a.
11. Jiang, Y., *Fabrication and characterisation of novel ultrasound transducers*, in *School of Metallurgy and Materials*. 2013, University of Birmingham.
12. Babaluo, A.A., M. Kokabi, and A. Barati, *Chemorheology of alumina–aqueous acrylamide gelcasting systems*. Journal of the European Ceramic Society, 2004. **24**(4): p. 635-644.
13. Zhou, J. and J.P. Lucas, *Hygrothermal effects of epoxy resin. Part I: the nature of water in epoxy*. Polymer, 1999. **40**(20): p. 5505-5512.
14. Ellis, T.S. and F.E. Karasz, *Interaction of epoxy resins with water: the depression of glass transition temperature*. Polymer, 1984. **25**(5): p. 664-669.
15. Wu, L., S.V. Hoa, and M.-T. Ton-That, *Effects of water on the curing and properties of epoxy adhesive used for bonding FRP composite sheet to concrete*. Journal of Applied Polymer Science, 2004. **92**(4): p. 2261-2268.
16. Van Assche, G. and B. Van Mele, *Interphase formation in model composites studied by micro-thermal analysis*. Polymer, 2002. **43**(17): p. 4605-4610.
17. Kingery, W.D., *Introduction to ceramics*. 1960: Wiley.
18. Somiya, S., et al., *Handbook of Advanced Ceramics: Materials, Applications, Processing and Properties*. 2003: Elsevier Science.
19. Bai, Y., et al., *(Ba,Ca)(Zr,Ti)O<sub>3</sub> lead-free piezoelectric ceramics—The critical role of processing on properties*. Journal of the European Ceramic Society, 2015. **35**(13): p. 3445-3456.
20. Jung, S.J., et al., *Surface Energy Driven Agglomeration and Growth of Single Crystal Metal Wires*. Nano Letters, 2011. **11**(3): p. 1294-1299.
21. Gartenby, A. *How Does Surface Tension Relate to Viscosity?* [Last accessed date 5/01/2016]; Available from: <http://www.cscscientific.com/csc-cientific-blog/bid/52996/How-Does-Surface-Tension-Relate-to-Viscosity>.
22. Matousek, A. *BCZT density*. 2013.

23. Zielinski, J.M. and L. Kettle. *Pharmaceutical Physical Characterization: Surface Area and Porosity*. 2013 [Last accessed date 12/02/2016]; Available from: [https://www.google.co.uk/url?sa=t&rct=j&q=&esrc=s&source=web&cd=1&cad=rja&uact=8&ved=0ahUKEwj0jebJgsrQAhUIJcAKHRSqDecQFgggMAA&url=https%3A%2F%2Fwww.researchgate.net%2Ffile.PostFileLoader.html%3Fid%3D5438f865d5a3f2bb438b45b4%26assetKey%3DAS%253A271831511044096%25401441821090658&usg=AFQjCNHA4aGqf03svu0em8muCLxTjnp1Bg&sig2=ucvo25\\_xz2Ofu6peYnQmVg&bvm=bv.139782543,d.bGs](https://www.google.co.uk/url?sa=t&rct=j&q=&esrc=s&source=web&cd=1&cad=rja&uact=8&ved=0ahUKEwj0jebJgsrQAhUIJcAKHRSqDecQFgggMAA&url=https%3A%2F%2Fwww.researchgate.net%2Ffile.PostFileLoader.html%3Fid%3D5438f865d5a3f2bb438b45b4%26assetKey%3DAS%253A271831511044096%25401441821090658&usg=AFQjCNHA4aGqf03svu0em8muCLxTjnp1Bg&sig2=ucvo25_xz2Ofu6peYnQmVg&bvm=bv.139782543,d.bGs).
24. Bauer, J.F., *Pharmaceutical Solids: Size, Shape, and Surface Area*. Journal of Validation Technology, 2009. **Winter 2009**.
25. Bjørnetun Haugen, A., et al., *Structure and phase transitions in 0.5(Ba0.7Ca0.3TiO3)-0.5(BaZr0.2Ti0.8O3) from -100 °C to 150 °C*. Journal of Applied Physics, 2013. **113**(1): p. 014103.
26. Bai, Y., *Vibrational energy harvesting using piezoelectric ceramics and free-standing thick-film structures*. 2015, University of Birmingham.
27. Guo, D., et al., *Application of gelcasting to the fabrication of piezoelectric ceramic parts*. Journal of the European Ceramic Society, 2003. **23**(7): p. 1131-1137.
28. Guo, D., et al., *Gelcasting of PZT*. Ceramics International, 2003. **29**(4): p. 403-406.
29. Guo, D., et al., *Anti-crack machining of PZT ceramics for fabricating piezocomposites by using gelcasting technique*. Materials Science and Engineering B-Solid State Materials for Advanced Technology, 2003. **99**(1-3): p. 25-28.
30. Garcia-Gancedo, L., et al., *Application of gel-casting to the fabrication of 1-3 piezoelectric ceramic-polymer composites for high-frequency ultrasound devices*. Journal of Micromechanics and Microengineering, 2012. **22**(12).
31. Zhang, D., B. Su, and T.W. Button, *Microfabrication of Three-Dimensional, Free-Standing Ceramic MEMS Components by Soft Moulding*. Advanced Engineering Materials, 2003. **Vol.5(12)**: p. 924-927.
32. Olhero, S.M., et al., *Innovative fabrication of PZT pillar arrays by a colloidal approach*, in *Journal of the European Ceramic Society* 2012. p. 1067-1075.
33. Bergstrom, L., *Handbook of Applied Surface and Colloid Chemistry Volume 1*, ed. K. Holmberg. Vol. 1. 2002: JOHN WILEY & SONS, LTD. 201-215.
34. Guo, D., et al., *Water based gelcasting of lead zirconate titanate*. Materials Research Bulletin, 2003. **38**(5): p. 807-816.
35. Lewis, J.A., *Colloidal Processing of Ceramics*. Journal of the American Ceramic Society, 2000. **83**(10): p. 2341-2359.
36. Napper, D.H., *Polymeric stabilization of colloidal dispersions*. 1983: Academic Press Incorporated.
37. Jiang, C., et al., *Gelcasting of aluminum nitride ceramics using hydantion epoxy resin as gelling agent*. Ceramics International, 2013. **39**(8): p. 9429-9433.
38. Chen, B., et al., *Gel-casting of beta-TCP using epoxy resin as a gelling agent*. Journal of the European Ceramic Society, 2008. **28**(15): p. 2889-2894.
39. Xiang, J.H., Y. Huang, and Z.P. Xie, *Study of gel-tape-casting process of ceramic materials*. Materials Science and Engineering a-Structural Materials Properties Microstructure and Processing, 2002. **323**(1-2): p. 336-341.
40. Zhang, D., B. Su, and T.W. Button, *Preparation of concentrated aqueous alumina suspensions for soft-molding microfabrication*. Journal of the European Ceramic Society, 2004. **24**(2): p. 231-237.
41. Khan, A.U., B.J. Briscoe, and P.F. Luckham, *Interaction of binders with dispersant stabilised alumina suspensions*. Colloids and Surfaces A: Physicochemical and Engineering Aspects, 2000. **161**(2): p. 243-257.

42. Ewais, E.M.M. and A. Safari, *Gelation of water-based PZT slurries in the presence of ammonium polyacrylate using agarose*. Journal of the European Ceramic Society, 2010. **30**(16): p. 3425-3434.
43. Gilissen, R., et al., *Gelcasting, a near net shape technique*. Materials & Design, 2000. **21**(4): p. 251-257.
44. Jiang, C., et al., *Preparation of high performance AlN/Hydantion composite by gelcasting and infiltration processes*. Ceramics International, 2014. **40**(1, Part B): p. 2535-2538.
45. Wonisch, A., et al., *A Comprehensive Simulation Scheme for Tape Casting: From Flow Behavior to Anisotropy Development*. Journal of the American Ceramic Society, 2011. **94**(7): p. 2053-2060.
46. Liu, X., Y. Huang, and J. Yang, *Effect of rheological properties of the suspension on the mechanical strength of Al<sub>2</sub>O<sub>3</sub>-ZrO<sub>2</sub> composites prepared by gelcasting*. Ceramics International, 2002. **28**(2): p. 159-164.
47. Gang Jian, et al., *Effect of solid content variations on PZT slip for tape casting*. Processing and Application of Ceramics, (2012). **6**(4): p. 215-221.
48. Xue, J., et al., *Gelcasting of Aluminum Nitride Ceramics*. Journal of the American Ceramic Society, 2010. **93**(4): p. 928-930.
49. Dongliang, J. and Z. Jingxian, *Properties of Carbide Ceramics from Gelcasting and Pressure-less Sintering*. IOP Conference Series: Materials Science and Engineering, 2011. **18**(20): p. 202001.
50. Xie, R., et al., *Gelcasting of alumina ceramics with improved green strength*. Ceramics International, 2012. **38**(8): p. 6923-6926.
51. Otsubo, Y., *Rheology Control of Suspensions by Soluble Polymers*. Langmuir, 1995. **11**(6): p. 1893-1898.
52. Hsieh, Y.L., J.M. Regenstein, and M.A. Rao, *Gel Point of Whey and Egg Proteins Using Dynamic Rheological Data*. Journal of Food Science, 1993. **58**(1): p. 116-119.
53. Liu, G., et al., *Rheological characterization and shape control in gel-casting of nano-sized zirconia powders*. Ceramics International, 2014. **40**(9, Part A): p. 14405-14412.
54. Mao, X., et al., *Investigation of New Epoxy Resins for the Gel Casting of Ceramics*. Journal of the American Ceramic Society, 2008. **91**(4): p. 1354-1356.
55. Castkova, K., et al., *Chemical Synthesis, Sintering and Piezoelectric Properties of Ba<sub>0.85</sub>Ca<sub>0.15</sub>Zr<sub>0.1</sub>Ti<sub>0.9</sub>O<sub>3</sub> Lead-Free Ceramics*. Journal of the American Ceramic Society, 2015. **98**(8): p. 2373-2380.
56. Tsai, D.-S., *Pressure buildup and internal stresses during binder burnout: Numerical analysis*. AIChE Journal, 1991. **37**(4): p. 547-554.
57. Lee, H.-Y., et al., *Effect of sintering temperature on the secondary abnormal grain growth of BaTiO<sub>3</sub>*. Journal of the European Ceramic Society, 2000. **20**(6): p. 731-737.
58. Wu, J., et al., *Sintering temperature-induced electrical properties of (Ba<sub>0.90</sub>Ca<sub>0.10</sub>)(Ti<sub>0.85</sub>Zr<sub>0.15</sub>)O<sub>3</sub> lead-free ceramics*. Materials Research Bulletin, 2012. **47**(5): p. 1281-1284.
59. Huan, Y., et al., *Grain Size Effects on Piezoelectric Properties and Domain Structure of BaTiO<sub>3</sub> Ceramics Prepared by Two-Step Sintering*. Journal of the American Ceramic Society, 2013. **96**(11): p. 3369-3371.

# **Chapter 7 Optimisation of the gel casting process for lead-based powders**

## **7.1 Introduction**

Although the fabrication of lead free high frequency ultrasound transducers with random composite structure for medical imaging is the main focus of this thesis, lead based transducers have also been studied so that a true comparison of performance can be made. Therefore, gel casting systems based on PZT powders and hydantoin epoxy resin were studied. Generally, the premix solution of gel casting system does not contain ceramic powder; therefore, for the PZT and hydantoin epoxy resin gel casting system, the optimum amine hardener with PHR = 18 g per 100 g of resin that was developed for the lead free system, and reported in Chapter 6, was also utilised for the lead based system. In the search for the optimum composition of a gel casting slurry, the main constituents including dispersant and resin concentration and solids loading have been studied and are reported in this chapter. Bulk samples have been fabricated in the form of discs and bars and their properties characterized in order to study the property trend before applying the process to the fabrication of ultrafine random composite structures. The specific requirements of a gel casting system suitable for the fabrication of bristle blocks with fine scale pillar structures have been outlined and discussed in detail in Chapter 6, so are not repeated here.

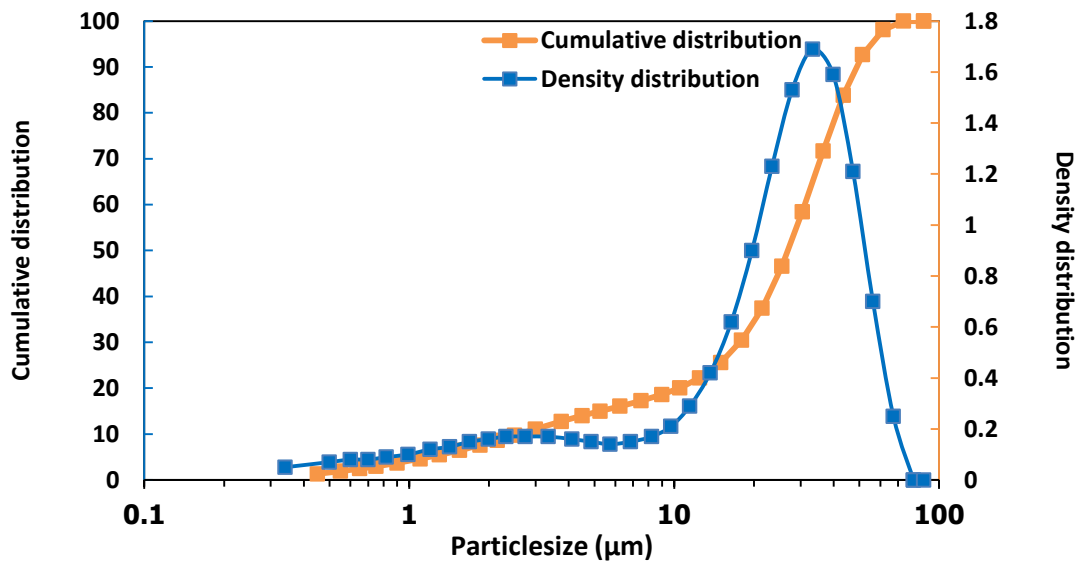
## 7.2 Optimisation of lead based powder and slurries

### 7.2.1 Lead based powder characterisation

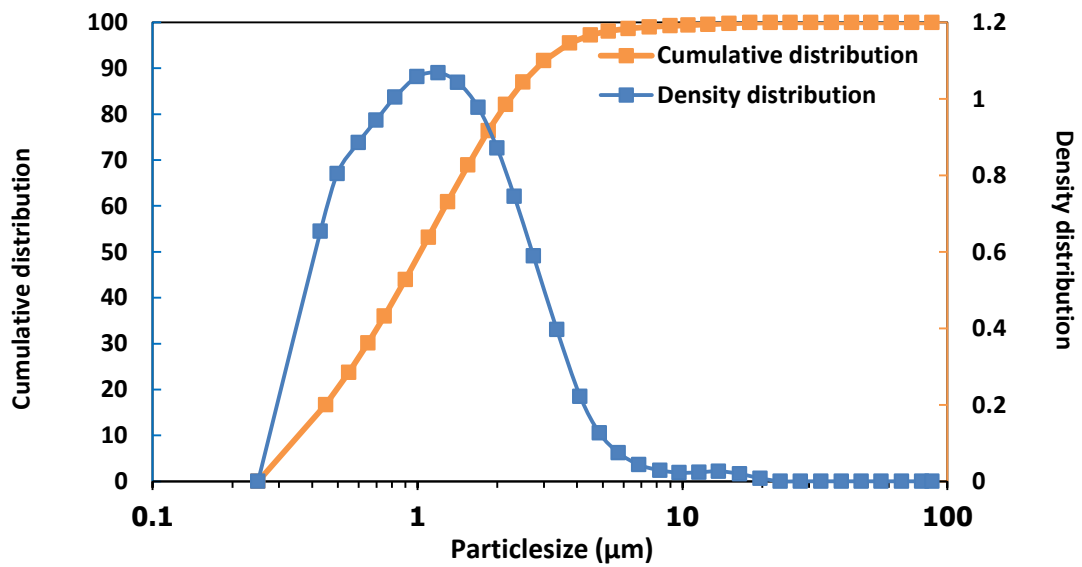
#### 7.2.1.1 Particle size analysis

A commercial PZT powder TRS 610 was selected for this study. The particle size distribution of the as-received powder is shown in Figure 7.1 (a) to have a bimodal distribution with peaks centred at 26.95  $\mu\text{m}$  and 2.60  $\mu\text{m}$ , respectively indicating significant agglomeration. After vibro milling for 48 hrs the average particle size was reduced to around 1.2  $\mu\text{m}$  with an almost unimodal distribution, indicating the agglomerates had been broken down. Using Equation 6.2, and assuming the powders are spherical and nonporous, the specific surface area (SSA) and the density of the PZT powders ( $7.95 \text{ g/cm}^3$ ) [1] can be used for calculating the average particle size. The SSA of the PZT powders in the as-received condition and after vibro-milling were measured by BET single point nitrogen adsorption to be  $1.4325 \text{ m}^2/\text{g}$  and  $1.6302 \text{ m}^2/\text{g}$ , respectively. These values equate to calculated average particle size values of 0.53  $\mu\text{m}$  and 0.46  $\mu\text{m}$ , respectively. A similar discrepancy in the particle sizes measured by the two techniques was also found for the 50 BCZT powders. The BET measurement may be more reliable for the measurement of the primary particle size in the as-received powder because the nitrogen gas can penetrate the agglomerate structures. Figure 7.2 (a) shows the SEM micrograph of as-received powders, the powder morphology has a doughnut shape granules from spray drying. The agglomeration can be seen with a broad range of powder size from less than 5  $\mu\text{m}$  to over 30  $\mu\text{m}$ , the large agglomerates were broken down after the powders were vibro-milled for 48 hrs., leading to the fine particles as seen in Figure 7.2 (b).



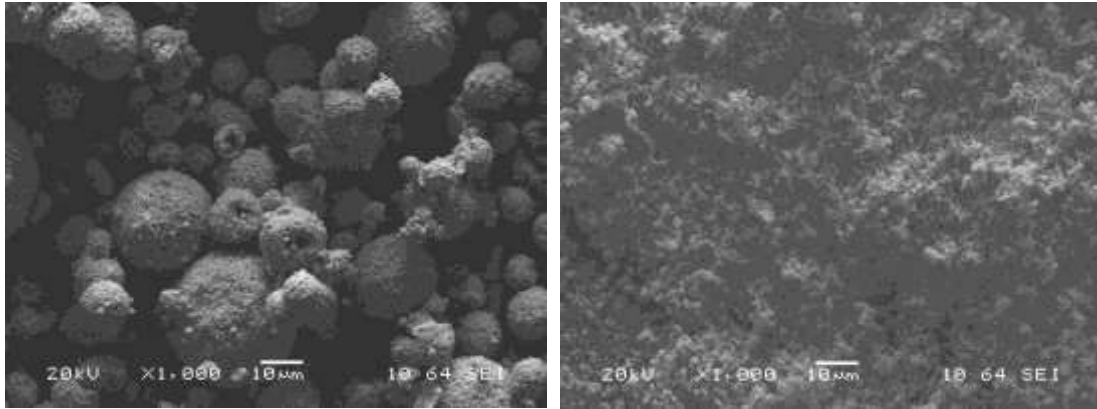


(a)



(b)

Figure 7.1 The particle size distribution of the (a) as-received PZT powder and (b) PZT powder after vibro-milling for 48 hrs.



(a)

(b)

**Figure 7.2 SEM micrographs of (a) as-received PZT powders and (b) after vibro-milling for 48 hrs.**

### **7.2.1.2 Crystalline material structure**

Figure 7.3 shows the XRD patterns of the as-received PZT powders and discs sintered at 1200 °C. Both XRD patterns can be indexed as a tetragonal perovskite phase, the patterns of as-received powder matched with ICSD code : 86136 [2], the pattern being similar to  $\text{Pb}(\text{Zr}_{0.52}\text{Ti}_{0.48})\text{O}_3$ . A slight shift in peak positions was noticed in the sintered ceramic compared to the as-received powder. According to Bai [3], the XRD pattern of sintered samples shifts because the La element, which was claimed by the company as the dopant for soft PZT, was only fully incorporated into the PZT structure during the sintering process.

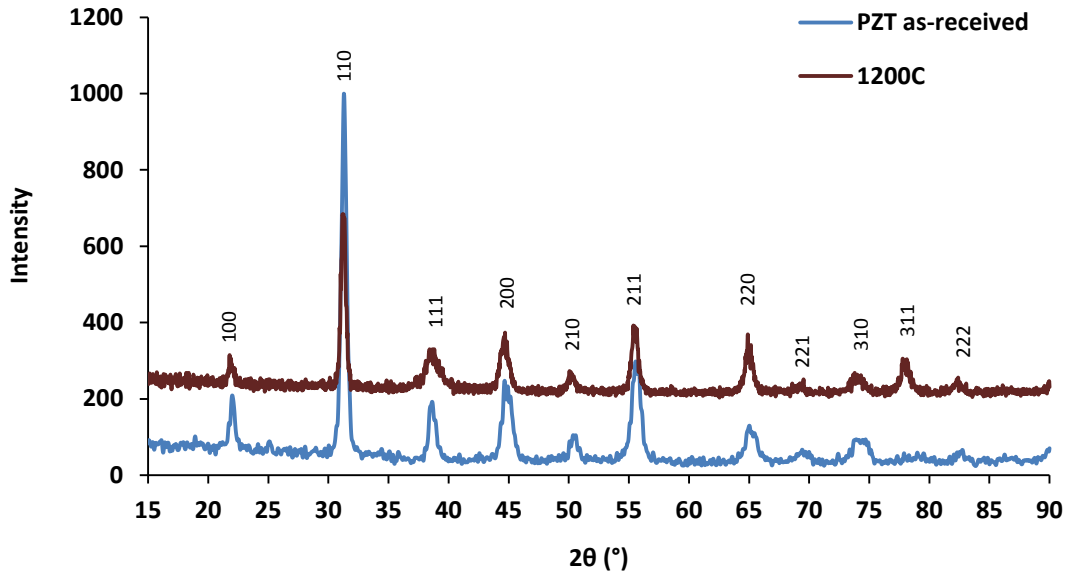


Figure 7.3 XRD patterns of PZT as-received powder and PZT discs sintered at 1200 °C.

### 7.2.2 Organic burnout

As the gel casting system in this project was based on a water soluble epoxy resin burnout of the resin and any other organics is one of the most important steps to be considered in order to achieve complete removal of polymer and determine the appropriate heating rate and sintering profile. The pyrolysis process of polymer in dried PZT gel cast sample during sintering in air was monitored by using thermal analysis technique (TGA/DSC). Generally, epoxy resin is expected to completely burnout before the ceramic starts to sinter; therefore, in this project, only PZT powder was studied the pyrolysis process and the data was also considered to be representative for the gel cast 50BCZT system.

A gel cast PZT sample with 48 vol% solids loading and resin content of 20 wt% epoxy resin was prepared and then dried for 24 hrs at room temperature, 24 hrs in an oven at 40°C followed by a further 2 hrs at 100 °C before starting this experiment. Figure 7.4 shows the TGA (wt% loss) and DSC (mW/mg) data of the sample

measured in air at 5 °C/minute. It can be seen that the main exothermic peak in DSC occurs at approximately 320 °C with a corresponding weight loss in the temperature range 200 °C - 420 °C, which can be attributed to the burnout of all the additives in the PZT compact. The total weight loss is around 3.08 wt% which is in agreement with calculated weight loss value of 3.12 wt% (epoxy resin, amine hardener and dispersant). This confirms that the organic additives in the gel cast green sample were decomposed completely before 420 °C.

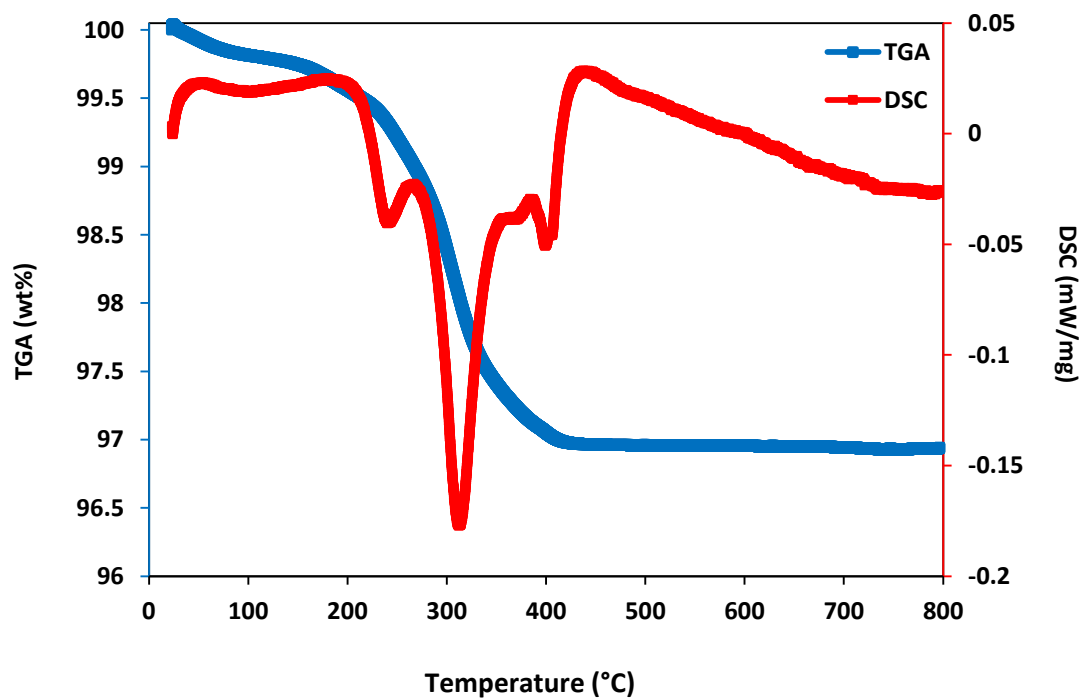


Figure 7.4 Thermal analysis of a gel cast PZT green compact with 20% resin in premixed solution at 48 Vol % solids loading measured at 5°C/minute.

## 7.2.3 Lead based slurries characterisation

### 7.2.3.1 Influence of dispersant concentration on viscosity of lead based slurry

As mentioned in section 6.3.2.1, homogeneous, flowable, low viscosity and stable slurries with high ceramic solids loading are required for gel casting [4-6]. Generally, the dispersant can be utilised as an additive for enhancing the slurry viscosity. Therefore, for the PZT gel casting system, the effect of dispersant on the PZT slurry was studied in order to search for the optimum dispersant concentration that minimizes the viscosity. The experiment was carried out under the same conditions as for the 50BCZT slurry and using the same dispersant (solution of an ammonium salt of an acrylic polymer in water ( $\text{NH}_4\text{PAA}$ ) or Dispex AA4040) as it is well known being a good dispersant for aqueous ceramic systems [7-10], as described in Section 6.3.2.1.

Figure 7.5 shows the influence of dispersant concentration on the viscosity behaviour of PZT slurries with 48% vol solids loading and 20% resin content at a shear rate of  $100 \text{ s}^{-1}$ . It can be clearly seen that the optimum dispersant concentration was 1.0 wt% which provided the lowest viscosity of the slurry with a value of 0.14 Pa.s. This result confirms that the viscosity of slurries can be minimised by an appropriate addition of dispersant which is in agreement with the result obtained from the 50BCZT slurry and the result reported by Jiang [7]. Compared to 50BCZT, the viscosity of the PZT gel casting slurry required a lower concentration of dispersant to achieve the minimum viscosity value. This might be due to the difference of the average particle size between these two powders. According to Olhero *et al.* [10, 11], slurries containing finer powders exhibit higher viscosities as the finer powders have higher specific surface areas and therefore require more dispersant to completely cover the particle surfaces. As presented in section 6.3.1.1, the average particle size of 50BCZT powder after vibro-milling for 7 hrs. was around  $0.94 \mu\text{m}$ , compared to

1.2  $\mu\text{m}$  for the vibro milled PZT powder. Therefore, at the same vol% solids loading and resin content, the optimum dispersant concentration of the 50BCZT gel cast slurry was higher (2.4 wt%) compared to the 1wt% for the PZT slurry.

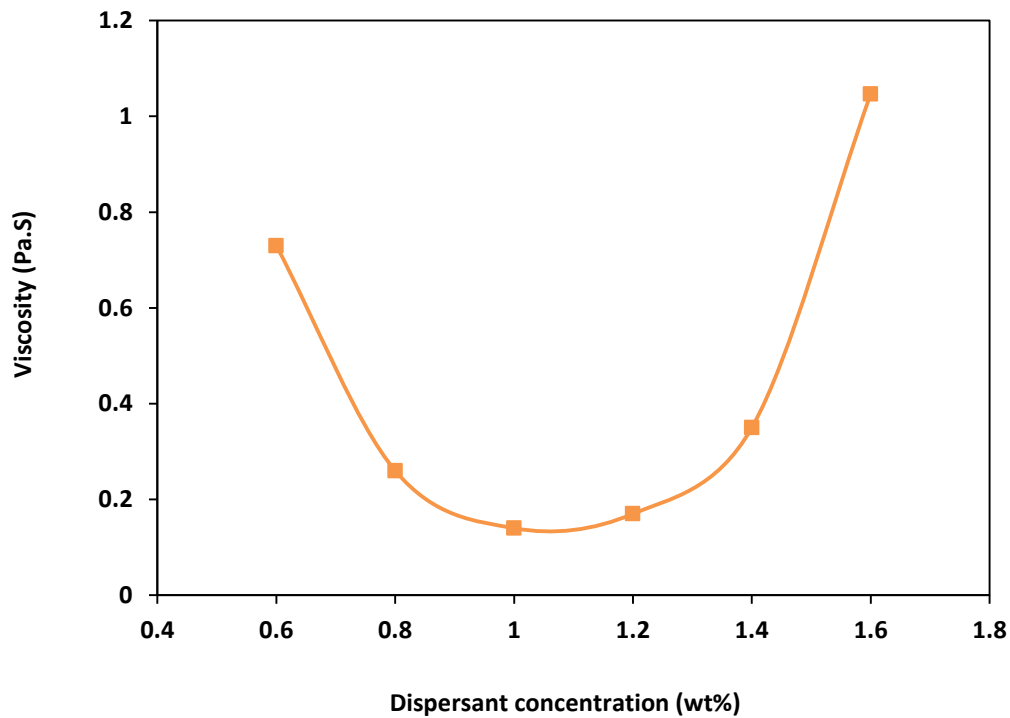


**Figure 7.5** Viscosity of the PZT slurry with 48% vol solids loading and 20 wt% resin contents as a function of dispersant concentration measured at the shear rate  $100 \text{ s}^{-1}$ .

### **7.2.3.2 Influence of solids loading on viscosity of lead based slurry**

The rheological curves of PZT slurries at various solids loadings with 20 wt% resin content and 1 wt% dispex AA4040 (based on dry solid) are shown in Figure 7.6.

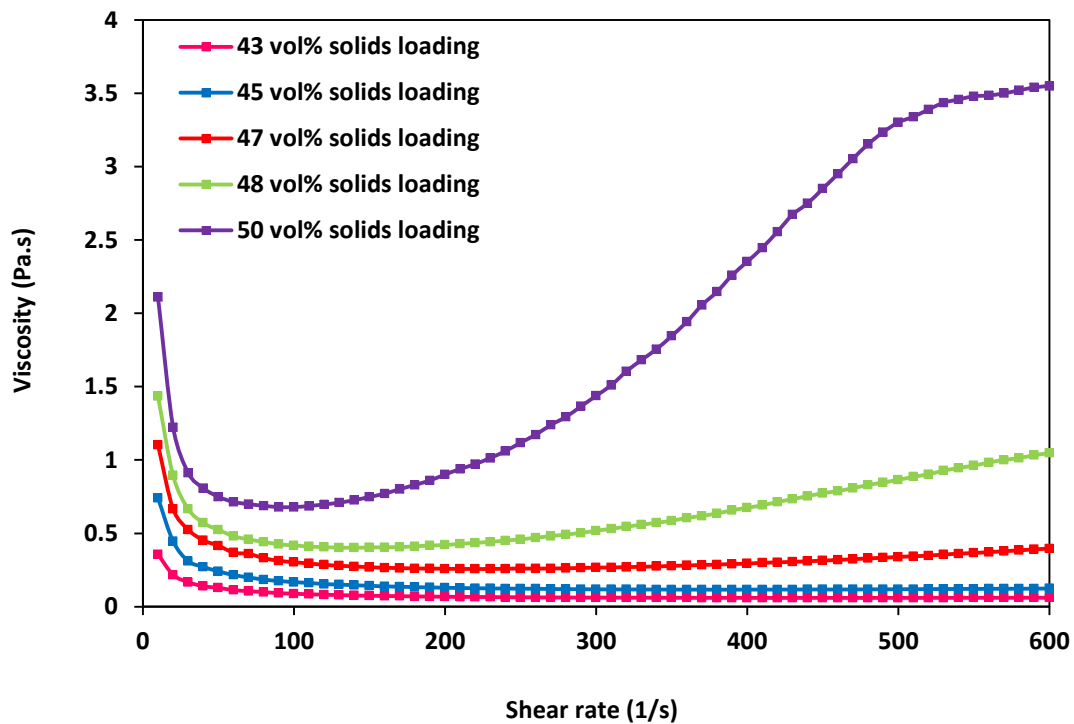


Figure 7.6 Viscosity curves as a function of shear rate of the PZT slurry at various solids loadings with 20 wt% resin content using optimum dispersant concentration and hardener content.

Compared to the results for 50BCZT slurries (see Figure 6.3.2.2), all the PZT slurries also exhibit non-Newtonian flow behaviour [12], and the viscosity changed with changing volume fraction and shear rate. For slurries with 43, 45, 47 and 48 Vol% solids loading, the higher viscosities of slurries were found at low shear rate as the thermal motion of ceramic particles was dominant over the viscous force while at high shear rate, the slurries exhibited shear thinning behaviour and most slurries exhibited an approximately constant viscosity as the viscous forces dominated the structure of the slurry [13-15]. This implies that the differences in viscosity are more significant at low shear rate for solids loadings ranging from 43 vol% solids loading to 47 vol%. All slurries exhibited a viscosity lower than 1 Pa.s at shear rate  $100 \text{ s}^{-1}$

which means they were suitable for the gelcasting process. At high shear rate, the viscosity of the slurry with 48 vol% solids loading tended to slightly increase. However, at the highest shear rate measured ( $600 \text{ s}^{-1}$ ), the viscosity was still lower than  $1 \text{ Pa}\cdot\text{s}$ . The viscosity of the 50 vol% solids loading slurry showed obvious shear thickening behaviour with viscosity  $>1 \text{ Pa}\cdot\text{s}$  at a shear rate of  $600 \text{ s}^{-1}$ . This might be due to the slurry containing too high a solids loading. Therefore, the viscous force did not overcome the attractive force between particles, resulting in flocculation during measurement and increasing of viscosity. Therefore, the optimum solid loading was determined as 48 vol%.

### **7.2.3.3 Influence of resin content on viscosity and gelation time of lead free slurry**

Viscosity measurements as a function of shear rate of PZT slurries with 48 vol% solids loading, 1 wt% Dispex AA4040 after mixing with optimal hardener, and resin contents ranging from 10 wt% to 40 wt %, are shown in Figure 7.7. Compared to 50BCZT slurries (see Fig 6.3.2.3), the PZT slurries exhibited lower viscosity due to the larger particle size and lower specific surface area of the PZT vibro-milled powder. It can be seen that the viscosity of lead based slurries were also affected by resin content. All lead based slurries displayed a shear thinning behaviour and viscosity.



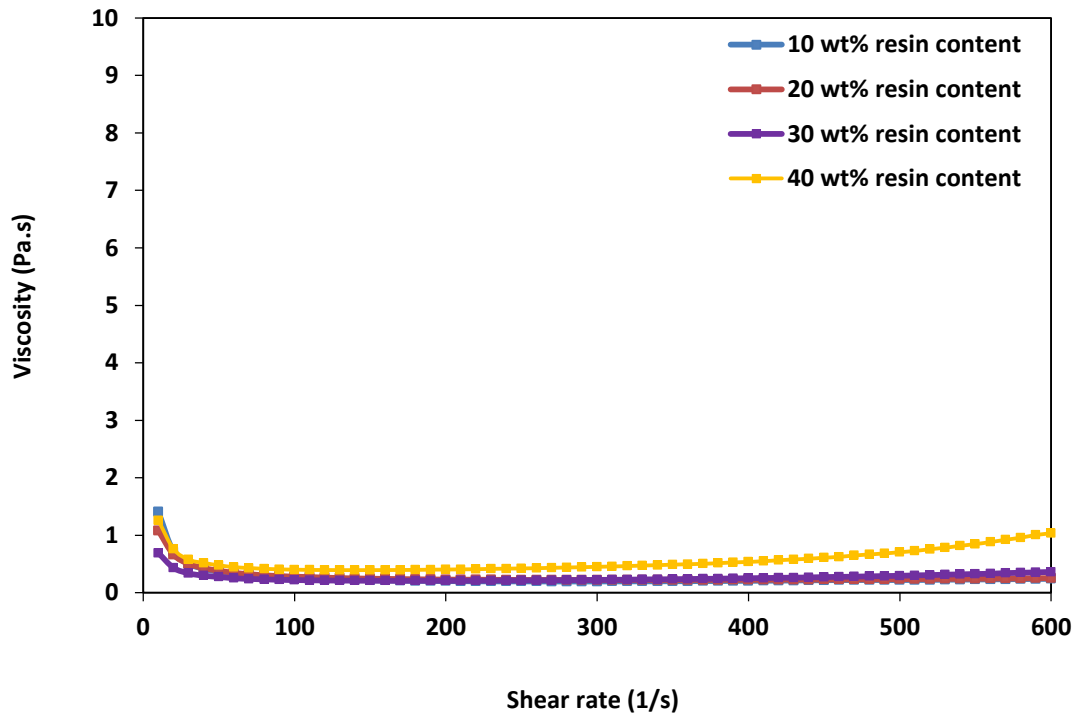


**Figure 7.7** Viscosity curves as a function of shear rate of the PZT 48 vol % solids loading slurry at various resin contents loading using optimum dispersant concentration and hardener content.

gradually increased with increasing hydantoin epoxy resin content which is in agreement with the 50BCZT gel casting system. Possible reasons for the increase in viscosity with an increase of resin content have been discussed in section 6.3.2.3.

As mentioned in Chapter 6, the viscosity of slurry at shear rate of  $100 \text{ s}^{-1}$  should be lower than  $1.0 \text{ Pa.s}$  in order to ensure that the slurry has flowability for casting into the mould cavity. With increase in resin content from 10 wt% to 40 wt%, the viscosities at shear rate  $100 \text{ s}^{-1}$  increased from 0.22 to 0.25 Pa.s, respectively. This means all slurries presented a good fluidity during the casting process, even at the highest resin concentration of 40 wt%, the viscosity of slurry tended to slightly increase. However, at highest shear rate ( $600 \text{ s}^{-1}$ ), the viscosity of the gel casting system was still lower than  $1 \text{ Pa.s}$  and still acceptable for casting. The available time

for mixing, casting and degassing was also studied. As mentioned in section 6.3.2.3, there are several criteria for the indication of the gelation time. The time taken for an abrupt increase in the viscosity of the slurry has been taken as the most applicable for this project. The gelation time of PZT slurries with 48 vol% solids loading, 1 wt% of Dispex AA4040 at various resin contents were determined by measuring the viscosity as a function of time at a constant shear rate of  $0.1 \text{ s}^{-1}$  and temperature of  $25^\circ\text{C}$ . The start time is taken after the slurries have been mixed with hardener. Figure 7.8 shows the effect of hydantoin epoxy resin concentration on gelation behaviour. It can be clearly seen that all of the slurries presented a period with constant viscosity and then the viscosity of slurries of all resin contents increased dramatically, which are in agreement with the results from the 50BCZT slurries and other research projects [7, 14, 16, 17]. It can be observed that with an increase of resin content from 10, 20, 30 to 40 wt%, the gelation time decreased from approximately 28, 18, 11 to 9 minutes, respectively. As the gelation time should not be less than 10 minutes or more than 70 minutes in order to achieve high efficiency production, in term of gelation time, therefore, 10, 20 and 30 wt% resin contents are suitable for the gel casting process.

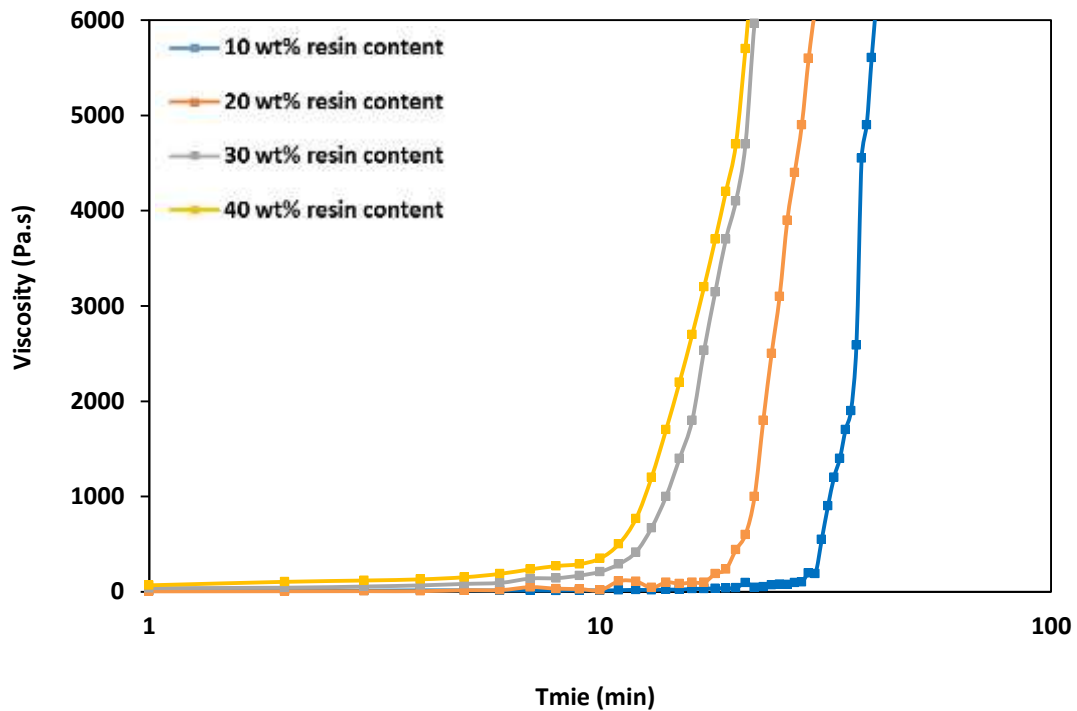


Figure 7.8 Viscosity curves as a function of time of the PZT 48 vol % solids loading slurry at various resin contents loading using optimum dispersant concentration and hardener content.

### 7.3 Characterization of lead based gel cast green bodies

Lead based gel cast green samples were produced at room temperature by using the optimum hardener content and with 48 vol% solids loading at different resin contents using the casting processes developed for 50BCZT and described in Chapter 6. Figure 7.9 shows a typical gel casting sample of around 12 mm in diameter and around 1.5 mm in height after demoulding and drying prepared from PZT powders. Green 50BCZT and PZT samples were almost identical in appearance with good geometrical replication from the mould, no visible cracks and also having sufficient strength for handling. Figure 7.10 shows the SEM micrographs of the fracture surfaces of the gel cast green bodies obtained from 48 vol% solids loading with resin contents ranging from 10 wt% - 40 wt%.



**Figure 7.9 Green PZT gel cast sample obtained from 48 vol% solids loading with 20wt% resin and 1 wt% Dispex AA4040 after demoulding and drying.**

All green PZT samples presented a uniform structure with no large defects, indicating an homogeneous structure. Moreover, the particle outlines were also less distinct at higher resin contents while the outlines were more obvious in the samples with lower resin content. This is in agreement with the SEM fracture surfaces of green PZT samples reported by Jiang [7] and 50BCZT gel cast samples reported in Chapter 6.

It can be seen in Figure 7.11 that the resin content has a strong influence on green density and shrinkage as they both increased with an increase of resin content, leading to homogeneous microstructures and enhanced sintering rate, the results are also in agreement with PZT 45 vo% solids loading using EGDGE as an epoxy resin reported by Jiang [7] and similar to the results obtained from green 50BCZT samples presented in section 6.4.

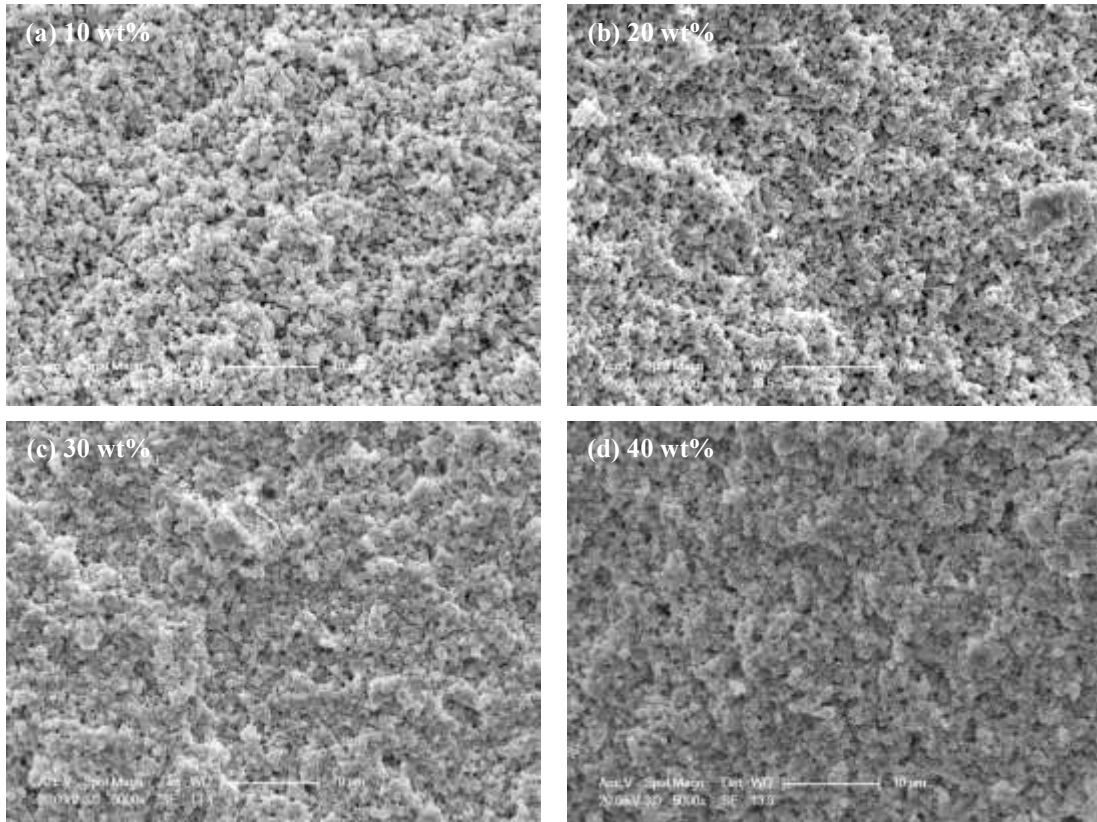


**Figure 7.10 SEM micrographs of fracture surface of PZT green bodies obtained from 48 vol% solids loading with various hydantoin epoxy resin concentrations (a) 10 wt% (b) 20 wt% (c) 30 wt% (d) 40 wt% after demoulding and drying.**

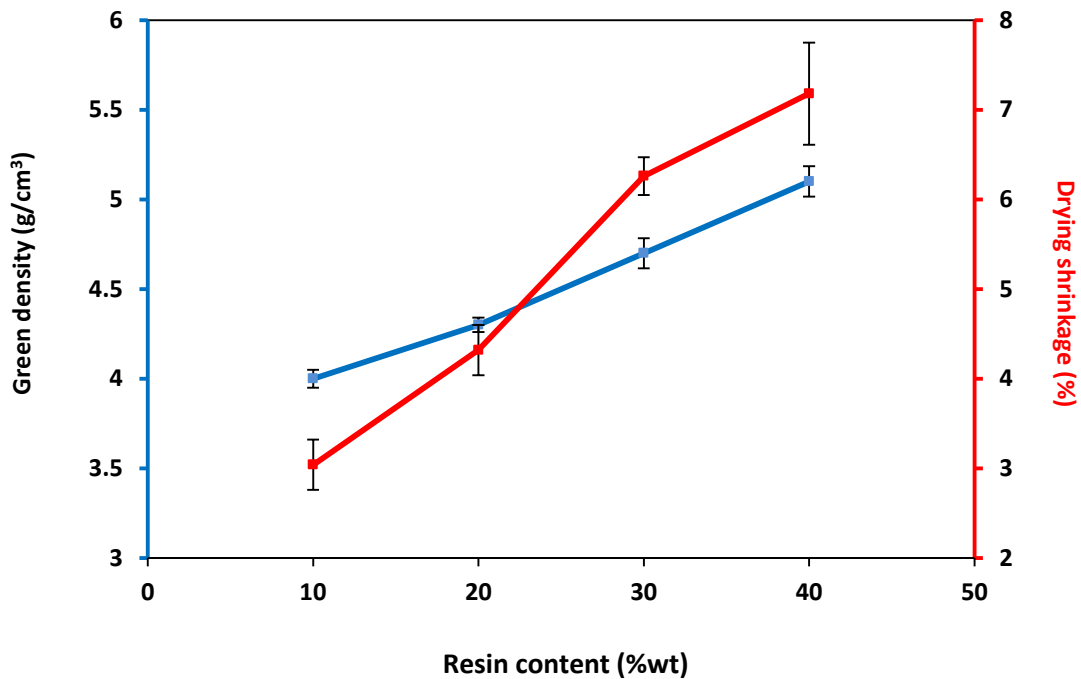


**Figure 7.11** Green density and drying shrinkage of PZT gel cast green samples versus resin content at a solid loading of 48 vol%.

Figure 7.12 shows the green strength of green PZT gel casting sample obtained from 48 vol% solids loading at various resin contents. It can be seen that the green sample with the highest resin content presented the highest green strength which is also similar to the trend of increasing green strength of 50BCZT gel casting samples. The increase of hydantoin epoxy resin content from 10 wt% to 40 wt% led to a corresponding increase in the green strength from 24 MPa to 58 MPa. As mentioned in section 6.4, this can be attributed to the higher resin contents leading to enhanced green density and a correspondingly higher green strength. Therefore, the green PZT gel cast samples possessed higher green strength values than the green 50BCZT samples. However, it has been reported by Xie *et al.* [18] that green PZT samples obtained from 55 vol% solids loading and 20 wt% hydantoin epoxy resin provided a green strength of around 48 MPa. This might be due to the difference in vol% solid

loading and type of dispersant. According to Jiang [7], the green strength of green PZT gel cast samples with 45 vol% solids loading reached a maximum value of 38 MPa at 40 wt% EGDGE epoxy resin. Thus the hydantoin epoxy resin enhances the green density and green strength of samples as it provided the higher values of both properties. These initial studies provided the conclusion that the green strength obtained from these green samples were sufficient for demoulding and handling as the green strength were higher than 10 MPa. which are required for successful demoulding of green samples.

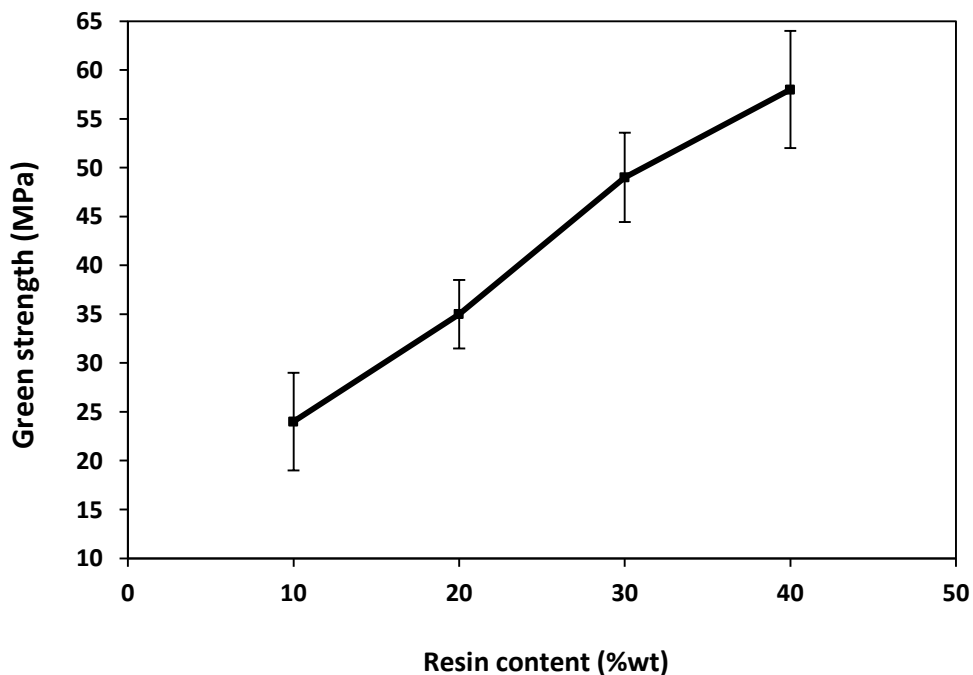


**Figure 7.12 Green strength of the gel cast PZT samples obtained from 45 vol% solids loading at various resin contents.**

## 7.4 Characterization of lead based gel cast sintered bodies

The influence of resin content on the sintered properties including sintered density and shrinkage,  $d_{33}$ ,  $k_p$ ,  $\epsilon^T$  and the dielectric loss tangent also have been studied. Figure 7.13 presents the effect of resin content on sintered density and shrinkage of sintered PZT gel cast samples prepared from 48 vol% solids loading at various resin contents and sintered at 1200 °C. It can be seen that with increasing resin content, the sintering shrinkage and sintered density decreased. Increasing resin content from 10 wt% to 40 wt% resulted in a decrease in sintered density from 7.61 g/cm<sup>3</sup> to 7.39 g/cm<sup>3</sup>. This trend is in agreement with the results obtained from sintered 50BCZT samples, and the sintered density values are similar to those of sintered PZT samples with 45 vol% solids loading using EDGDE resin reported by Jiang [7] and Olhero *et al.* [10].

The SEM micrographs of the fracture surfaces of sintered gel cast samples obtained from 48 vol% solids loading PZT slurries with various hydantoin epoxy resin contents are presented in Figure 7.14. The grain sizes of samples were approximately 1 μm. The relatively dense and homogeneous microstructure can be observed with all samples. However, the sintered sample with higher resin content presented the highest amount of porosity which is also in agreement with the SEM micrograph of 50BCZT samples sintered at 1425 °C.



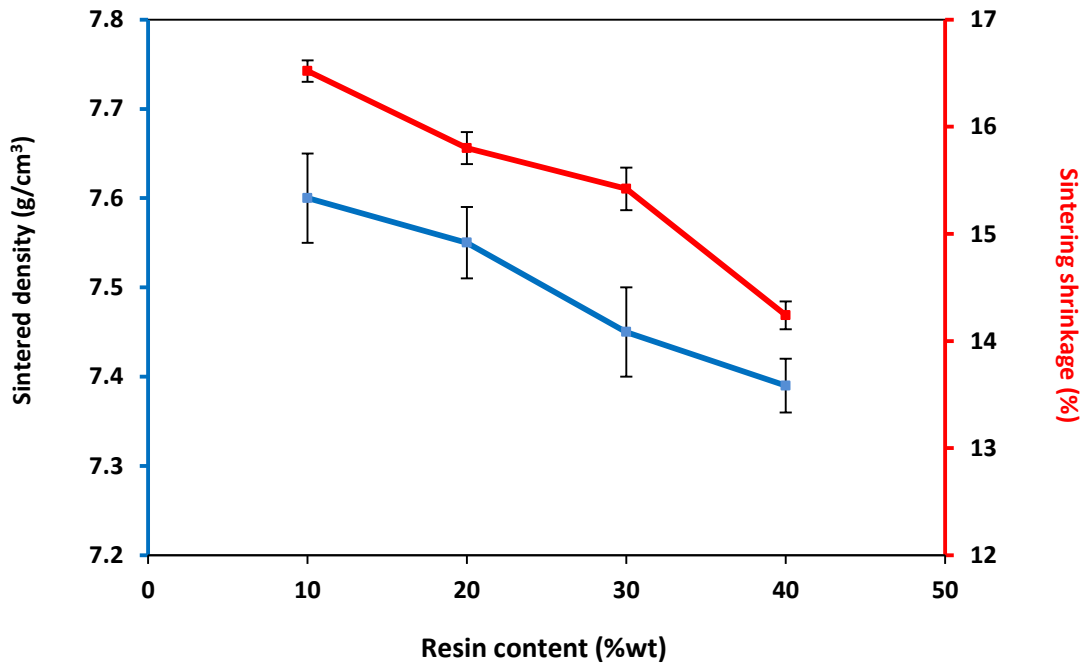
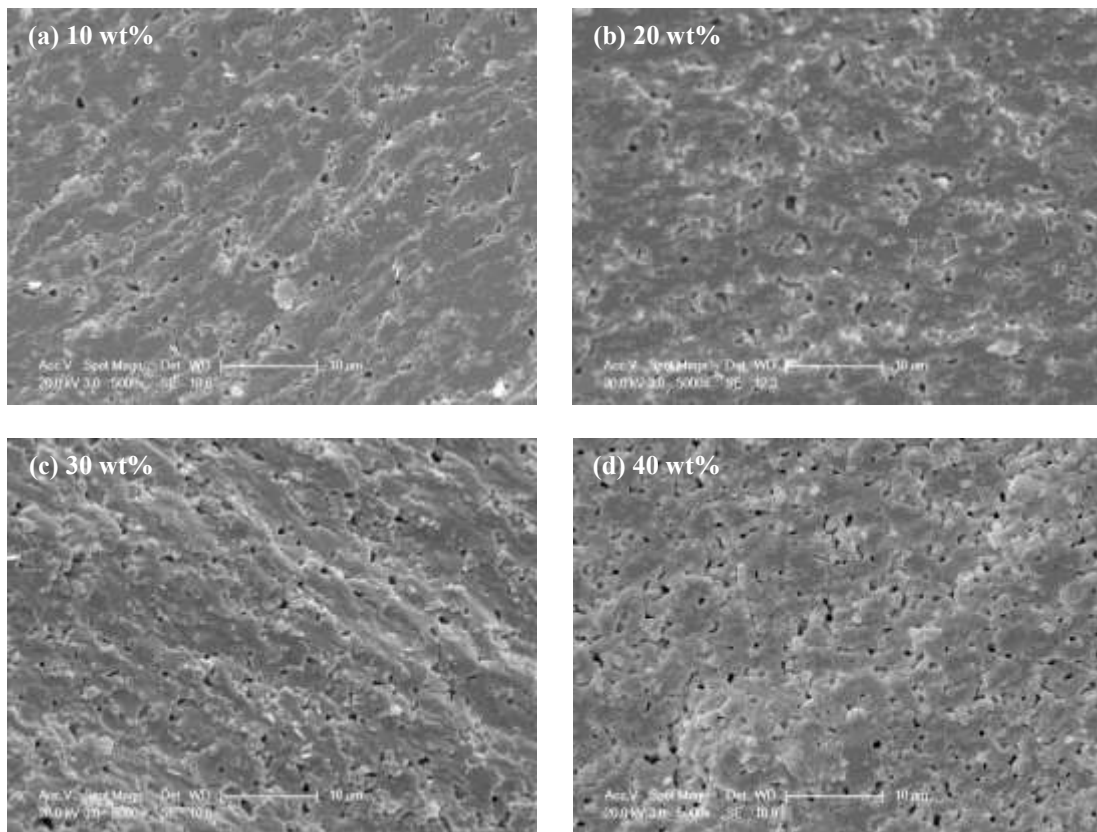


Figure 7.13 Sintered density and sintering shrinkage of PZT gel samples at a solid loading of 48 vol% sintered at 1200°C versus resin content.

Figures 7.15 and 7.16 show the influence of resin content on  $d_{33}$ ,  $k_p$ ,  $\epsilon^T$  and the dielectric loss tangent of PZT gel cast green samples sintered at 1200 °C versus resin content at solid loading 48 vol%. It can be seen that with increasing resin content, the piezoelectric and dielectric values increased while the dielectric loss tangent decreased, the sintered sample with 30 wt% resin content presented the highest  $d_{33}$ ,  $k_p$ ,  $\epsilon^T$  values of around 480 pC/N, 0.5 and 2765, respectively with the lowest dielectric loss tangent of around 2.32%. However, at 40 wt% resin content, the properties deteriorate which is also similar to the results observed in sintered 50BCZT sample at different resin contents (Section 6.5.1).



**Figure 7.14 SEM micrographs showing the fracture surfaces of sintered gel cast samples obtained from 48 vol% solids loading PZT slurries with various hydantoin epoxy resin concentrations (a) 10 wt% (b) 20 wt% (c) 30 wt% (d) 40 wt%.**

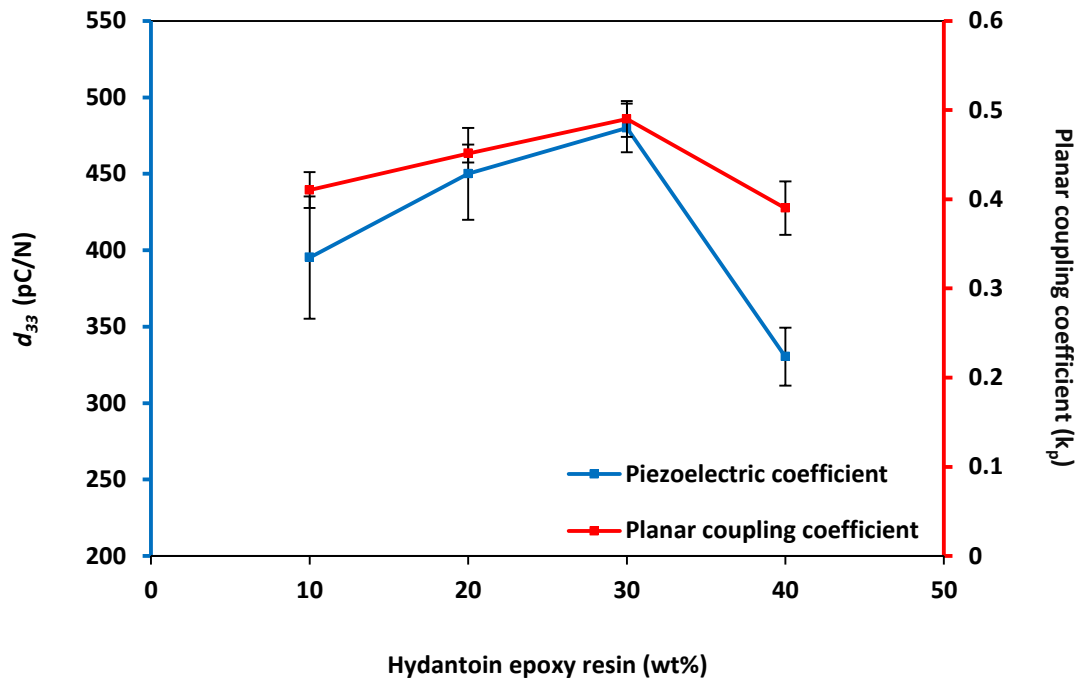


Figure 7.15 Piezoelectric coefficient and planar coupling of PZT gel cast samples at a solid loading of 48 vol% sintered at 1200°C versus resin content.

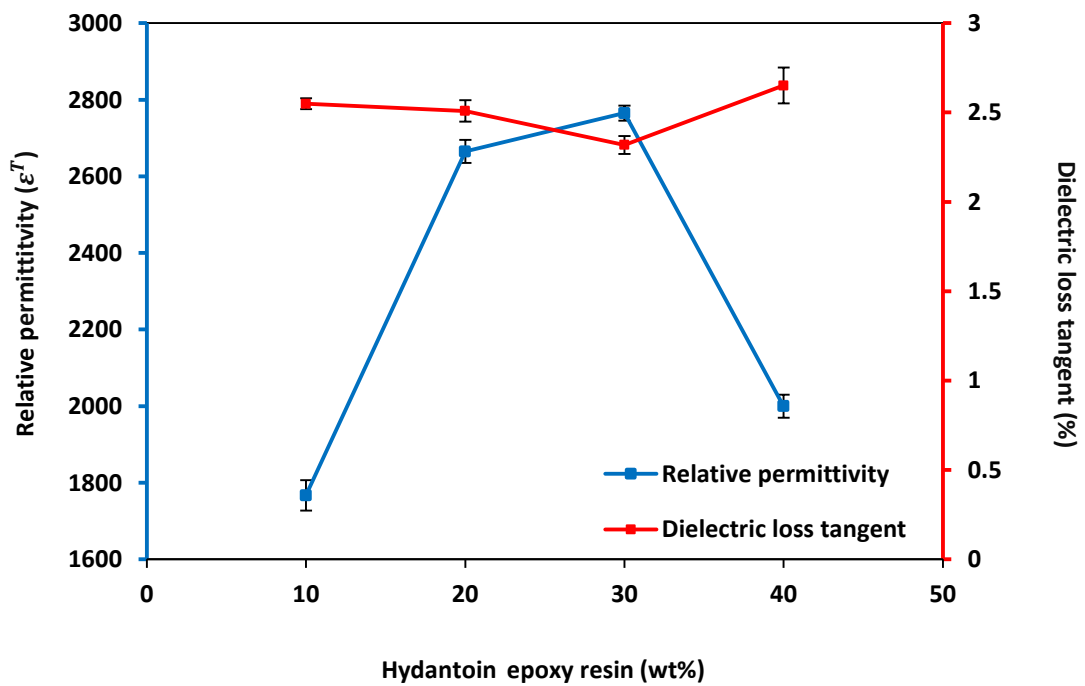


Figure 7.16 Permittivity and dielectric loss tangent of PZT gel cast samples at a solid loading of 48 vol% sintered at 1200 °C versus resin content.

## 7.5 Summary

This chapter has reported on the lead based PZT powders and bulk gel cast samples based on a hydantoin epoxy resin and amine hardener system. The influences of dispersant, solid loading and resin content on the rheological behaviour of the slurries were studied, followed by characterisation of the green and sintered density, green strength, drying and sintering shrinkage, piezoelectric and dielectric properties. The results obtained can be summarised as follows:

- (1) The dispersant is effective in producing stable suspensions, with 1 wt% dispersant based on the dried PZT powder weight exhibiting the lowest viscosity.
- (2) The viscosity increased with an increase of solid loading, and the optimum solid loading was determined as 48 vol% as it offered the highest solids loading with acceptable viscosity for this gel casting system.
- (3) The viscosity increased with an increase of resin content while the gelation time was shortened from 28 to 9 minutes when the resin content increased from 10 wt% to 40 wt%.
- (4) For green samples, a gradual reduction in porosity and increase in green density, drying shrinkage and green strength were observed with an increase of resin content. The highest green strength of around 58 MPa was achieved at a resin content of 40 wt%.
- (5) For sintered samples, an increase of resin content resulted in a decrease of the sintered density and sintering shrinkage. The highest  $d_{33}$ ,  $k_p$  and  $\varepsilon^T$  and lowest dielectric loss tangent was observed with a 30 wt% resin content. However,

deleterious effects on the piezoelectric and dielectric properties were found at 40 wt% resin content.

(6) A gel cast PZT slurries with 48 vol% solids loading, resin content of 20 - 40 wt% and the dispersant concentration was 1.0 wt% were selected for fabrication of 1-3 piezoelectric composites.

## 7.6 References

1. *High Performance soft PZT*. [Last accessed 23/09/2017]; Available from: <http://www.trstechnologies.com/Materials/High-Performance-PMN-PT-Piezoelectric-Single-Crystal>.
2. Corker, D., et al., *A neutron diffraction investigation into the rhombohedral phases of the perovskite series*. Journal of Physics: Condensed Matter, 1998. **10**(28): p. 6251.
3. Bai, Y., *Vibrational energy harvesting using piezoelectric ceramics and free-standing thick-film structures*. 2015, University of Birmingham.
4. Guo, D., et al., *Application of gelcasting to the fabrication of piezoelectric ceramic parts*. Journal of the European Ceramic Society, 2003. **23**(7): p. 1131-1137.
5. Guo, D., et al., *Gelcasting of PZT*. Ceramics International, 2003. **29**(4): p. 403-406.
6. Guo, D., et al., *Anti-crack machining of PZT ceramics for fabricating piezocomposites by using gelcasting technique*. Materials Science and Engineering B-Solid State Materials for Advanced Technology, 2003. **99**(1-3): p. 25-28.
7. Jiang, Y., *Fabrication and characterisation of novel ultrasound transducers*, in *School of Metallurgy and Materials*. 2013, University of Birmingham.
8. Garcia-Gancedo, L., et al., *Application of gel-casting to the fabrication of 1-3 piezoelectric ceramic-polymer composites for high-frequency ultrasound devices*. Journal of Micromechanics and Microengineering, 2012. **22**(12).
9. Zhang, D., B. Su, and T.W. Button, *Microfabrication of Three-Dimensional, Free-Standing Ceramic MEMS Components by Soft Moulding*. Advanced Engineering Materials, 2003. **Vol.5**(12): p. 924-927.
10. Olhero, S.M., et al., *Innovative fabrication of PZT pillar arrays by a colloidal approach*, in *Journal of the European Ceramic Society* 2012. p. 1067-1075.
11. Olhero, S. and J. Ferreira, *Influence of particle size distribution on rheology and particle packing of silica-based suspensions*. Powder Technology, 2004. **139**(1): p. 69-75.
12. Wonisch, A., et al., *A Comprehensive Simulation Scheme for Tape Casting: From Flow Behavior to Anisotropy Development*. Journal of the American Ceramic Society, 2011. **94**(7): p. 2053-2060.
13. Xiaogang Xu, Z.W., Xiangwei Wu, Jiu Lin, Xiuyan Wang, *Rheology and chemorheology of aqueous LiAlO<sub>2</sub> slurries for gel-casting*. Ceramics International, 2009. **35**: p. 2191-2195.

14. Rui Xie, K.Z., Xueping Gan, Dou Zhang, *Effects of Epoxy Resin on Gelcasting Process and Mechanical Properties of Alumina Ceramics*. Journal of the American Ceramic Society, 2013. **96**(4): p. 1107-1112.
15. Liu, X., Y. Huang, and J. Yang, *Effect of rheological properties of the suspension on the mechanical strength of Al<sub>2</sub>O<sub>3</sub>-ZrO<sub>2</sub> composites prepared by gelcasting*. Ceramics International, 2002. **28**(2): p. 159-164.
16. Xie, R., et al., *Gelcasting of alumina ceramics with improved green strength*. Ceramics International, 2012. **38**(8): p. 6923-6926.
17. Liu, G., et al., *Rheological characterization and shape control in gel-casting of nano-sized zirconia powders*. Ceramics International, 2014. **40**(9, Part A): p. 14405-14412.
18. Xie, R., et al., *Fabrication of Fine-Scale 1–3 Piezoelectric Arrays by Aqueous Gelcasting*. Journal of the American Ceramic Society, 2014: p. n/a-n/a.

# **Chapter 8 Characterization of lead free and lead based 1-3 random piezocomposites**

## **8.1 Introduction**

The main aim of this project is to develop a gel casting process suitable for the fabrication of lead free random composites for use in high frequency medical ultrasound transducers. The optimisation and characterisation of lead free and lead based gel casting systems were presented in Chapters 6 and 7 respectively. In this chapter, the fabrication of 50BCZT and PZT 1-3 random composites using these gel casting systems is reported and discussed.

## **8.2 Fabrication of Green lead based and lead free randomised structures**

### **8.2.1 Lead free randomised structures**

As discussed in Chapter 6, the green strength of gel cast samples increased with the increasing amount of resin in the slurry, with the 40 wt% resin concentration having the highest value. However, this resin content also resulted in a decrease of sintered density, and dielectric and piezoelectric properties compared to lower resin concentrations, and was, therefore, considered not ideal for the fabrication of 1-3 composites. Slurries with a resin concentration of 30 wt% provided the best piezoelectric properties for bulk ceramics. However, to investigate the effect of resin content on the green stage fabrication of randomised 1-3 segments a number of

casting and demoulding trials were carried out for the complete range of resin contents reported in Chapter 6.

Gel cast slurries with 45 vol% of BCZT powder were prepared with resin contents of 10, 20, 30 and 40 wt% with the optimum dispersant concentration (2.4 wt%) and cast into negative PDMS soft moulds which had been replicated from the Si-master moulds of the randomised structure. The height of the pillar cavities in the mould was  $\sim 150 \mu\text{m}$ . After the slurries had been cured and dried, the samples were slowly demoulded, as explained in section 5.1.3.1. Figure 8.1 shows SEM micrographs of the randomised BCZT structures. The green segments prepared from the slurry containing 10 wt% resin were mostly broken off at their base with the stock. For the 20 wt% resin samples, only a small number of ceramic segments remained on the stock. The remaining pillars were found as broken segments, collapsed, and trapped in the cavity of the PDMS mould. Thus gel casting slurries with resin contents 10 wt% and 20 wt% were not suitable for the fabrication of 1-3 composites. There are a number of possible reasons for this behaviour. The green strength of the samples fabricated with 10 and 20 wt% resin contents provided insufficient green strength (18 and 20 MPa, respectively) and, therefore, the ceramic segments were unable to resist the peeling stresses during demoulding. The surface area-volume ratio of the micro segments was also an important factor affecting the demoulding ability of composites. The surface area of the composite increases significantly with increasing the aspect ratio of the pillars and segments. Therefore, high aspect ratio structures lead to higher frictional and demoulding forces, causing an increased susceptibility for the pillars to crack, deform, collapse, break and buckle [1, 2]. Another factor relates to the manual demoulding process that was used in this work,



which could cause a non-uniform force during peeling the soft mould from the bristle block.

For the samples fabricated with 30 and 40 wt% resin contents, most of the ceramic segments on the 2x2 mm square area of randomised composites were found to be successfully demoulded, with only a few collapsed and broken segments, as can be seen in Figure 8.1 (c) and (d). The ceramic segments prepared from 30 wt% resin content stood in the place and position that they were replicated from the soft mould. However, it was found that a few segments were missing from the top left corner. Some segments of randomised structure prepared from slurries with 40 wt% resin were also missing from the centre of the sample due to the Si segments of the master mould being damaged. As would be expected, samples with higher resin content, and therefore higher green strength, are preferred for the fabrication of the ceramic segments. The systems with higher resin contents also exhibit increased drying shrinkage of the green structures as discussed in section 6.4, the highest drying shrinkage being observed for the 40 wt% resin content. However, the choice of resin content for the fabrication of 1-3 composites needs not only to consider the green strength of the ceramic segments, but also the piezoelectric and functional properties. Thus, although a resin content of 40 wt% offered improved green strength compared to systems with 30 wt% resin, the latter system produced sintered materials with better properties in bulk ceramics, whilst also offering sufficient green strength for demoulding the fine scale structures. Therefore, 30 wt% resin content was selected for fabricating lead free composites in further work.

High magnification micrographs of segments with randomised structures prepared from slurries with 50BCZT 45 vo% solids loading and 30% resin content are

presented in Figure 8.2 (a) and (b). These images show that the green stage of 50BCZT segments has a smooth and homogeneous surface. Dense segments with ultrafine feature sizes and well-defined structure and edges can be observed, with no cracks or distortions. This agrees well with reports of gel cast lead free piezoelectric structures fabricated with a regular shape [3]. Therefore, it can be confirmed that this gel casting system provided excellent replication of the Si master mould structures in lead free ceramic and proves the feasibility of using the combination of gel casting and soft moulding methods for the fabrication of bristle block structures for lead free 1-3 composites with randomised structure. Figure 8.2 (a) also shows the aspect ratio of the ceramic segments. The height of the composite is around 141.79  $\mu\text{m}$  (the drying shrinkage is approximately 5.47 %) and the smallest feature size of the segment is around 5  $\mu\text{m}$ , representing an aspect ratio up to 30, which is higher than that of  $\text{Ba}_{0.6}\text{Sr}_{0.4}\text{TiO}_3$ (BST) regular pillars reported by Olhero et al (the smallest feature size of the segment is around 83  $\mu\text{m}$  and an aspect ratio was around 4) [3].

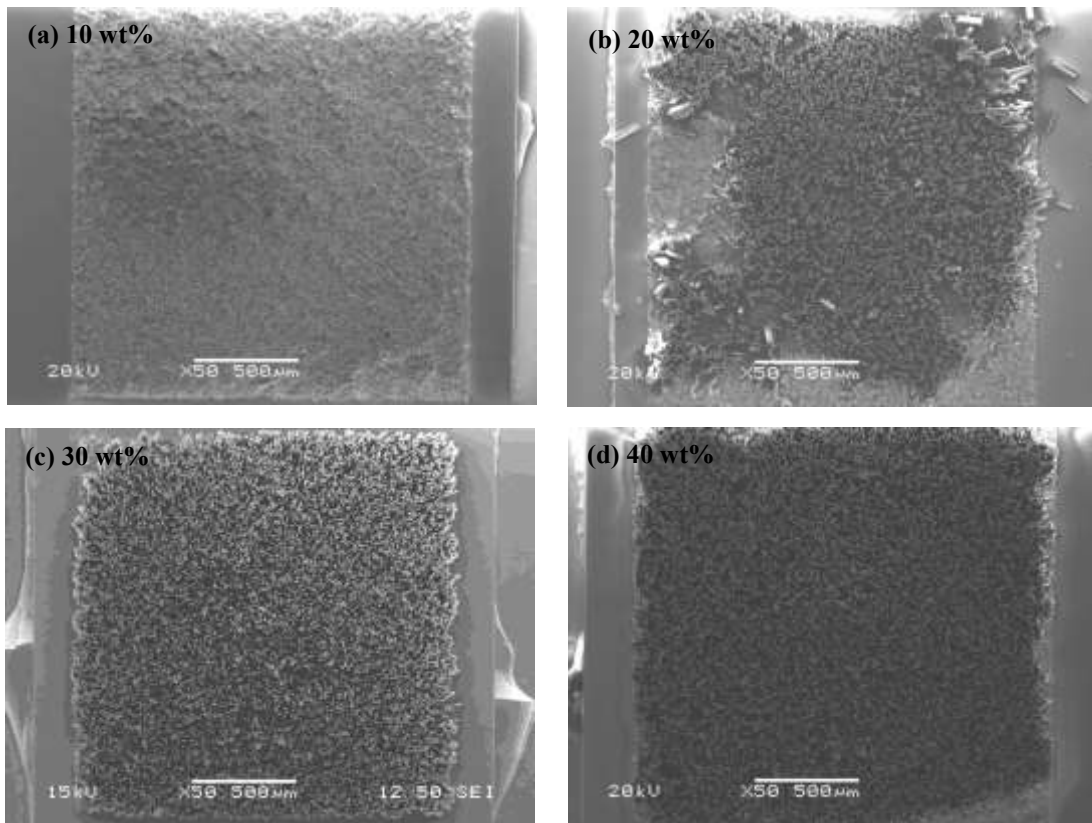


Figure 8.1 SEM micrographs showing the top-view of demoulded randomised 50BCZT structures prepared from gel casting slurries with 45% solids loading with (a) 10 wt%, (b) 20 wt%, (c) 30 wt% and (d) 40 wt% resin contents.

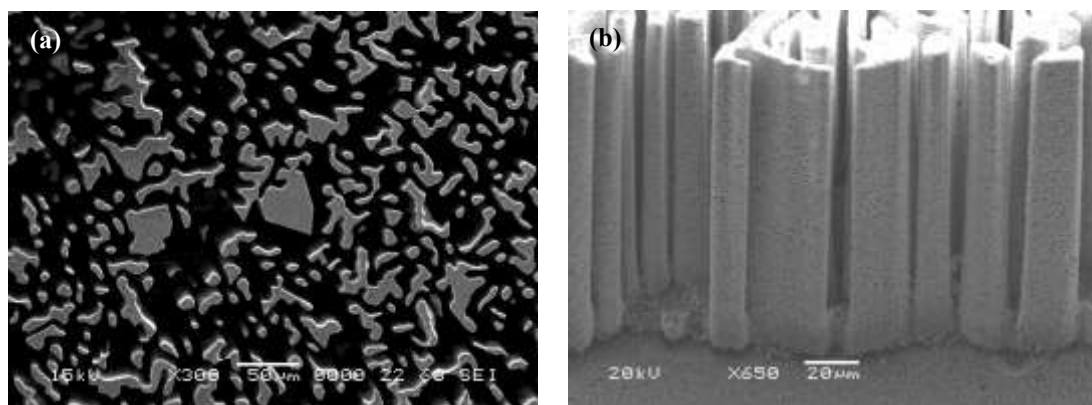


Figure 8.2 SEM micrograph of (a) the top view (b) detailed side view of the randomised 50BCZT segments fabricated by gel casting slurry with 45% solids loading and 30 wt% resin content after drying and demoulding.

## 8.2.2 Lead based randomised structures

According to the results from section 7.3, the influence of resin contents on the green strength of green PZT segments presented a similar trend to that of 50BCZT, higher green strength can be achieved with increasing resin content in the slurries. Although 40 wt% resin contents offered the highest green strength, the key piezoelectric properties were reduced. The best functional properties of bulk sintered PZT samples were observed for samples fabricated with 30 wt% resin content. Therefore, to enable the selection of the resin content for further work, gel cast samples of the randomised structures were prepared from slurries with a range of resin contents and 48 wt% solids loading PZT. The microstructure of the demoulded segments are presented in Figure 8.3. For a resin content of 10 wt% there are no ceramic segments remaining after demoulding. For samples with 20 wt% resin content, some of the segments were found to be collapsed, broken off or were trapped inside the mould, and only a few of them were demoulded successfully. This is in agreement with the results from the 10 wt% and 20 wt% resin content slurries of 50BCZT 45 vol% system. It has been reported from Jiang [4] that green state randomised PZT structures produced using 10 wt% resin content gel cast systems with 45 vol% solids loading that no segments survived demoulding and only 30% of ceramic pillars were observed in structures produced using slurries with 20 wt% resin content. The work of Jiang [4] used an EGDGE resin system, whereas in this project, it can be clearly seen that a greater number of ceramic segments can be demoulded due to the hydantoin epoxy resin providing higher green strength and enabling a higher vol% solids loading [5, 6]. However, gel cast slurries with resin contents 10 wt% and 20 wt% were considered not suitable for fabricating 1-3 composites. At 30 and 40 wt%

resin contents, most of the segments were found to be completely demoulded, a result of the green strength of the pillars increasing with increasing resin contents, in agreement with Jiang [4] and Olhero *et al.* [7]. Only a few segments were observed to be collapsed or missing at the uppermost part of the structure produced with 30 wt% resin content, and at the top centre and centre and to the right of the samples produced with 40 wt% resin content. PZT ceramic segments prepared by using 30 wt% and 40 wt% EGDGE epoxy resin contents reported that only 40% wt% resin showed complete ceramic segments after demoulding and over 50% of the segments prepared from 30 wt% resin content slurries were observed to have survived the demoulding process [4]. It can thus be concluded that the gel casting system using hydantoin epoxy resin improved the green strength of randomised structures. This is in agreement with Xie *et al.* [8], who concluded that the hydantoin epoxy resin produced higher green strength ceramics compared to other epoxy resin systems with the same resin content [9, 10]. In Xie's work, green square ceramic segments were completely demoulded and exhibited smooth and homogeneous surfaces with no cracks for samples using 20 wt% resin content, but the aspect ratio of the structures was only 5. In this work, the highest green strength can be achieved by using 40 wt% resin content. However, piezoelectric and functional properties of bulk samples with 40 wt% resin content were decreased as shown in section 7.4. For further work, therefore, a compromise between green strength and piezoelectric and functional properties had to be made, and 30 wt% resin content was selected as the optimum resin content for a gel casting system with 48 vol% PZT. High magnification micrographs of segments with randomised structures prepared from PZT 48 vo% solids loading and 30% resin content are presented in Figure 8.4 (a) and

(b). The ultrafine feature size of PZT segments can be replicated from PDMS soft mould, a smooth and homogeneous surface with no cracks were observed. The height of the composite is around 140.61  $\mu\text{m}$  (the drying shrinkage of PZT bristle block structure is approximately 6.26 %) and the smallest feature size of the segment is around 4.28  $\mu\text{m}$ , representing an aspect ratio up to 33. The properties and replication characteristics of the samples from slurries with 30 wt% resin confirmed that this gel casting system was suitable for fabricating the 1-3 randomised structure as an active material for transducers.

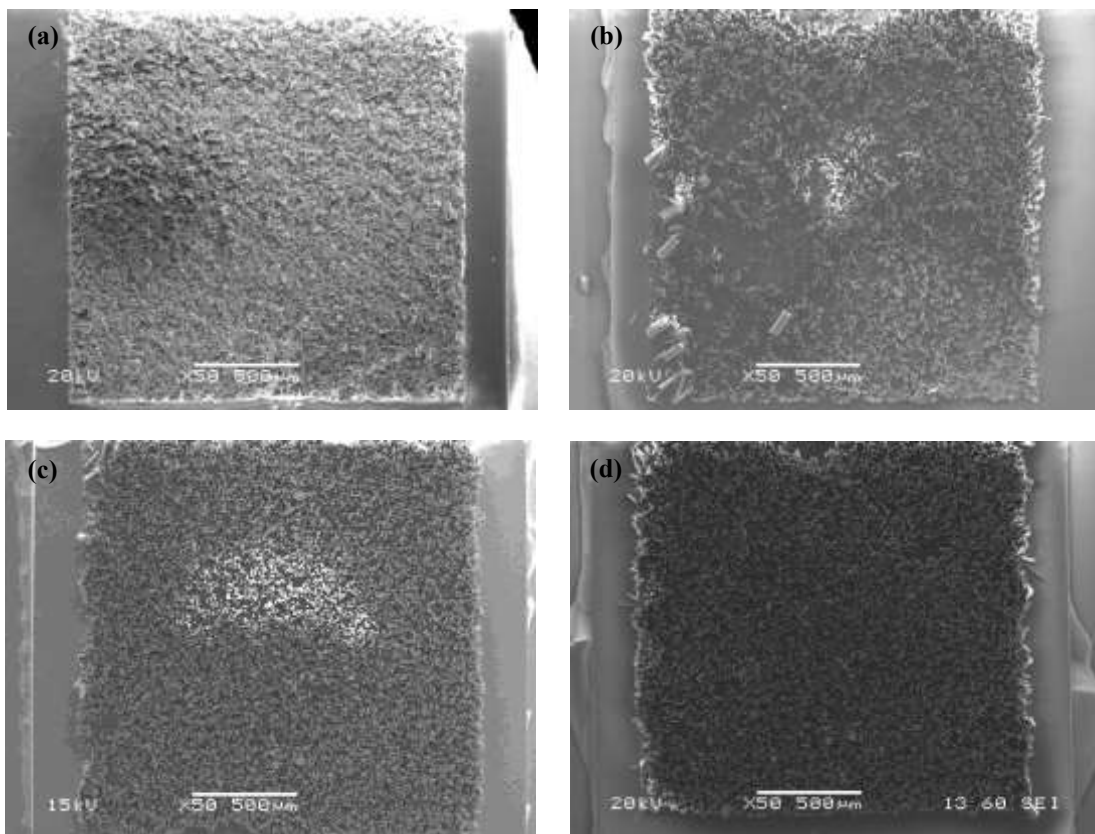


**Figure 8.3 SEM micrographs showing the top-view of demoulded randomised PZT structures prepared from gel casting slurries 48% solids loading with (a) 10 wt%, (b) 20 wt%, (c) 30 wt% and (d) 40 wt% resin contents.**

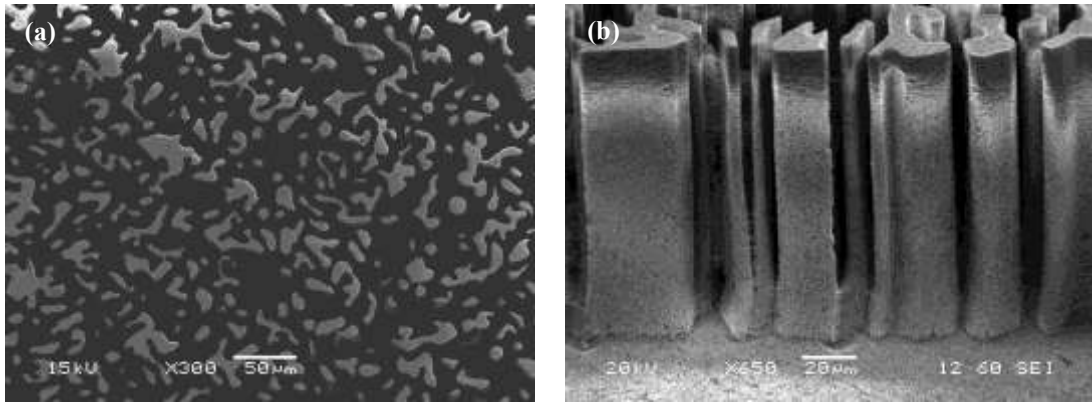


**Figure 8.4** SEM micrograph of (a) the top view (b) detailed side view of the randomised PZT segments fabricated by gel casting slurries with 48% solids loading and 30 wt% resin content after drying and demoulding.

### **8.3 Sintered lead based and lead free randomised structures**

Bristle block structures fabricated from 50BCZT and PZT were sintered and characterised in order to observe any defects and distortion effects happening during sintering and to enable comparison between the green and sintering stages. PZT samples were sintered at 1200°C while the 50BCZT ceramic segments were sintered at various temperatures between 1300°C to 1500°C to study the influence of the sintering temperature not only on the microstructure but also on the grain size.

#### **8.3.1 Sintering of lead free randomised structures**

The microstructures of randomised 50BCZT segments were studied by sintering at 1300, 1325, 1350, 1375, 1400, 1425, 1450, 1475 and 1500°C using the sintering profile as detailed in section 5.1.2.3. Figure 8.5 shows the SEM micrograph of a bristle block in the green state, and after being sintered at 1300 °C so that the microstructures can be compared. It can be seen that after sintering the bristle block

structure has an area of approximately 1.6 x 1.6 mm square, and it is clear that some of the ceramic segments have broken off the base, tilted or collapsed and only 70% of the segments survived. However, collapsed segments will not necessarily affect the 1-3 composite performance because they can be removed during lapping as reported by Jiang [4]. The absence of segments around the edge will be one of the most problematic for making the piezocomposites as it will reduce the diameter of composite that can be produced.

However, the tendency to lose of the missing segments around the edge of the bristle block decreased with increased sintering temperature as shown in Figure 8.6 a (i) to j (i). This may relate to the sintering temperature of 1300°C being too low to allow the segments to be sintered to full density, as indicated by the results presented in section 6.5.2. The relative density of bulk ceramics sintered at 1300 °C was only 5.06 g/cm<sup>3</sup> (~ 88% theoretical density) and consequently the strength may not have been high enough to keep the randomised segments in their original positions. When sintering temperature was increased, the number of collapsed and tilted segments also increased. Although collapsed segments were considered as not affecting the performance of resulting composites, an increase of tilting could change the overall ceramic volume fraction which may affect the piezocomposite performance [4]. Figure 8.7 (a) and (b) shows optical micrographs of the top view of 1-3 composites sintered at 1400 °C and 1425 °C. It can be clearly seen that when the sintering temperature is increased, the segments became more tilted, joined with neighbouring segments, and became larger in lateral dimensions. This will result in the volume fraction of ceramic being increased in the composite, with a consequential change in performance as discussed in section 8.5.

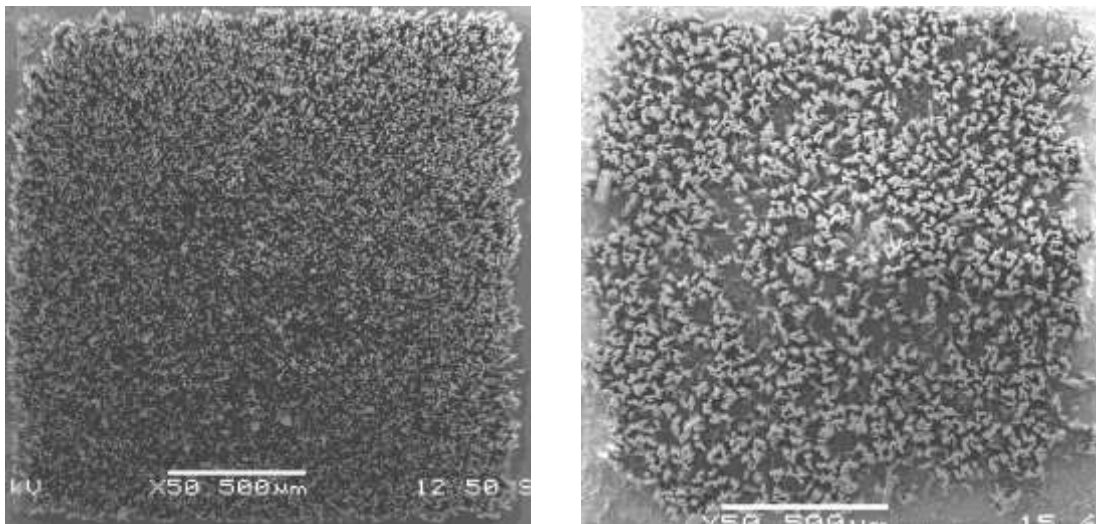


The side views of the bristle blocks sintered at temperatures from 1300 °C - 1500 °C are presented in Figure 8.6 a (ii) – j (ii), respectively where the height and grain size of the segments can be seen. It can be seen that with increasing sintering temperature, the height of the segments reduced with more joining of segments with their neighbours, as shown in Figure 8.7 (b), resulting in an expansion in lateral dimensions. This results is not only an increase in ceramic volume fraction, but also an increase in the sintering shrinkage in the height dimension as presented in Table 8.1.

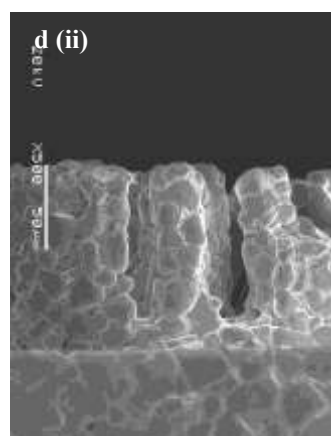
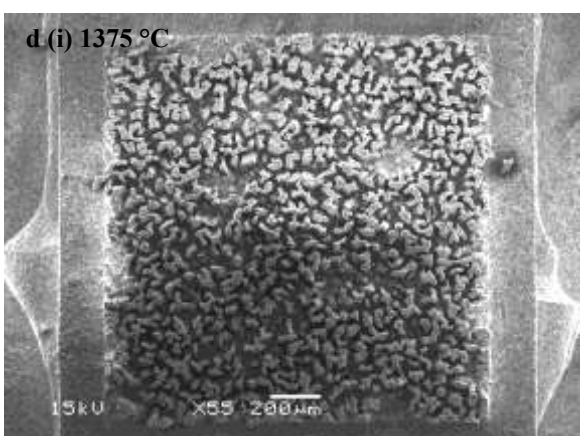
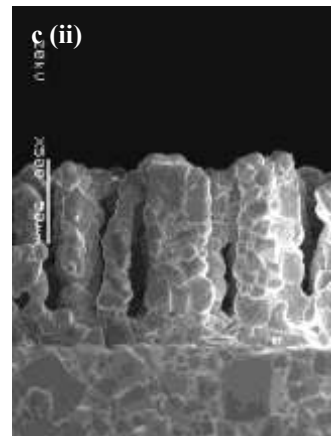
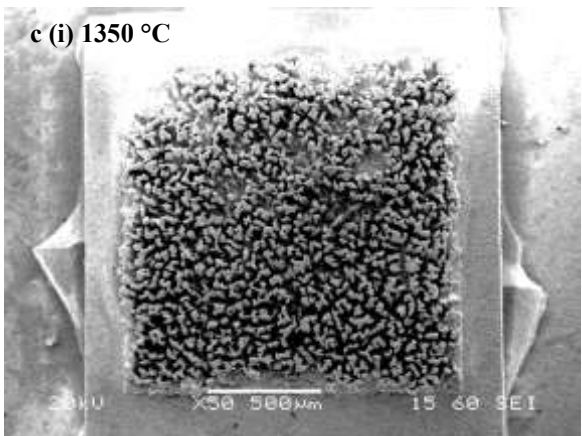
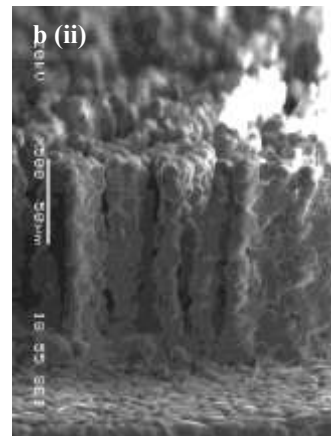
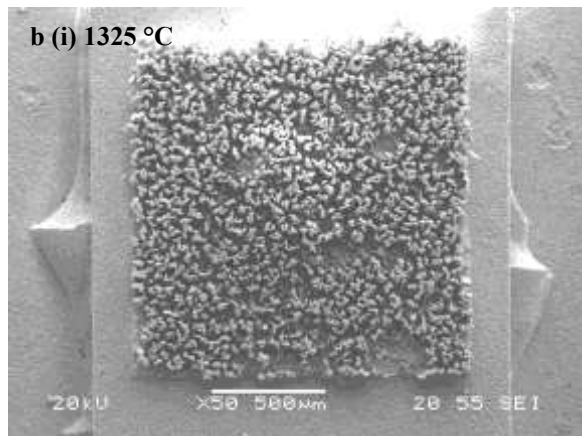
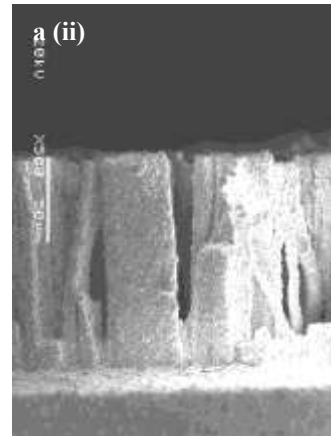
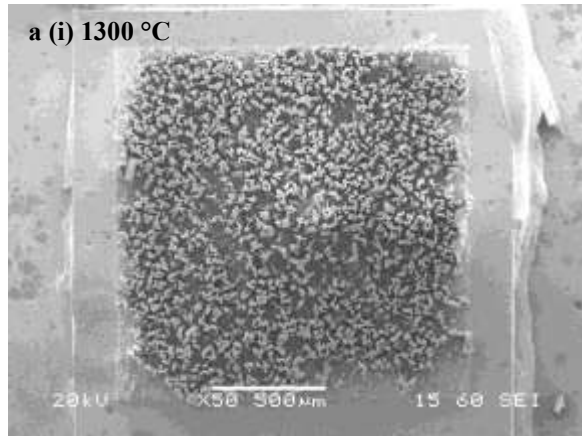
The grain size and feature size of the randomised structures increased with increasing sintering temperature with a resulting decrease in the aspect ratio. Table 8.1 shows the average height, grain size, finest feature size, aspect ratio and sintering shrinkage of segments sintered at temperatures between 1300 °C - 1500 °C. The average grain size of the segments increased with increasing temperature showing the same trend as reported for bulk samples in Chapter 6.5.2 However, at the same sintering temperature, the average grain sizes of segments were found to be smaller than for the bulk samples. Sintering of the pillar segments represents a different situation to that of bulk materials. On the one hand, grains within the segments are less constrained by surrounding material and perhaps could be expected to grow larger. On the other hand, there may be a restriction in the supply of material required for grain growth, resulting in smaller grains. The categories of sintering which are dependent on composition can be divided into 4 groups - solid state sintering, liquid phase sintering, vitrification and viscous sintering [11]. For BaTiO<sub>3</sub>, liquid phase sintering is normally considered as the main sintering process. During densification, the initial stage will start when some degree of atomic mobility is achieved, followed

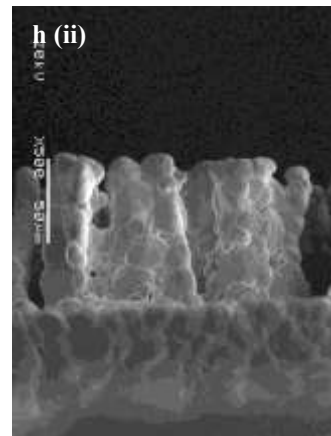
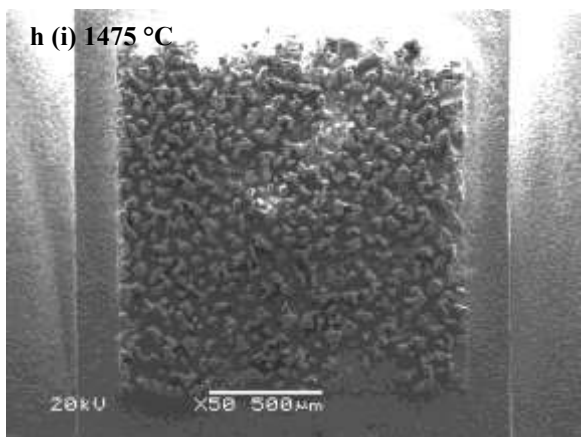
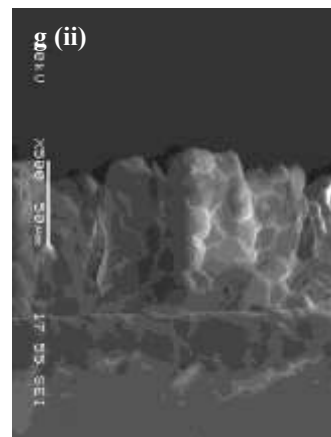
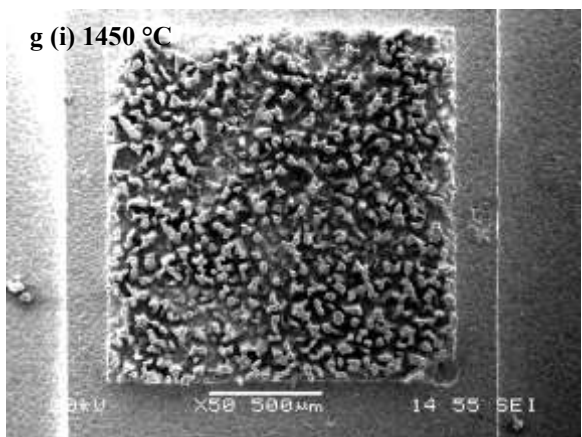
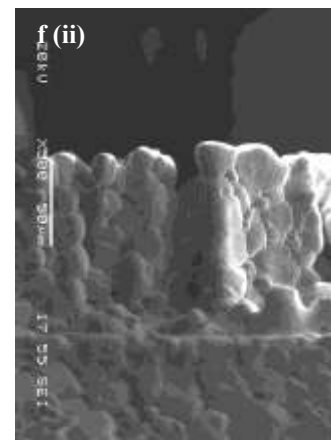
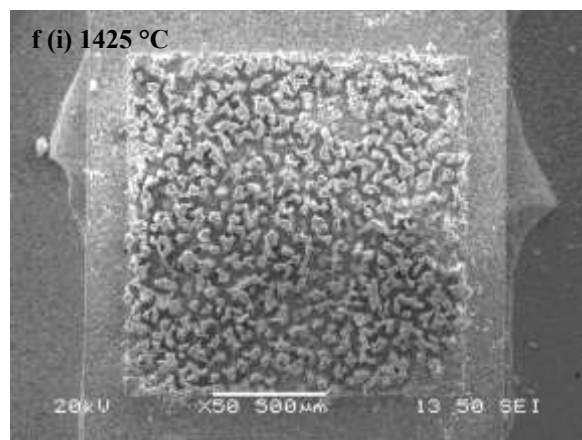
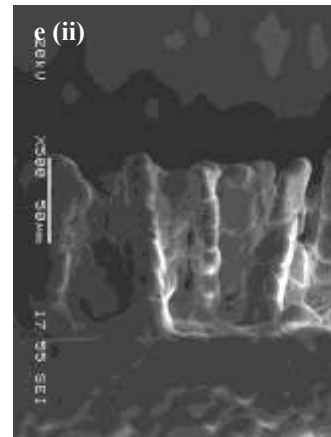
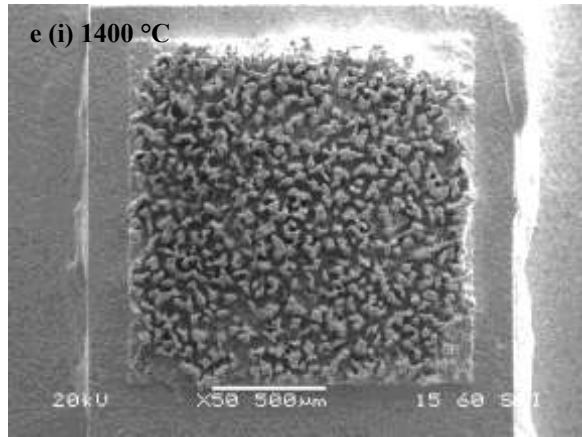
by the intermediate state in which the microstructure consists of a three dimension network of particles. During this stage, the grain growth rate increases significantly and is most pronounced in the final stage. However, due to their geometry, ceramic segments have less material available for sintering and grain growth, leading to lower boundary mobility and insufficient liquid surface available during the liquid phase sintering process, with non uniform interfacial. These factors may lead to the constraining of grain growth in the ceramic segments [12].

Thus, although the overall structure of randomised segments is maintained during sintering, most segments cannot keep the shape characteristics of their green stage due to the grain growth during sintering and some segments joining with their neighbours resulting in an overall increase in feature size compared to the green structures.



**Figure 8.5 SEM micrograph of the top view of the randomised 50BCZT segments (a) before and (b) after sintering at 1300 °C.**





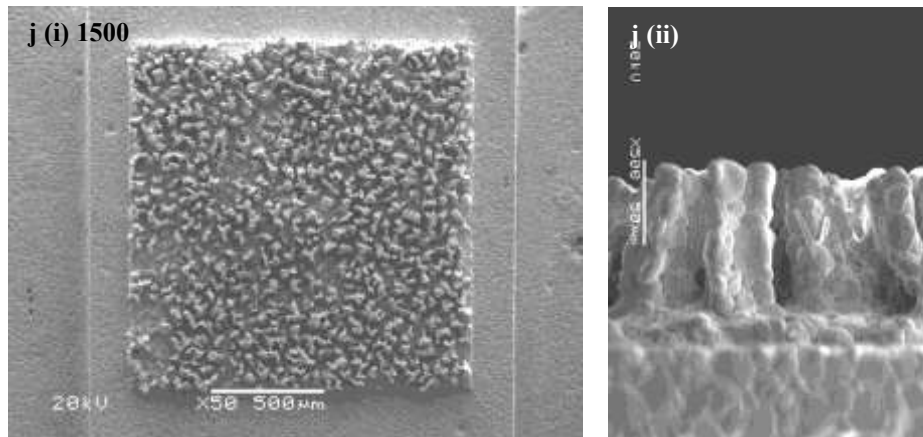


Figure 8.6 SEM micrographs of a(i) to j (i) top view and a(ii) to j (ii) the cross section of bristle blocks of 50BCZT randomised segments after sintering at 1300 - 1500 °C.

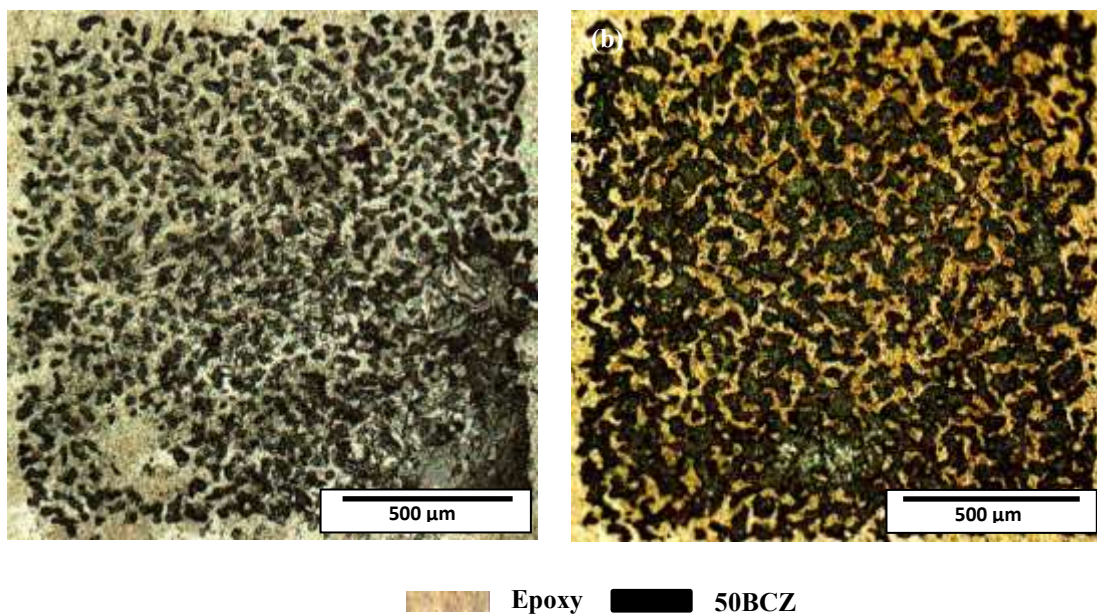


Figure 8.7 Optical image of overview of randomised 50BCZT 1-3 composites after sintering at (a) 1400 °C with ceramic volume fraction of 51.70 % (b) 1425 °C with ceramic volume fraction of 58.5 %.

**Table 8.1 The average height, grain size, finest feature size, aspect ratio and % sintering shrinkage of 50BCZT segments sintered at temperatures of 1300 °C - 1500 °C.**

Sintered temperature (°C)	Average height of segments (µm)	Average grain size of segments (µm)	Finest feature size (µm)	Aspect ratio	Sintering shrinkage (%)
1300	122.95	5.2	17	~ 6	13.28
1325	117.22	11.72	17.22	~ 6.8	17.32
1350	112.25	15.59	18.09	~ 6.2	20.83
1375	107	15.65	26.26	~ 4	24.53
1400	105.96	15.83	25.49	~ 4	25.26
1425	102.15	16.30	27.88	~ 3.60	27.95
1450	96.71	16.90	33.13	~ 2.91	31.79
1475	90.75	18.14	33.97	~ 2.67	36
1500	88.03	20.93	39.93	~ 2.20	37.91

### 8.3.2 Sintering of PZT randomised structures

A comparison of green stage and sintered stage PZT segments is presented in Figure 8.8 (a) and (b), respectively. It can be seen that the distance between segments and the size of segments are almost the same in the sintered state as in the original green structure. Compared to 50BCZT segments, PZT segments present less change in structure, which may relate to the smaller grain growth during sintering, in agreement with the report by Jiang [4]. It also can be observed that relatively few segments were collapsed and tilted. As mentioned in 8.3.1, the collapsed segments can be removed during the lapping process. Figure 8.9 (a) and (b) show the top view and side view of the surface morphology of PZT randomised segments after sintering at 1200 °C. The height of the composite is around 128 µm; therefore, the sintering shrinkage in height is approximately 8.96 %. Compared to 50BCZT randomised



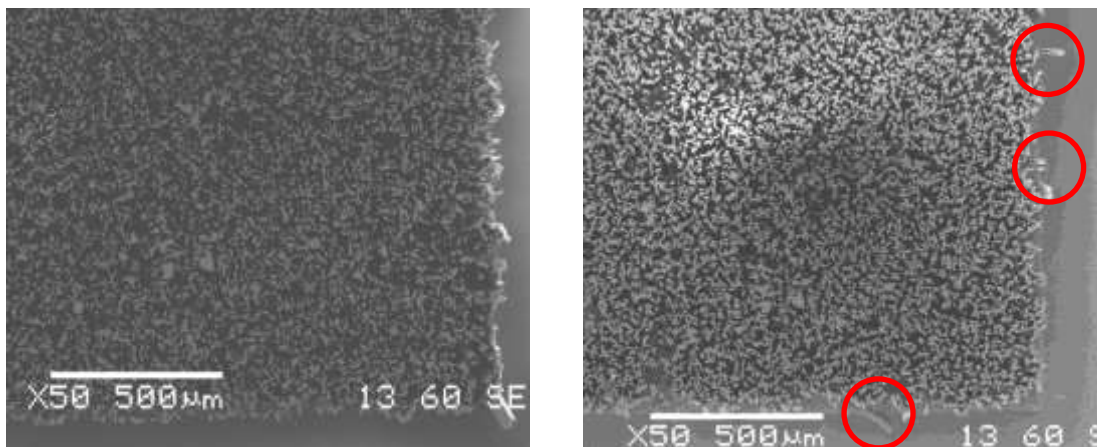


**Figure 8.8 SEM micrographs of top view of randomised PZT segments (a) before and (b) after sintering at 1200 °C.**

segments, the PZT segments presented smooth surfaces and sharp angles as in the green state. The grain size is approximately 1-2  $\mu\text{m}$  which is similar to those of the PZT pillars with 45 vol% solids loading and 40 wt% resin content fabricated by gel casting and sintered at 1200 °C, reported by Jiang [4], PZT pillars with 55 vol% solids loading with 15% wt hydantoin epoxy resin sintered at 1120 °C fabricated by gel casting reported by Xie [8] and PZT pillars fabricated by VPP sintered at 1150 °C reported by Dou [13] and bulk PZT samples reported in section 7.4. The grain sizes of PZT segments are much smaller than those 50BCZT segments, in line with the results of bulk gel-cast samples reported in chapters 6 and 7. After sintering, the segment structure was backfilled with epoxy, followed by lapping away the stock layer and surplus epoxy in order to achieve the required thickness with parallel surfaces and exposed ceramic segments on both faces. Figure 8.10 presents the optical image of a PZT randomised 1-3 composite approximately 1.6 x 1.6 mm square. It can be observed that some segments are missing that may have broken off due to the non-uniform forces during demoulding. 1-3 composites can be achieved

with high ceramic volume fraction of 46% and the finest feature size of segment around  $5.85\ \mu\text{m}$  can be observed in the image as a small spots. This shows that an aspect ratio up to approximately 20 has been achieved.

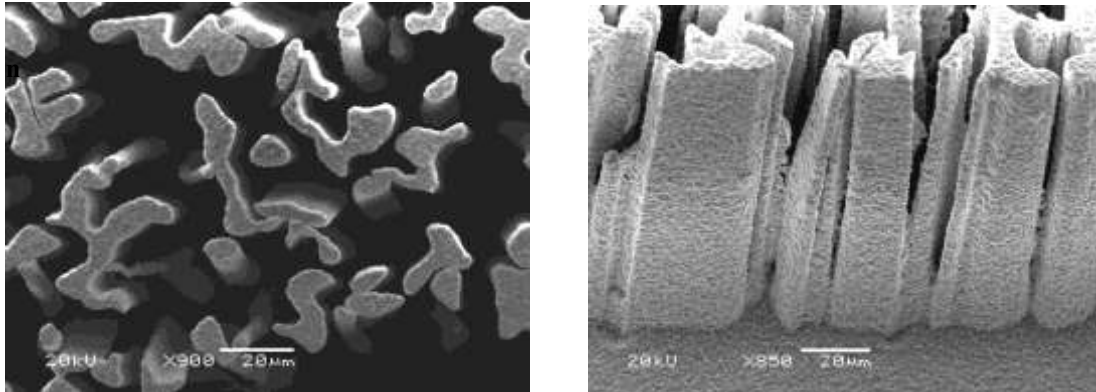


**Figure 8.9 SEM micrographs of (a) top view and (b) lateral side of randomised PZT segments.**

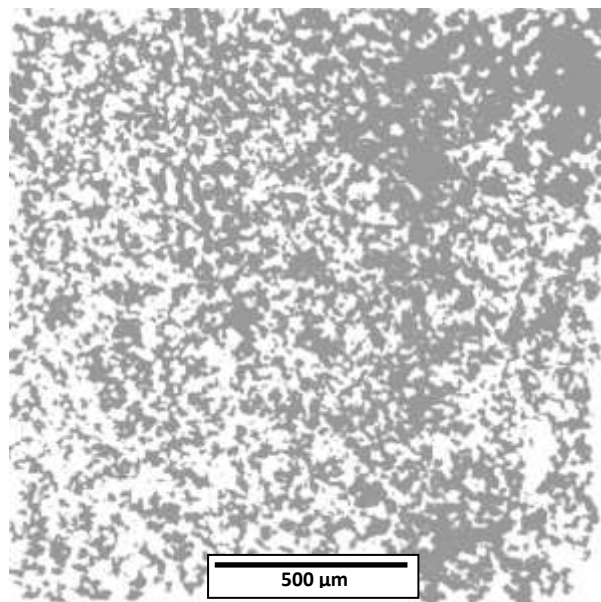


**Figure 8.10 Optical images of a random composite with ceramic volume fraction of 46%.**



## **8.4 Impedance analysis of lead free and lead based 1-3 randomised composites**

50BCZT bristle blocks were sintered at various temperatures between 1300 °C - 1500 °C while PZT bristle blocks were sintered at 1200 °C. The bristle blocks were then encapsulated with epoxy resin as explained in section 5.1.3.3 in order to fabricate 1-3 composites, followed by lapping the excess epoxy and stock layer of ceramic to achieve the 1-3 composites with the required thickness.

### **8.4.1 Impedance analysis of lead free 1-3 randomised composites**

1-3 composites of 50BCZT were lapped to different thicknesses as shown in Table 8.2. Figure 8.11 (a) and (b) present the electrical impedance and phase spectra of 50BCZT 1-3 randomised composites produced from bristle blocks sintered at temperatures of 1300 °C - 1500 °C. A broad frequency range between 100 kHz to 60 MHz is displayed but only one peak corresponding to the thickness mode resonance without any spurious modes were observed. This confirms that the randomised structure and dimensions of the ceramic segments suppressed the unwanted modes and only the thickness dimension resonance mode can be seen. These results are in agreement with the results of 1-3 composites with triangular geometry [14], [15], pseudo random pillar geometry [16] and random geometry [17] as explained in section 3.3.2.

It can also be noticed that a difference in impedance spectra and phase occurred with various thickness of 1-3 composites. For example, 50BCZT 1-3 composites sintered at 1425 °C and 1450 °C had thicknesses of 56  $\mu\text{m}$  and 45  $\mu\text{m}$ , respectively, and the

phase and impedance spectra at the resonant frequencies changed as anticipated. As the thickness of the 1-3 composite increased, the resonant frequencies were pushed to lower values, corresponding to equation 2.1 as explained in section 3.3.2. Compared to impedance spectra measured from PZT 1-3 composite, the impedance spectra obtained from 50BCZT were observed to be broader and the resonant and anti-resonant frequencies were not seen very clearly when measured without an applied bias voltage. Use of a bias voltage (40V) results in the resonance peaks becoming clearer.

One explanation for this behaviour could be that during poling, almost all dipole moments in each domain become fully aligned with the applied electric field. After poling, some of dipole moments stayed aligned but some of them might relax or switch to other angles due to the curie temperature being relatively close to room temperature. Also, the use of corona poling may not be so effective for 50BCZT. These dipole misalignments may be sufficient to dampen the resonant response of the composites. However, with DC bias on, the misaligned dipole moments may realign enabling the resonant and anti-resonant frequencies to be observed more clearly. An alternative hypothesis relates to the large grain size of 50BCZT materials. For the 50BCZT pillar structures, only a few grains are observed in each pillar as shown in Figure 8.6 a (ii) – j (ii); Therefore, the proportion of grain size to pillar height are much lower than for the corresponding PZT pillars. Therefore, even just one or two grains with misaligned dipole moments could have a larger effect on the measured properties compared to PZT. The large 50BCZT grains may also act more like single crystals than bulk sintered ceramics. However, the precise reason for this phenomenon is a matter for further investigation.

The thickness, ceramic volume fractions, resonant and anti-resonant frequencies of the 1-3 composites produced from 50BCZT are shown in Table 8.2. In this work, the resonant and anti-resonant frequencies have been determined by manually scanning the raw data for the maximum and minimum values. The thickness of the composites varied between 40 - 56  $\mu\text{m}$  resulting in operating frequencies between 40 MHz to 56 MHz. The ceramic volume fraction of all 50BCZT 1-3 composites ranged between 48 % - 59 % which is higher than the designed value of 40%. This may be caused by the grain growth during sintering leading to the larger grain sizes, and would also affect the acoustic impedance of the composites as discussed in section 8.5.2.

Thus, the gel casting route has been shown suitable for the fabrication of 50BCZT 1-3 composites with random geometries operating at frequencies over 30MHz and with no unwanted resonance modes, However, the BCZT material is still being investigated and so the properties and characteristics are currently not well understood. Some variables such as depolarisation after poling still need further investigation.

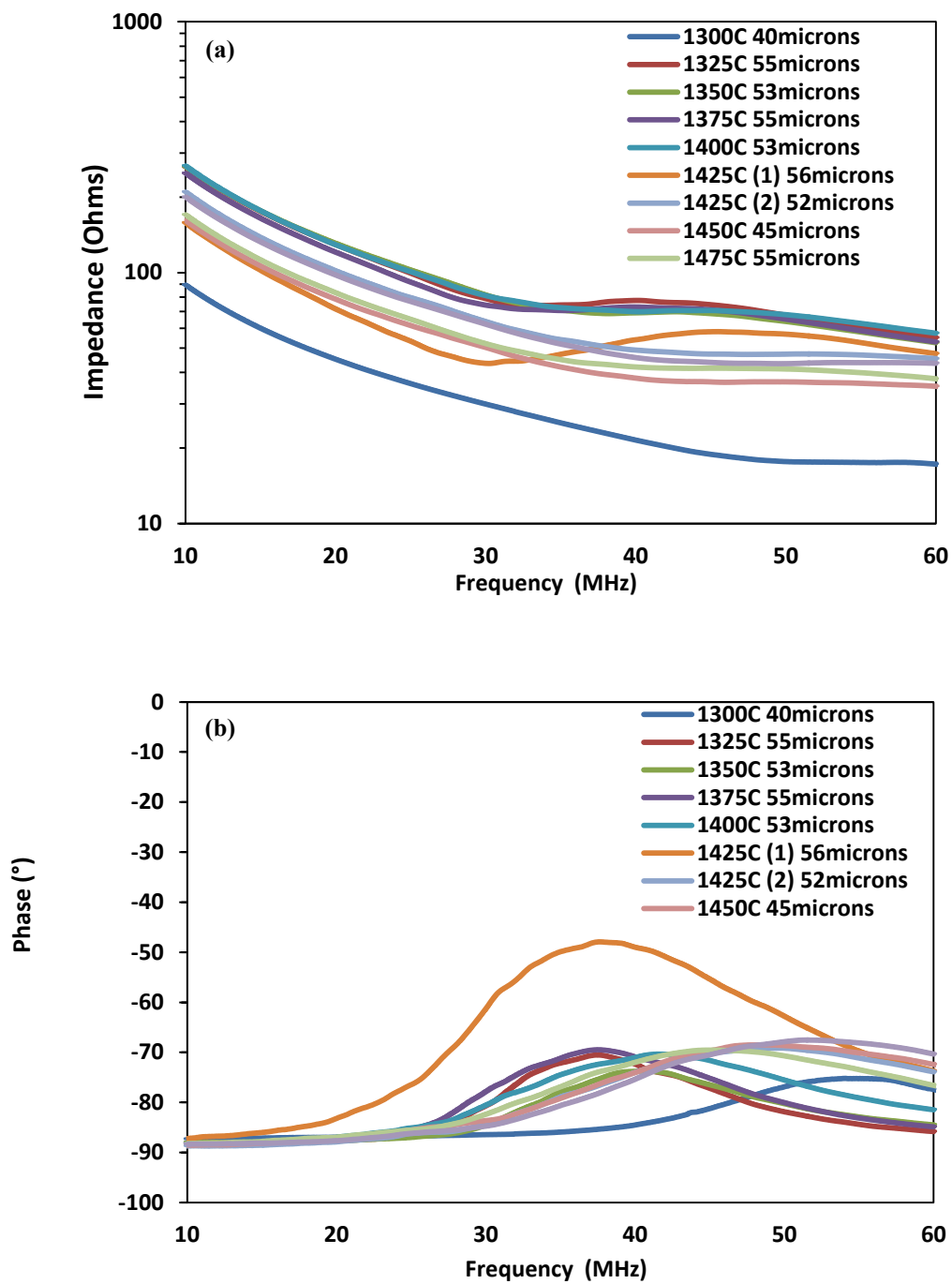


Figure 8.11 Impedance (a) and (b) phase magnitude diagrams measured from 50BCZT randomised 1-3 composites sintered at 1300 °C - 1500 °C with different thicknesses, using a bias -40 volts.

**Table 8.2 Summary of 50BCZT randomised composites sintered at 1300 °C - 1500 °C.**

Sintered temperature (°C)	1-3 composite thickness (μm)	Ceramic volume fraction (%)	Resonant frequency (MHz)	Anti-resonant frequency (MHz)
1300	40	48.56	56.28	57.86
1325	55	49.32	32.75	40.12
1350	53	50.15	38.25	42.75
1375	55	50.50	35.18	39.62
1400	52	51.70	40.18	44.93
1425 (1)	56	58.50	30.18	45.50
1425 (2)	52	52.87	47.37	51.31
1450	45	58.70	45.87	48.62
1475	55	52.84	43.77	45.35
1500	50	54.12	49.62	53.93

#### **8.4.2 Impedance analysis of lead free 1-3 randomised composites**

Figure 8.12 (a) and (b) show the electrical impedance spectra and phase of PZT 1-3 composites sintered at 1200 °C. It can be observed, as found in 50BCZT 1-3 composites, the electrical impedance spectra and phase of both 1-3 composites only exhibit one peak corresponding to the thickness resonance. This shows that the random geometries and dimensions of the PZT ceramic bristle blocks also effectively inhibit the spurious modes in agreement with the impedance spectra and phase of 50BCZT composites and research as mentioned in section 8.4.1. Note that there was no requirement to use a bias voltage for the impedance characterization of the PZT composites. Two PZT 1-3 composites with thickness 40 and 58 μm both showed sharp and clearly defined peaks their respective resonant frequencies. In addition, the thickness of composites also affected the resonant frequencies of impedance spectra

and phase as seen in Figure 8.12. The thicker composite had a lower resonant frequency as expected. The information of height, ceramic volume fraction, resonant and anti-resonant frequencies are presented in Table 8.2. Both composites presented the ceramic volume fraction approximately 40% which is in agreement with the desired value and PZT randomised composite with 45 vol% solids loading report by Jiang [4]. According to the resonant and anti-resonant frequencies, the operating frequencies of composite with 40 and 58  $\mu\text{m}$  thickness can be predicted around 30 MHz and 60 MHz, respectively as expected. This also confirms that the PZT 1-3 composites can be produced with various dimensions, geometries, and thickness to meet the requirement of various frequencies by using the gel casting method.

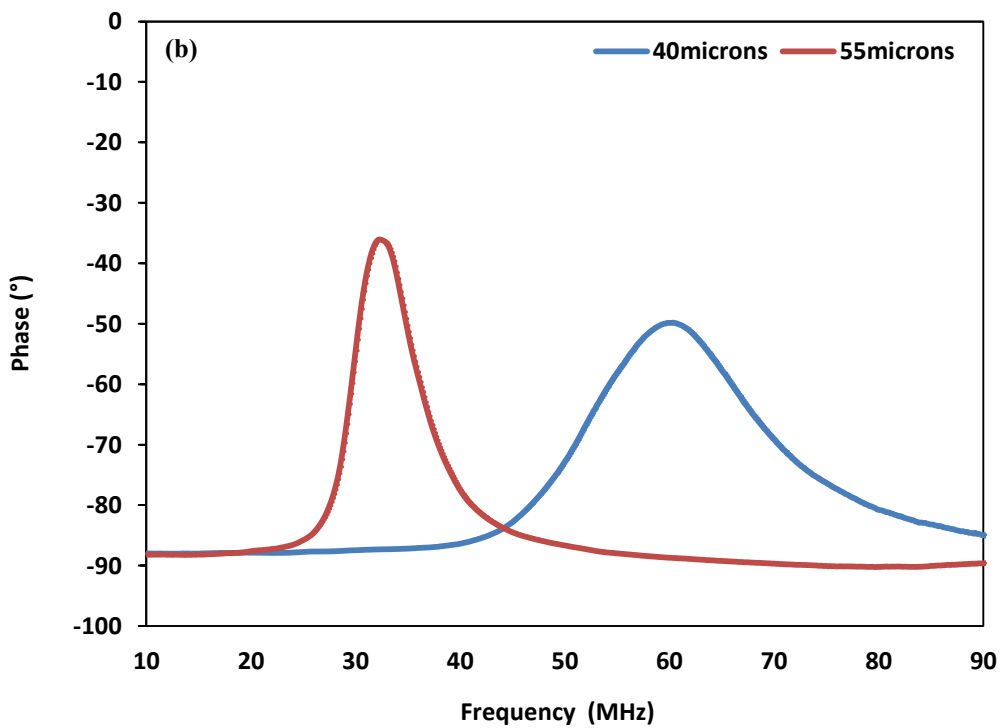
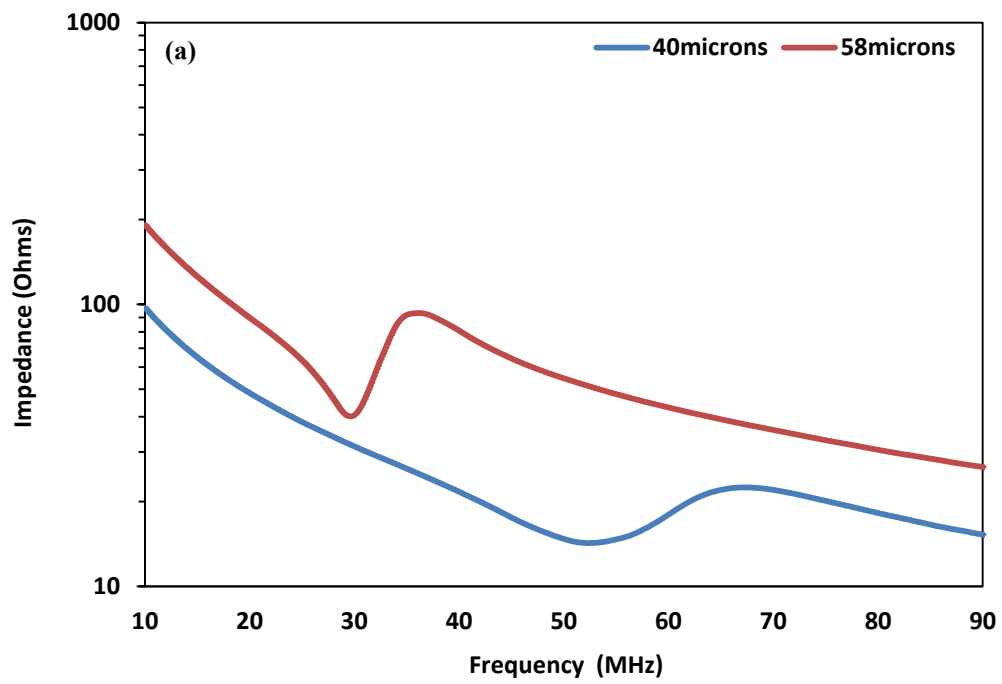


Figure 8.12 Impedance (a) and (b) phase magnitude diagrams measured from PZT randomised 1-3 composites sintered at 1200 °C with different thickness.

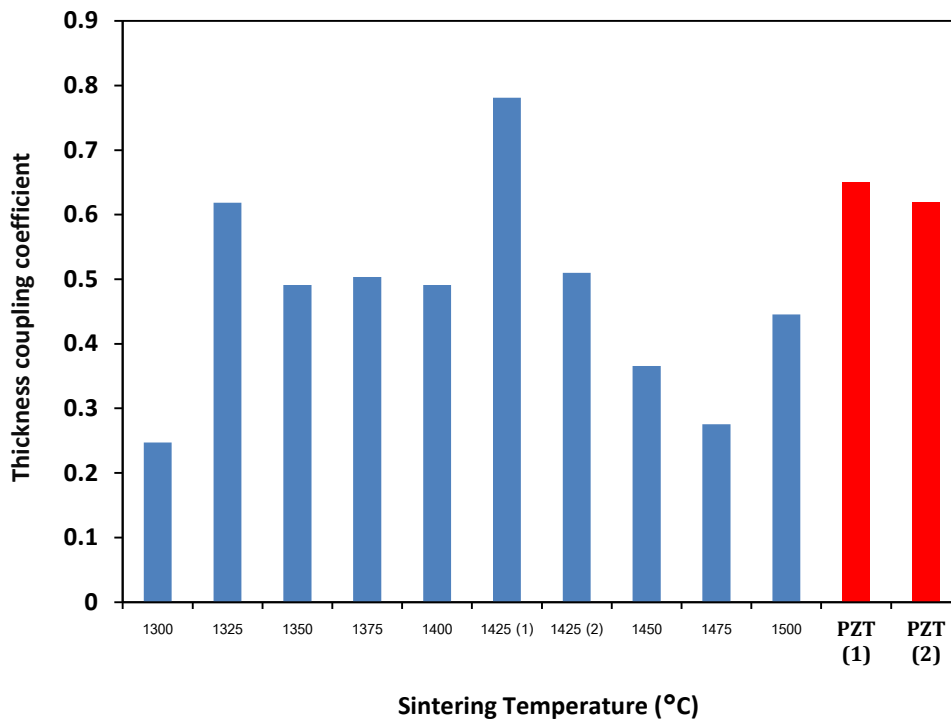
**Table 8.3 Summary of PZT randomised composites sintered at 1200 °C.**

Sintered temperature (°C)	1-3 composite height (µm)	Ceramic volume fraction (%)	Resonant frequency (MHz)	Anti-resonant frequency (MHz)
1200 (No.1)	40	46	52.25	67.15
1200 (No.2)	58	43	29.01	35.33

## **8.5 Functional performance of lead free and lead based 1-3 randomised composites**

As explained in Chapter 3, the thickness coupling coefficient ( $k_t$ ) is one of the most important key parameters for assessing the composite performance, and relates to the ability of the composite to convert between electrical and mechanical energy when the applied electric field and vibration are in the thickness direction. In order to achieve a high performance composite,  $k_t$  should be as close to 1 as possible. The thickness coupling coefficients of 50BCZT 1-3 composites sintered at various temperatures are shown in Figure 8.13. The highest value of  $k_t = 0.78$  was measured from the composite sintered at 1425 °C sample 1 with a thickness = 56 µm, and the lowest value of approximately  $k_t = 0.25$  was found from the composite sintered at 1300 °C. This may be caused by the microstructure in Figure 8.6 a (ii). For PZT composites, they both presented higher  $k_t$  values than all the BCZT composites except for one of the 50BCZT samples sintered at 1425 °C sample 1 as expected. Compared to the  $k_t$  values ranging from 0.5-0.68 obtained from composites with PZT 45 %vol solids loading reported by Jiang [4], the  $k_t$  values obtained from PZT with 48 %vol solids loading in this work have similar values.

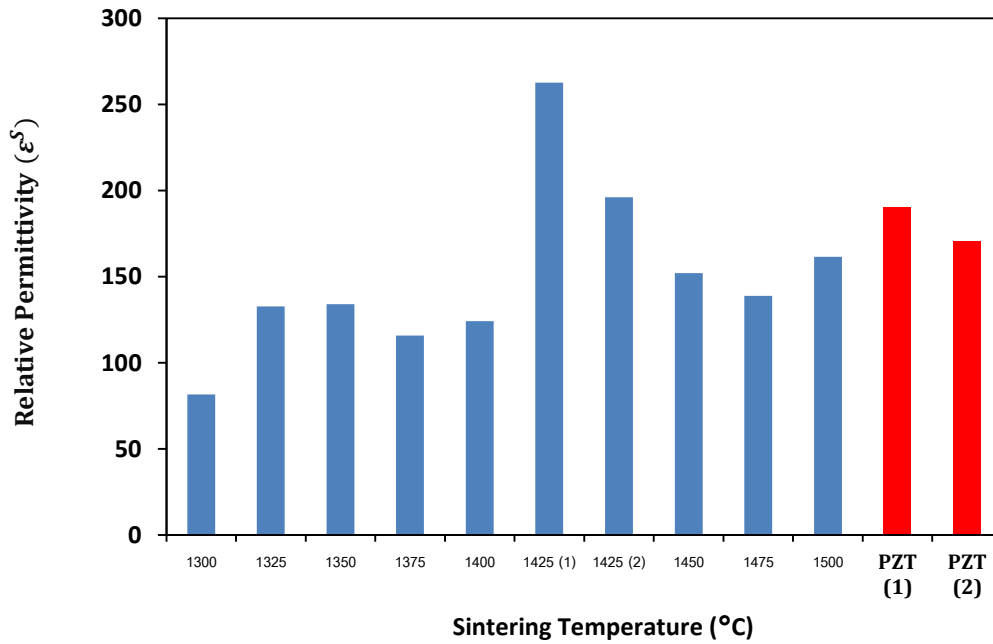




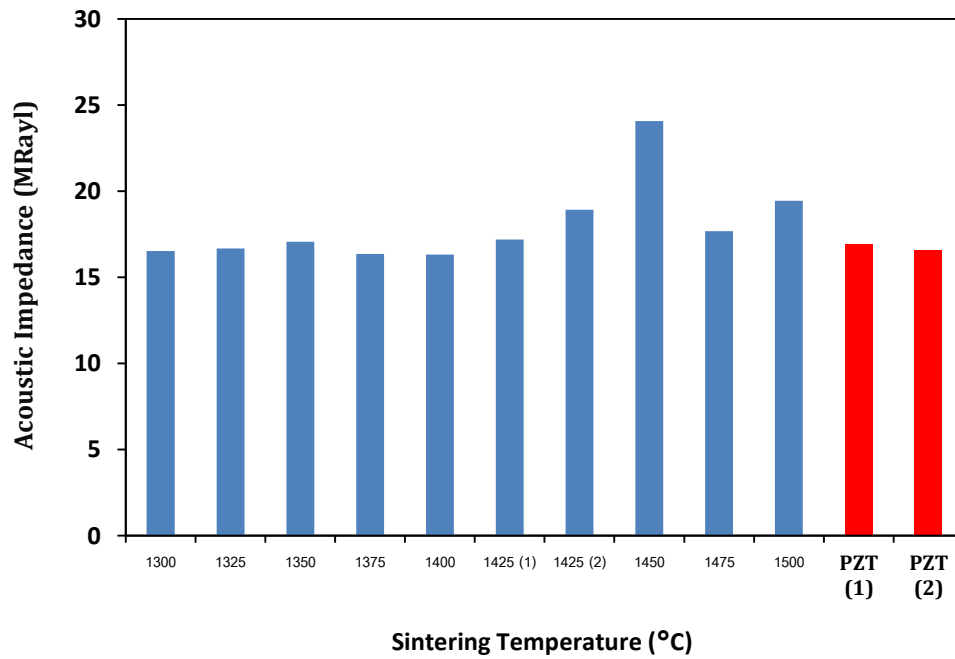
**Figure 8.13 Thickness coupling coefficient ( $k_t$ ) of the 50BCZT randomised composites sintered at 1300 °C - 1500 °C and PZT randomised composites sintered at 1200 °C.**

Figure 8.14 shows the relative permittivity at constant strain of 50BCZT randomised composites sintered at various temperatures and PZT composites sintered at 1200 °C. The relative permittivity of the composite is related to the relative permittivity and relative density of the individual phases, and their volume fractions in the composite. For 50BCZT 1-3 composites, the highest relative permittivity (262) was observed for the 50BCZT composite sintered at 1425 °C which possessed the highest thickness with 56  $\mu\text{m}$  and largest ceramic volume fraction (58.5%), while the composite sintered at the same temperature with thickness 52  $\mu\text{m}$  presented a lower ceramic volume fraction (52.9%) and a correspondingly lower  $\epsilon^S$  (193). The smallest value was found for the composite sintered at 1300 °C. This sample not only had the lowest ceramic volume fraction (48.6%) but also, based on the data for the bulk 50BCZT ceramics presented in Chapter 6, the ceramic phase itself may have a lower

density (see section 6.5.2). The PZT composites with thickness 40  $\mu\text{m}$  and 58  $\mu\text{m}$ , had relative permittivity values of 190 and 170, respectively. These results are reasonable considering the fact that the ceramic volume fraction of 40  $\mu\text{m}$  composite (46%) is higher than that of the 58  $\mu\text{m}$  composite (43%).



**Figure 8.14** Relative permittivity at constant strain ( $\epsilon^S$ ) of the 50BCZT randomised composites sintered at 1300 °C - 1500 °C and PZT randomised composites sintered at 1200 °C.



**Figure 8.15 Acoustic impedance of the 50BCZT randomised composites sintered at 1300 °C - 1500 °C and PZT randomised composites sintered at 1200 °C.**

Figure 8.15 shows the acoustic impedance  $Z_a$  of 50BCZT and PZT composites. For 50BCZT, it can be seen that the composite sintered at 1450 °C with highest ceramic volume fraction (58.70%) exhibited the highest  $Z_a$ . For the two composites sintered at the same temperature (1425 °C), the composite with higher ceramic volume fraction exhibited a slightly lower value of  $Z_a$ . This opposite to what would be expected, but may be indicative of the errors in both the calculation of the volume fraction, and the measurement of  $Z_a$ . As explained in section 2.2.3 and equation 2.3, the acoustic impedance increases with increasing density and sound velocity. The density of the composite relates to relative volume fractions of ceramic and epoxy resin, as the velocity of sound in the ceramic phase is higher than in the epoxy. Therefore, a composite with higher ceramic volume fraction should have a higher density and much faster sound velocity, resulting in higher acoustic impedance. For PZT composites, the acoustic impedance of both composites showed similar values

which are in agreement with the acoustic impedance of PZT randomised composites reported by Jiang [4].

## 8.6 Summary

Lead based and lead free bristle block randomised structures were fabricated by utilising a gel casting process with a soft moulding replication route. Slurries with resin concentrations of 30%wt and 40% wt resin could be successfully demoulded from the PDMS soft moulds. The green stage of both the 50BCZT and PZT piezoelectric materials presented dense segments in green stage with homogeneous, smooth surfaces, no visible cracks, and segments with accurately replicated irregular shapes and well-defined edges. Ceramic segments with the height approximately 140  $\mu\text{m}$  were observed in both materials. However, 50BCZT offered a smallest feature size 5  $\mu\text{m}$ , resulting in an aspect ratio up to 30 while PZT bristle block structures presented the feature sizes as low as 4.28  $\mu\text{m}$ , corresponding to an aspect ratio up to 33.

It was found that the grain size of the 50BCZT segments were smaller than those of bulk ceramics sintered at the same temperature, and the grain size increased with increasing sintering temperature, resulting in microstructural issues in the sintered bristle blocks. The average heights and aspect ratios of ceramic segment at various temperatures ranged from 88  $\mu\text{m}$  - 123  $\mu\text{m}$  and 2.2 – 6, respectively. PZT ceramic segments had much smaller grain size and, after sintering, the segments retained the original structure from the green stage.

1-3 composites were successfully fabricated from the BCZT and PZT bristle block structures. For the PZT composite, the ceramic volume fraction was close to the

desired value while for the 50BCZT composites the ceramic volume fraction were found to be higher due to the microstructural distortions during sintering. The resonant and anti-resonant frequencies in the impedance spectra of 50BCZT 1-3 composites can only be observed by using bias voltage. However, only one resonance peak corresponding to the thickness mode was observed in all samples, with a complete absence of spurious modes. This shows that randomised structures with various dimensions, geometries, and thicknesses can be fabricated by the gel casting method to meet the requirement of various frequencies and effectively diminished the spurious modes. PZT composites offered generally higher thickness coupling coefficients than 50BCZT composites, where the highest value was measured for samples sintered at temperature 1425 °C. The relative permittivity values were affected by the ceramic volume fraction of the composite. Therefore, the composites with the higher ceramic volume fraction had higher values. The highest acoustic impedance was obtained for a 50BCZT composite sintered at 1450°C with a ceramic volume fraction of 58.70%.

## 8.7 References

1. Chandra, D. and S. Yang, *Stability of High-Aspect-Ratio Micropillar Arrays against Adhesive and Capillary Forces*. Accounts of Chemical Research, 2010. **43**(8): p. 1080-1091.
2. Hesketh, P.J., et al., *Microfabricated Systems and MEMS V: Proceedings of the International Symposium*. 2000: Electrochemical Society, Incorporated.
3. Olhero, S.M., et al., *Microfabrication of high aspect ratio BST pillar arrays by epoxy gel casting from aqueous suspensions with added water soluble epoxy resin*. Materials Research Bulletin, 2014. **60**: p. 830-837.
4. Jiang, Y., *Fabrication and characterisation of novel ultrasound transducers*, in *School of Metallurgy and Materials*. 2013, University of Birmingham.
5. Xie, R., et al., *Gelcasting of alumina ceramics with improved green strength*. Ceramics International, 2012. **38**(8): p. 6923-6926.
6. Jiang, C., et al., *Gelcasting of aluminum nitride ceramics using hydantion epoxy resin as gelling agent*. Ceramics International, 2013. **39**(8): p. 9429-9433.

7. Olhero, S.M., et al., *Innovative fabrication of PZT pillar arrays by a colloidal approach*, in *Journal of the European Ceramic Society* 2012. p. 1067-1075.
8. Xie, R., et al., *Fabrication of Fine-Scale 1–3 Piezoelectric Arrays by Aqueous Gelcasting*. *Journal of the American Ceramic Society*, 2014: p. n/a-n/a.
9. Mao, X., et al., *Investigation of New Epoxy Resins for the Gel Casting of Ceramics*. *Journal of the American Ceramic Society*, 2008. **91**(4): p. 1354-1356.
10. Mao, X., et al., *Rheological characterization of gel casting system based on epoxy resin*. *Ceramics International*, 2009. **35**: p. 415-420.
11. Kingery, W.D., *Introduction to ceramics*. 1960: Wiley.
12. Somiya, S., et al., *Handbook of Advanced Ceramics: Materials, Applications, Processing and Properties*. 2003: Elsevier Science.
13. Dou, Z., *Fabrication of ceramic micro-components*, in *School of metallurgy and materials*. 2005, University of Birmingham: university of Birmingham.
14. Brown, J.A., et al., *Fabrication and performance of high-frequency composite transducers with triangular-pillar geometry*. *Ultrasonics, Ferroelectrics and Frequency Control*, IEEE Transactions on, 2009. **56**(4): p. 827-836.
15. Yin, J., et al. *Geometry effect on piezo-composite transducers with triangular pillars*. in *2008 IEEE Ultrasonics Symposium*. 2008.
16. Hao-Chung, Y., et al. *A study of 1-3 pseudo-random pillar piezocomposites for ultrasound transducers*. in *Ultrasonics Symposium (IUS), 2011 IEEE International*. 2011.
17. Demore, C., et al. *1–3 piezocomposite design optimised for high frequency kerfless transducer arrays*. in *IEEE Ultrason. Symp*. 2009.

# **Chapter 9 High frequency transducer fabrication, characterisation and imaging**

## **9.1. Transducer fabrication**

PZT and 50BCZT 1-3 composites have been fabricated and characterised as explained in Chapter 8 and four of them were selected to be taken forward and used as the active element in high frequency transducers. The selected 50BCZT composites can be identified in Table 8.2 as those sintered at 1425 °C with thicknesses of 56  $\mu\text{m}$  and 52  $\mu\text{m}$ , which were used for the fabrication of unfocussed and focussed transducers respectively. Transducers were also fabricated from the two PZT composites listed in Table 8.3, with the 40  $\mu\text{m}$  and 58  $\mu\text{m}$  thick composites selected for unfocussed and focussed transducers respectively. In this chapter, the transducer fabrication and characterisation are described. Fabrication and some initial characterisation were carried out in Birmingham to ensure the transducers were working at their intended frequencies, and more detailed characterisation was then undertaken at the University of Glasgow.

The overall transducer design was based on previous work [1, 2]. This necessitated having the composites laser cut to a diameter of approximately 1.6 mm, ensuring the area was selected to minimise the incorporation of any defective areas where, for example, there may be missing or damaged pillar segments, as shown in Figure 9.1 (a). Laser cutting was carried out in the School of Mechanical Engineering, University of Birmingham using a Laser Multi Axis, and a picture of a cut composite is shown in Figure 9.1 (b). The laser cut composites were checked by impedance

analysis to ensure that they were still piezoelectrically active, and this indicated that the resultant focused PZT, focused 50BCZT, unfocussed PZT and unfocussed 50BCZT transducers would have operating frequencies around 35, 40, 50 and 35 MHz respectively.

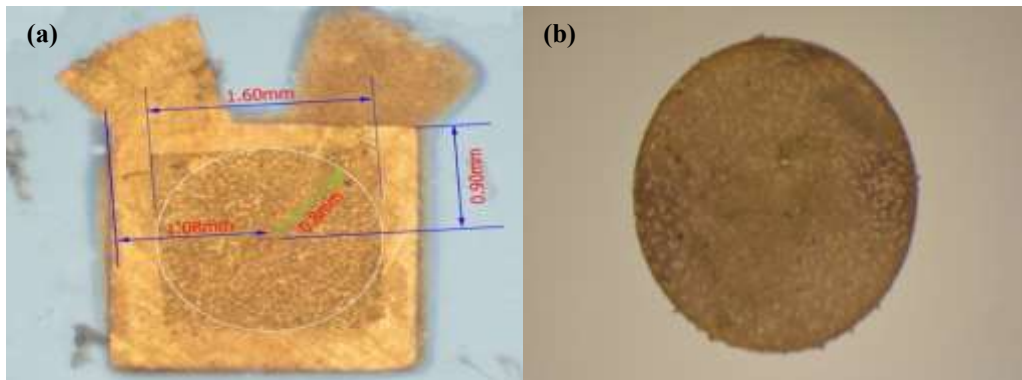


**Figure 9.1 Photograph of (a) 1-3 random composite with dimensions marked for laser cutting, and (b) laser cut 1-3 composite with diameter approximately 1.6 mm.**

In previous work in the Functional Material Group at University of Birmingham [3-5], and some similar work from other groups [6], an SMA electrical connector has been adopted as a transducer housing which requires modification of the centre pin and other internal components. However, this method proved difficult to reproduce reliably due to internal bonding issues [1]. Therefore, in this project, the focussed and unfocussed transducers were fabricated by using the procedures developed by AFM Ltd [7]. A flow diagram of the transducer fabrication procedure is shown in Figure 9.2. There are three main steps. Firstly the replication of the mount master, secondly the replication of the backing insert former. Finally these two components are combined together in a third set of procedures.



In the first step, a polytetrafluoroethylene (PTFE) mount master were utilised for the central positioning of the composites. For fabrication of the focussed transducers, 2 portions of PDMS was prepared as explained in 5.1.1 for replication the mount master and backing insert former. The first portion was poured on top the mount master (as presented in Figure 9.2 (b)), after the PDMS was cured, the PDMS soft mould was peeled off (see Figure 9.2 (c)) and used for positioning and curving the composite. In the second step the backing insert former made from brass was slowly cast using another portion of PDMS mixture in order to forming the soft mould for casting tungsten epoxy and supporting the connected wire as presented in Figure 9.2 (f).

The laser cut composite with diameter approximately 1.6 mm as presented in Figure 9.1 (b) was positioned on the mount master with glue (acrylic emulsion with water, Kuretake Co., Ltd.). The PDMS mould replica from the mount master was slowly placed over the composite. Once the soft mould touched the composite's surface on the mount master, the composite was gently pressed to take the soft mould shape (see Figure 9.2 (d)). After leaving at room temperature for 3-5 minutes for the glue to set, the soft mould was gently removed leaving the composite on the mount master. A copper wire was placed at the edge of the composite's surface using a small amount of silver epoxy as shown in Figure 9.3 (a) and (b).

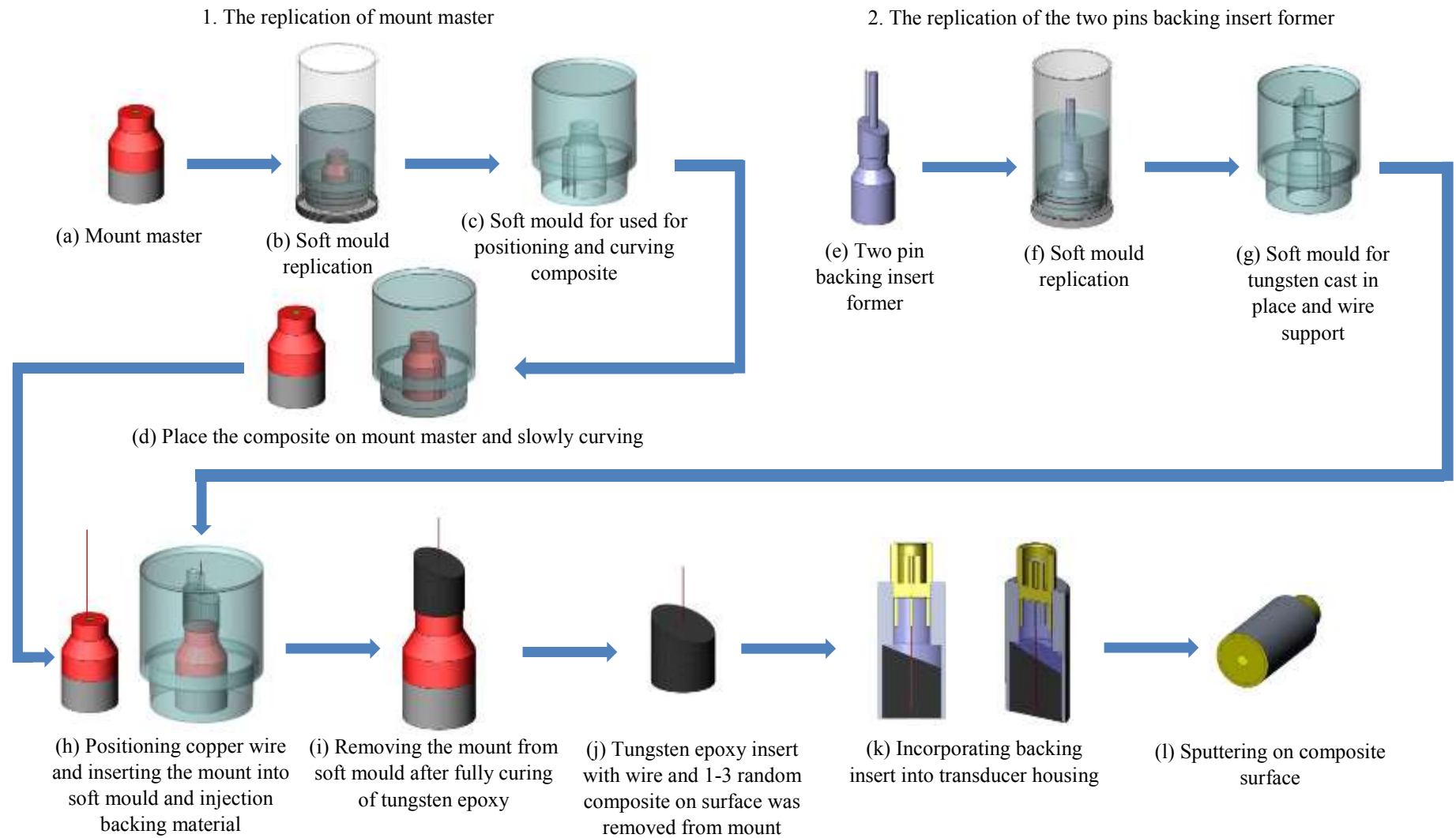


**Figure 9.2 Illustration of the fabrication procedures of transducer (adopted from [1]).**

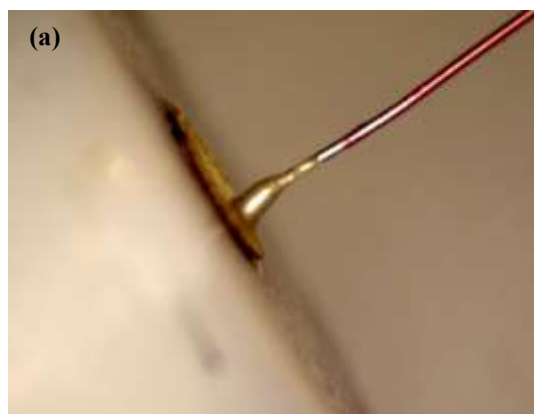


**Figure 9.3 Photograph of (a) The small bulb of silver epoxy fixed the wire on the random composite (b) the copper wire attached on the surface of the random composite on the PLA/PTFE mount master.**

After that the mount assembly with the wire on top was put in an oven at 40°C for 15 minutes to ensure that the conductive silver epoxy was properly set. The mount was slowly inserted into the PDMS soft mould replicated from two pins backing insert former (formed in step 2) ensuring that the wire was also gently inserted through the hole (see Figure 9.2 (h)). According to Webster, tungsten epoxy was adopted as a backing material instead of silver epoxy because it can be cast into shape with low viscosity, resulting in a backing material without porosity. The tungsten powder was

mixed with CY1301/HY1300 (Aradite, UK) at the tungsten volume fraction of approximately 0.3 in order to achieve the appropriate viscosity suitable for casting [1]. The tungsten mixture was degassed for 5 minutes to minimise bubbles, followed by injection into the soft mould using a syringe needle. This technique is called “cast in place”. After the soft mould was fully filled in its cavity with the tungsten mixture, the mould was placed in an oven at 45°C for 30 minutes to allow any air bubbles to rise to the top of the soft mould where they could be removed with a syringe needle. After that the whole assembly was left at room temperature for 24 hours and then moved into an oven at 40°C for 10 minutes. The soft mould was then cut and the mount was gently removed, followed by removing the tungsten epoxy from the metal/PTFE mount with the composite stuck on the tungsten epoxy backing as shown in Figures 9.2 (i) and (j). Figure 9.4 presents the photograph of 1-3 random composite and tungsten epoxy backing layer casted onto the 1-3 random composite. The tungsten epoxy with the transducer element on top was fitted into a stainless steel housing, followed by connecting the copper wire to the centre pin of an MCX connector by soldering and then the connector was fitted into another end of housing (Fig 9.2 (k)). The surface of composites was gently cleaned and then sputtered with a thin layer of Cr and thick layer of Au, respectively (Fig 9.2 (l)). Figure 9.5 presents an example of completed transducers produced using this method. However, some active area of 1-3 random composite of the focussed PZT transducer was broken during curving, resulting in the imperfect curve in the active area of the focussed transduce as shown in Figure 9.6.

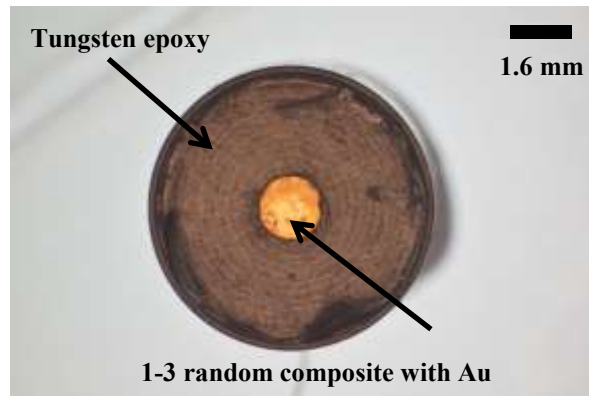


Figure 9. 4 Photograph of 1-3 random composite with diameter 1.6 mm stuck onto the cast tungsten epoxy backing.

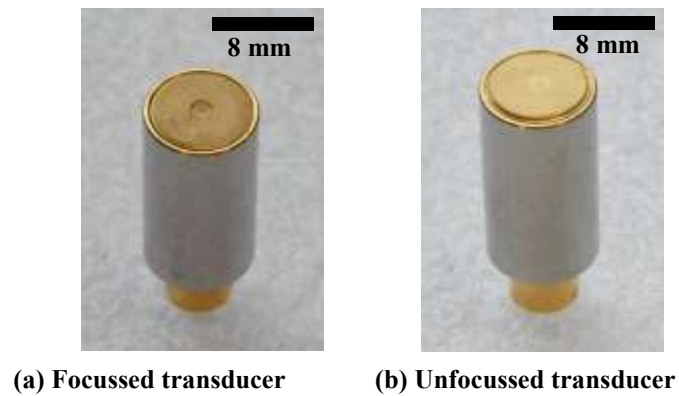


Figure 9. 5 Photograph of completed (a) focussed transducer and (b) unfocussed transducer.



Figure 9. 6 The photograph of the imperfect curve within the active area of a focused PZT transducer.

## 9.2 Transducer characterisation

### 9.2.1 Electrical impedance

Figure 9.7 presents the electrical impedance spectra and phase magnitude of the focussed and unfocussed PZT and 50BCZT transducers. The impedance data of the transducers are similar to those of the respective 1-3 composites, as presented in Figures 8.11 and 8.12. The results demonstrate that the transducers are functional, even the focussed PZT transducer with a defective active area in which the intended curved geometry was not fully achieved (see Figure 9.6). The lead free transducers were measured with a DC bias of -40 volts in order to determine the resonance peaks more clearly. However, even under this DC bias condition, the  $f_r$  and  $f_a$  of the focussed 50BCZT transducer were still not clearly defined. The resonant frequencies of transducers occurred in the range that they were expected as shown in Figures 9.7 and 9.8. The focussed PZT, unfocussed PZT and unfocussed 50BCZT transducers show operating frequencies at 32 MHz, 55 MHz and 33 MHz (from the raw data), respectively while  $f_r$  and  $f_a$  of focussed 50 BCZT could not be observed but the operating frequency was subsequently obtained by pulse-echo testing. It can be seen clearly that none of the transducers exhibit lateral resonance in the board frequency range of 10-80 MHz and only the thickness mode resonance is present. The results correspond well to a focussed PZT random composite transducer fabricated using a gel casting method reported by Jiang [2]. In comparison, lead based transducers with operating frequencies of 36 MHz and 45 MHz fabricated with composites comprising regular circular pillar geometries and fabricated using a VPP route have been reported to have lateral modes at around 50 MHz and 75 MHz, respectively

[2, 8]. Also, lead based transducers with regular square pillar composites fabricated by a dice and fill method, as reported by Brown et al. [9], have 2 or more resonance modes due to the design of the composite.

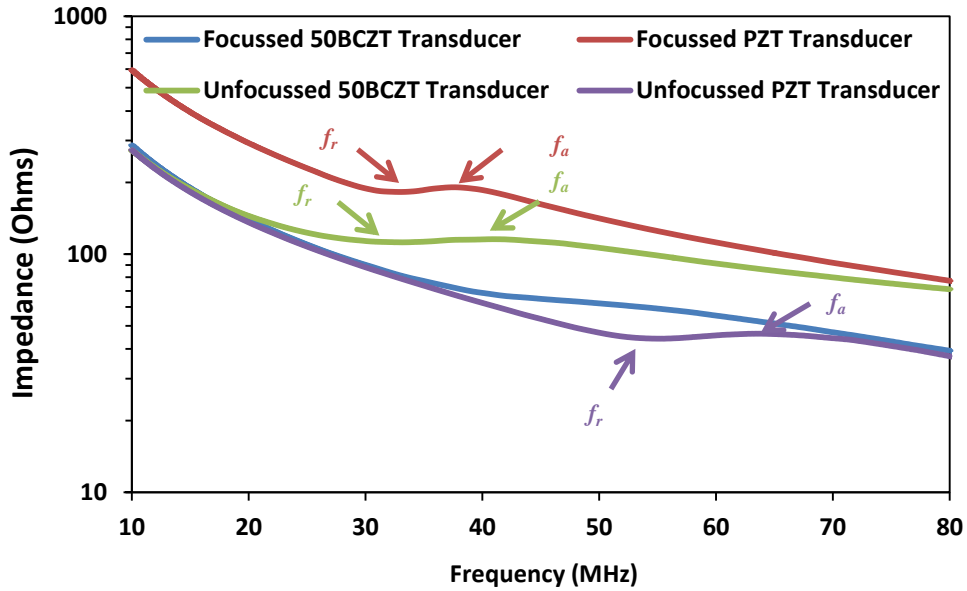


Figure 9.7 Electrical impedance and phase measured from transducers, using a bias -40 volts for the 50BCZT transducers.

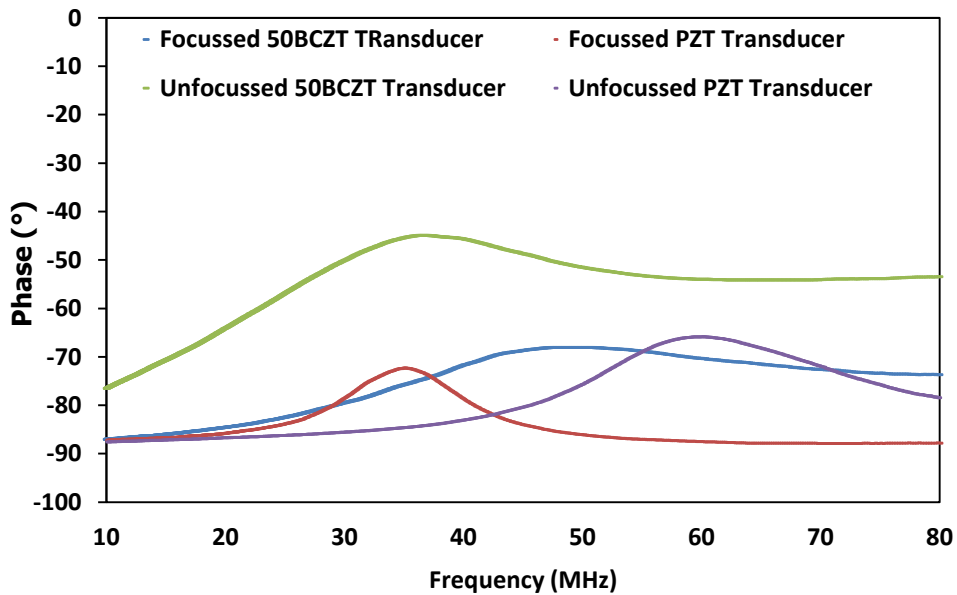


Figure 9.8 Phase magnitude diagram measured from transducers, using a bias -40 volts for the 50BCZT transducers.

### 9.2.2 Pulse-Echo response

The pulse-echo responses of all transducers were measured by using flat quartz as a target. Figures 9.9 - 9.12 present the results for the focussed PZT, focussed 50BCZT, unfocussed PZT and unfocussed 50BCZT transducers, respectively. The spatial pulse length, axial resolution and other characteristics of the all transducers including operating frequency, bandwidth and fractional bandwidth at -6 dB have been calculated and are shown in Table 9.1. It can be seen from the pulse-echo data that the centre frequencies of the focussed 50BCZT, focussed PZT, unfocussed 50BCZT and unfocussed PZT transducers are 40 MHz, 35 MHz, 35 MHz and 50 MHz respectively, which is in agreement with the impedance spectroscopy data presented in Figure 9.7.

The pulse-echo responses of focussed PZT transducer suffered due to the imperfect curve of active material. The axial resolutions of all transducer were defined as one-half of the spatial pulse length as presented in equation 2.7. The spatial pulse length (SPL) can be calculated by substitution of the number of wavelengths, speed of sound in water and frequency of each measurement into the equation 2.6 and then the axial resolution can be defined as presented in Table 9.1. It can be clearly seen that the best axial resolution (shortest length) in this measurement can be obtained from the shortest spatial pulse length and highest frequency which in this case is obtained for the unfocussed PZT transducer with the spatial pulse length 88.92  $\mu\text{m}$ . The results are also in agreement with the results of bandwidth and fractional bandwidth at -6dB (see in Table 9.1). Compared to a narrow bandwidth, a broad bandwidth transducer generates a shorter spatial pulse length resulting in an improvement of axial resolution. A PZT transducer with operating frequency around 30 MHz and



fabricated using a random composite was reported by Jiang [2] to have a bandwidth at -6 dB was 13 MHz, corresponding well to the 35MHz 50BCZT transducer. However, the 35 MHz PZT transducer presents lower bandwidth than expected, which may relate to the imperfect curving of the composite. A VPP composite transducer with a regular geometry of composite was reported to have a bandwidth of 29 MHz [8]. However, all transducers fabricated using gel casting with random composite geometries have resulted in lower bandwidths, which also may relate to the composite geometry.

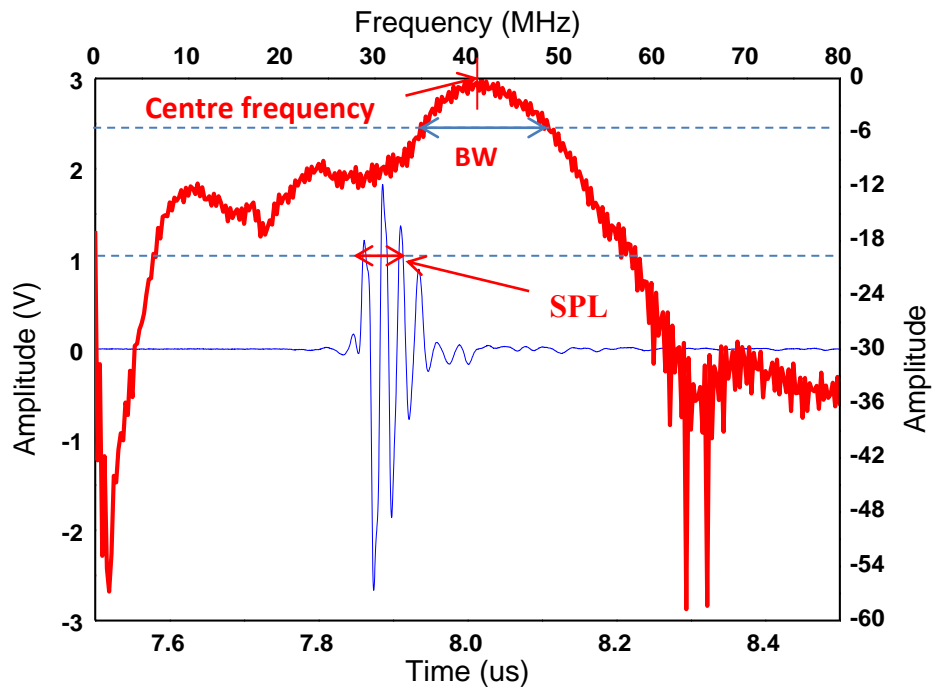


Figure 9.9 Pulse-echo measured from focussed 50BCZT transducer at focus in time and frequency domain, showing frequency, bandwidth.

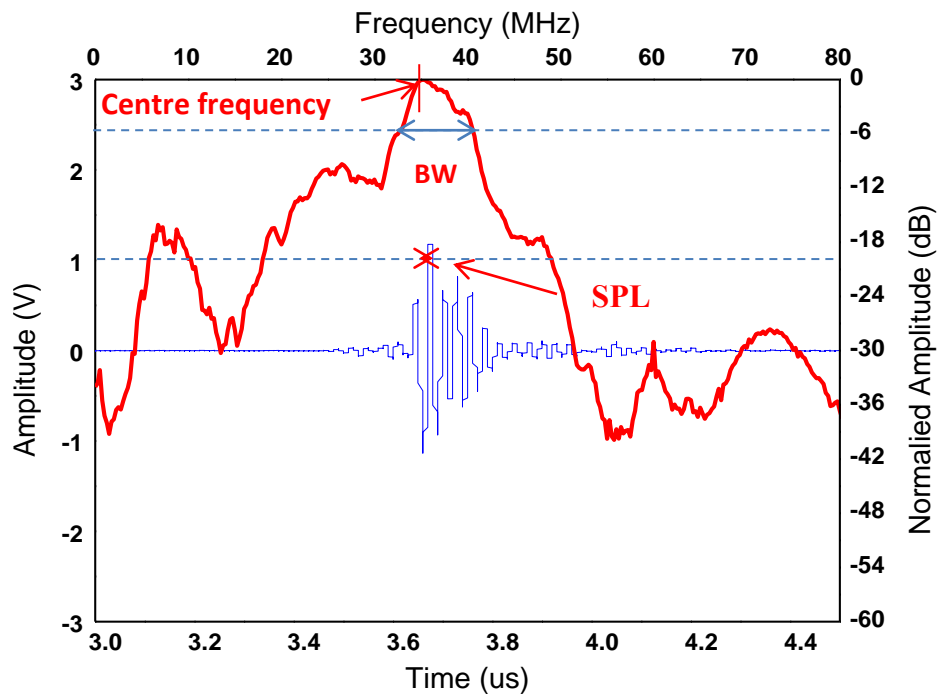


Figure 9.10 Pulse-echo measured from focussed PZT transducer at focus in time and frequency domain, showing frequency, bandwidth and spatial pulse length.

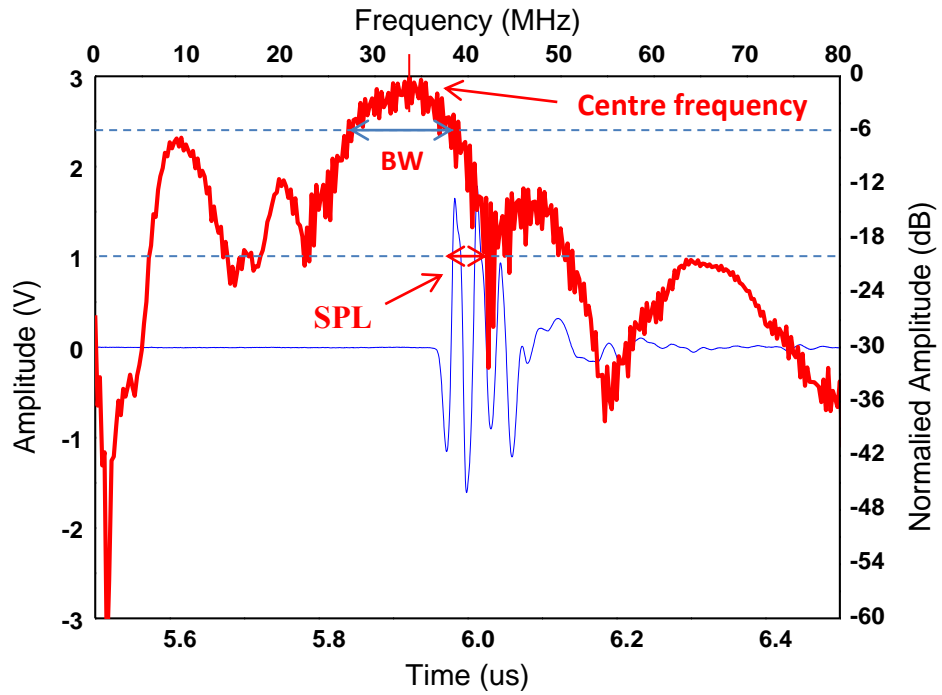


Figure 9.11 Pulse-echo measured from unfocused 50BCZT transducer at focus in time and frequency domain, showing frequency, bandwidth and spatial pulse length.

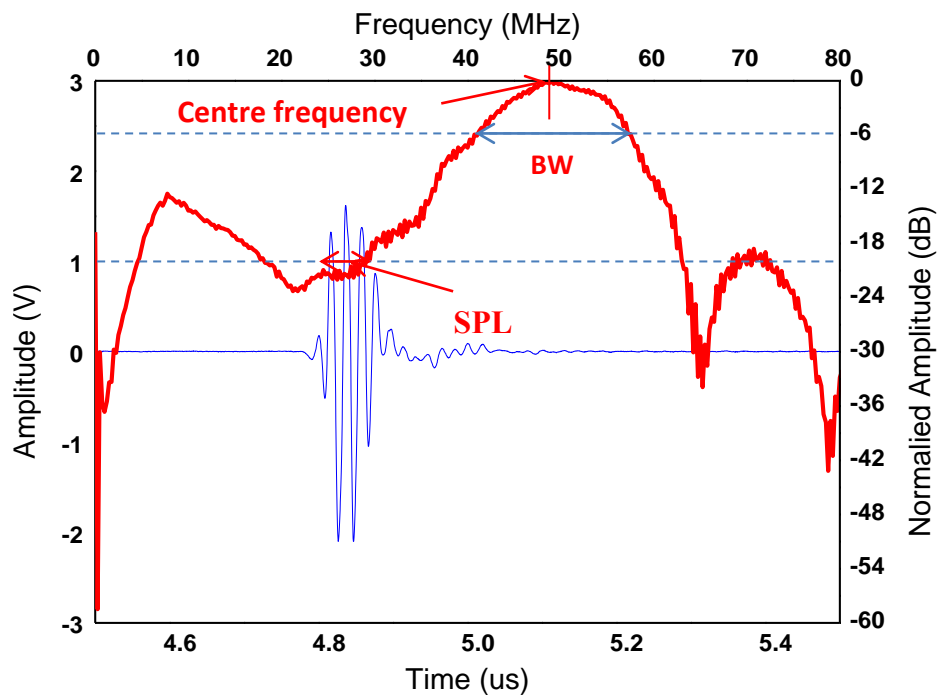


Figure 9.12 Pulse-echo measured from unfocused PZT transducer at focus in time and frequency domain, showing frequency, bandwidth and spatial pulse length.

**Table 9.1 Characteristics and properties of focussed 50BCZT, focussed PZT, unfocussed 50BCZT, unfocussed PZT transducer.**

Transducers	Pulse-echo Measurement							B-Scan Measurement		
	Spatial pulse length ( $\mu\text{m}$ ) at -20 dB	Axial resolution ( $\mu\text{m}$ ) at -20 dB	Maximum frequency (MHz) at -6dB	Minimum frequency (MHz) at -6dB	Center Frequency (MHz) at -6dB	Bandwidth (MHz) at -6dB	Fractional bandwidth (%) at -6dB	Near field (mm)	Focal Zone (mm)	Divergence (mm)
<b>Focussed 50BCZT</b>	111.15	55.57	35	50	40	15	37.5	~ 0-3.4	3.4-7.5	> 7.5
<b>Focussed PZT</b>	211.71	105.85	33	40	35	7	20	~ 0-5	Cannot identify due to the fabrication problem	> 5
<b>Unfocussed 50BCZT</b>	127.02	63.51	27	40	35	13	37.14	0-8	--	> 8
<b>Unfocussed PZT</b>	88.92	44.46	40	57	50	17	34	~ 0-5.5	--	> 5.5

### **9.2.3 Tungsten wire phantom imaging**

The set up for the tungsten wire scan experiment was carried out with support from the Medical and Industrial Ultrasonics (MIU), The University of Glasgow. The set up was shown in Figure 5.10. A pulser/receiver DPR/500, remote pulse box RS RP-H2, NI PXIe controller, frame, scanning stage and stage controller, were set up for this measurement and connected to a computer with a LabView interface to control the scanning directions and MATLAB to process the data. The transducer was positioned on a JRS RP-H2 stage box which was placed on the frame in order to prevent the vibration during testing. The transducers were scanned over a set of 25  $\mu\text{m}$  diameter tungsten wires in water with the step size between each wire of 1 mm. A schematic of the test system is shown in Figure. 9.13.

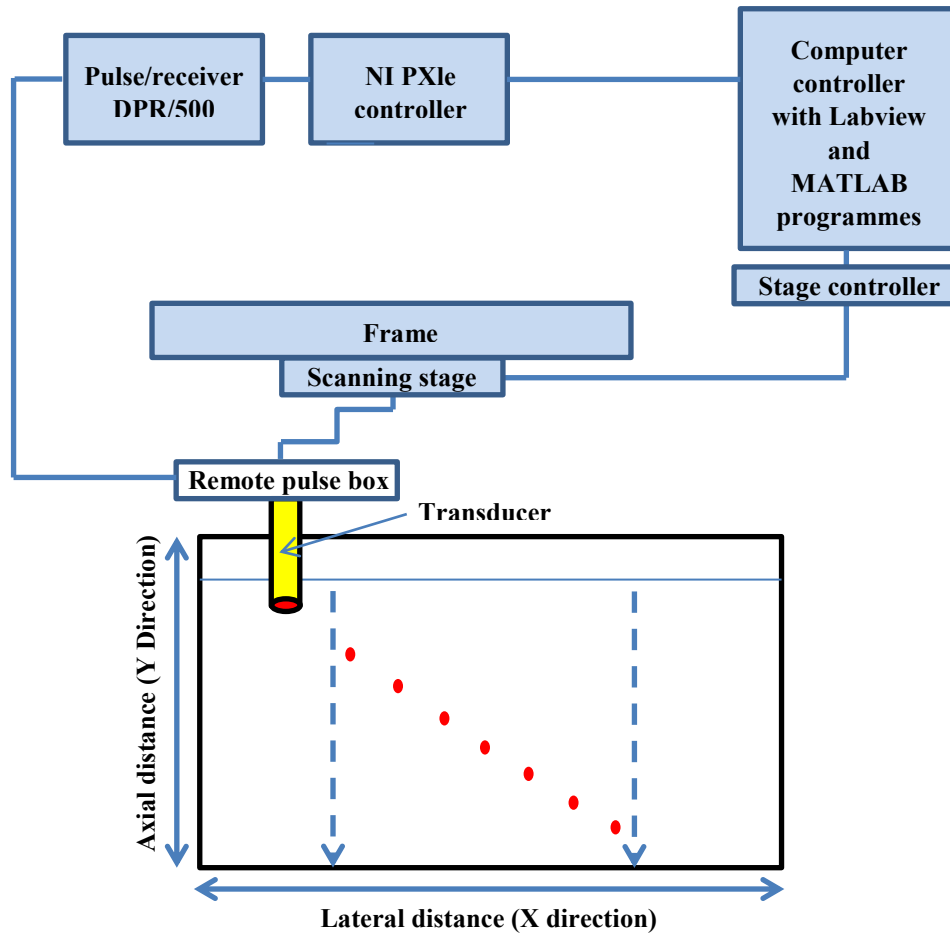


Figure 9.13 Schematic illustration of the tungsten wire phantom scanning experiment in which the transducer travelled along the lateral distance at different depth between transducer and tungsten wires.

The B-scan images of the wires scanned by the four transducers are shown in Figure 9.14. In each experiment, MATLAB was used for creating all B-scan images by taking the median values of the 7x7 matrix from the absolute value raw data. B-Scan images from all transducers confirmed that the transducers are able to function and create images of the fine tungsten wires at a range of distances from the transducers. The B-scan images from three of the transducers clearly show all the wires at different distances from the transducers. However, compared with other transducers, the B-scan image of wires obtained from the unfocussed PZT transducer with

operating frequency 50 MHz cannot be seen clearly when the ultrasound wave travelled longer than ~5 mm. as shown in Figure 9.14 (d). This is due to the reduced penetration of the ultrasound at the higher frequency of this transducer. With increasing axial distance, the focused and unfocussed PZT transducers show a greater change of the image with lateral distance. As can be seen in figure 9.14 (b), the lateral distance of each wire increased with increasing axial distance and also the B-scan image of each wire is slightly bent. This unexpected result is possibly due to the area of the 1-3 random composite for this focussed PZT transducer not being curved uniformly as shown in Figure 9.6.

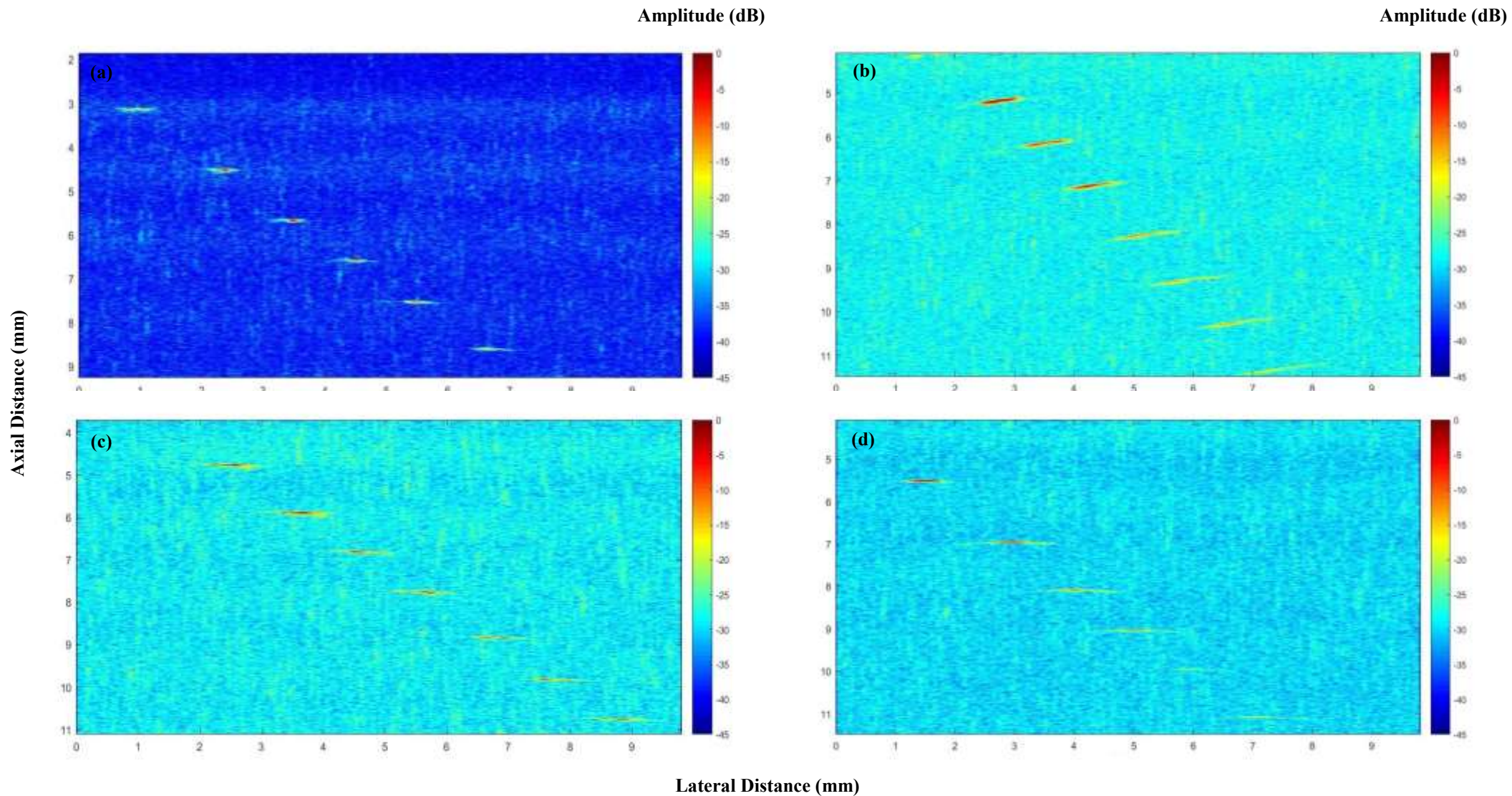


Figure 9.14 B-scan images of a set of 25  $\mu\text{m}$  tungsten wires at different distances using (a) focussed 50BCZT, (b) focussed PZT (c) unfocussed 50BCZT and (d) unfocussed PZT transducers.



The amplitude at different axial travelling distances of the transducers is shown in Figure 9.15. For the focussed PZT transducer, the highest amplitude was observed at the distance between transducer and wires of around 5.17 mm and the amplitude then decreased with increasing the distance. Similarly, the amplitude of focused 50BCZT transducer increased with increasing the axial distance and hit the peak at around 5.5 mm, followed by decreasing when the distance between the transducer and wires increased. These results are in agreement with near field, focal zone and far field of transducer beam shape expected from focused transducers. However, the unusual result from focussed PZT transducer may relate to the active composite was not curved with a right radius of curvature. The amplitude trend of unfocussed PZT decreased with the increasing of penetration depth which is also in agreement with the beam shape of unfocussed transducer that typically has a near field and divergence zone. For the unfocussed 50 BCZT transducer, the amplitude increased with increasing axial distance and hit a peak when the distance between transducer and wire was about 5.9 mm and then the amplitude remained approximately constant. Figure 9.16 shows the amplitude of all transducers when they travelled at different depths. The value at -6dB has been used to define the beam zone which is stated in Table 9.1.

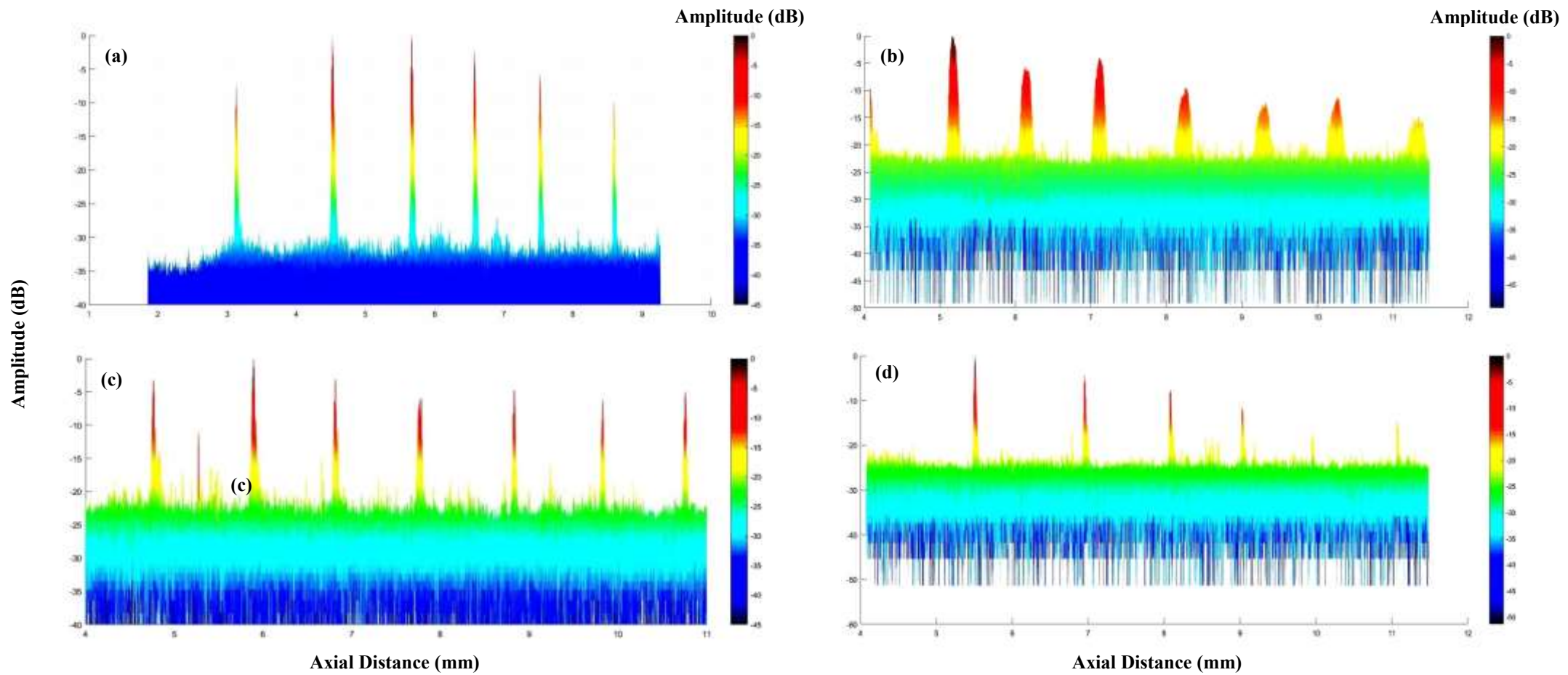
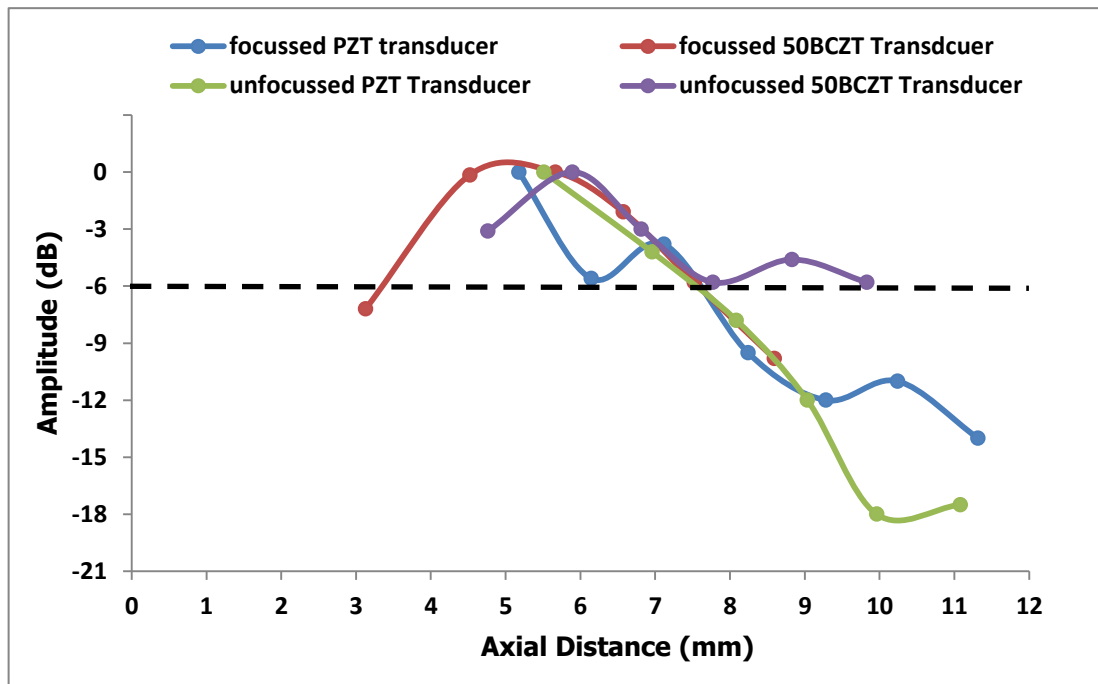


Figure 9.15 The 2D B-scan images of the amplitude at different travelling distance of (a) focussed 50BCZT, (B) focussed PZT (c) unfocussed 50BCZT and (d) unfocussed PZT transducers.



**Figure 9.16** The amplitude at different travelling distance of focussed PZT, 50BCZT, unfocussed PZT and unfocussed 50BCZT transducers, cut off at -6dB.

From the B-scan measurements, the lateral and axial resolutions of the focussed and unfocussed transducers at different distances were defined by calculating the lateral and axial distance at -6 dB of each tungsten wire. Figure 9.17 presents an example of the 3D images including amplitude (dB), lateral distance (mm) and axial distance (mm) of the focussed 50BCZT transducer when scanned all wires. From this data, the axial and lateral resolution of the transducer can be defined. Figure 9.18 shows an example of 2D images of the amplitude, axial and lateral distance of the focussed 50BCZT transducer when the transducer scanned all the wires and an enlarged view of the second wire at -6dB. Therefore, the axial and lateral resolution of transducer along the travelled distance can be calculated. By doing this with all wires, the axial and lateral resolution of each transducer could be defined, and this is presented in Figures 9.19-20. The axial resolutions of three transducers remain approximately

constant when the distance between the transducer and wires increased. However, the data obtained from focused PZT transducer presents an unexpected trend due to the problem during construction. The lateral resolutions of focussed and unfocussed transducers present results which are in agreement with their beam zone as discussed above.

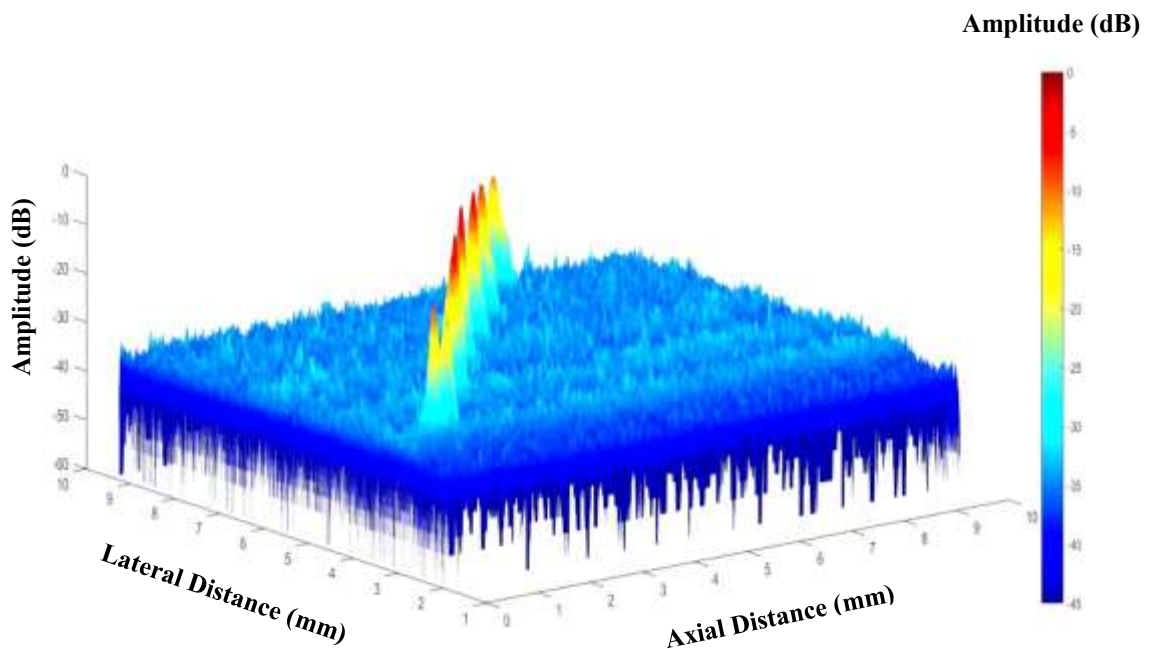


**Figure 9.17** Schematic illustrate 3D B-scan image for calculating the axial and lateral resolution at -6dB of a set of tungsten wires obtained from the focussed 50BCZT transducer.

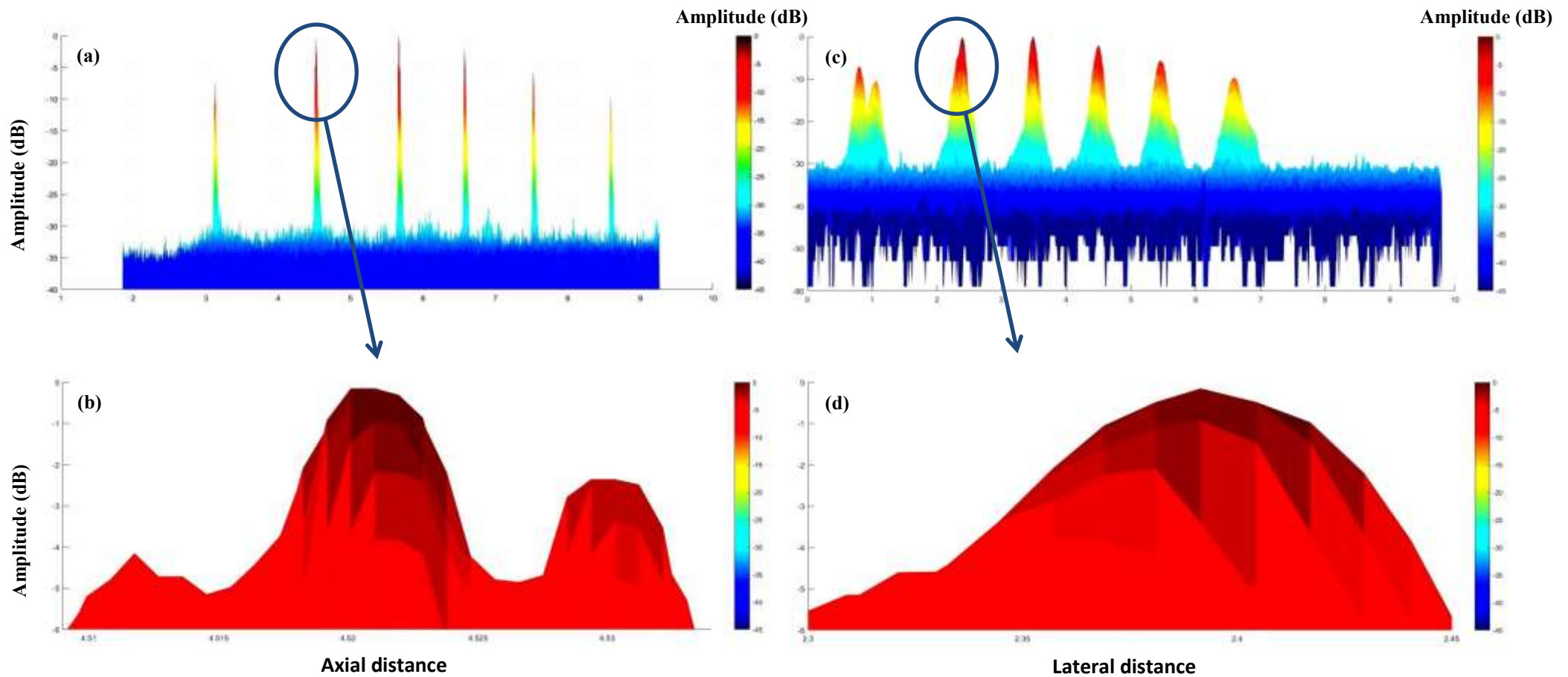


Figure 9.18 Illustration of (a) the axial distance (b) close up data of the axial distance and amplitude when focussed 50BCZT scanned the second wire transducer at -6 dB (c) the lateral distance (b) close up data of lateral distance and amplitude when focussed 50BCZT scanned the second wire transducer at -6 dB for calculating the axial and lateral resolution at -6 dB.

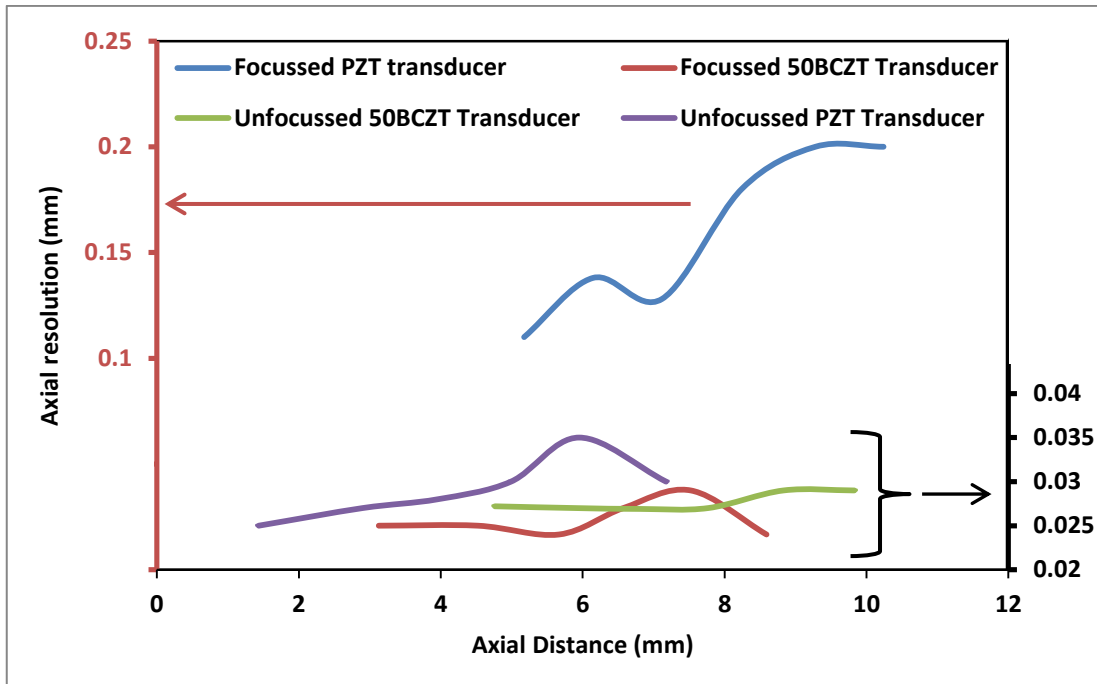


Figure 9.19 Axial resolution of focused and unfocussed PZT and 50 BCZT transducers at different distances, measured at -6dB.

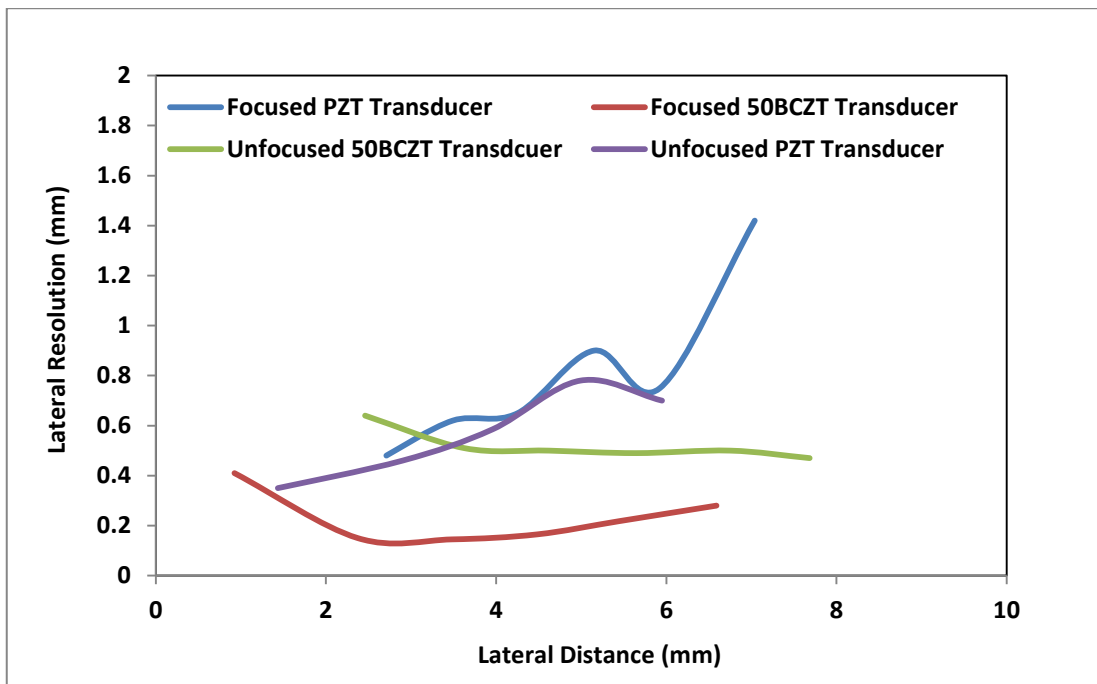


Figure 9.20 The Lateral resolutions of focused and unfocussed PZT and 50 BCZT transducers travelled at different distances, measured at -6 dB.

### 9.3 Imaging of agar phantom and tissue

The scanning of tungsten wires in agar was also carried out at the University of Glasgow, using wires with diameters approximately 100, 200 and 200  $\mu\text{m}$  in 8% of 3  $\mu\text{m}$   $\text{Al}_2\text{O}_3$ , in the agar. The experimental set up is shown in Figure 9.21. The agar phantom images shown in Figure 9.22 confirmed that 3 transducers provided clear wire images including the boundary of agar and petri dish. Only the unfocussed PZT transducer was unable to resolve the boundary of the agar.

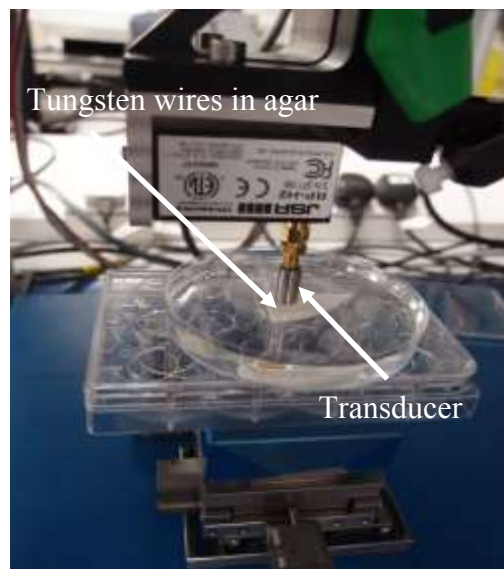


Figure 9.21 Photograph of B-scan of Tungsten wires in agar 8%  $\text{Al}_2\text{O}_3$ .



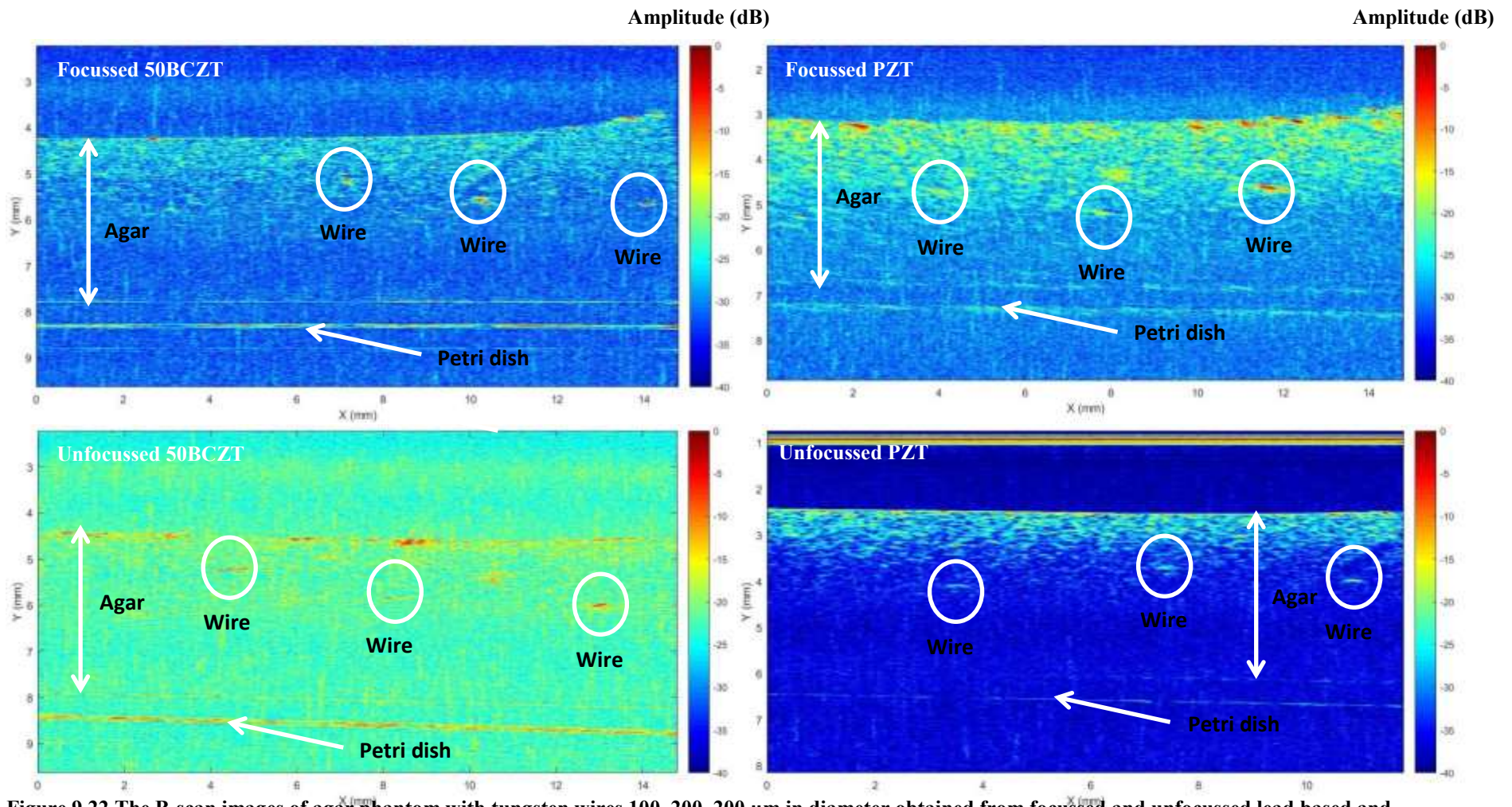
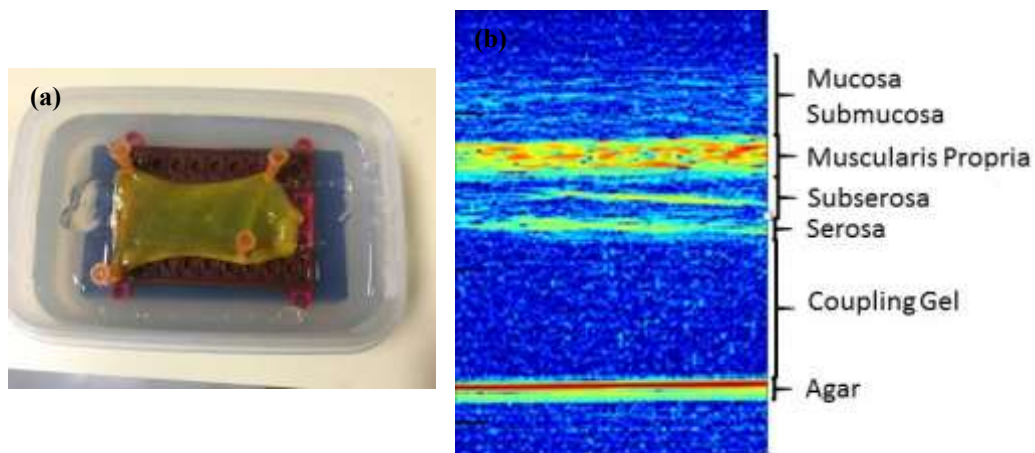


Figure 9.22 The B-scan images of agar phantom with tungsten wires 100, 200, 200  $\mu\text{m}$  in diameter obtained from focussed and unfocussed lead based and lead free transducers.



For tissue scanning, a pig bowel was utilised as the scanning tissue and the scanning were carried out in Clinical Research Centre Tayside at the University of Dundee. The pig bowel structure includes mucosa, submucosa, muscularis propria, subserosa and serosa regions as shown in 9.23 (b). The B-scan images of thin pig bowel sample using focussed 50BCZT transducer (40 MHz) and focussed PZT transducer (35 MHz), these two images are compared side by side as presented in Figure 9.24. The results show that the two transducers provide the images with a good resolution. The main structures of the pig bowel can be seen clearly with both transducers, which is in agreement with the results from Cox [10]. It can be concluded that the quality of the B-scan image created from the focused 50BCZT high frequency transducer is comparable with the PZT transducer.



**Figure 9.23** The photograph of (a) pig bowel with a thickness 2.5 mm submerged in phosphate buffered saline (PBS) at pH 7.4 and (b) the pig bowel structure obtained using an AFM PZT transducer by Dr. Benjamin F Cox (Clinical Research Centre Tayside at University of Dundee) [10].

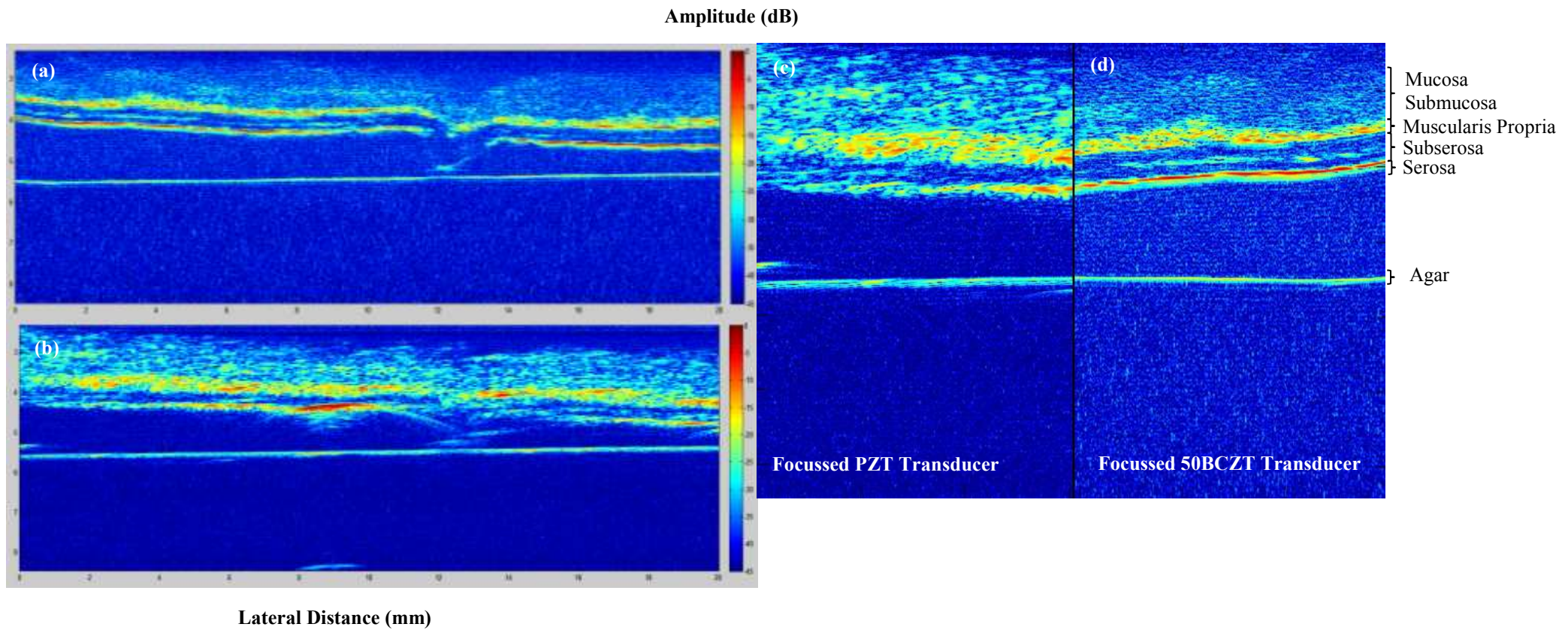


Figure 9. 24 B-scan images of pig bowel from (a) focussed 50BCZT , (b)focussed PZT transducer travelled by 20 mm lateral distance and (c) the side by side comparison of (c) focussed PZT and (d) focussed 50BCZT transducer.

## 9.4 Summary

Focussed and unfocussed lead based and lead free transducers were successfully fabricated using the composites with randomised structure and fabricated by gel casting as the active materials. The focussed 50BCZT, unfocussed 50BCZT and unfocussed PZT transducers were formed in the correct geometries, but the focussed PZT was not uniformly curved. However, the electrical impedance and pulse-echo testing confirmed that all the transducers were functional at high frequencies, in agreement with the results obtained from the respective 1-3 composites. The shortest spatial pulse length at -20 dB was obtained from the transducer with highest operating frequency which was the unfocussed PZT transducer with an operating frequency of 50 MHz. This transducer had the boardest bandwidth and the best resolution compared with the other 3 transducers. The focussed PZT transducer presented unexpected results including the narrow bandwidth, distorted B-scan images of wire phantoms with a bent, undefined focal zone which may be due to the imperfect curving of the active material. In comparison the focussed 50BCZT presented shorter spatial pulse length, boarder bandwidth and defined beam zone with the near field about 0-3.4 mm, focal zone about 3.5-7.5 mm and far field greater than 7.5 mm.

The performance of the transducers was also confirmed by carrying out B-scanning of an agar phantom. The images showed that all transducers functioned properly and provided clear images of the 3 wires, agar boundary and petri dish. The two focussed transducers were selected for tissue imaging, with the images clearly showing the structure of pig bowel and demonstrating that the focussed 50BCZT transducer is comparable with the PZT transducer.

## 9.5 References

1. Webster, R.A., *Passive materials for high frequency piezocomposite ultrasonic transducers*, in *School of Metallurgy and Materials*. 2010, University of Birmingham.
2. Jiang, Y., *Fabrication and characterisation of novel ultrasound transducers*, in *School of Metallurgy and Materials*. 2013, University of Birmingham.
3. Button, T.W., et al., *Net-shape ceramic manufacturing as an aid to realize ultrasonic transducers for high-resolution medical imaging*, in *2005 IEEE Ultrasonics Symposium, Vols 1-4*. 2005. p. 1625-1628.
4. Webster, R.A., *High frequency ultrasonic transducers with fine scale 1-3 piezocomposite structures* 2005, University of Birmingham: University of Birmingham.
5. Sanmartín, D.R., *Fabrication and characterisation of high frequency ultrasound transducers*, in *Department of Metallurgy and Materials*. 2007, University of Birmingham. p. 68.
6. MacLennan, D., et al., *Properties and application-oriented performance of high frequency piezocomposite ultrasonic transducers*, in *2007 IEEE Ultrasonics Symposium Proceedings, Vols 1-6*. 2007. p. 100-103.
7. Carl Meggs AFM Ltd, *the procedures developed for high frequency ultrasound transducer*. 2015.
8. MacLennan, D., *Fundamental Characterisation and Early Functional Testing of Micromoulded Piezocomposites*, in *Department of Bioengineering*. 2009, University of Strathclyde. p. 259.
9. Brown, J.A., et al., *Fabrication and Performance of a 40-MHz Linear Array Based on a 1-3 Composite with Geometric Elevation Focusing*. *IEEE Transactions on Ultrasonics, Ferroelectrics, and Frequency Control*, 2007. **54**(9): p. 1888-1894.
10. Cox, B.F., *Pig bowel imaging* 2016, Clinical Research Centre Tayside, University of Dundee.

# Chapter 10 Conclusions and future work

## 10.1 Conclusions

1-3 PZT piezocomposites with random structure for high frequency ultrasound transducer application have been studied and reported in previous work. The random geometry of segments provides high performance and eliminates spurious resonant modes. In addition, materials based on PZT are the most extensively used piezoelectric materials in ultrasound transducer applications due to their excellent properties. However, PZT contains lead (Pb) as a main constituent element which is very toxic and harmful to human health and the environment. The lead free 50BCZT has been reported as an alternative to PZT because it provides relatively high dielectric and piezoelectric properties similar to PZT. Therefore, in this thesis, for the first time, random lead free composites have been studied and fabricated by using a gel casting and soft moulding technique. Also, for the first time, focussed and unfocussed lead free high frequency transducer incorporating random 1-3 lead free composites as active materials have been fabricated. The aims and objectives for this project were outlined in Chapter 4. It now remains to explore to what extent these have been achieved.

In this work lead free and lead based gel casting slurries were prepared by using hydantoin soluble epoxy resin and amine hardener. The influence of hardener and resin concentrations and curing temperature on the polymerisation between epoxy resin and amine hardener were studied by preparing premix solutions with different hardener and resin contents. The optimum value of amine hardener was found to be 18 g per 100 g resin. Increasing curing temperature was found to accelerate the

reaction rate as the gelation time was decreased. The activation energy of the polymerisation reaction of this gel casting system was calculated to be 82 kJ/mol, in good agreement with literature. With increasing resin content in the premix solution, the elastic modulus and the strength of gel can be enhanced while the gelation time was decreased.

The problems of air trapped in the casting can be prevented by de-airing in vacuum before and after casting. The influences of dispersant, resin and solid loading on the viscosity behaviour of lead free and lead based slurries were elucidated. The optimum amounts of dispersant based on the dried powder weight of lead free and lead based were 2.4 wt% and 1 wt%, respectively, resulting in minimum viscosities in the two systems. An increase in solids loading increased the viscosity of the slurries, and the optimum solids loadings for the lead free and lead based systems were 45 vol% and 48 vol% solids loading, respectively. Increasing resin content was found to increase the viscosity of the slurries, decrease gelation time and sintered density, and result in higher trapped porosity. However, green density and green strength were enhanced. The maximum green strength values of 55 MPa and 58 MPa were achieved in green 50BCZT and PZT samples which were consolidated from the slurries with 45 vol% and 48vol% solids loadings, respectively with 40 wt% epoxy resin. These values were higher than conventional gel casting systems and also other water-soluble epoxy resins such as EGDGE.

For the lead free 50BCZT gel casting system, the highest  $d_{33}$  and  $k_p$  values of 330 pC/N and 0.43 respectively were achieved from gel cast samples consolidated from slurries with 45 vol% solids loading and 30 wt% resin sintered at 1425 °C. The sintering temperature has a complicated influence on grain size and properties.

However, the optimum sintered temperature was 1425 °C as it offered the highest  $d_{33}$ ,  $k_p$  and  $\epsilon^T$  values with the lowest dielectric loss tangent. For the lead based PZT gel casting system, the highest  $d_{33}$ ,  $k_p$  and  $\epsilon^T$  values and lowest dielectric lost tangent were observed in sintered PZT sample produced using a slurry with 30 wt% resin content. A deleterious effect on the piezoelectric and dielectric properties was found for both the 50BCZT and PZT gel casting systems with 40 wt% resin content.

Lead free and lead based bristle blocks with randomised structures have been achieved by using the gel casting and soft moulding techniques. The green bristle block structures from both powder compositions obtained from 30 wt% and 40 wt% resin had dense segments with homogeneous, smooth surfaces, no cracks and well-defined, accurately replicated ceramic segments. The smallest lateral feature size of around 5  $\mu\text{m}$  and aspect ratio up to 30 were achieved by from a 50BCZT slurry with 45 vol% solids loading and 30 wt% hydantoin epoxy resin, while the lead based random structures with smallest lateral feature size of around 4.28  $\mu\text{m}$  and aspect ratio up to 33 were achieved from a PZT slurry with 48 vol% solids loading and 30 wt% hydantoin epoxy resin.

The broad impedance spectra with only a single thickness mode resonance between 100 kHz to 60 MHz were achieved for both 50BCZT and PZT 1-3 randomised composites. However, 50BCZT composites required the application of a DC bias voltage in order to clearly observe the resonance. An increase in thickness of 1-3 composite resulted in lower the resonant frequencies. The absence of spurious modes confirmed that the randomised structure and dimension of the ceramic segments were appropriate for high frequency transducer applications. The 50BCZT random 1-3

composites were had higher volume fractions than expected, caused by grain growth during sintering which will also affect the acoustic impedance of composites.

PZT random 1-3 composites exhibited higher  $k_t$  values than the corresponding BCZT composites. The thickness coupling coefficient of 50BCZT random 1-3 composites varied with sintering temperature, ranging from 0.24 - 0.78 with the highest value achieved for samples sintered at 1425 °C, while the relative permittivity was affected by the ceramic volume percentage of the composite.

Focussed and unfocussed lead free and lead based transducers have been fabricated using the random 1-3 composites as active materials. Lead free focussed and unfocussed complete transducers required the application of a DC bias voltage for impedance measurement, in the same way as the lead free composites. Pulse echo responses demonstrated the operating frequencies of the focussed lead based and lead free transducers were around 40 and 35 MHz, respectively while the operating frequencies of the unfocussed lead free and lead based transducers were observed at 35 MHz and 50 MHz respectively. B-scan images obtained by scanning tungsten wire and pig bowel tissues using the focussed lead based and lead free transducers produced images with good resolution, and demonstrated clearly the structure of the pig bowel. Thus it has been established that the focussed 50BCZT transducer is comparable with the PZT transducer.

Thus the aims of objectives of the project have been achieved in full. The results confirm that not only PZT but also 50BCZT powders can be used for the fabrication of random 1-3 composites for high frequency transducer applications via gel casting and soft mould techniques. The dielectric and piezoelectric properties of 50BCZT gel



cast samples were generally inferior to those obtained from PZT. However, the complete transducers had comparable resolution.

## **10.2 Suggestions for future work**

The focussed and unfocussed lead free and lead based transducers have been achieved and reported in this thesis, which can be regarded as the initial step for studying and development of random lead free composites fabricated using gel casting and soft mould techniques. Although the lead free composites and transducers have been successfully fabricated with relatively good performance and resolution, several problems were encountered which are worthy of further investigation as outlined below. The optimisation of the gel casting system should be studied with a focus on elucidating the interaction and polymerisation reactions in systems containing ceramic powders, water soluble epoxy resin, hardener and dispersant in slurries, looking for improvements in green strength, reduced viscosity, increased solids loading and gelation time.

Other selections of dispersants, epoxy resins and hardeners, and other lead free powders can be considered for enhancing the piezoelectric, dielectric and functional properties and performance of transducers.

In this work the demoulding process was carried out by hand and was dependent on the experience and skill of the operator. An automated demoulding process should be developed which would provide more reliability and control of the process.









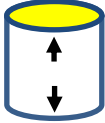

Further work on the 50BCZT materials and composites would elucidate the structure and phase analysis in order to understand more clearly the complex and interrelated

issues such as grain growth during sintering, de-polarization, DC bias voltage requirement and optimisation of the poling process.

The transducer fabrication process is also complex and very dependent on the experience and skill of the operator. In further work, the process should be developed further, looking to integrate techniques such as wire bonding to the composite and the use of motorised stages to minimise faults from manual handling.

## Appendix I : Vibration modes and piezoelectric coefficient of standard samples with electrode on the top and bottom

Table I-1 Vibration modes and piezoelectric coefficient of standard samples with electrode on the top and bottom [1-3].

Vibration modes	direction of Polarization
Transverse length mode 	
Thickness shear mode 	
Radial mode 	
Thickness extension mode 	
Thickness length mode 	

## Appendix II : Material Properties from electrical impedance and capacitance.

Table I-2 Material properties and formulation.

Properties	Formula used
$k_p$	$k_p = \sqrt{\left(2.51 \cdot \frac{f_a - f_r}{f_r} - \left(\frac{f_a - f_r}{f_r}\right)^2\right)}$
$k_t$	$k_t = \sqrt{\frac{\pi}{2} \cdot \frac{f_r}{f_a} \cdot \tan\left(\frac{\pi}{2} \cdot \frac{f_a - f_r}{f_a}\right)}$
$Z_a$	$Z_a = \rho \cdot v$
$v$	$v = 2f_a h$
$\rho_{\text{composite}}$	$\rho = \rho_{\text{piezoceramic}} V_{\text{volume fraction of piezocomposite}} + \rho_{\text{epofix}} V_{\text{volume fraction of epofix}}$
$\varepsilon^T$	$\frac{C_L h}{A \varepsilon_0}$
$\varepsilon^S$	$\frac{C_h h}{A \varepsilon_0}$

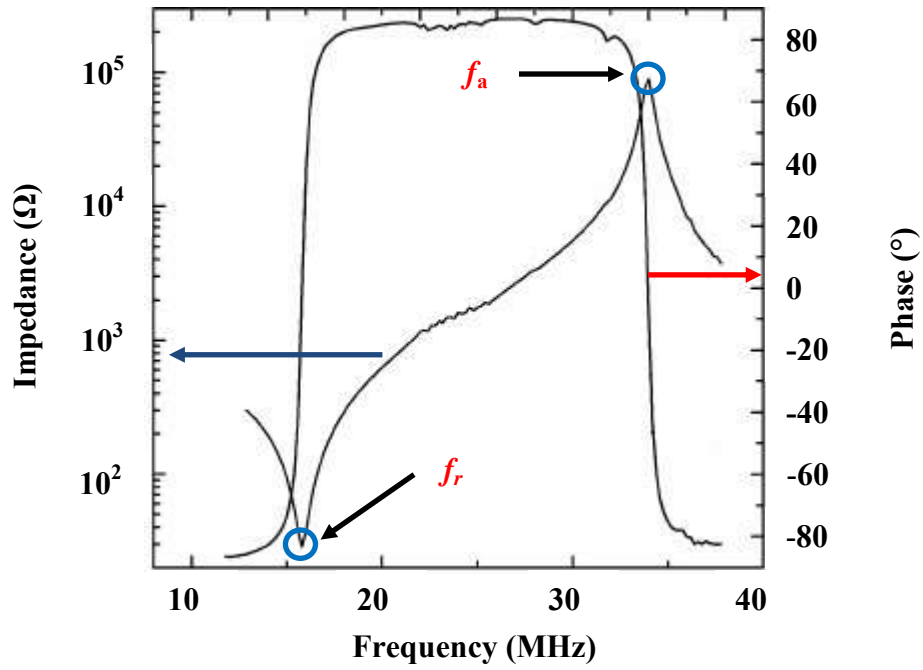


Figure II-1 Impedance and phase angle of a piezoelectric resonator as a function of frequency [4].

## Appendix III : Conference Presentations

Table III-1 Conference presentations.

Name	Paper	Conferences	Year	Place
T.Thongchai, Y. Jiang, C.Meggs, T. W. Button, A. Matousek, H. Hughes	Lead-Free BCZT 1-3 Randomised Composites for High Frequency Ultrasonic Transducer	Electroceramics XV	2016	Limoges, France
T.Thongchai, Y. Jiang, C.Meggs, T. W. Button, A. Matousek, H. Hughes	Evaluation of the functional behavior of lead-free BCZT-based randomized composites for medical ultrasonic imaging applications	International Symposium on Piezocomposite Applications	2015	Dresden, German
Y. Jiang, T.Thongchai, Y. Bai, C.Meggs, T. W. Button, A. Matousek, P. Tofel, H. Hughes	Lead-Free Piezoelectric Materials and Composites for High Frequency Medical Ultrasound Transducer Applications	2014 IEEE International Ultrasonics Symposium	2014	Chicago, Illinois, USA

## References

1. Fialka, J. and P. Benes. *Comparison of methods of piezoelectric coefficient measurement.* in *Instrumentation and Measurement Technology Conference (I2MTC), 2012 IEEE International.* 2012.
2. Fialka, J. and P. Benes, *Comparison of Methods for the Measurement of Piezoelectric Coefficients.* IEEE Transactions on Instrumentation and Measurement, 2013. **62**(5): p. 1047-1057.
3. Standization, E.C.f.E., *Piezoelectric properties of ceramic materials and components in Part 1 : Terms and definitions* 2002, cenelec.
4. Ahn, C.W., et al., *Piezoelectric and Ferroelectric Properties of Lead-Free Bi4-xNdxTi2.97V0.03O12 Ceramics.* Ferroelectrics, 2006. **331**(1): p. 129-134.